THE DEVELOPMENT, OPERATION AND EVALUATION OF TWO YEARS OF REAL-TIME SHORT-TERM PRECIPITATION FORECASTING PROCEDURE

by

© A. Bellon

A thesis submitted to the Faculty of Graduate Studies and Research of McGill University in partial fulfilment of the requirements for the degree of Doctor of Philosophy.

Department of Meteorology
McGill University
Montreal

March 1981

ABSTRACT

Digital weather radar data have been used with a simple pattern recognition technique to automatically generate precipitation forecasts in the zero to three hours range. Forecasts performed during a two year real time experiment are evaluated and compared with other basic procedures. The verification process has led to a preliminary "radar climatology" for the Montreal region in the form of maps showing areas of predominant growth or decay of precipitation patterns.

The desirability to extend both the spatial and temporal scales of precipitation forecasts necessitated the incorporation of satellite data into the system. Thus, an algorithm yielding probability of rain from GOES visible and infrared imagery and simultaneous radar data is applied over an area the size of eastern Canada. Satellite data are mapped by means of a conic projection on a constant resolution Cartesian grid to facilitate overlay with synoptic charts. A pattern recognition technique is applied to 16 sub-areas of the entire map and it has proved successful in tracking the displacement of the probability of rain contours. The potential of the satellite data for hydrological purposes is also discussed.

RÉSUMÉ

Les données digitales de radar ont été utilisées avec un algorithme basé sur la théorie de concordance des configurations pour produire automatiquement des prévisions de précipitation à court terme allant jusqu'à trois heures. Les prévisions fournies au Bureau de Prévisions du Québec pendant l'expérience en temps réel qui a duré deux ans ont été évaluées et comparées avec d'autres méthodes de base. Le processus de vérification a conduit à l'établissement d'une carte climatologique radar pour la région de Montréal mettant en évidence les lieux characterisés par un surcroît de développement ou de dissipation d'orages.

La nécessité d'étendre l'échelle temporelle et spatiale des prévisions a forcé l'incorporation des données de satellite dans le système de prévisions. Ainsi, les images digitales prises en rayonnement visible et infrarouge par satellite géostationnaire GOES en conjonction avec les données de radar ont permis de déduire la probabilité de pluie sur une étendue comprenant la moitié est du Canada. Pour en faciliter la comparaison avec les cartes synoptiques, les données sont présentées sur une projection conique avec une résolution constante. La même technique de concordance des configurations appliquée dans chacune des 16 subdivisions de la carte, a demontré qu'il est possible de suivre les zones de probabilité de pluie. Le potentiel de ces données pour besoins hydrologiques est aussi examiné.

ACKNOWLEDGEMENTS

This research was sponsored and directly supported by the MSRB branch of the Canadian Atmospheric Environment Service through the offices of its Assistant Deputy Minister, Dr. A.E. Collins, the Chief of the Satellite Data Laboratory, Mr. E.G. Morrissey (satellite), and by Dr. S. Clodman and Mr. B. Muller (radar).

I am personally indebted to my supervisor, Dr. G.L. Austin, for his guidance and advice throughout the performance of both the radar and satellite projects. In addition, I would like to acknowledge the helpful assistance of members of the Stormy Weather Group, particularly that of Dr. J. S. Marshall and of Mr. E. H. Ballantyne, and of Messrs. R. Fichaud, H. Allard, B. Marois and other personnel of the Bureau de Prévisions du Québec, for their cooperation during the SHARP experiment.

I am grateful to Mr. S. Lovejoy who, in conjunction with my supervisor, derived the theoretical foundations of the original procedure on which much of the satellite work reported here has been based. I am thankful to Drs. Don Wylie, Fred Mosher and Dave Martin, of the University of Wisconsin, who procured the GOES satellite data and the necessary navigation routines.

The contribution of Dr. S. Radhakant and of Mrs. A. Kilambi, who wrote the SHARP archiving program and the output routines for the satellite maps, is greatly appreciated. The satellite pictures and

most of the drawings were generated by Miss U. Seidenfuss, while the text was typed by Mrs. E. Pedersen.

The radar was originally obtained from AFGL and its operation is supported by the National Research Council and the Quebec government.

CHAPTER I

INTRODUCTION

When this research was formulated toward the middle of the 1970's, digital radar data was becoming routinely available at the McGill Weather Radar Observatory. Hence, the primary goal was to devise a reliable, real-time, automated, short-term (0 - 3 h) precipitation forecasting system using a single radar and based on an extrapolation procedure described by Austin and Bellon (1974). Equally important was the analysis of the results in order to assess the performance of the project, the limiting skill due to the extrapolation procedure used, the usefulness of alternate techniques and possible meteorological implications.

Extension of forecasts to longer time intervals (3 - 6 h) necessitates a much larger areal coverage, on account of the rapid movement of rain patterns. For eastern Canada, given unlimited financial resources, a network of 20 or more radars was required, but vast oceanic areas would still not be covered. Hence, practical considerations dictated the obvious solution of detecting rain from satellite. By the late 1970's, research in this domain had progressed significantly. The rain delineation scheme developed by Lovejoy and Austin (1979a), which combines radar and satellite data, was particularly suited to our objectives. Therefore, it seemed sensible, as a supplementary goal, to combine the latter technique with that already tested for forecasting the movement of radar echoes. The increased coverage includes most of southeast Canada and the adjacent parts of the United States viewed by SMS/GOES-E[1] totalling (1500 x 2000) km^2. This step takes us into the synoptic scale and, eventually, may lead to interactions with numerical prognostic models as outlined by Browning (1979).

---

[1]Synchronous Meteorological Satellite/Geo-stationary Operational Environmental Satellite-East (North America).

1.1 Review of Past Research

Since the work presented in this thesis can be divided into two main sections, namely "radar only" and "radar-satellite" research, the review of the literature follows an equivalent structure.

The idea of using radar records of precipitation for forming short-term weather forecasts has been inherent in radar meteorology since its inception. Hilst and Russo (1960) pioneered the use of the maximum cross-correlation coefficient as the objective extrapolation predictor in forecasting precipitation echoes. In addition, the forecasted precipitation distribution was compared with the actual precipitation pattern by an additional correlation technique. Cross-correlation patterns are normally obtained from digital arrays of data by computer, although Zawadzki (1973) has demonstrated a photographic technique. Prior to the advent of digital radar data, simple extrapolation techniques which did not require computer hardware were devised as in Kessler (1961). Boucher (1963) classified precipitation echoes into three distinct categories for forecast purposes: squall lines, precipitation edges and amorphous fields with the latter exhibiting the highest predictability. Kessler and Russo (1963) and Kessler (1966) returned to a mathematical treatment of the forecast problem. With the help of a computer program, statistical parameters are assigned to digitized weather patterns as average intensity, variance, pattern bandedness, orientation of bands, ellipticity and characteristic pattern length. The cross-correlation coefficient, γ, is efficiently calculated by assuming it to be in a simple exponential form. The magnitude of its maximum value, γ_{max}, is an indication of pattern development, while its location represents the best estimate of the pattern average motion. Wilson (1966) extended their work by examining the behaviour of γ_{max} as the time interval between patterns is increased and related it to precipitation types. Wilson also recognized

that small-scale features in an echo pattern are "redundant and highly perishable information" which need not be forecasted.

Actual forecasts and verification of radar echoes displacement were performed by Wilk and Gray (1970) and Zittel (1976) by adopting the extrapolation of a linear least square fit through successive positions of echo centroids. This technique is successful for weather situations characterized by scattered, isolated storms of such size that can be defined by means of a proper threshold. Difficulties arise when echoes cross map boundaries, merge, split or undergo drastic changes during successive time intervals. Clustering techniques with a higher degree of computer sophistication have been devised and tested with some success by Duda and Blackmer (1972) and updated by Blackmer et al (1973). The so-called SRI (Stanford Research Institute) model has also been applied to track cloud motions by Wolf et al (1977). This technique is conceptually appealing but may not be able to cope with complex weather systems and is not suitable for rapid execution on a minicomputer installation. The "global" cross-correlation technique applied to the entire radar coverage as advocated by Austin and Bellon (1974) is more appropriate for weather patterns with a relatively large characteristic scale length. PPI (Plan Position Indicator), VIL (Vertically Integrated Liquid water - see Greene (1972)), or CAPPI (Constant Altitude PPI) maps may be used, although the latter is preferable since it is relatively easy to obtain, avoids ground clutter and is better related to surface rainfall than the VIL parameter. Leese et al (1971) also chose the cross-correlation method for obtaining cloud motions from satellite data. Muench (1976) experimented with a simple technique which follows the leading and trailing edge of weather patterns. Interaction of local forecasts of various meteorological parameters, including precipitation, with predictions from numerical models has been achieved by the Model Output

Statistics (MOS) approach, Klein and Glahn (1974). The incorporation of this model into the AFOS (Automation of Field Operations and Services) program is summarized by Klein (1976).

Elvander (1976) presented the results of an experiment where he compared the performance of the above three techniques, that is, the least-square fit of centroid motion, the SRI model and the "global" cross-correlation on the same digital data set. The results were favourable to the "Canadian" technique adopted in this work. It is particularly suitable for those parts of the world where the weather patterns are of the frontal type governed by a strong jet stream and hence with a motion in one predominant direction. In this climate situation, the frequency of air mass storms moving in different directions is greatly reduced, thus discounting the necessity of a technique tracking individual echoes.

Turning to satellite related research, aerospace technology had progressed to such a pace that by the beginning of the 1970's visible and infrared imagery was available in digital format. In fact, some of the earlier work concerning pattern recognition methods involved the tracking of cloud elements from satellite data as already mentioned in Leese et al (1971) and Endlich et al (1971). Our main concern is not the motion of clouds but of rain areas. However, before considering their motion, considerable work has been directed, and is still continuing, towards rain amount estimation schemes from satellite imagery. The research in that field is thus relevant to the present topic.

A comprehensive review of satellite rainfall estimation methods up to 1973 was gathered by Martin and Scherer (1973). It summarizes, among others, the pioneering work of Woodley and Sancho (1971), Martin and Suomi (1972), Sikdar (1972), Follansbee (1973), and Gruber (1973), the latter adopting a 'convection parameterization scheme rather than a predominantly empirical relation between cloud characteristics and precipitation'.

A comparison of radar-determined cloud height and reflected solar radiance was made by Reynolds and Von der Haar (1973) while Griffith and Woodley (1973) investigated the correlation between cloud height and cloud brightness. Daily rainfall was obtained by Follansbee and Oliver (1975) by estimating from IR imagery the time that an area was covered by rain-producing clouds and applying a climatological rain rate. A similar approach was undertaken by Kilonsky and Ramage (1976) in extracting monthly rainfall from highly reflective clouds over the tropical Pacific Ocean. More recently, Stout et al (1979) and Griffith et al (1978) used cumulo-nimbus life history techniques in refining rainfall measurements. Scofield and Oliver (1977) derived a procedure in the form of a flow diagram (decision tree) involving a visual examination of the rate of anvil growth, merging cells and overshooting tops from enhanced IR images in order to derive an appropriate rainfall rate associated with cumulo-nimbus clouds. Reynolds and Smith (1979) extended their technique by using remapped radar, rain gauge and synoptic data. Since most of the above techniques were tested on regions of convective activity particularly in the tropics, Wylie (1979) attempted with some success, to apply them to a non-tropical area, namely the Montreal region.

Of significant importance are the concluding remarks of the review paper by Martin and Scherer (1973): "Based on bivariate frequency distribution of brightness versus temperature, Gruber concluded that brightness enhancing or infrared technique alone may be inadequate to deduce details of convective activity.... This implies that better estimates of rainfall will come from visible and IR observations <u>combined</u> than from either used alone". However, with the exception of a note on image differencing by Reynolds et al (1978), this recommendation had not been acted upon until the two-wavelength pattern-recognition technique of Lovejoy and Austin (1979a) was introduced. The application of this algorithm to rain amount estimation is discussed in Lovejoy and Austin (1979b).

1.2 Scope of Thesis

The present work describes the operation of the SHARP (SHort-term Automated Radar Prediction) project undertaken by the Atmospheric Environment Service of Canada as an experimental real-time test which started with the 1976 summer season. Two years of 3 km CAPPI data are analyzed in terms of the spatial error of the forecast displacement. A verification of forecast and actual rainfall intensities is performed by means of the CSI (Critical Success Index) parameter, and the skill of the extrapolation technique is evaluated relative to other basic methods. A geographical distribution of storm growth and decay is then derived and related to topographical features. The salient aspects of the SHARP test were published in Bellon and Austin (1978).

The possibility of varying the CAPPI height as a function of weather types as well as the effects of decreasing the time interval between correlations are examined in chapter V. A development and dissipation program and the forecasting of differential motion are attempted in chapter VI, with marginal improvement with respect to the basic technique.

Chapter VII is totally dedicated to satellite related work. It presents an extension of the fundamental treatment of satellite data by Lovejoy and Austin (1979a) but applied over the synoptic scale. It is refined by the development of the notion of a probability of rain map, the determination of rain areas trajectories, and by the derivation of an empirical relationship between rainfall rate from radar and probability of rain from satellite.

CHAPTER II

THEORY AND DATA BASE

2.1 Basic Forecast Technique

The fundamental forecast procedure used in this real-time experiment is a linear extrapolation of precipitation patterns, for a duration of one to three hours, according to the "status quo" assumption, that is, all echoes within radar range are translated by an equal amount proportional to a calculated past motion, and without any modifications to their area or intensity distribution. It is realized that this elementary approach often referred to as "nowcasting" does not reflect the true "state of affairs" in the atmosphere. However, as further research reported in Chapter VI will demonstrate, the incorporation of a statistical storm development technique was not expected to yield markedly improved results. Likewise, the differential motion algorithms attempted by other investigators, e.g. Blackmer et al (1973), were not only complicated, time consuming and required a larger computer, but had not yet proven themselves on a large number of cases. Moreover, we were encouraged by the comparison by Elvander (1976) which demonstrated the superiority of the technique described here.

While one can deplore the lack of meteorological input to our technique, it is realized that the short time interval under consideration does not at present permit the acquisition and processing of potentially useful radiosonde data, stability indices and regions of convergence and divergence with their associated upward and downward air motions. If these parameters were available at the desirable space and time resolution, no macro-scale theory presently exists which can incorporate them into a procedure capable of successfully altering the course and structure of observed radar echoes, although we believe this to be a most fruitful area of future research. Recently, some attempts have been reported by Zawadzki (1978 and 1980) and by Thomas and Houghton (1979).

In a pilot real-time experiment, it is believed to be more appropriate to start from a basically simple technique, which has already demonstrated some hope of success, with the intention of an eventual comparison with subsequent improved models. Finally, since the products were to be received and interpreted by meteorologists on duty, a simple mode of output was desirable as opposed to the unpredictable modification of the original data set performed by yet unproved forecast techniques.

In essence, the forecast procedure consists of making digital (CAPPI) Cartesian maps at 3 km with a minicomputer on line with the radar and matching the pattern on two maps 1 h apart by means of a statistical pattern recognition algorithm (Austin and Bellon 1974). The lag of the best match, and hence, the pattern displacement, is determined by the location of the maximum cross-correlation coefficient defined below.

2.2 Definition of the Cross-Correlation Coefficient

The cross-correlation coefficient, γ, between two patterns indicates the degree of matching which exists between them as their relative position in space or time, or both, are varied with respect to each other. The rigorous mathematical definition is given by

$$\gamma(x_o,y_o,\Delta t) = \frac{1}{N\sigma_i\sigma_{i+1}} \iint [F(x,y,t_i)-\overline{F(t_i)}][F(x+x_o,y+y_o,t_{i+1})-\overline{F(t_{i+1})}]dxdy \quad (2.1)$$

where

a) $\gamma(x_o,y_o,\Delta t)$ is the cross-correlation coefficient between two patterns separated by a time interval $\Delta t = t_{i+1}-t_i$ and by a spatial lag given by (x_o,y_o).

b) $F(x,y,t_i)$ is the two dimensional intensity distribution of the pattern at time t_i. In our case, the pattern is a digital rainfall map on a 64 x 100 array with a spatial resolution of 7.5 km x 4.8 km. While the intensity resolution of radar digital maps can be arbitrarily large, e.g. 16 or 32 levels, it is convenient to degrade it to a coarser scale without significantly affecting the final result. Hence, in cross-correlation computation, $F(x,y,t_i)$ has been quantized into 5 integer values such that $0 \leqslant F \leqslant 4$.

c) $N = \iint dxdy$ is the area of integration containing both patterns. While the digital CAPPI maps extend up to a range of beyond 300 km, the CAPPI data are true at 3 km up to a range of only 170 km with a first elevation angle of 0.6°. Beyond this range, the appearance of precipitation patterns is increasingly dependent on height and beam filling effects. However, in order to be able to issue forecasts well in advance of a storm arrival, the maximum range of correlation has been extended to 205 km. A subsequent analysis (Chapter IV) revealed that this is still within the limits of good radar quality. As a result, the number of matched pairs in the computation of γ is about 3600 at zero lag.

d) $\overline{F(t_i)}$ is the average value of field F over the area N at time t_i, i.e.

$$\overline{F(t_i)} = \frac{\iint F(x,y,t_i)\, dxdy}{N}$$

e) σ_i is the standard deviation of F over N at time t_i.

$$= \left\{ \frac{\iint [F(x,y,t_i) - \overline{F(t_i)}]^2\, dxdy}{N} \right\}^{\frac{1}{2}}$$

In view of the mathematical definition adopted, γ is properly normalized, $-1 \leqslant \gamma \leqslant 1$. The maximum value is obtained when a pattern is correlated with

itself, or with a constant times itself, i.e. $\gamma = 1$ if $F(x,y,t_i) = k.F(x,y,t_{i+1})$ and x_o and y_o are both zero. For two antisymmetric patterns for which $F(t_i) = -k.F(t_{i+1})$, $\gamma = -1$. Hence, both positive and negative partial contributions to the magnitude of γ are possible, the latter case arising when an element with a value higher than the average of the overall pattern is matched with an element of the other pattern having a value inferior to its corresponding average.

The presence of boundaries and the motion of patterns through them necessitate some consideration. In order to avoid spurious contributions to γ, only that portion of $F(t_{i+1})$ which was also within maximum range at time t_i is correlated with $F(t_i)$. The elements of $F(t_{i+1})$ which became within that range during the time interval $\Delta t = t_{i+1}-t_i$ are omitted.

When locating the lag of maximum correlation γ_{max} at (x'_o, y'_o), it is advisable to make use of time saving computer techniques, particularly when the correlation is performed on relatively slow minicomputers. The first step is to adopt a reasonable first guess in directing the computation of γ at lags close to the expected maximum. Prior to the first forecast of each sequence, the initial guess may be the motion of the centre of gravity of the precipitation system, or some climatological average velocity, and, for all subsequent forecasts, the displacement computed from the previous forecast. Since this guess may, at times, be erroneous, a relatively large matrix of cross-correlation coefficients must be formed in order to contain γ_{max}, necessitating a very large number of useless computations. Thus, the cross-correlation matrix is first roughly estimated at every second lag, reducing the number of operations by a factor of 4. If the value of γ_{max} falls on a boundary of the cross-correlation matrix, the latter is further enlarged until γ_{max} is completely enclosed by it. After a maximum has been located on the "coarse grid", the computational process is re-initialized

with the lag of γ_{max} as the initial guess. This is the "fine grid" correlation where the value of γ is calculated at every lag, except where it has already been computed on the coarse grid. Additional execution speed can be acquired if the matching of zero pairs is ignored, and if the two arrays of radar data are equivalenced to two one-dimensional vectors.

Note that the exact derivation of γ involves operations on variables in decimal form, a rather time consuming procedure on small computers. Since the number of pairs to be matched is at least 3000, and each partial contribution to γ at one lag (x_o,y_o) essentially requires four such operations (two subtractions, one multiplication and one addition), the total time required to locate γ_{max} (after about 50 lags or 600,000 operations) may often exceed 3 minutes. This amount is a significant portion of the 5-minute period allocated to SHARP. Originally, the problem was avoided by assuming the pattern averages to be zero and accumulating in integer mode a pre-calculated product according to an arbitrary function of $F(t_i)$ and $F(t_{i+1})$. Normalization of the sum was approximated by dividing only by N. The rigorous computation of γ was performed only at the lag of γ_{max}. However, toward the end of the 1977 test, it was realized that γ could be calculated in integer mode while still following the exact mathematical definition at no extra cost in time, thus avoiding all arbitrary corrections.

Let $A(x_o,y_o)$ be the "HITS" matrix between pattern $F(t_i)$ and $F(t_{i+1})$ at a spatial lag of (x_o,y_o). This matrix can be quickly obtained solely with integer operations. The $(i,j)^{th}$ element of the matrix, a_{ij}, denotes the number of occurrences in which the (j-1)th intensity integer of $F(t_i)$ falls on the (i-1)th intensity integer of $F(t_{i+1})$ when the former is translated by a lag of (x_o,y_o). The average of the two fields can then be expressed as

$$\overline{F(t_i)} = \frac{1}{N} \sum_{j=1}^{5} \sum_{i=1}^{5} (j-1)\, a_{ij}$$

and

$$\overline{F(t_{i+1})} = \frac{1}{N} \sum_{j=1}^{5} \sum_{i=1}^{5} (i-1)\, a_{ij}$$

where

$N = \sum_i \sum_j a_{ij}$ is the number of matching pairs.

The standard deviation becomes

$$\sigma_i = \left\{ \frac{\sum_{i=1}^{5} \sum_{j=1}^{5} a_{ij} \left((j-1) - \overline{F(t_i)} \right)^2}{N} \right\}^{\frac{1}{2}}$$

and

$$\sigma_{i+1} = \left\{ \frac{\sum_{i=1}^{5} \sum_{j=1}^{5} a_{ij} \left((i-1) - \overline{F(t_{i+1})} \right)^2}{N} \right\}^{\frac{1}{2}}$$

The cross term of equation 2.1 is computed as

$$\sum_{i=1}^{5} \sum_{j=1}^{5} a_{ij} \left[(i-1) - \overline{F(t_{i+1})} \right] \left[(j-1) - \overline{F(t_i)} \right]$$

Since the above operations necessitating floating point mode are performed only over the (5 x 5) matrix rather than for each (I,J) element of the correlated patterns, computation time is drastically reduced. The location of γ_{max} can be obtained as quickly as with the integer approximation originally devised, namely in about 45 seconds.

While the auto-correlation and Eulerian correlation, discussed in Zawadzki (1973), may reveal some interesting characteristics of the precipitation patterns, we shall concern ourselves only with the Lagrangian or cross-correlation. The latter incorporates changes in the shape and internal structure of a precipitation pattern. It records the modifications which occur in time as observed by an observer moving with the average velocity of the storm. If, for any given time interval Δt, the spatial lag (x'_o, x'_o) is

such that γ is maximized, then this lag is a measure of the average displacement of the storm during the time interval Δt. The most probable velocity is then given by $\overline{V} = \sqrt{u^2 + v^2}\ (\overline{u}', \overline{v}')$ where $u = \frac{x'_o}{\Delta t}$ and $v = \frac{y'_o}{\Delta t}$ and $(\overline{u}', \overline{v}')$ is the unit vector defined by the (x'_o, y'_o) pair. The extent to which γ_{max} is greater than γ for the surrounding lags indicates the level of confidence which can be assigned to the measurement of the translation (x'_o, y'_o).

Since the magnitude of γ_{max} has been commonly assumed to be a measure of pattern predictability as in Wilson (1966), consideration must be given to the factors affecting it. It is readily apparent that, since it reflects changes in pattern appearance, γ_{max} decreases as the time interval separating them increases. For a constant Δt, radar patterns undergoing rapid development or dissipation will yield a lower γ_{max} than those behaving more like a steady state configuration. The former are usually of a convective and/or frontal nature, while the latter are associated with widespread upward air motion of a low pressure passage, especially in late spring or early fall. The intensity distribution of a digital pattern is also significant. In particular, the higher rainfall rates, which contribute a proportionally larger weight to γ, are less likely to be long lasting, while the very low rates, especially those of small areal extent, constitute highly perishable information. When the precipitation pattern is composed of radar echoes moving in different directions, a relatively low value of γ_{max} will be obtained since, at the lag of their average motion, mismatches may occur between the various patches. In some cases, this effect is noticeable by the appearance of secondary maxima. A similar reduction of γ_{max} occurs when differential motion exists between a widespread precipitation system

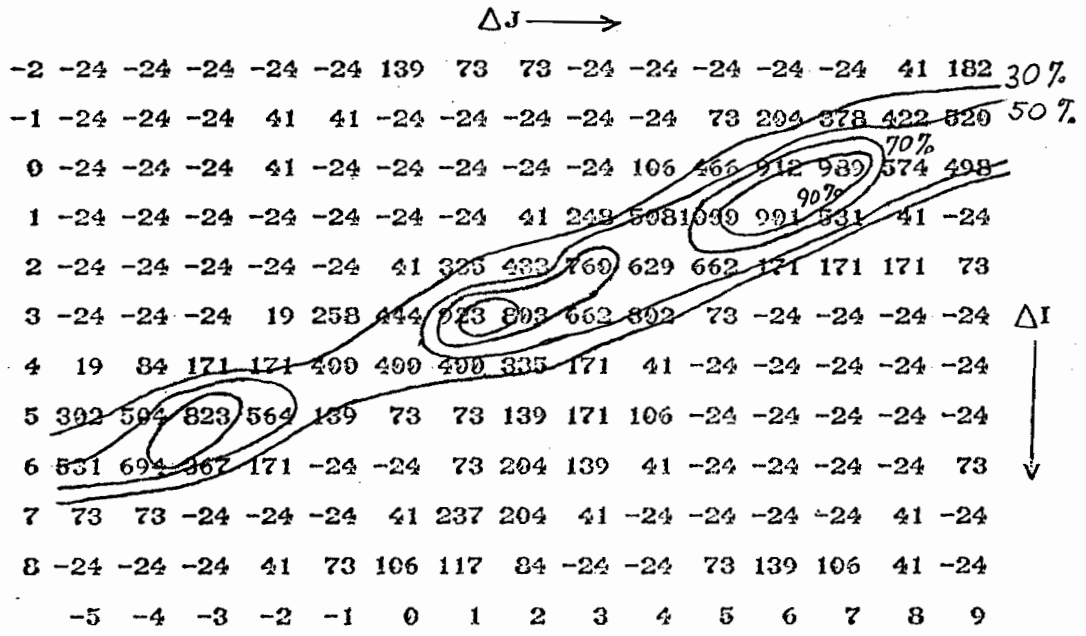

Fig. 2.1a. Cross-correlation of a thin precipitation line taken 30 minutes apart. The magnitudes of γ are normalized with respect to γ_{max}, where $\gamma_{max} = \gamma(1,5) = 0.375$.

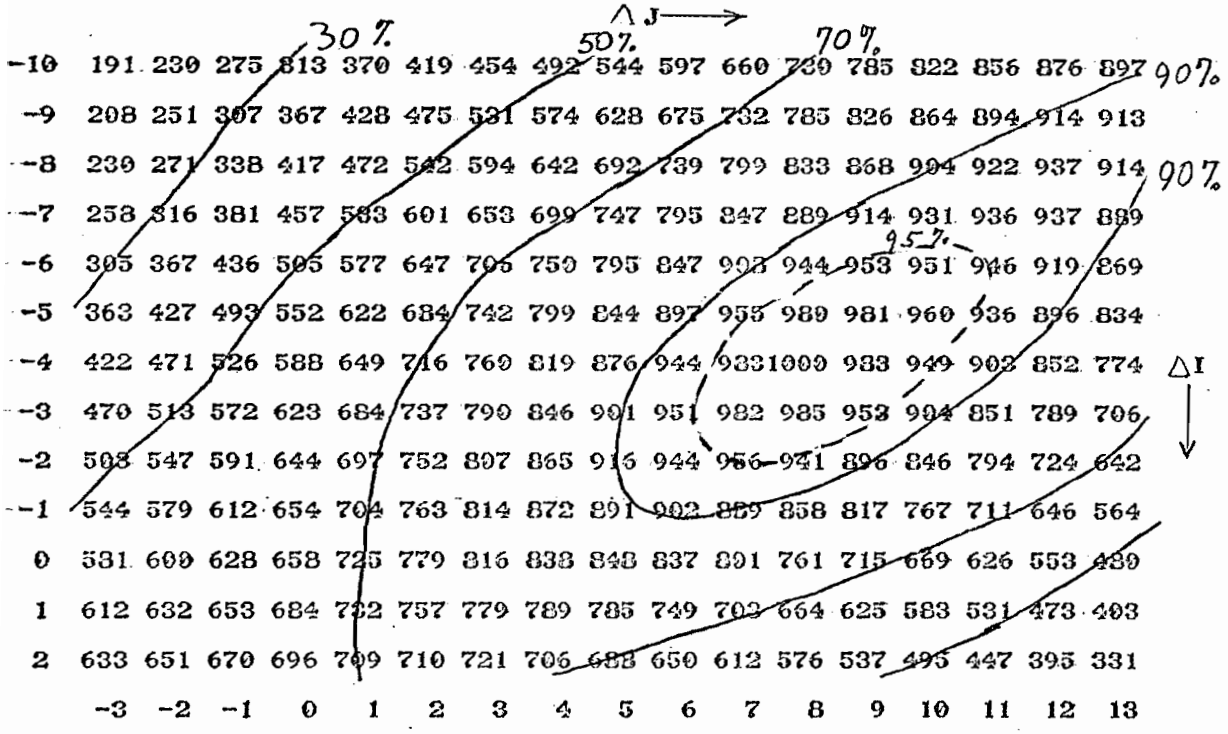

Fig. 2.1b. Cross-correlation of an extensive precipitation pattern taken an hour apart. The magnitudes of γ are normalized with respect to γ_{max} where $\gamma_{max} = \gamma(-4,8) = 0.626$.

and the higher reflectivity cores embedded in it. Finally, the scale length of the patterns being correlated has a determining influence on both the magnitude of γ_{max} and on the gradient of γ at neighbouring lags.

Figs 2.1a and 2.1b are examples of a cross-correlation matrix, illustrating two extreme situations. Fig. 2.1a is the cross-correlation matrix of a thin squall line taken 30 minutes apart. Its NE-SW orientation is clearly visible and its scale length can be inferred as being only of a few grid lengths (~ 10 km wide[1]), and perpendicular to its elongation as evidenced by the rapid drop of correlation values. The magnitude of γ_{max}, at a lag of (1,5) corresponding to a velocity of 52 km h^{-1} from 281°, is 0.375, a fairly low value for a time scale of 30 minutes. It indicates that the various elements of the squall line have radically altered their structure and/or that they have not moved at their common average velocity. The existence of marked secondary maxima illustrates a periodicity in cell distribution. The example portrayed in Fig. 2.1b is the correlation between two extensive precipitation areas - (300 x 150) km^2 - one hour apart. The visual appearance of the cross-correlation pattern is drastically simpler. There is a broad region of high relative correlation - above 0.90 γ_{max} - signifying that the position of γ_{max} is not strongly localized. The area enclosed by the 95% γ_{max} contour can be arbitrarily defined as the "region of uncertainty", whose extent is a measure of the deviation of possible motions about the most probably displacement denoted by the lag of γ_{max}.

---

[1] The example is based on a manually digitized data set with a spatial resolution of 5.1 km derived prior to the real-time test.

2.3 Advent of Digital Data

Before proceeding to a detailed description of the field experiment, let us review the development work required for the manipulation of raw digital data into useful maps which serve as input to the forecasting program.

Prior to the 1974 summer season, the data recorded at the McGill Weather Radar Observatory were available on heat sensitive paper in PPHI[1] format at an approximate height of 10,000 feet (Marshall and Ballantyne (1970)). Data in polar form were recorded on 35 mm film for all elevation angles. HARPI's[2] at selected range gates were similarly stored (Zawadzki and Ballantyne (1968)). As retrieval was a tedious process, quantitative analysis of radar data was restricted to a limited number of cases, otherwise processing escalated to a very lengthy task. However, the advent of digital data not only prompted the immediate execution of a real-time short-term precipitation forecast experiment and facilitated its verification analysis, but also provided the speed essential to similar large volume data processing frequently necessary in hydrology and radar climatology. The transition to a digital format became a sudden reality thanks to rapid technological advances in the field of computer science, in particular, to the "off the shelf" availability of relatively low-cost, but efficient minicomputers and their peripherals. An acute problem to be surmounted was the acquisition and recording of a fast data rate in an efficient manner so that the magnetic tape will last a reasonable length of time. Since precipitation data usually comprise about less than 10% of the data sites in three dimensions, a proper data compression algorithm as well as the elimination of ground clutter were imperative.

---

[1] PPHI: Plan Position with Height Indicator.

[2] HARPI: Height Azimuth Range Plan Indicator.

2.3.1 Data Processing

The natural radar coordinates are range R, azimuth θ, and elevation angle ϕ. The azimuth spacing of the McGill Radar, set at 0.6° is made just finer than the beam width of 0.85° so that there are 600 returns or "pips" per revolution. The 149 range divisions or "bins" are linearly spaced 750 meters apart at close ranges between 8.25 and 36.00 km (bin #1 to #37). From bin #38 to #149 at 373 km, the divisions increase exponentially from 750 meters to nearly 8 km in such a way that the bin length is equal to twice the azimuthal resolution (1.2°), that is $R_{n+1}=R_n + 2R_n\theta$ for $n > 37$ where R_n is the range at the start of the n'th bin and $\theta = 0.6°$ is expressed in radians. In exponential form, the above relationship becomes $R_n = R_{37}e^{0.020971(n-37)}$ for $n > 37$ where R_{37} is the range at the start of the 37^{th} bin at 35.25 km.

The area of each bin thus varies from less than 0.5 km^2 to nearly 60 km^2. The number of data points in a full rotation, performed in 10 seconds, is 9×10^4. The duration of a complete cycle of the radar antenna is five minutes. It involves 24 stepped rotations, starting at 0.6° above the horizon, increasing exponentially to 34.4°, and then returning to its original starting position. Hence, the whole cycle consists of over 2×10^6 data points.[1]

A tape archiving program records the data in log-range B-Scan format as it enters the minicomputer directly from the radar interface. To reduce tape consumption, four reflectivity values are packed into one 16-bit word,

---

[1] The description presented here applies to data recorded before the fall of 1976. Presently the resolution of the data has been increased to 3.6×10^6 data per cycle as follows:

pips x bins x no. of elevation angles = data/cycle

375 x 400 x 24 = 3.6×10^6. The range divisions are exponential over the entire range of 12.5 km $\leq$ R $\leq$ 400 km. Their length is 0.01R for $12.5 \leq R \leq 200$ and 0.005R for $200 \leq R \leq 400$. The first elevation angle has also been lowered to 0.3°.

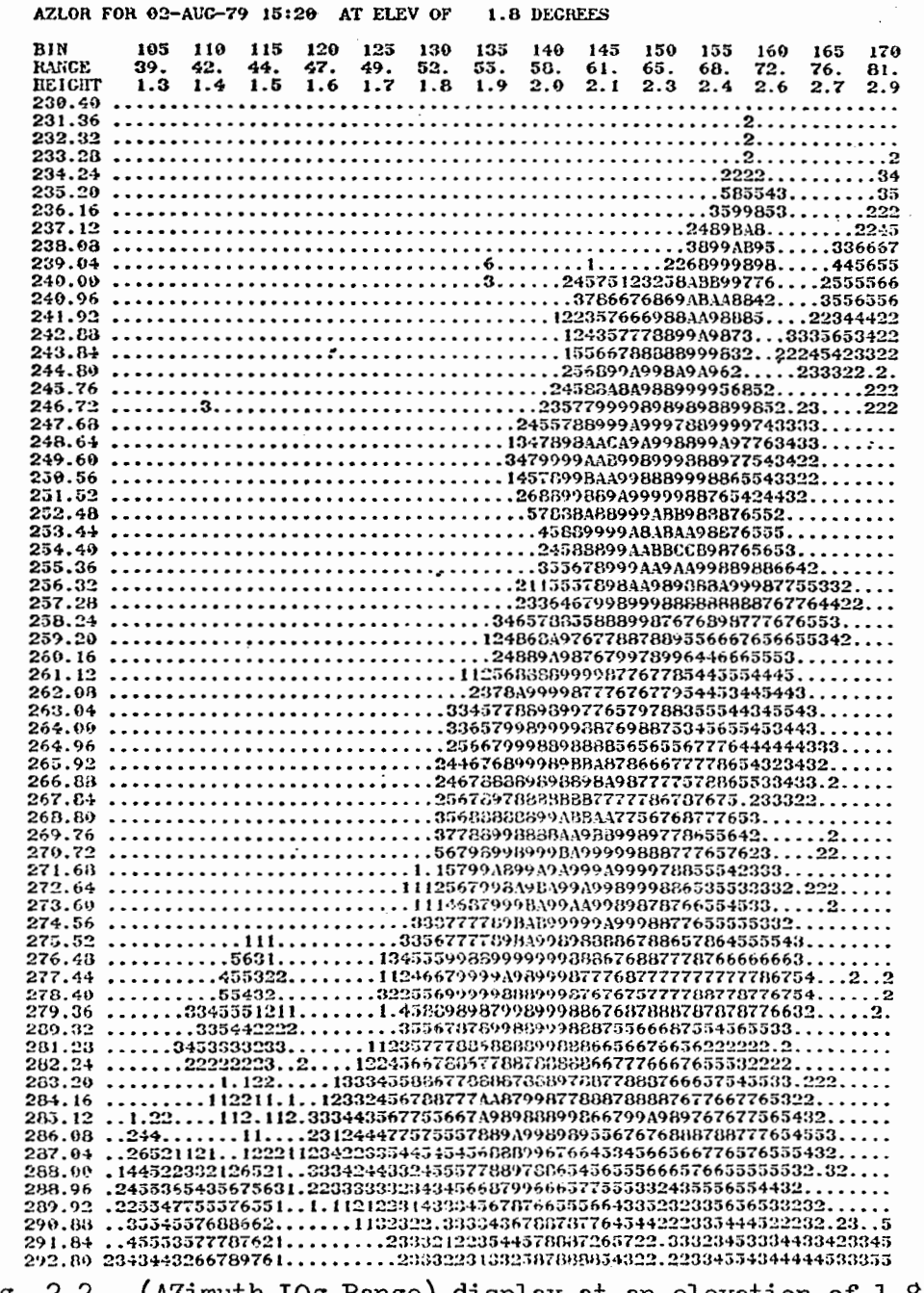

Fig. 2.2. (AZimuth LOg Range) display at an elevation of 1.8 degrees at 1520 EST 2 August 1979. Azimuth is read vertically while the radar range bin number, the range and height in km are provided horizontally across the top of the display. The location of this sector is shown in Fig. 2.6 by a dashed line. Note that a better reference with the four cardinal points is obtained by rotating this display by 180 degrees. The lower thresholds in dBz and mm h^{-1} corresponding to the intensity levels are given below.

level	1	2	3	4	5	6	7	8	9	A	B	C	D	E	F
dBz	16	20	24	28	32	36	40	44	48	52	56	60	64	68	72
mmh^{-1}	0.37	0.65	1.15	2.05	3.65	6.49	11.5	20.5	36.5	64.9	115	205	365	649	1150

or four bits per data site, allowing a range of magnitudes from 0 to 15. Each level is kept 4 dBz wide from 16 to 76 dBz. Data are then grouped into 5-word blocks, where the first word provides the elevation and azimuth information. A zero suppression technique has been incorporated by which, after masking the nearby ground clutter, a block, that is, 16 radially consecutive data points, containing only zeroes, is not recorded.

Data for any elevation angle can be easily dumped in their natural coordinates to form a display commonly known as AZLOR (AZimuth LOg Range), an example of which is given in Fig. 2.2. Here the data are displayed in their optimum resolution, revealing the gradient of reflectivity distribution and the finer, small scale features of radar echoes. However, in order to obtain a proper spatial perspective of precipitation patterns, it is essential to operate a transformation from polar (R,θ) to a Cartesian (I,J) grid, according to the following equations:

$$I = I_o - R_G \cos\theta \qquad \text{and}$$

$$J = J_o + R_G \sin\theta \qquad \text{where}$$

(I,J) : refers to the row and column pair of an array

θ : clockwise aximuth from north

R_G : range R in units of grid length

(I_o,J_o) : radar location on array.

In view of the above discussion concerning data density as a function of range, it is evident that, upon a coordinate transformation, a considerably larger number of polar points will fall inside a grid area at close range than inside one near the edge of the display. For a typical (6×6) km^2 grid area, this number varies from about 300 at 15 km to 15 at intermediate ranges (100 km), down to 4 or 5 at 200 km. Since we can attribute only one

value to each matrix element, some form of averaging must be imposed. However, it should be performed in such a way that the reduction in the quantity of data points, that is, from 9×10^4 to less than 6×10^3, will entail a minimal loss of information. Since we believe rainfall rate is a meteorologically significant parameter whereas radar reflectivity is only pertinent because it is what the radar measures directly, the most appropriate form of smoothing is to average with respect to rainfall rate. Hence, for all polar dBz intensity values falling within a certain grid area, their corresponding rainfall rates are added and an average rate is derived by dividing the sum by the total number of polar points inside the Cartesian grid. Since, for display purposes, we are restricted to ascribing only one character per matrix element while rainfall rates may span over three orders of magnitude, the matrix element is loaded with one of 16 approximately logarithmic rainfall rate intensity levels whose thresholds contain the computed average rate. This procedure can be illustrated as follows:

1) $I_i \rightarrow R_i$: convert digital dBz levels to rainfall rate according to the Marshall-Palmer equation $Z = 200\ R^{1.6}$

2) $S = \sum_i R_i$: integrate the rainfall rates.

3) $N = \sum_i$: total the number of polar data inside (I,J) Cartesian grid areas.

4) $\overline{R} = \frac{S}{N}$: compute average rainfall rate.

5) $\overline{R} \rightarrow \overline{I}$: replace average rainfall rate by appropriate intensity level.

Other, more expedient, but not as meaningful techniques can also be performed like displaying the highest polar dBz level inside each grid area, or the simple average of the polar levels, that is,

$$av(I) = \frac{\sum_i I_i}{N}$$

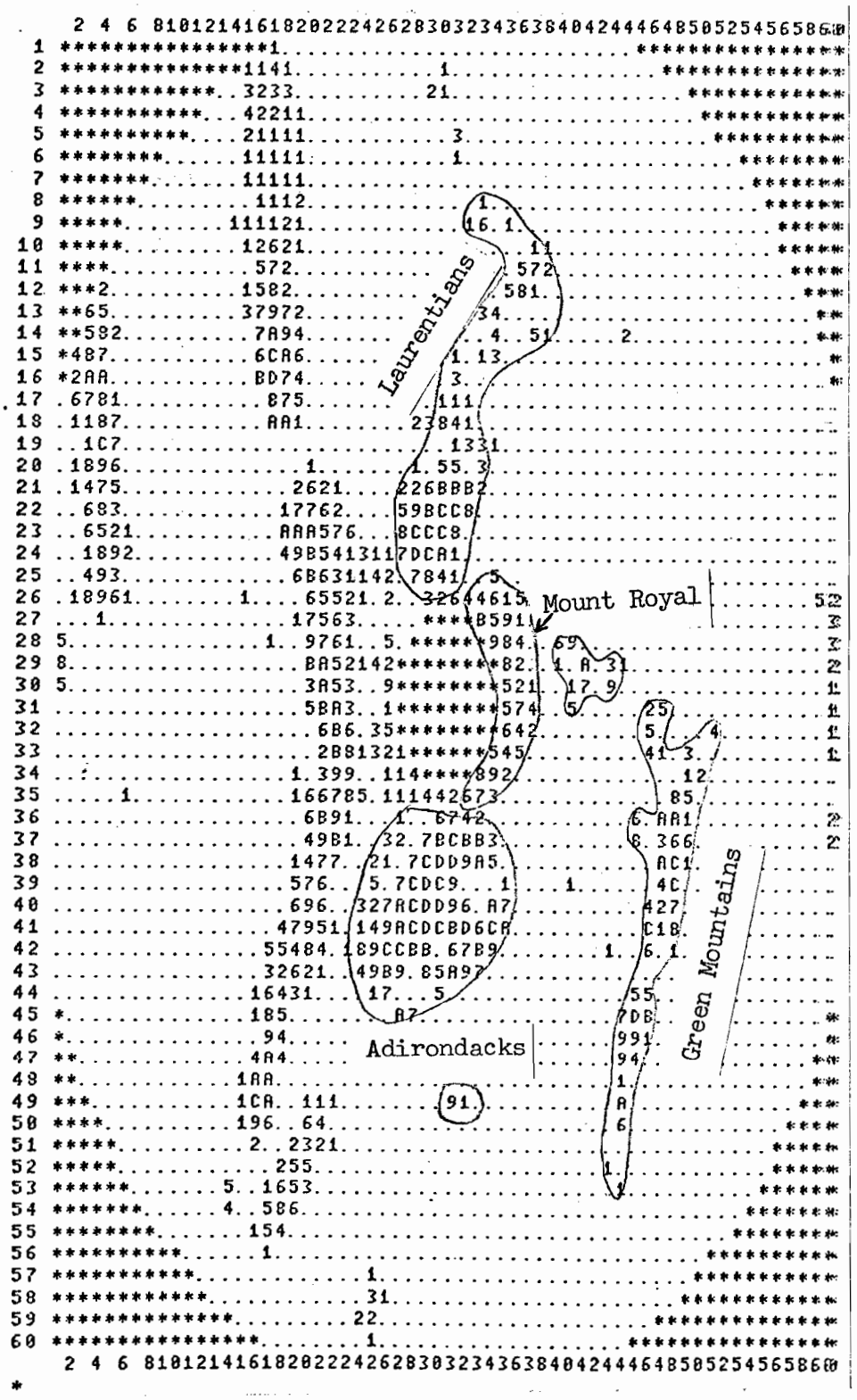

Fig. 2.3. Cartesian PPI of the first elevation angle (0.6 degrees) at 1128 EST 13 June 1975. The minimum and maximum range is 30 and 203 km with a grid length of 6.4 km. Note the extensive ground clutter of this lowest elevation angle. Since 1976, radar returns lower than 1 km have been suppressed in order to reduce tape consumption caused mainly by ground echoes. The rainfall rate scale is given below.

level	1	2	3	4	5	6	7	8	9	A	B	C	D	E	F
mmh^{-1}	1.2	1.9	2.9	4.5	7.0	10.8	16.6	25.5	39.2	60.4	93.1	143	221	340	523

Note that since Z and R are not linearly related,

$$av(I) \neq \overline{I}$$

This fact is particularly evident in instances of tight sub-grid gradients of rainfall rates predominant in convective storms. Actual computations for these examples have revealed that the total waterflux over the map area could be underestimated by as much as 50% using av(I). In situations of continuous uniform precipitation, differences of less than 5% were noted between the two techniques.

2.3.2 Digital Displays of Radar Echoes

a) PPI (Plan Position Indicator)

The most familiar display of radar data is a PPI of a complete rotation at any elevation angle, Fig. 2.3. Each of the levels displayed represents the average rainfall rate over the corresponding (I,J) grid. Though not particularly evident in this example, similar displays are characterized by the presence of a "halo", a region of lower levels, surrounding the precipitation pattern, Pytlowany and Scherer (1975). It is the outcome of the incomplete filling of the Cartesian grid by the polar data. The area of the precipitation patterns is accordingly overestimated but not the total rainflux over the grid. For the same reason, small scale rainfall gradients are sharply reduced. However, tests have confirmed that the total flux, whether computed from the raw polar data, or from the degraded Cartesian display, remains unaltered.

These digital displays can be obtained from a minicomputer at the reasonable time of less than 1 minute (usually 30 seconds), depending on the amount of zero suppression, or, conversely, of areal coverage for a particular elevation angle. The size of the elemental grid area $A_{(I,J)}$,

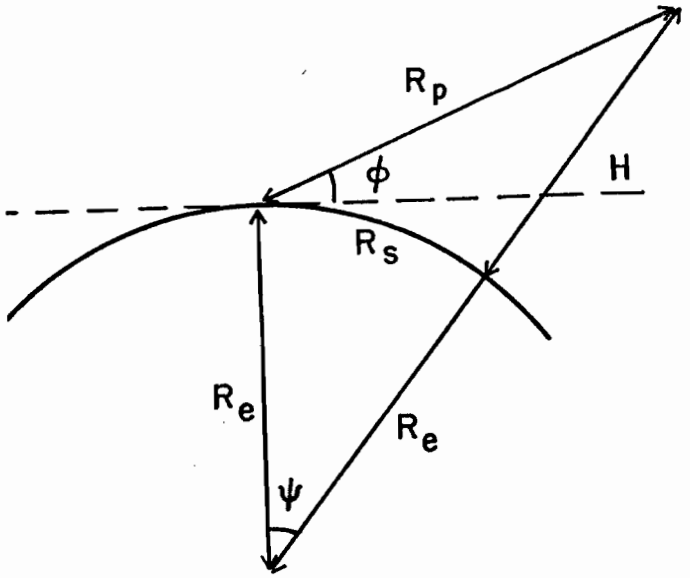

H: Height above earth's surface

R_e: Earth's radius

ϕ: Elevation angle with respect to horizon

R_p: Plane range along beam direction

R_s: Range along earth's surface

$$H + R_e = \left[R_e^2 + R_p^2 - 2R_eR_p\cos(90^\circ + \phi)\right]^{\frac{1}{2}} \qquad \text{cosine law}$$

$$\psi = \tan^{-1}\left(\frac{R_p\cos\phi}{R_e + R_p\sin\phi}\right)$$

$$R_s = R_e\psi \doteq R_p\cos\phi$$

For normal refraction, replace R_e by $R_e' = 4/3\ R_e$

For all practical R_p and ϕ, $R_s \doteq R_p$

ϕ	R_p (km)	R_s (km)	Difference (km)	Height (km)
0.6	200.950	200.890	0.060	4.48
2.3	200.950	200.598	0.352	10.7
0.6	100.586	100.568	0.018	1.65
5.6	100.586	99.991	0.595	10.4
2.3	40.824	40.783	0.041	1.74
6.7	40.824	40.522	0.302	4.86
14.8	40.824	39.421	1.403	10.5

Fig. 2.4. Calculation of beam height above the earth's surface as a function of range and elevation angle.

is a function of the array dimensions and of the chosen maximum range R_{max} of the display. In practice, R_{max} = 200 km, much less than the instrumental maximum range of 400 km. It is desirable to force $A_{(I,J)}$ as small as possible. This may be achieved by increasing the matrix size while keeping R_{max} relatively large. This approach must satisfy core and output constraints, as well as considerations of an increased execution time for analysis on any small computer. If a reduction in R_{max} becomes necessary but, as is the case in short-term forecasting, it is desirable to monitor the motion of a storm as soon as it is radar detectable, a procedure could be adopted which off-centres the radar to a position downwind of the prevailing or expected motion of the precipitation echoes. As a result, at the cost of sacrificing information beyond medium ranges on the downwind side of the radar, both a large R_{max} and a reduced $A_{(I,J)}$ will be attained.

Note that the shape of $A_{(I,J)}$ is not a square in true plan. It is realized that, on account of the unequal horizontal and vertical character spacing of output devices, the PPI display becomes conformal only if the grid lengths in the E-W and N-S directions are made proportional to the aspect ratio, usually 3:5. The dimensions of the matrix are similarly chosen. Finally, the corners of the matrix are devoid of data if a constant R_{max} is desired in all directions, thus reflecting the familiar radar video. Minimal computational effort is required to fill them with the available data.

b) CAPPI (Constant Altitude Plan Position Indicator)

It is known that the usefulness of PPI's, particularly for forecasting purposes, is limited on account of the range dependence of the height. At low elevation angles, a considerable area at close ranges is essentially obliterated by ground clutter while at higher elevations, the radar beam

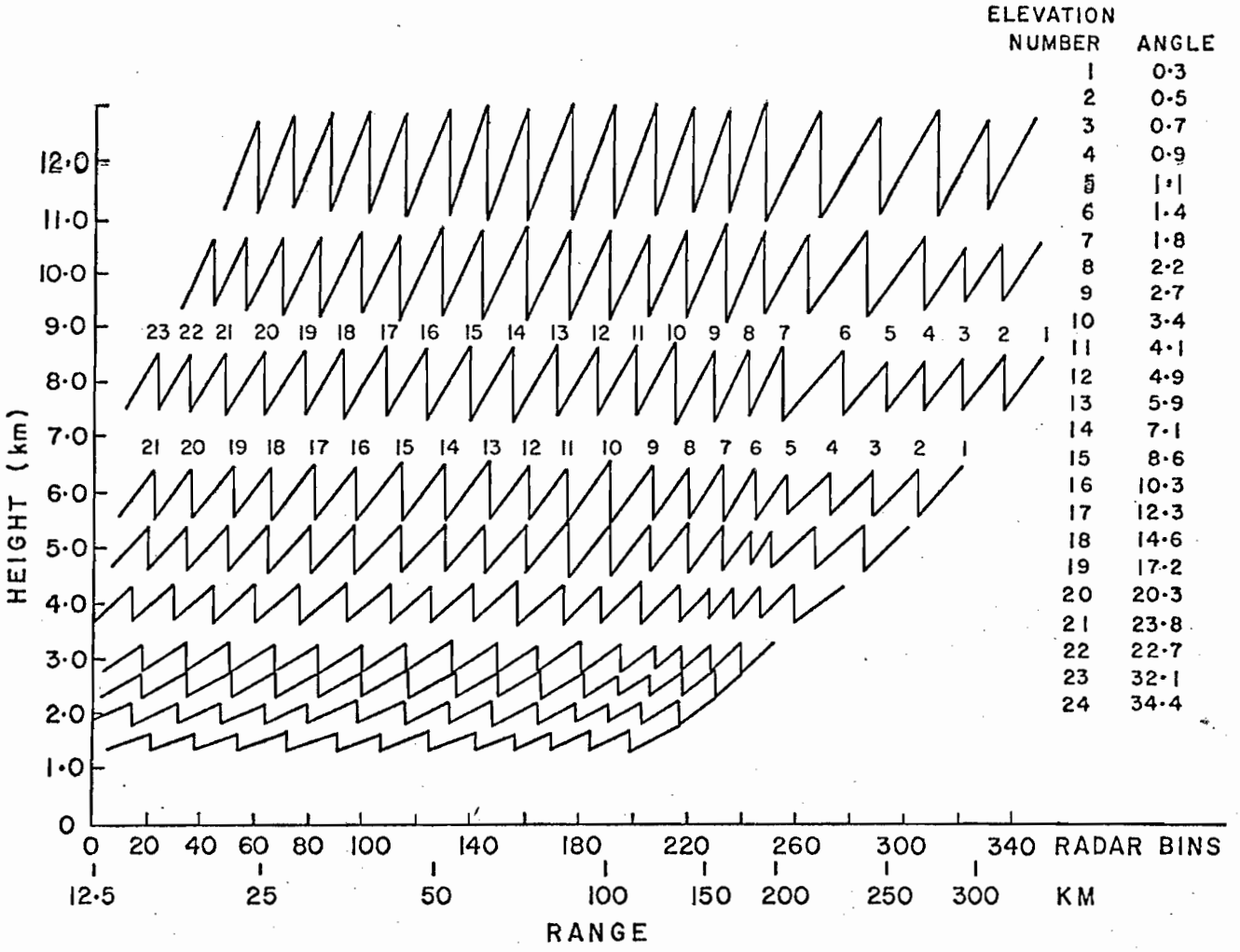

Fig. 2.5. Plot showing the segments of the beam centre at selected constant heights for the antenna elevation programme since October 1976.

scans the major portion of the map area at a height above the region of possible precipitation echo returns. Hence, it is imperative to produce CAPPI's as input to a forecasting algorithm as well as for appropriate display of precipitation patterns.

The initial stage of CAPPI production consists in deriving a plot of height versus range for all elevation angles. As illustrated in Fig. 2.4, this relationship can be derived accurately from geometrical considerations without assuming any approximations for the curvature of the earth. Examples are also provided revealing that for most relevant ranges and heights, the plane range is essentially equal to the range along the earth's surface. The discrepancy only reaches 1.4 km ($\sim$ 25% of a typical grid length) at short ranges and steep elevation angles yielding a height of 10 km. Since we shall concern ourselves mainly with the 3 km level, this difference is ignored in CAPPI production. Refraction of the radar beam through the atmosphere is accounted for by the usual 4/3 earth's radius approximation. With these assumptions, an H vs R plot can be drawn as in Fig. 2.5, emphasizing the annuli yielding CAPPI's at selected heights. Because of the logarithmic scaling of range bins and elevation angles, the number of range bins per each annulus or elevation is nearly constant. Note that during the 1976 season when the first elevation angle was at 0.6°, a 3 km CAPPI was "true" at 3 km only up to about 170 km, sloping upward to 4.5 km at a range of 200 km. Because of the relatively large number of elevation angles in forming any CAPPI, the height oscillation of the beam centre is very small, varying from 300 m at 3 km to about 800 m at 10 km. Artifacts in CAPPI's caused by coarse resolution are thus avoided, Mohr and Vaughan (1979). However, comparatively large beamwidth at far ranges must be taken into consideration. With the help of Fig. 2.5, a Cartesian CAPPI is readily

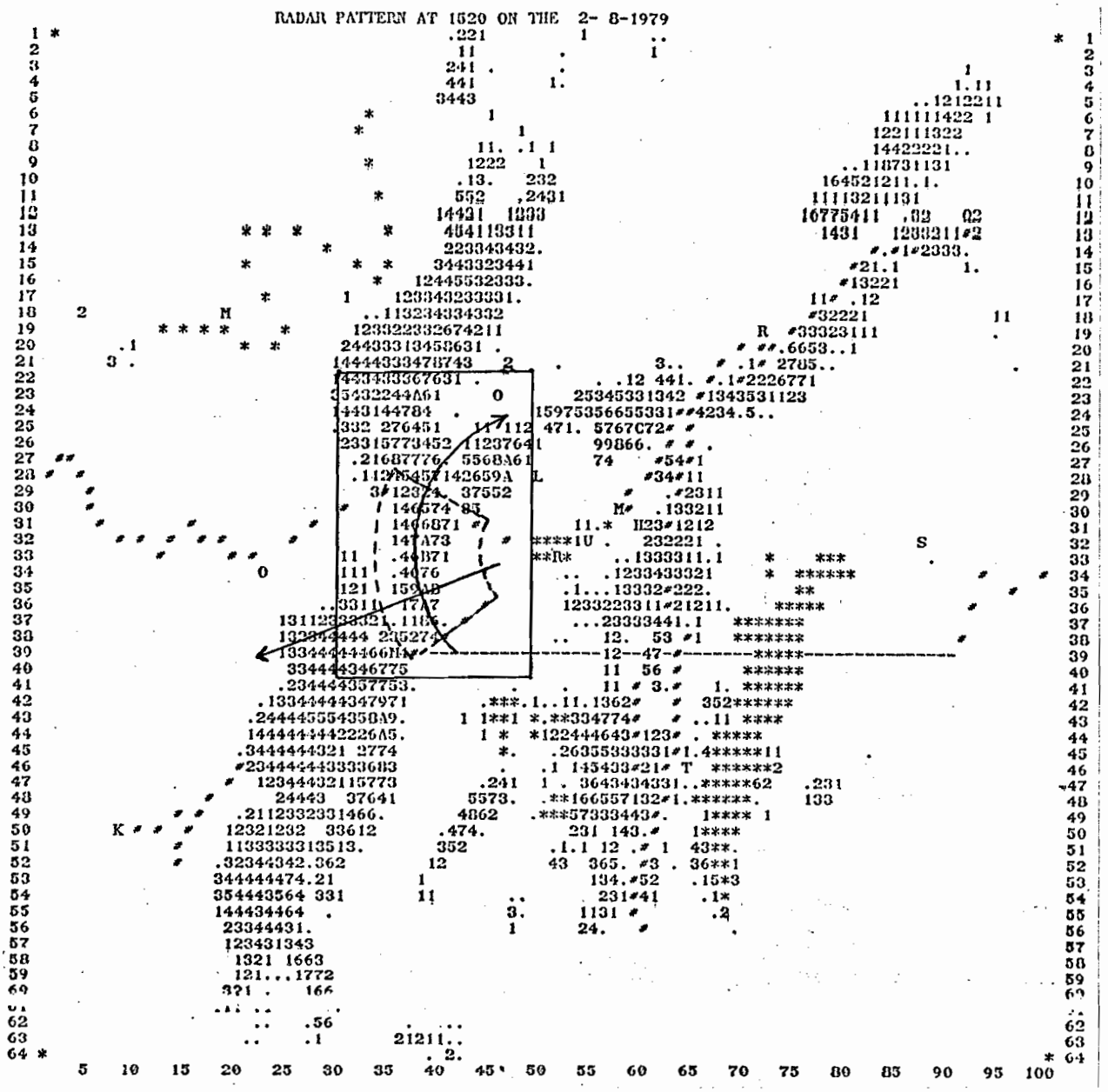

Fig. 2.6. CAPPI at a height of 3 km at 1520 EST 2 August 1979. The maximum range along an E-W or N-S direction is 240 km but extends to 330 km at the corners. For conformality, the information is presented in a 64 x 100 matrix resulting in a grid area of (7.5 x 4.8) = 36 km^2. Most ground clutter near the radar is eliminated but persistent echoes in the S and SE are masked out by '*' symbols which also delineate a shadow effect in the NW. Geography is indicated by '#' symbols. The lower thresholds of the precipitation rate in mm h^{-1} corresponding to the intensity levels are given below.

level	·	1	2	3	4	5	6	7	8	9	A	B	C	D	E	F
mmh^{-1}	trace	1	2	3	5	8	13	20	30	40	50	75	100	150	200	300

obtainable in a synthetic process by transformation only data in those range intervals from each elevation angle which are located at the requested height. Fig. 2.6 represents a CAPPI at 3 km but CAPPI's at any height can be produced. Care must be taken that in a series of CAPPI's at various heights, their spacing be chosen such that the data for each level are independent. Note that in Fig. 2.6, the ground clutter is eliminated although high mountain peaks in the south and southeast return a persistent and sizeable echo and is thus masked out by '*' symbols.

The time required to produce a digital CAPPI is about 2 minutes, but may be reduced to 30 seconds. This technique takes advantage not only of the fact that there are far more polar than Cartesian points but also that the density of polar data is an inverse function of the range. Hence, instead of using all the polar points necessitating a coordinate transformation for each one, the program can skip a progressively larger number of data in azimuth and range as the latter decreases while striving to maintain an almost uniform data density throughout the display. Tests have shown that the essential features of the precipitation area and structure have been preserved. This quick mode of CAPPI production becomes essential when employed prior to a pattern recognition algorithm, thus assuring us of achieving a short-term precipitation forecast within a reasonable delay from the time of data acquisition.

c) Map Magnification

It is recognized that the size of $A_{(I,J)}$ encountered in displays of a 360° scan are generally of poor areal resolution. We are reminded that short-term precipitation forecasts need not be confined to the prediction of a system movement. A detailed examination of the internal structure within a storm, both in the horizontal and vertical scale, will undoubtedly

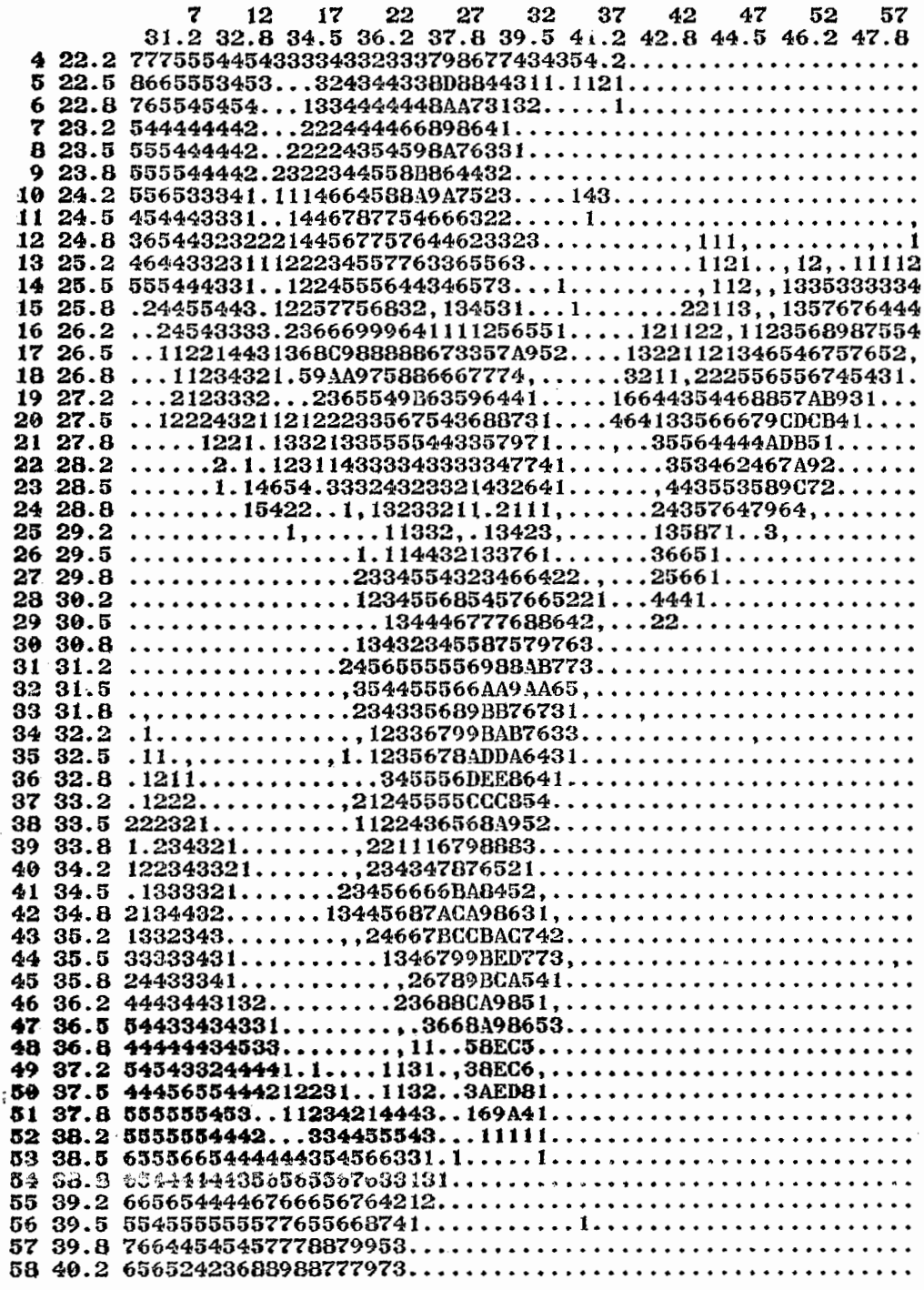

Fig. 2.7. 'Zoom' map at a height of 4 km of the rectangular area indicated in Fig. 2.6. The resolution is (2.5 x 1.6) = 4 km^2 which is equivalent to a magnification of 9. Note the better representation of cell centres and rainfall rate gradients obtained using the finer resolution. The ultimate resolution if that obtained with the AZLOR display of Fig. 2.2.

uncover useful information to a forecaster in assessing a storm severity which cannot be deduced either from its motion or from its rainfall intensity at one height. Taking full advantage of the computer power, programs are available which by inputting the size and location of a sub-area within a coarse resolution map, that sub-area is magnified, thus achieving a reduction in resolution, Fig. 2.7. The essentials of the procedure can be summarized as follows. If a magnification of K is desired for a sub-area of a (MxN) coarse resolution map, the program performs the transformation from polar coordinates to an imaginary Cartesian grid of (KM x KN) dimensions. By neglecting all data outside the chosen sub-area, core requirements of a minicomputer are easily satisfied. The effective magnification is dependent upon the range and size of the sub-area. The number of polar data per Cartesian grid of the expanded map must be calculated for suitable averaging. In this respect, it may happen that at remote ranges, the polar bin size is greater than the Cartesian grid area, resulting in "holes" in the magnified map denoting locations for which N = 0. Though undesirable, this does not constitute a serious error. These locations are easily recognized by a symbolic character or may be filled by an appropriate interpolation. Finally, since the Cartesian grid areas are significantly reduced, the simple expedient of representing them with the largest polar intensity may be appropriate as a quick alternative.

d) Cross-Sections

Vertical inspection of three-dimensional radar data can be achieved by three types of cross-sections.

i) REI (Range Elevation Indicator) Fig. 2.8a

This display is obtained by fixing the azimuth and collecting data at all desired ranges for all elevation angles. This display is highly distorted on account of the range dependence of the height. The contours of

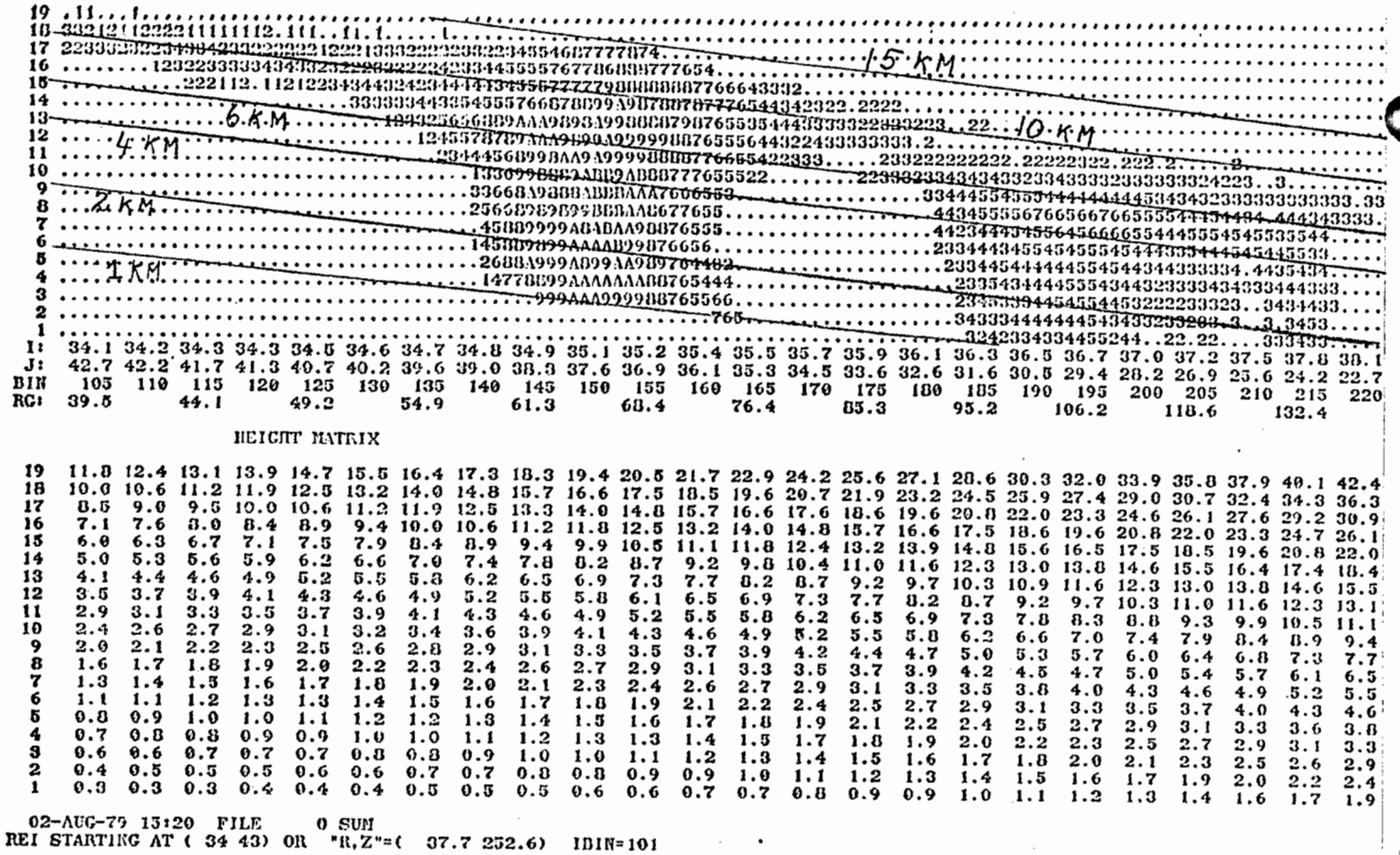


```
I:  34.1 34.2 34.3 34.3 34.5 34.6 34.7 34.8 34.9 35.1 35.2 35.4 35.5 35.7 35.9 36.1 36.3 36.5 36.7 37.0 37.2 37.5 37.8 38.1
J:  42.7 42.2 41.7 41.3 40.7 40.2 39.6 39.0 38.3 37.6 36.9 36.1 35.3 34.5 33.6 32.6 31.6 30.5 29.4 28.2 26.9 25.6 24.2 22.7
BIN  105  110  115  120  125  130  135  140  145  150  155  160  165  170  175  180  185  190  195  200  205  210  215  220
RG:  39.5       44.1       49.2       54.9       61.3       68.4       76.4       85.3       95.2      106.2      118.6      132.4

                    HEIGHT MATRIX

19  11.8 12.4 13.1 13.9 14.7 15.5 16.4 17.3 18.3 19.4 20.5 21.7 22.9 24.2 25.6 27.1 28.6 30.3 32.0 33.9 35.8 37.9 40.1 42.4
18  10.0 10.6 11.2 11.9 12.5 13.2 14.0 14.8 15.7 16.6 17.5 18.5 19.6 20.7 21.9 23.2 24.5 25.9 27.4 29.0 30.7 32.4 34.3 36.3
17   8.5  9.0  9.5 10.0 10.6 11.2 11.9 12.5 13.3 14.0 14.8 15.7 16.6 17.6 18.6 19.6 20.8 22.0 23.3 24.6 26.1 27.6 29.2 30.9
16   7.1  7.6  8.0  8.4  8.9  9.4 10.0 10.6 11.2 11.8 12.5 13.2 14.0 14.8 15.7 16.6 17.5 18.6 19.6 20.8 22.0 23.3 24.7 26.1
15   6.0  6.3  6.7  7.1  7.5  7.9  8.4  8.9  9.4  9.9 10.5 11.1 11.8 12.4 13.2 13.9 14.8 15.6 16.5 17.5 18.5 19.6 20.8 22.0
14   5.0  5.3  5.6  5.9  6.2  6.6  7.0  7.4  7.8  8.2  8.7  9.2  9.8 10.4 11.0 11.6 12.3 13.0 13.8 14.6 15.5 16.4 17.4 18.4
13   4.1  4.4  4.6  4.9  5.2  5.5  5.8  6.2  6.5  6.9  7.3  7.7  8.2  8.7  9.2  9.7 10.3 10.9 11.6 12.3 13.0 13.8 14.6 15.5
12   3.5  3.7  3.9  4.1  4.3  4.6  4.9  5.2  5.5  5.8  6.1  6.5  6.9  7.3  7.7  8.2  8.7  9.2  9.7 10.3 11.0 11.6 12.3 13.1
11   2.9  3.1  3.3  3.5  3.7  3.9  4.1  4.3  4.6  4.9  5.2  5.5  5.8  6.2  6.5  6.9  7.3  7.8  8.3  8.8  9.3  9.9 10.5 11.1
10   2.4  2.6  2.7  2.9  3.1  3.2  3.4  3.6  3.9  4.1  4.3  4.6  4.9  5.2  5.5  5.8  6.2  6.6  7.0  7.4  7.9  8.4  8.9  9.4
 9   2.0  2.1  2.2  2.3  2.5  2.6  2.8  2.9  3.1  3.3  3.5  3.7  3.9  4.2  4.4  4.7  5.0  5.3  5.7  6.0  6.4  6.8  7.3  7.7
 8   1.6  1.7  1.8  1.9  2.0  2.2  2.3  2.4  2.6  2.7  2.9  3.1  3.3  3.5  3.7  3.9  4.2  4.5  4.7  5.0  5.4  5.7  6.1  6.5
 7   1.3  1.4  1.5  1.6  1.7  1.8  1.9  2.0  2.1  2.3  2.4  2.6  2.7  2.9  3.1  3.3  3.5  3.8  4.0  4.3  4.6  4.9  5.2  5.5
 6   1.1  1.1  1.2  1.3  1.3  1.4  1.5  1.6  1.7  1.8  1.9  2.1  2.2  2.4  2.5  2.7  2.9  3.1  3.3  3.5  3.7  4.0  4.3  4.6
 5   0.8  0.9  1.0  1.0  1.1  1.2  1.2  1.3  1.4  1.5  1.6  1.7  1.8  1.9  2.1  2.2  2.4  2.5  2.7  2.9  3.1  3.3  3.6  3.8
 4   0.7  0.8  0.8  0.9  0.9  1.0  1.0  1.1  1.2  1.3  1.3  1.4  1.5  1.7  1.8  1.9  2.0  2.2  2.3  2.5  2.7  2.9  3.1  3.3
 3   0.6  0.6  0.7  0.7  0.7  0.8  0.8  0.9  1.0  1.0  1.1  1.2  1.3  1.4  1.5  1.6  1.7  1.8  2.0  2.1  2.3  2.5  2.6  2.9
 2   0.4  0.5  0.5  0.5  0.6  0.6  0.7  0.7  0.8  0.8  0.9  0.9  1.0  1.1  1.2  1.3  1.4  1.5  1.6  1.7  1.9  2.0  2.2  2.4
 1   0.3  0.3  0.3  0.4  0.4  0.4  0.5  0.5  0.5  0.6  0.6  0.7  0.7  0.8  0.9  0.9  1.0  1.1  1.2  1.3  1.4  1.6  1.7  1.9

  02-AUG-79 15:20  FILE     0 SUM
REI STARTING AT ( 34 43) OR "R,Z"=(  37.7 252.6)  IBIN=101
```

Fig. 2.8a. REI display starting at grid pair (34,43) of map on Fig. 2.6 which corresponds to an azimuth of 253 degrees and extends from bin number 101 to 220 (42 to 140 km). The (I,J) pair of every fifth datum is given along the horizontal while the elevation number is provided vertically on the display. The "height matrix" enables the drawing of the constant height lines.

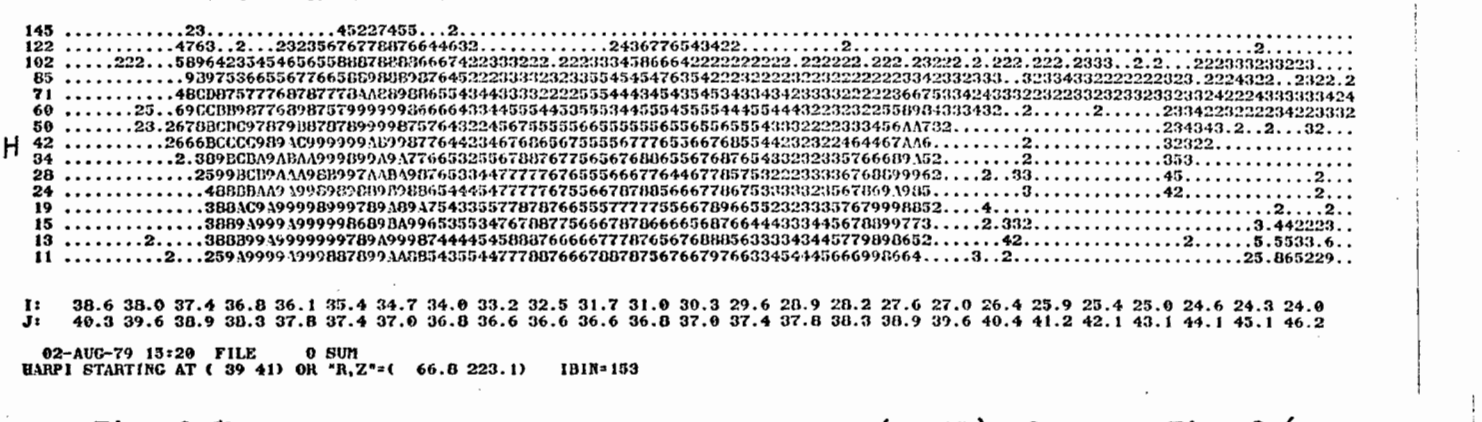

```
I:  38.6 38.0 37.4 36.8 36.1 35.4 34.7 34.0 33.2 32.5 31.7 31.0 30.3 29.6 28.9 28.2 27.6 27.0 26.4 25.9 25.4 25.0 24.6 24.3 24.0
J:  40.3 39.6 38.9 38.3 37.8 37.4 37.0 36.8 36.6 36.6 36.6 36.6 36.8 37.0 37.4 37.8 38.3 38.9 39.6 40.4 41.2 42.1 43.1 44.1 45.1 46.2

  02-AUG-79 15:20  FILE     0 SUM
HARPI STARTING AT ( 39 41) OR "R,Z"=(  66.8 223.1)  IBIN=153
```

Fig. 2.8b. HARPI display starting at grid pair (39,41) of map on Fig. 2.6 along bin #153 at 67 km. The vertical scale is in 1/10 of a km. The path along the horizontal is given by the (I,J) pairs shown below the display. The rainfall rate scale of both Figs. 2.8 is that of Fig. 2.2.

constant height are straight lines resulting from the peculiar spacing of the range bins and elevation angles.

(ii) HARPI (Height Azimuth Range Position Indicator) Fig. 2.8b.

Here, all data at any prescribed range bin are displayed along a certain azimuthal arc for all elevation angles. Since a maximum of only 128 characters can be conveniently printed on a line, this arc is merely 128 x 0.96° = 123°. All data being at a unique range, the vertical scale of elevation angles can be easily related to the height above the ground with exponentially increasing divisions.

iii) General Cross-Sections

Again, the high versatility of computer programs enables us to depart from the historical cross-sections described above which are fixed by instrumental constraints, and gain a greater freedom in choosing the orientation of vertical cuts. Software has been developed which permits a cross-section through a path defined by a set of coordinate pairs on the Cartesian map. Both the horizontal and vertical scale can be specified at will. Numerous examples are found in Chapter V.

e) ETPPI (Echo Top PPI)

This display, Fig. 2.9, provides the height in km of the highest echo return exceeding any desired rainfall intensity. In order to avoid ground clutter contamination, only the heights above the 3 km level are presented. We are reminded that at far ranges, the minimum height is a function range. In view of the close relationship between storm severity and echo-top height, the usefulness of this display is readily realized. However, caution must be taken to recognize the presence of interference, noise, or non-hydrometeorological targets like airplanes which may not be smoothed out by a filtering technique.

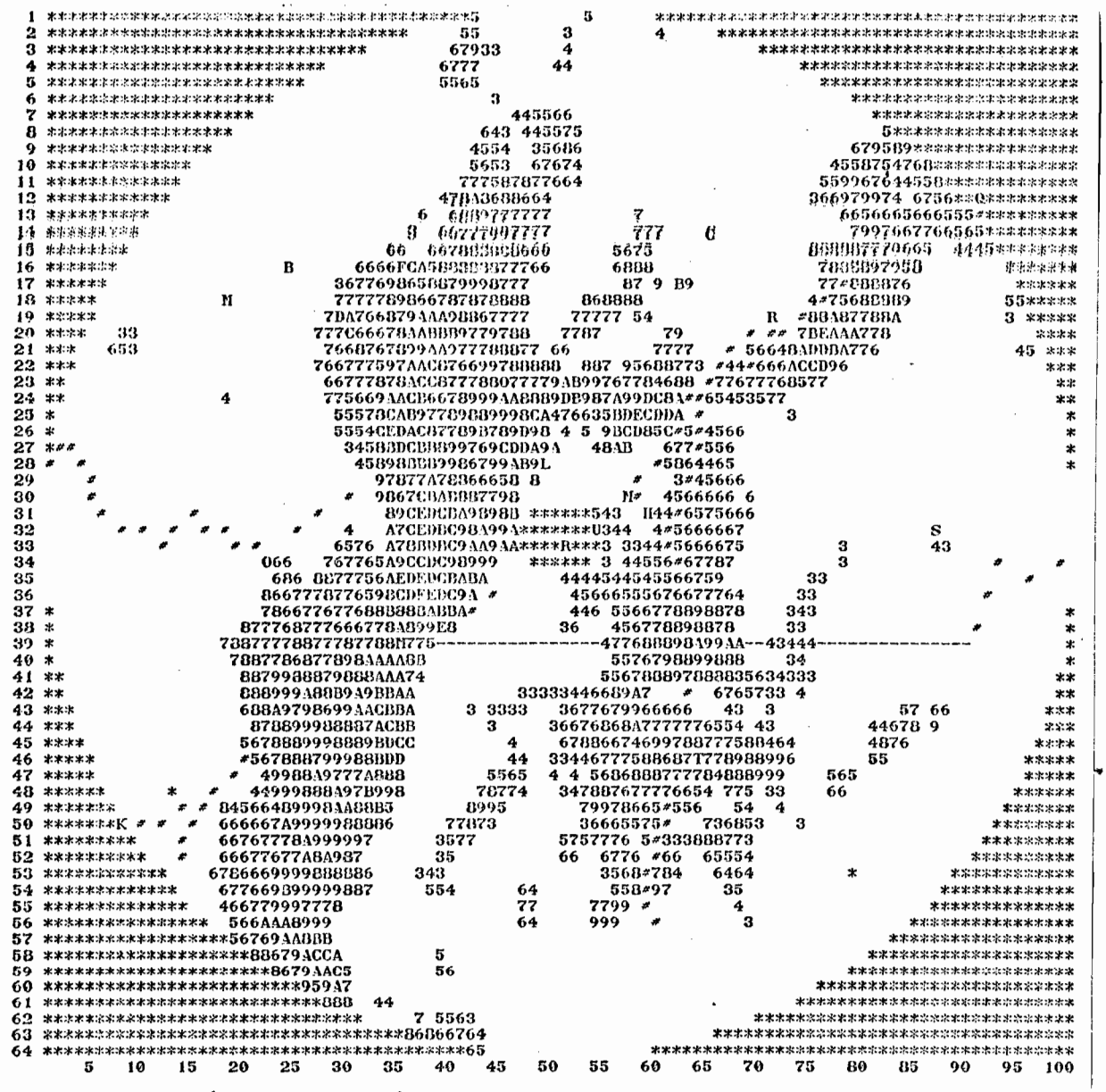

Fig. 2.9 ETPPI (Echo Top PPI) at 1520 EST 2 August 1979. The alphanumerics indicate the height in km of the highest echo return above an arbitrary threshold value of 24 dBz. Note that A to F implies heights of 10 to 15 km respectively.

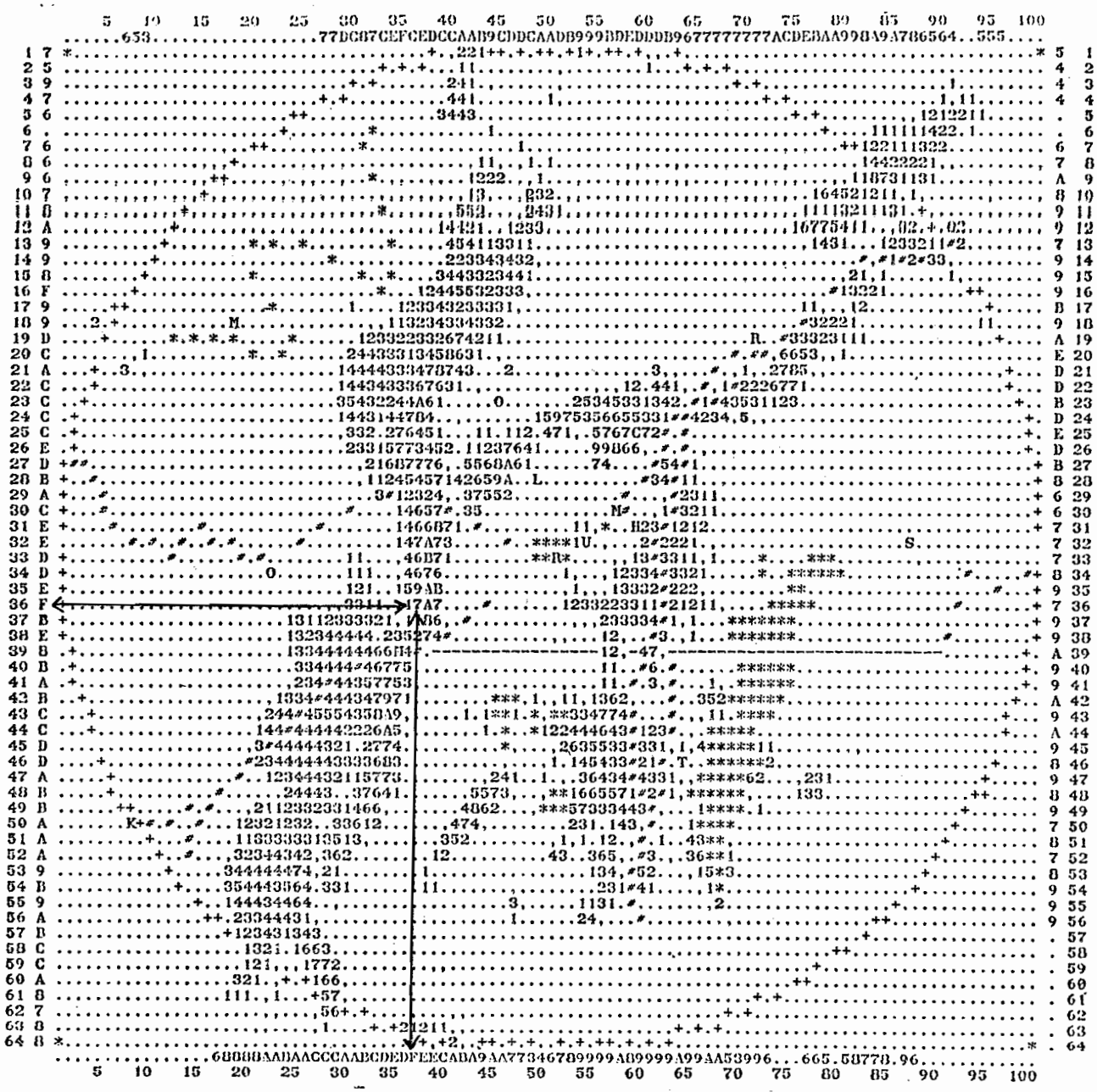

Fig. 2.10. CAPPHI (CAPPI with Height Indicator) at 1520 EST 2 August 1979. As an example, the height "F" (15 km) in the southwest quadrant can be pinpointed by triangulation as illustrated.

Fig. 2.11. Rainfall accumulation map from 1200Z 1 July 1979 to 1200Z 2 July 1979. Note the large accumulation and steep gradient north of the radar which was caused by a quasi-stationary storm.

.	1	2	3	4	5	6	7	8	9	A	B	C	D	E	F	G	H	J	K	L	M	N
1	2	4	6	10	15	20	25	30	35	40	50	60	70	80	90	100	120	140	160	180	200	

The lower and upper threshold in mm corresponding to each character is indicated above.

f) CAPPHI (CAPPI with Height Indicator)

This display, Fig. 2.10, combines the features of a CAPPI with information from an ETPPI. Thus, in addition to the regular rainfall levels on the map, the height in km of the heighest radar return is supplied around the perimeter. By triangulation applied separately to each quadrant, the grid area corresponding to the highest echo can be located. Although ambiguities do arise, this drawback does not reduce its desirability among forecasters

g) Hydrological Displays

With maps being available every 5 minutes, it is a simple procedure to accumulate the rainfall over each grid and thus obtain the spatial distribution of rainfall amounts following the passage of a storm system. An example is provided in Fig. 2.11.

Although a 3 km CAPPI was the only output provided to the weather office, from 1976 to 1978, all the displays described in this section are now available. A similar effort in the United States is described by Saffle (1976) in conjunction with D/RADEX (Digitized RADar EXperiment).

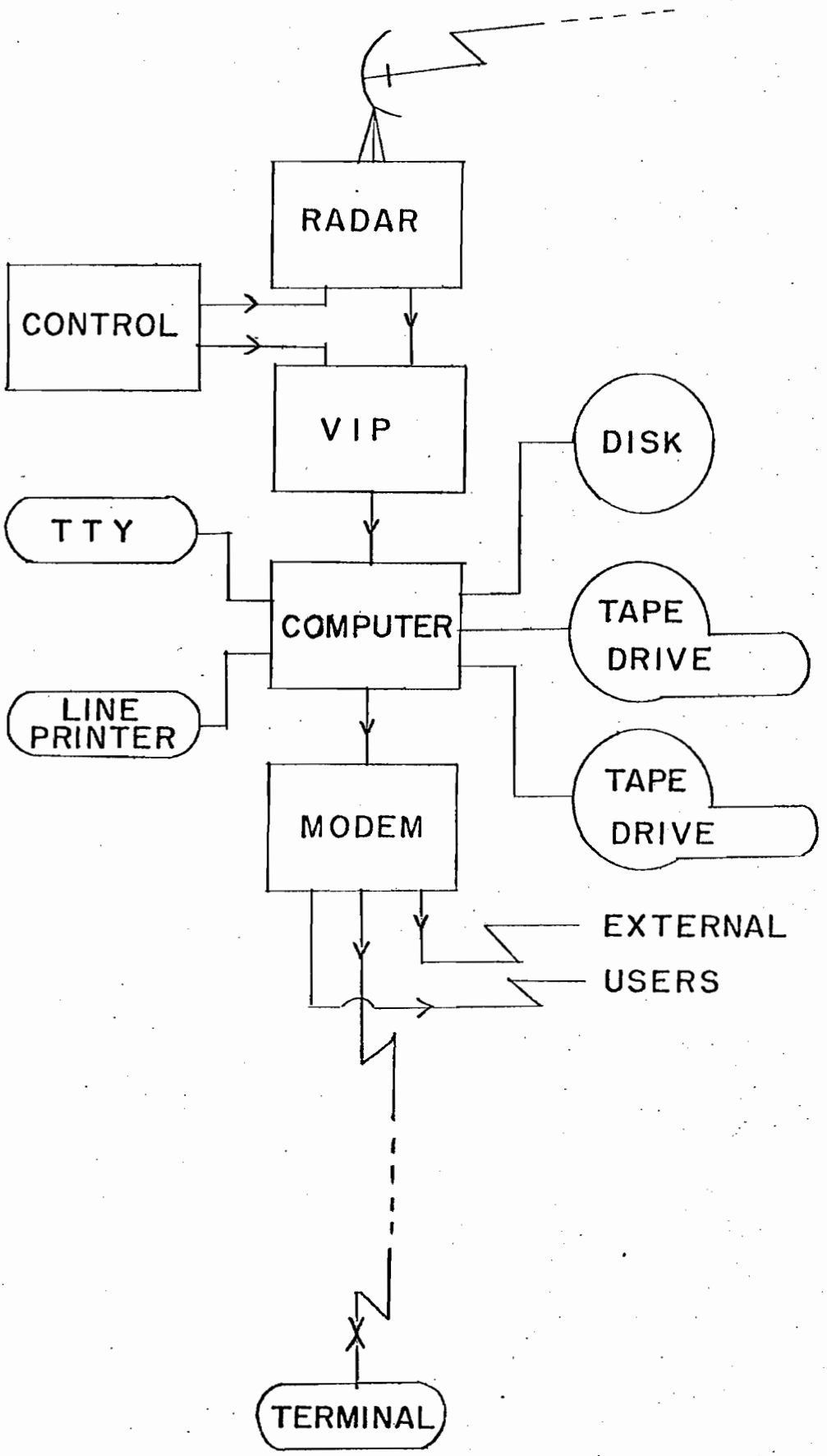

Fig. 3.1: System hardware configuration

CHAPTER III
PROJECT OPERATION

3.1 Description of Test

3.1.1 Hardware

The implementation of a real-time forecasting system requires the interfacing of radar, computer and communications equipment. The hardware configuration used in the performance of the test is shown in Fig. 3.1. The principal elements are:

a) Radar: The resolution of the McGill Radar at Ste-Anne-de-Bellevue has been discussed in the previous chapter. The main engineering characteristics are listed in Table 3.1 below.

TABLE 3.1 Properties of the McGill weather radar

Wavelength	10 cm
Antenna diameter	10 m
Peak power	1.4 MW
Pulse repetition rate	60 Hz
Pulse length	1 μs
Minimum detectable signal	16 dBZ
Dynamic range	80 db
Rotation period	10 s
Number of elevation angles	26 (24 are recorded)
Number of range bins	148 or 400
Number of azimuths recorded	600/rotation or 375
Three-dimensional scan period	5 min

A complete description of the McGill Radar can be found in Marshall and Ballantyne (1975).

b) Controls: An antenna programmer imparts a rotation rate of 6 r.p.m. and executes a stepped elevation sequence providing a complete 3D scan every five minutes.

c) DVIP or Digital Video Integrator Processor: The analogue data is smoothed and sorted into a data set of 148 logarithmically spaced bins, 600 azimuths and 24 elevation angles every five minutes. Each of these data sites is represented as one of 15 intensity levels or zero.

d) Computer: The computer, a PDP11/40, with 32 K of core has a Fortran compiler. Its function is to record the digital radar data sent by the radar interface on one of two tape drives for a period of five minutes and, consequently, to retrieve the data for use in the forecasting algorithm. The computer includes a 2.4 MByte disk where program sub-routines as well as some data sets reside. The output peripherals consist of a fast line printer/plotter and a slow teletype at 30 characters/sec. The latter is also employed to issue commands to the computer monitor when executing or editing programs.

e) Modem: A modem, an acronym for modulator demodulator, converts the digital information into an analogue signal at the input side at the radar site and performs the reverse function at the other end, that is, at the Quebec Region Forecast Office 15 km away. The telephone line is half duplex but this advantage was not put to use on account of the total automation of the SHARP program and of the severe constraints imposed on the computer with regard to other tasks. The transmission rate is appropriate for the 30 character/sec. terminal at the output. Additional users may hook up directly in parallel fashion and receive the same data transmitted from the radar site. The forecast map, in the form of a (64 x 100) matrix, comprises a total of 6528 characters, including carriage control characters. The

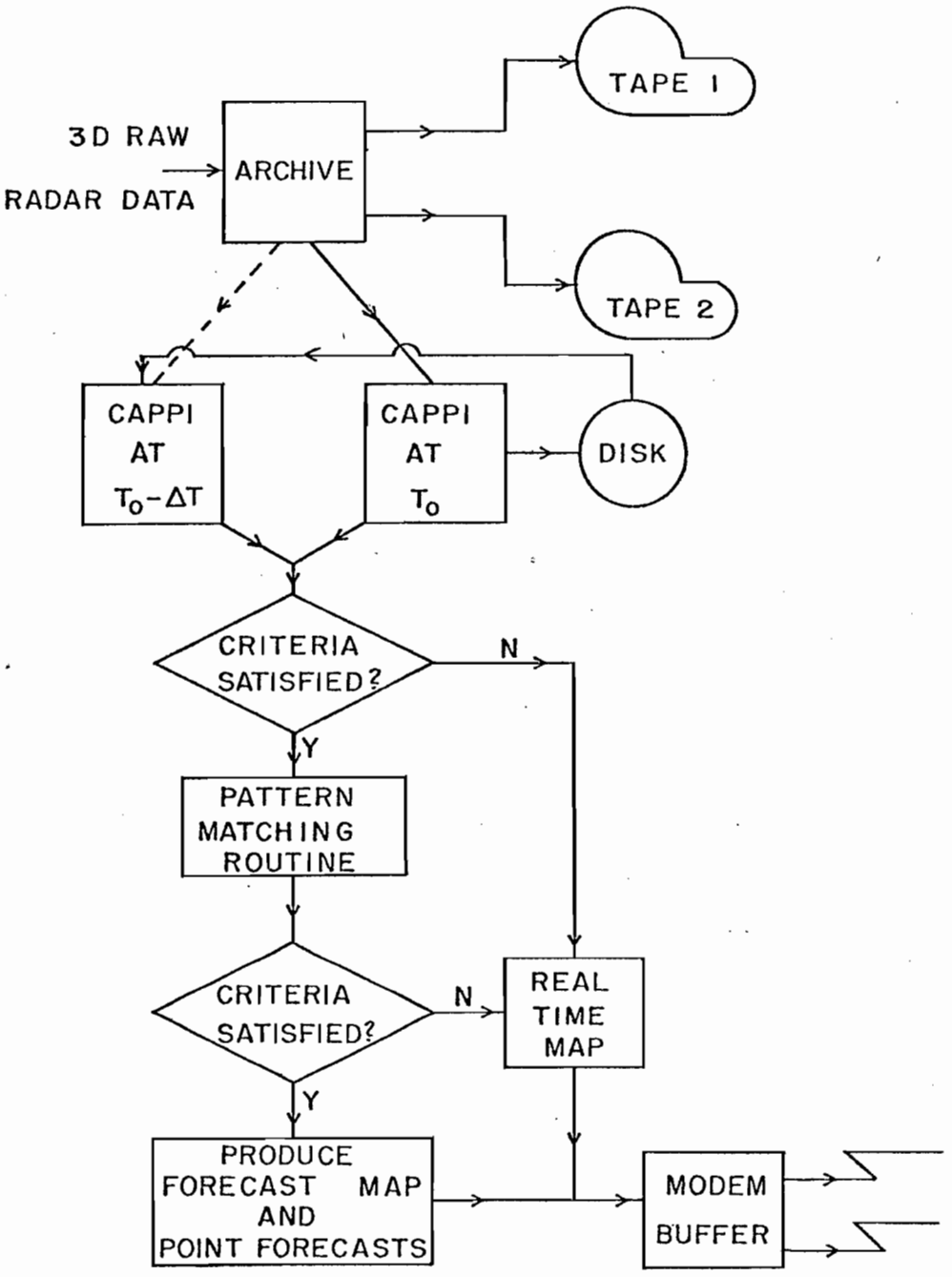

Fig. 3.2. System software configuration

complete output is thus received in approximately 3 1/2 minutes. During the 1979 summer season, the output maps were also displayed on a colour TV screen at the forecast office. This peripheral also permitted a playback of the last seven CAPPI maps.

3.1.2 Software

The development of the required software had been continuing for a number of years in a simulated or non-operational milieu. During the initial phase of this research project, considerable effort has been devoted to adapt the software to function in a real-time operational environment and to be as efficient as possible in a comparatively slow electronic machine. In particular, the choice of a suitable fast correlation algorithm as well as the necessity of using properly averaged constant altitude data has been emphasized.

A simplified flow diagram of the forecast procedure software is sketched in Fig. 3.2. The salient components are:

a) Archiving Routine. This program, unlike all the other routines written in Fortran, is coded in assembly language suitable for the minicomputer. After recognizing the radar "cycle start", it takes all the raw 3D data in spherical coordinates and eliminates blocks of zeroes as well as most of the ground echoes to minimize tape consumption. The pertinent data is then combined into 4K buffers with position indicators for recording on the first tape drive, or on the second if the first one is full. Inherent in this program is also a routine necessary for the transmission of the forecast map simultaneously with the archiving. Data recording is performed for 11 cycles every hour, that is, for 55 minutes.

b) CAPPI Production: Once an hour, for a maximum duration of 5 minutes, a series of programs queued in "batch" mode constituting the forecasting procedure, is executed. At first the CAPPI program reads the raw data of

the last cycle and sorts out only the relevant portion required for the synthesis of a 3 km CAPPI. The tape is then repositioned for proper recording at the start of the next cycle. The latest map, at time T_o, is stored on disk and recalled at time $(T_o + \Delta T)$ for matching to yield the next forecast. Before proceeding to the cross-correlation routine, the intensity resolution is degraded to 5 levels (0 to 4) and checks are performed on both the T_o and $(T_o - \Delta T)$ maps. These are tests for sufficient areal coverage (at least 2% coverage within a range of 205 km), for the absence of anomalous propagation, and for an acceptable time interval ΔT, $(10 \leqslant \Delta T \leqslant 120$ min). The permanent ground echoes are excluded by means of a mask.

c) Pattern Matching Routine. This is the crucial segment of the process which obtains the best match between the current map, $F(T_o)$, and the one stored from the previous forecast, $F(T_o - \Delta T)$. When a forecast sequence is started, the first guess originally used was that of the motion of the centre of gravity. However, when echoes cross the boundary of the display, the apparent motion of the centre of gravity provides a misleading hint. Since an analysis of a simulated test of 1975 summer data showed a predominant motion from about 260°, a velocity of 30 km h^{-1} from that direction was chosen as the first estimate of pattern displacement. In subsequent forecasts, the computed velocity from the previous hour is used as the initial guess. The routine includes a sub-program which detects the presence of a secondary maximum on the "coarse grid" cross-correlation matrix and, if found, performs an additional "fine grid" cross-correlation around it. In addition, if the lag of γ_{max} coincides with the boundary of the correlation matrix, the latter is expanded until it is completely enclosed by it. The "coarse" and "fine grid" matrices are both transmitted to the Forecast Office since they provide useful information on the degree of confidence which can be assigned

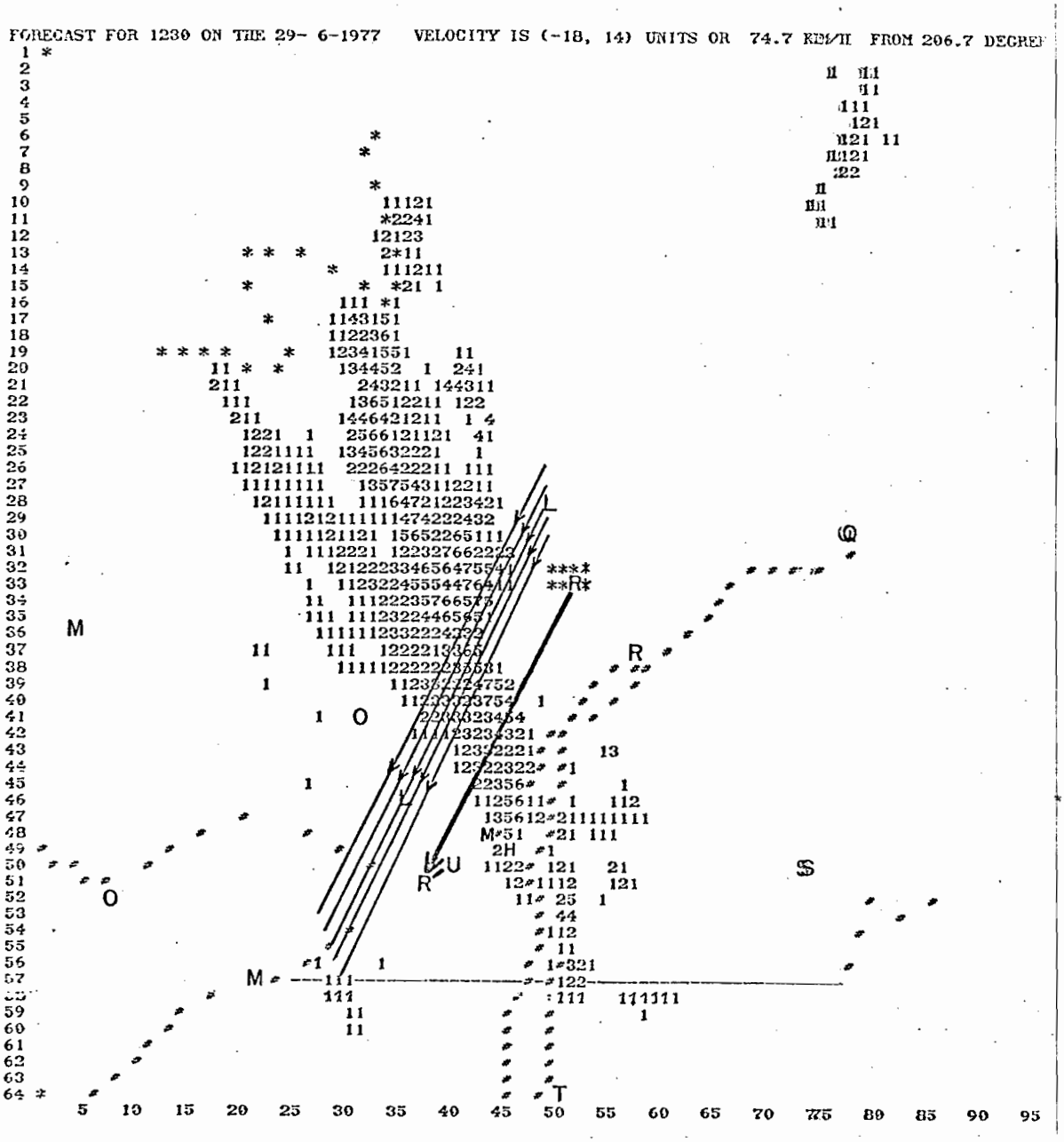

Fig. 3.3a. Two-hour forecast map as a 3 km CAPPI produced by translating the background geography (in # symbols) in the opposite direction of the incoming weather, thus preserving all information inside the matrix. The vector displacement is indicated by RR' which denotes the original and final position of the radar. The rainfall rate scale is that of Fig. 2.6.

to the forecast vector and on the relative probability of other possible motions. Significant work has been done in devising fast computer techniques to enable this program to run as quickly as possible. The employed version generally takes less than two minutes.

d) Forecast Map. The forecast is made by translating the current map by the appropriate vector and removing the ground echoes. A geography overlay is then applied. However, to prevent loss of data through the map boundary, particularly serious at high forecast speeds, a "relativistic" approach has been adopted whereby the geographical background is shifted in the opposite direction by an equal amount. The result, Fig. 3.3a, is sent to the modem buffer which is transmitted as soon as archiving of the next 5-minute cycle begins.

e) Station Forecasts. Special purpose line forecasts, that is, rainfall intensities vs time, Fig. 3.3b, are provided for 12 prescribed stations by searching through the data, in steps proportional to the forecast vector, along a path opposite the expected storm trajectory and originating at each station. In order to take into account possible cross-range errors, the line trajectory is expanded into a sector of 16°. The largest rainfall rate intensity within each arc at constant time lags from the points of interest is registered.

A more useful approach was developed in 1977 when the line forecasts for the 6 most pertinent stations also included the two grid points north and south of the station. Thus, depending on the angle between the forecast vector and a north-south line, the structure or appearance of the incoming radar echoes is faithfully reflected in this particular display; the best effect is obtained with motion perpendicular to a north-south line, that is from near 270 degrees. The time resolution of this output is 5 or 10

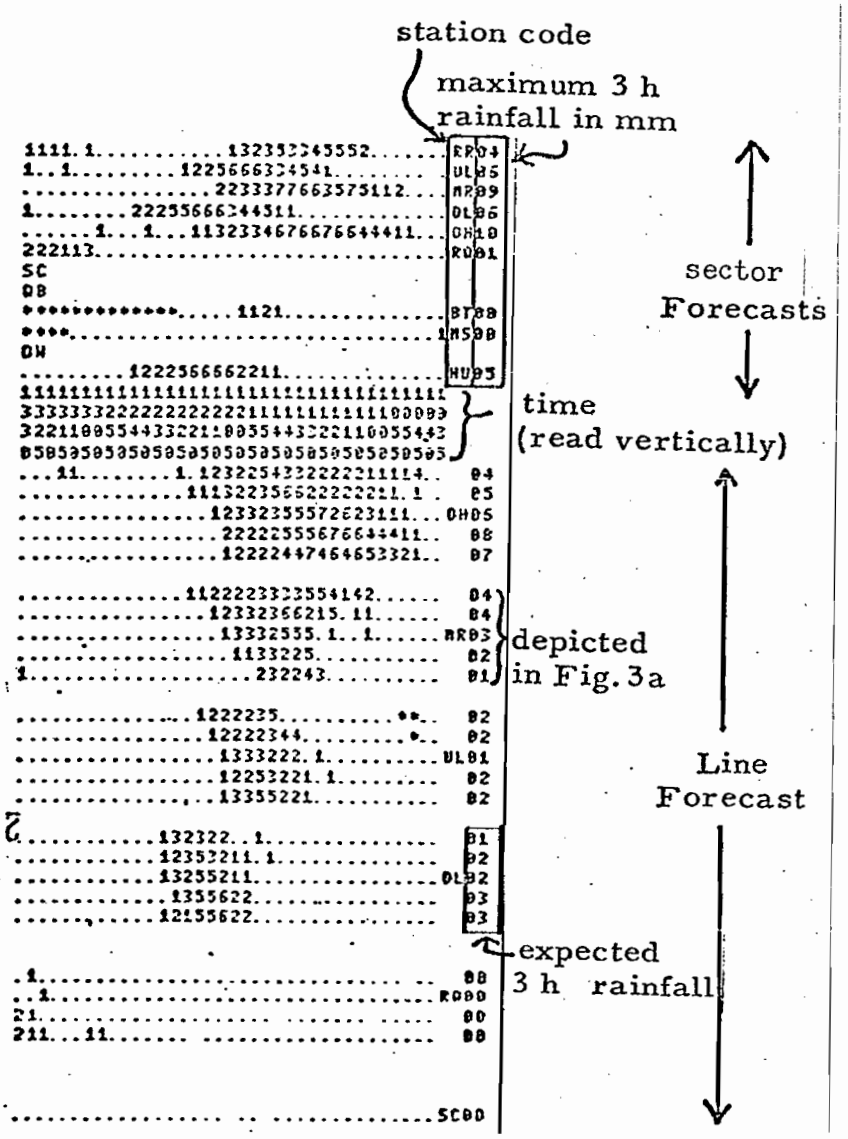

Fig. 3.3b. Station forecasts accompanying map of Fig. 3.3a. Sector forecasts give the highest rainfall intensity with a 16° arc. Line forecasts for the station location as well as for two grid areas north and south of it reflect the configuration of the upcoming echoes as a function of time. The expected 3 h rainfall accumulation (mm) is also provided.

minutes, depending on the speed of the storm and on the time available for transmission before the start of the archiving cycle. The rainfall rates for each interval are summed to yield an estimated rainfall accumulation in millimetres for the three-hour period. When this parameter appears at the end of a sector forecast, it indicates the maximum or extreme rainfall possible for the next three hours. The most likely precipitation amount is the quantity following the line forecasts. These also bring into sharper focus any expected gradient of precipitation in the neighbourhood of a station. In Fig. 3.3b, a decreasing north-south gradient, 4 mm to 1 mm, can be seen for the Mirabel, (MR), station, while ste-Agathe, (OH), shows a reverse effect but with higher accumulations. Dorval, (UL), reveals the absence of a significant gradient. The approach of intense rain over populated areas is thus more readily visualized by means of such station forecasts than would have been the case with the sole presentation of the map array of data.

f) Time Sharing allows the simultaneous archiving of new data and the transmission of the forecast map from the modem buffer. The additional forecast products, that is, the cross-correlation matrices and the station forecasts, are sent separately prior to the beginning of the archiving cycle.

g) Timing The forecast products are sent to the Quebec Region Forecast Office at one-hour intervals from the start of the program. They are generated automatically without the necessity of an operator. The timing of each step of the forecasting program at maximum load is sketched below.

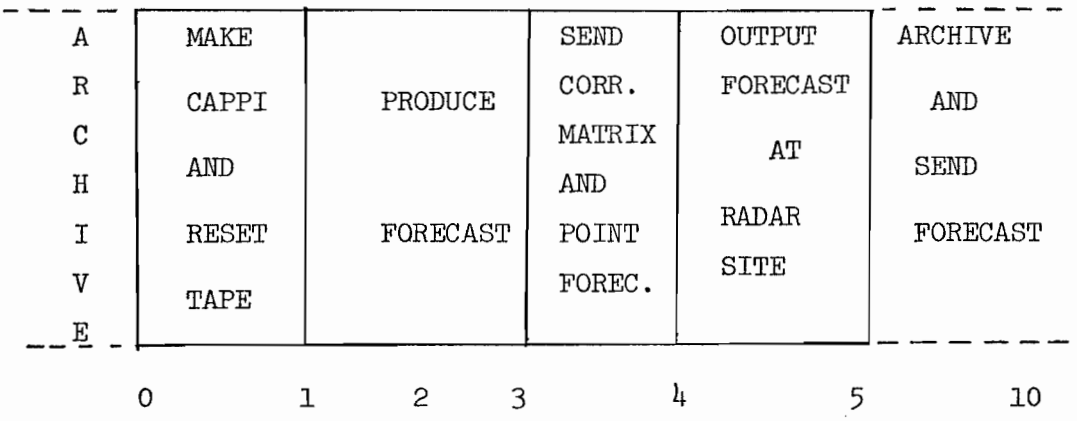

Fig. 3.4 Timing sequence of major tasks

When archiving is completed and a forecast is required, the tape is repositioned to a location corresponding to the beginning of the cycle and the 3 km CAPPI is extracted. This task rarely exceeds one minute. The correlation algorithm consumes less than two minutes because of the fast integer technique in the calculation of γ described in section 2.2. The correlation matrices and the station forecasts are transmitted in less than a minute. If more than 30 seconds are available before the start of the next cycle, the forecast map is also output on the line printer at the radar site.

3.2 Classification of Forecast Events

SHARP is designed to yield a two-hour forecast every hour on the basis of the pattern motion in the preceding hour. However, unlike the situation existing in a simulated test of pre-selected data, successful operation in a continuous real-time environment requires the capacity to cope with any eventuality. In particular, the forecast system must avoid gross errors,

since one major miscue resulting in a totally unacceptable forecast issued at the Weather Office would undermine the credibility of the entire effort. Thus, in practice, a number of conditions do arise when a forecast is neither possible or desirable, nor can it be safely attempted. In all these situations, a real time map is transmitted, with an appropriate computer message explaining the reason for the forecast omission.

Defining a forecast "event" as the time when a forecast is normally expected, the following ten occurrences are possible.

#1: All checks reveal that a forecast can be performed and sent to the Weather Office. The computer message accompanying the forecast reads as follows:

"Forecast for 1430 on the 15-5-1976. Velocity is (-3,9) units or 55 km h^{-1} from 240 degrees."

#2: "Radar pattern at 1230 on the 15-5-1976"

A real time map with the above message is sent when a forecast is omitted or rejected for reasons which are not specified in the other categories listed below. At the beginning of each weather sequence, when the program is initialized, a forecast cannot be attempted, but the real time map is sent with the above message. However, in order that the number of events coincide with the hours of operation, this situation is not tabulated as #2 (see Table 3.2).

#3: "Radar pattern at 1230 on the 15-5-1976

Insuf. coverage for forecast"

It is obvious that a minimum amount of data must be present on the CAPPI in order to apply the pattern recognition algorithm with a certain degree of confidence. Although the map extends to a range of 240 km, (330 km in 1977), it is desirable to scan the portion which does not depart significantly from the 3 km level. Hence, only the area within 205 km, consisting of about

3600 grid areas, is scanned for sufficiency. Prior to this check, the average mountain echo is removed by an interpolation scheme. At first, 100 units of area, or 2.8% coverage, was assumed to be adequate, but, after two weeks of operation, it became evident that many potentially good forecasts were not attempted. The existing SHARP program was not intended to constitute a final version, but a self-learning, flexible approach to an experiment open to helpful modifications in its details. Thus, the normal sufficiency requirement was lowered to 75 units. In addition, by the optional use of a switch at the computer console, the criterion can be further lowered to 40 units or 1.1% by on site personnel who can later judge the validity of the action and contact the Weather Office if an unrealistic forecast results.

#4: "Radar pattern at 1230 on the 15-5-1976
Computer motion poorly defined"

It is generally accepted that the magnitude of γ_{max} is a measure of the confidence which can be attached to the motion computed between two patterns. A high value implies a close resemblance and hence a well defined motion between them, while a low value denotes that their strong development, dissipation or rearrangement has masked their apparent motion, Wilson (1966). Following a similar process of trial and error as for the areal sufficiency requirement, the lowest acceptable magnitude for γ_{max} was initially set at 0.250, but was later decreased to 0.200 under normal operation. Again, the use of a switch permitted forecasts with $\gamma_{max} \geqslant 0.100$, though it was rarely used.

#5: "Radar pattern at 1230 on the 15-5-1976
Easterly motion was computed"

On a simulated test with 2 months of 1975 summer data, it was found that no physical motion was persistently coming from the east. On occasions, the

calculated easterly motion was the result of a mismatch of two patterns, and, when real, did not show consistency from hour to hour and was confined to the eastern portion of the map, on the south bank of the St. Lawrence River. Hence, no easterly motion is allowed in order to avoid erroneous forecasts. However, the summer of 1976 was considerably colder, resulting in a more frequent and realistic situation when an east-coast low actually caused rain patterns to be moving from the east. Forecasts were thus not issued on these occasions except when a later editing of the program permitted them if $\gamma_{max} \geq 0.400$. Although on a couple of weather sequences eastern motion persisted for a few hours, the uncertainty on the proper treatment of this situation still remains. As will be discussed in section 3.4 and chapter V, easterly motion associated with low, light precipitation is regarded as being more prone to forecasting error, particularly in the relation between the rainfall experienced at the ground and that derived from the 3 km level. This discrepancy by far outweighs any benefit which the knowledge of the displacement parameter might provide. From this consideration, the rejection of easterly motion does not constitute an unwarranted withholding of information, but instead, underlines the presence of circumstances which the SHARP program does not "pretend" to forecast adequately.

#6: "Radar pattern at 1230 on the 15-5-1976

Computed motion < 10 km h^{-1}".

When the calculated motion of a pattern is of the order of the resolution scale of the map, the forecast is unrealiable since both the speed and direction are highly quantized in preferred magnitudes and azimuths. With a grid area of (7.5 x 4.8) km^2, an arbitrary speed of 10 km h^{-1} has been set in order to permit the forecast. It is realized that in cases which fail to meet this

criterion, the sending of the real time map does not represent a great loss but a fair compromise over the possibility of a misrepresentation of the motion, particularly when extended to prolonged forecast lengths. Moreover, if anomalous propagation is not properly recognized, (see category #8), the computed motion from a pattern recognition technique is < 10 km h^{-1}, thus enabling the rejection of this spurious forecast.

#7: "Radar pattern at 1230 on the 15-5-1976

Computed motion > 99 km h^{-1}"

In the simulated test of 170 forecasts of 1975 summer data, no speeds exceeding 80 km h^{-1} were encountered. Hence, it seemed appropriate to limit the uppermost threshold of speed to 90 km h^{-1}. However, a few cases were observed in 1976 when potentially good forecasts were rejected on that basis. The upper limit was then raised to 99 km h^{-1}. Following a recommendation from the forecasters, this limit was eventually increased to 110 km h^{-1} for the duration of the 1977 season.

#8: "Radar pattern at 1230 on the 15-5-1976

Possible anoprop in the SE"

It is not unusual for intense anomalous propagation to develop during the night or early morning during the summer months. Its presence seriously disrupts the pattern recognition technique and would likely yield an erroneous motion for existing weather patterns. Fortunately, its presence can be automatically detected by observing the configuration of the mountain echo south-east of the radar. Under conditions of anomalous propagation, that ground echo assumes a radically different but peculiar aspect which is of greater intensity and extent than what is seen under normal atmospheric conditions. This configuration can be easily recognized, even under the presence of some weather echoes around it. It should be noted that although the message

points to the presence of anoprop only in the south-east, it is common to find similar patches of anomalous echoes in the southwest near Kingston and in the northeast near Three-Rivers, thus justifying the refusal to attempt any forecasts. Finally, if anomalous propagation was detected on the previous map but not on the present one, message #2 is issued. A more complete review of the treatment of anomalous propagation will be presented in section 3.43.

#9: "Radar pattern at 1230 on the 15-5-1975

Drastic motion change computed"

Prior to the transmission of each forecast, the calculated motion is compared with that of the previous hour. If a drastic difference is observed, it probably denotes an error in the calculated motion of either one of the forecasts. For precautionary measures, no forecast is attempted on the present map. An inspection of the 13 cases encountered throughout the 1976 test showed that in just over half this number was such a course of action justifiable. Consequently, its use was essentially discontinued in 1977 by setting the difference sufficiently large.

#10: "2 km radar pattern at 1230 on the 15-5-1976"

During the 1977 season, when precipitation did not reach the 3 km level, 2 km CAPPI's were sent in real time. The change in height was performed when judged appropriate by an operator. Forecasts were not attempted with this level until after the summer season. Results are discussed in Chapter V.

The forecasting test, after some initial computer problems, officially commenced on 1 June 1976 and was extended until 20 September of the same year. SHARP operated whenever weather of significant rain area occurred, or was expected over the Montreal area. The experiment was repeated during the 1977 summer season. However, unlike the case in 1976 when the SHARP program was run overnight even under a low probability of precipitation, the

1977 test was conducted less rigorously, yielding its place to other higher priority jobs for various scientific research projects.

During the 2-year period, 1852 events or hours, were recorded. They were distributed as follows:

event no.	description	'76	%	'77	%	'76+'77	%
1	forecasts	552	53.3	376	46.1	928	50.1
2	none of the ones listed here	24	2.3	8	1.0	32	1.7
3	insufficient coverage (<2%)	217	20.9	297	36.4	514	27.8
4	computed motion poorly defined, $\gamma_{max} < 0.200$	28	2.7	13	1.6	41	2.2
5	eastern motion detected	32	3.1	8	1.0	40	2.2
6	computed speed < 10 km h^{-1}	14	1.4	26	3.2	62	3.3
7	computed speed > 99 km h^{-1} in 1976, > 110 km h^{-1} in 1977	4	0.4	3	0.4	7	0.4
8	anoprop in the SE	152	14.7	36	4.4	166	9.0
9	drastic motion change	13	1.3	1	0.1	14	0.8
10	2 km CAPPI's	-	-	48	5.9	48	2.6
	Total	1036		816		1852	

Table 3.2 Distribution of events for both years of SHARP operation

It is seen that, over the course of the two seasons, 928 events, or 50% of the total, were forecasts. The other main events, namely insufficient coverage and anomalous propagation accounted for 28% and 9% of the total. The marked difference observed in the probability of event #8 is due in part to the lower priority assigned to SHARP in 1977. However, some of the cases classified under #6 are in fact instances of light anomalous propagation. A detailed examination of each occurrence of event #6 demonstrated that this was indeed the case 34 of the 62 times. Note a decrease in the occurrence of eastern

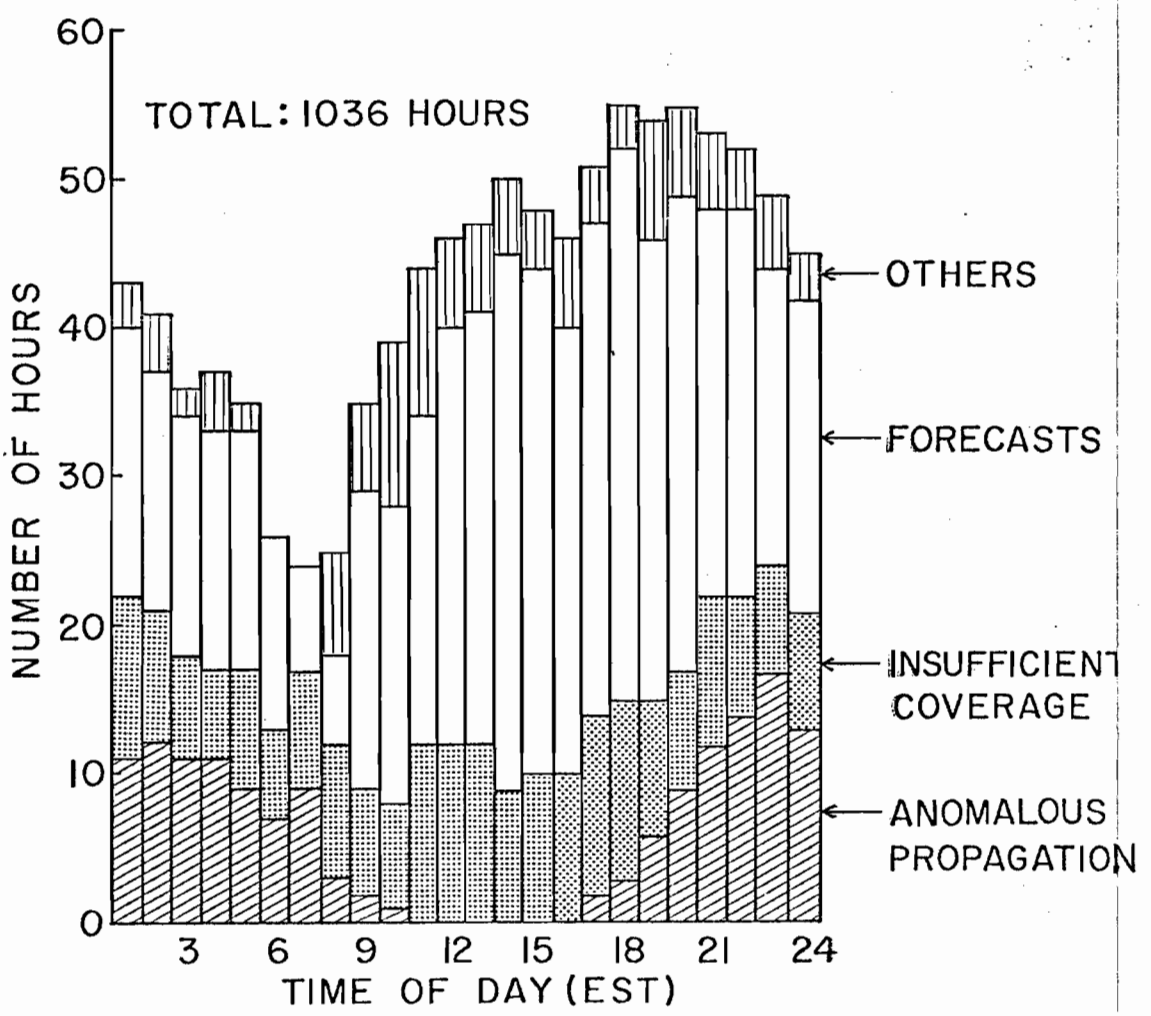

Fig. 3.5. Distribution of main events for 1976 as a function of time of day

motion, reflecting the absence in 1977 of vigorous east-coast lows. However, some of the situations favouring eastern motion were handled by 2 km CAPPI's. The significant increase in event #3 is in line with the observation that the patterns during the cooler summer of 1976 were of larger extent than in the relatively more convective summer of the following year.

The diurnal distribution of the 1036 "potentially forecastable events" for the 1976 season is illustrated in Fig. 3.5. This number constitutes nearly 40% of all possible hours. A significant portion of the events labelled "others" during mid-morning are pertaining to event #4 ($\gamma_{max} < 0.200$). In fact 22 of the 28 events classified as #4 occur during the 0900 to 1400 EST interval, denoting the rapid rearrangement of developing summer precipitation patterns. Note the strong incidence of anomalous propagation between 2000 and 0700 EST. The minimum in the total number of events in the early morning hours followed by a rapid rise at 0900 EST is due to both meteorological causes and hardware reliability on unattended overnight runs. In 1977, it is less prominent.

3.3 Operational Efficiency

The start of the real time SHARP test, originally scheduled for May 15th, 1976, was delayed for a 2-week period due to a computer malfunction. Originally believed to be a "bug" in the program software, the problem was finally traced by field service engineers to a loosely connected memory board which was being accessed only by the forecasting program, resulting in an apparent memory overflow. SHARP was not fully operational until June 3 when it ran successfully for 18 hours during a weather sequence, which in fact represented the first typical summer weather of 1976. From 3 June to 20 September, approximately 195 hours of operation were lost out of a total of 1230 hours with weather, for an efficiency rate of 84%. About 45 of the lost hours of operation, or 23%, did not represent potentially useful data for

forecasting purposes, i.e., anomalous propagation was present or the weather was far away or of insufficient coverage. In addition, the greater percentage of outages occurred in the 0000 to 0800 EST interval when the practical benefit of the information to users is diminished. On the other hand, the performance as a function of the day of the week resulted in a better reliability during weekdays than on weekends when persons familiar with the program execution were absent from the test site and thus unable to provide prompt recovery. Finally, the fact that the program was designed for the dual purpose of forecasting and data recording for scientific research added additional constraints to the system which reduced the overall efficiency of an otherwise single purpose configuration.

A breakdown of the major causes of program interruption with the estimated number of hours lost in 1976 is presented below:

a) Radar transmitter or antenna out of order - 23 hours

b) Interface problems preventing data from reaching the computer or the computer interpreting data as spurious pulses - 25 hours

c) Power failures, whether caused by intense electrical activity or by labour strikes - 10 hours

d) Inability to switch from one tape drive to the next, or both magnetic tapes reaching the endpoint - 35 h.

e) Transmission problems - 50 h.

Output at either site was lost when the paper feed failed to advance. Output was lost at both sites when the paper at the radar tore. Reaching the end of paper at the teletype terminal, leaving it or the modem off-line, accounted for additional losses.

f) Program "bombing" or termination at times of human absence. This occurred mainly during the early stages of the experiment -51 h.

g) Some timing errors were introduced when SHARP was operating on a manual mode. By manual mode is meant that other users could access the SHARP computer since data recording was not required during the time between forecasts. This was made possible by the acquisition of an extra minicomputer for the sole purpose of archiving radar data. However, during the unattended overnight runs, the SHARP computer was required to be on standby and eventually took over the archiving task as soon as the magnetic tape on the other computer reached the end point.

Timing errors also arose when more than one "cycle start" was recognized by the computer resulting in forecasts being made at intervals slightly different than one hour apart. Occasional operator misuse of the appropriate optional switches also resulted in the sending of a real-time rather than a forecast map.

It was not unrealistic to expect, at the end of the 1976 test, that causes d,e, and f would be significantly reduced in a rerun of the experiment under similar constraints. For example, 105 hours or nearly 55% of the total losses occurred in the first month of operation, prior to the delivery of the second computer. In 1977, only 84 hours (10%) were lost. About 32 of these occurred during a fortunately dry period in July when a modem failure prevented the transmission of data to the Weather Office but was available at the radar site. Radar hardware accounted for 24 hours while the remaining 28 hours were principally related to tape problems. The improved efficiency was evident during the critical early morning interval (0600 to 0800 EST). In 1976, that interval accounted for only 7% of the total events but reached 10% in 1977. Not included in the statistics of each year are the hours lost, ($\sim$ 30 per year), when the radar was left idle because the public forecast for the arrival of the precipitation proved to be too slow.

3.4 General Discussion of SHARP Performance

It is realized that in addition to a quantitative verification of the SHARP forecasts as reported in Chapter IV, there are other pertinent factors which have been noted during the test to which one cannot ascribe a numerical value. Nonetheless, knowledge so obtained through experience is invaluable in assisting in the development of an improved product or, at least, in underlining situations with which the technique is deficient.

3.4.1 Classification of Weather Situations

A parameter which is readily established as significant is the intensity of the precipitation. The weather systems may thus be divided into three broad classes:

a) Intense Precipitation. This is an event when rainfall rates greater than about 10 mm h^{-1} are observed. These events are either associated with frontal passages and usually organized into line systems, or are of the air mass type forming isolated convective systems. An examination of the forecasts indicates that the motion of these systems is generally well predicted by the SHARP procedure. They are of sufficient height to be intercepted by the 3 km CAPPI up to far ranges and are long lasting. The trajectory formed by hourly motion vectors displays a rectilinear, constant displacement.

b) Moderate Precipitation. This type is similar to the above but more widespread and with less intense precipitation. Occasional poor results due to echo decay, excessive coverage, or range dependence were encountered.

c) Light precipitation (< 3 mm h^{-1}). These events are often associated with low pressure systems with cold, winterlike weather in the form of low altitude drizzly precipitation and ephemeral patterns. The difficulties encountered with their prediction are discussed below.

3.4.2 Qualitative Analysis of Poorly Forecast Events

a) It became apparent from the early days in the operation of SHARP that light, widely scattered precipitation of low height does not lend itself to reliable forecasts. Some of the reasons are:

i) Low weather cannot be intercepted at far ranges where the first elevation angle of the antenna beam exceeds 3 km; as a result, the shape and intensity of the patterns are observed to be range dependent, i.e., intensifying and increasing in area as they approach the radar, and diminishing in area and intensity as they recede from the radar.

ii) Even at near ranges, experience indicates that the rainfall rate as observed by the radar at 3 km is significantly underestimated when compared with what actually falls at the ground. This is a reflection of the different rainforming mechanism between a convective storm and light, continuous rain generated from snow. Whereas in the convective process the 3 km level is a reliable estimate of what reaches the ground, most of the development in the winter-like situation often occurs below the 3 km height. A detailed examination of 2.0, 2.5 and 3.0 km levels presented in Chapter V will corroborate this statement. Hence, it is recommended that in light, low precipitation, the CAPPI height be lowered and the maximum range be decreased to achieve a better spatial resolution. When this is done, the enhancement of ground echoes particularly in the south and southeast is masked by special characters.

iii) It has also been observed that their motion is erratic from hour to hour, with patches suddenly appearing and disappearing at the 3 km level. This behaviour forces the pattern recognition program to erroneously interpret the regeneration of an area of vertical motion yielding precipitation which just peaks through the 3 km level as motion with respect to a previously

unrelated area of precipitation undergoing the same physical process. These difficulties are similar to those encountered with winter snowstorms when the detectability is an even more severe problem.

In general, when this type of precipitation is associated with a low pressure system approaching from the west, its motion is unusually fast, while when generated by an east coast low, the motion is quasi stationary and at times possesses an eastern component of velocity.

b) The performance of the SHARP program during the 1976 test has been reviewed in a qualitative fashion by a careful examination of the digital maps. In general, the following comments can be advanced:

i) In only less than ten cases was there truly a mismatch between the overall motion of the storm system as observed on the maps and that determined by the pattern recognition algorithm. In some instances, the mismatch was caused by the association of weather echoes at time T_o with anomalous propagation at $(T_o - \Delta T)$ when the latter had developed at locations other than the familiar southeast sector. Forecasters were immediately advised by telephone when this incongruity arose.

ii) Improper determination of pattern speeds also occurred when echo coverage exceeded 30 or 40% of the area being correlated, especially under conditions of widespread, uniform rain lacking predominant or long lasting structural features which would be recognizable by the pattern matching technique. In these circumstances, the relatively large percentage of rain areas at, or entering and leaving, the boundaries further complicated an accurate motion estimate. However, it is noted that, notwithstanding a considerable deviation from the true motion, usually an underestimation, the accurate forecast of the intensity of the rain at any point is considerably less dependent on the pattern velocity than on days of scattered convective storms or squall lines.

iii) The southeast sector of the radar is especially susceptible to inaccurate forecasts as it comprises most of the potentially difficult situations like light, widespread rain emanating from an east-coast low, a greater incidence of anomalous propagation and a boundary problem which is twice as serious as in any other sector. Most echo patterns travel from a WSW direction and thus parallel to the edge of the map in that region. Complications attributed to the simultaneous entering and leaving through the boundaries are more common since medium-sized echoes can often be touching all three margins. Moreover, when their approach toward the radar is constrained to medium or far ranges, the period of observation and eventual tracking is limited to merely 2 or 3 hours. The quality of the forecasts, which improves with the tracking time, is thus compromised. Equivalent difficulties are not experienced for situations when the weather appears close to the northwest boundaries. This case is often a cold front triggering a strong convective activity which normally descends southward and enters regions more amenable to better forecasts. In this respect, it would not be inappropriate to point out that the SE problem does not affect the regions served by SHARP.

iv) With the exception of one notable sequence, the rejection of eastern motion proved to be beneficial in discarding potentially erroneous forecasts, which for the most part included light, low precipitation confined in the south and southeast sector of the radar coverage.

v) It is not uncommon for other echo patches to be moving in different directions and speeds than the main storm. In many cases, post-analysis reveals that they are identifiable as secondary maxima on the cross-correlation matrix during the 1036 events of 1976, but in only 19 instances did they prove to represent the displacement of the entire echo pattern. A test of a pattern recognition technique accounting for regional differential motion is reported in Chapter VI.

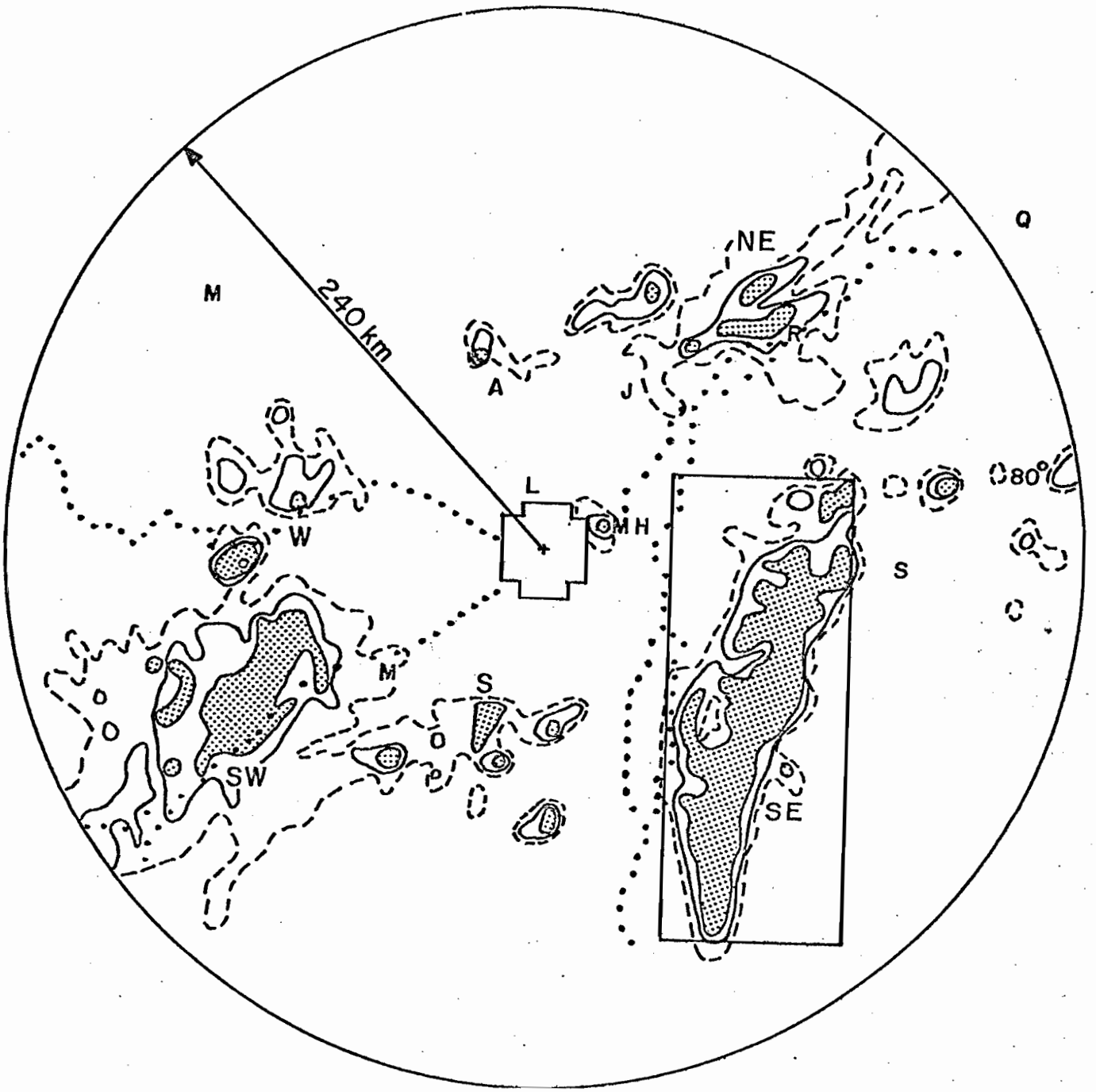

Fig. 3.6. Average configuration derived by summing and scaling 374 CAPPI maps (~187 hours) characterized by anomalous propagation.

vi) On about half-a-dozen days, occurrences of echoes decreasing in intensity as they approached the Montreal area were observed, particularly to the SW of the radar at a range of about 40 km. Other areas of peculiar storm behaviour included the generation of storms west of Lake St. Pierre and the formation of slow-moving echoes northeast of Ottawa and near Cornwall.

3.4.3 Anomalous Propagation

The presence of anomalous propagation, also referred as AP or anoprop, mixed with radar data proved to be a challenge to an automated radar prediction for its discrimination from weather echoes was essential for a successful test. In the absence of an instrumental ground clutter rejection technique described by Johnson et al (1975), a software method pertinent to the Montreal region was devised. Such a task was made possible by the fact that the presence of AP is associated with characteristic radar returns from mountains in the southeast sector. Before the operational test, maps from 1975 summer data with anomalous propagation were accumulated to yield an average configuration. (Fig. 3.6 represents a similar summation for 1976). The SHARP program performs a grid point by grid point comparison inside the rectangular area between the average anomalous propagation configuration and the existing radar echoes. The percentage of points with echoes on the map matching the outline of the anomalous propagation, PA, is contrasted with those that fall outside of it, PP, the latter likely denoting a precipitation value. This precaution is essential in order to avoid the situation of declaring anomalous propagation conditions when the chosen neighbourhood is completely covered with precipitation echoes. These two parameters are then plotted and by visual classification of the anomalous propagation intensity from the digital maps, a boundary is drawn dividing anoprop cases from light or non-existing anoprop conditions.

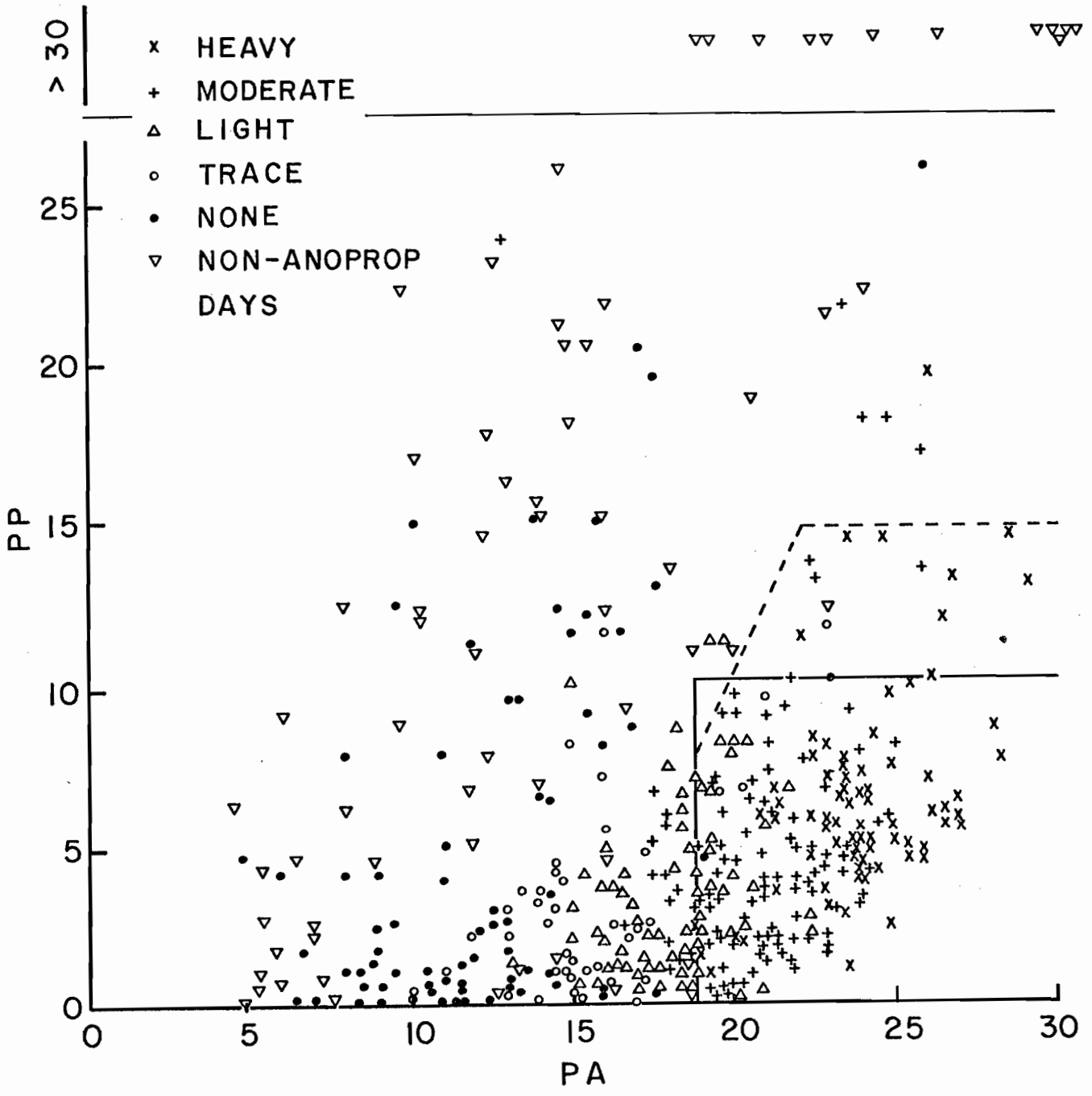

Fig. 3.7. Scatter diagram of the parameters PA and PP (refer to text) used to detect the presence of anoprop. The rectangular area shown defined anoprop since the 1976 test. An extension to the dashed line may be appropriate for future experiments.

For illustration, this procedure has been repeated for 1976 data. Fig. 3.6 is the result of 374 CAPPI summations spaced at 30 minute intervals for times when anoprop was, or about to be, in the southeast. In this display, the contribution from precipitation is effectively removed by averaging and applying a suitable lower threshold. The strong enhancement of the ground echo in the southeast is well exemplified. Note the large incidence of anoprop in the SW, W and NE of the radar as indicated. Each of the maps included in the summation is examined and the extent of the anoprop in the southeast is classified as shown in Fig. 3.7, which is the scatter plot of the parameters PA and PP. A few sets of points derived from randomly selected non-anoprop days are also added. It is seen that moderate and heavy anoprop cases are characterized by high values of PA and low values of PP. At the beginning of the 1976 test, anoprop was declared when

$$PA > 17 \text{ and } PP < 12$$

However, on fairly numerous occasions, anoprop was considered detected, and hence no forecasts were issued for conditions of light anoprop. Criteria for positive confirmation of anoprop were thus modified to

$$PA > 19 \text{ and } PP < 10$$

As an aside, it would seem more straightforward to ascertain the presence of anoprop by the simple expedient of a pattern recognition technique yielding a cross-correlation coefficient, γ, between the average anoprop configuration and the actual radar pattern in the defined rectangle. Results demonstrated that $\gamma > 0.650$ represent a positive confirmation of anoprop while a magnitude under 0.450 assures its absence. However, the interval $0.450 \leqslant \gamma \leqslant 0.650$ includes numerous cases of non-anoprop as well as various levels of anoprop conditions.

The success of the anomalous propagation recognition algorithm was evaluated as follows:

$$\text{Error} = \frac{\text{failures of detection + erroneous detections}}{\text{total number of events}} = \frac{7 + 9}{1036} = 1.5\%$$

Additional details can be found in Bellon and Austin (1977).

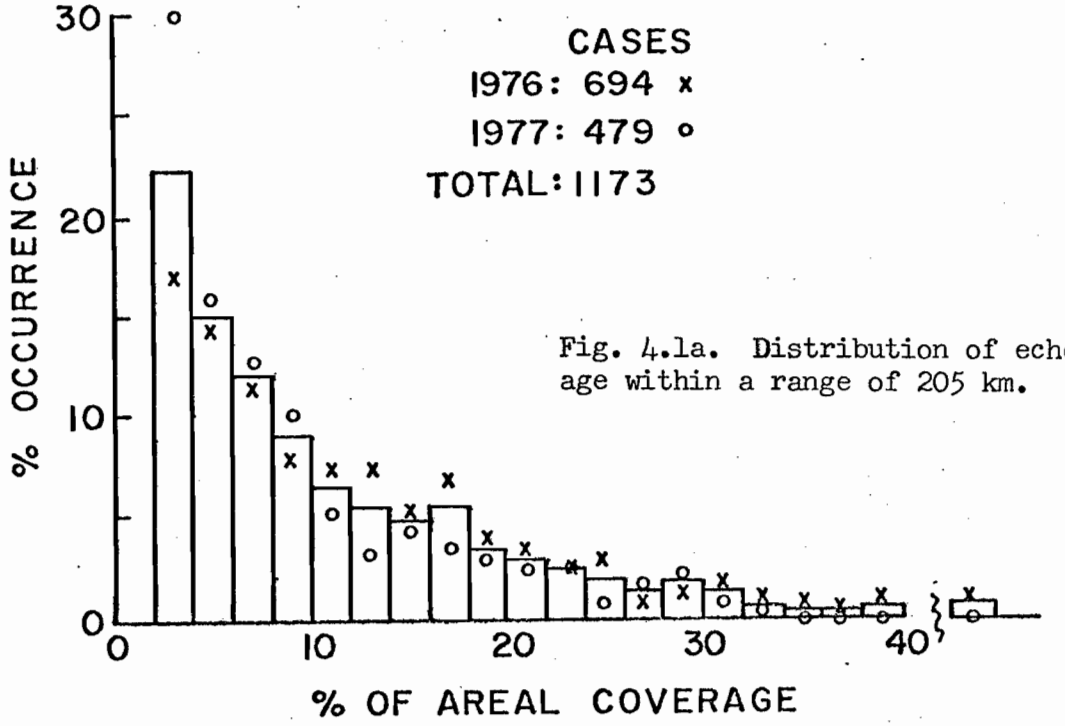

Fig. 4.1a. Distribution of echo coverage within a range of 205 km.

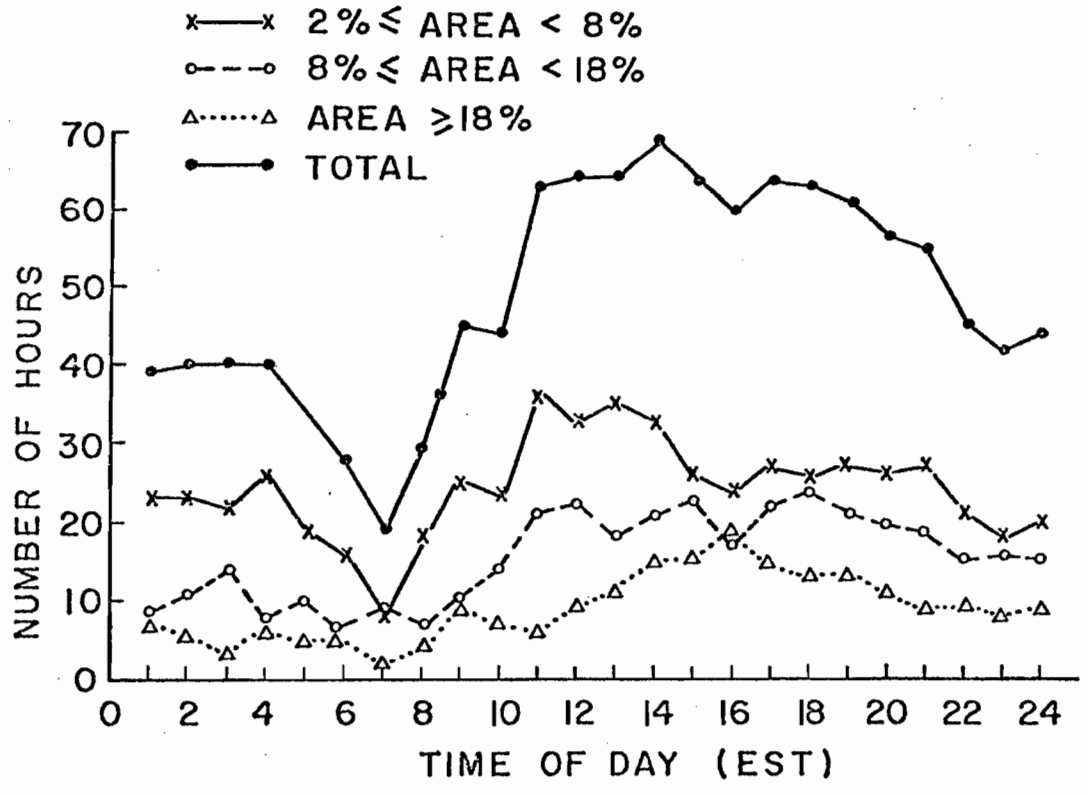

Fig. 4.1b. Distribution of light, medium and heavy echo coverage as a function of time of day.

CHAPTER IV
RESULTS AND VERIFICATION

4.1 General Radar Echoes Statistics

In the course of compiling various parameters pertaining to summer weather patterns, we have derived meaningful chacteristics of their average motion and appearance. These are presented before undertaking an analysis of the forecast results and verification

a) Areal Distribution

The distribution of echo coverage exceeding 2% within the 205 km range, and excluding anoprop, is presented in Fig. 4.1a. The histogram is based on 3 km CAPPI data from both summers of 1976 and 1977 which include a total of 1173 cases. It reveals that for nearly 50% of the cases, the areal coverage is less than 8%; for over 80% of the events, it is less than 18%, while 99% of the time it is under 40%. Comparison between the two years shows that 1976 had fewer instances of light coverage, (43% vs 59% for coverage less than 8%), but more cases of heavy coverage (6.0% vs 1.7%) for cases exceeding 30% coverage). The latter were being caused by a greater occurrence in 1976 of widespread continuous rain generated by low pressure systems passing directly over the Montreal area, or by the intensification of east-coast lows spreading a wide band of light to moderate rain over the major portion of the eastern sector of the radar screen. The variation of three classes of areal coverage as a function of the time of day is plotted in Fig. 4.1b. Note the relatively large number of occurrences of light coverage in the early morning and mid-day hours and an increased likelihood of medium and heavy coverage in the afternoon and evening.

The cumulative frequency distribution of rainfall rate thresholds exceeding a certain size, Fig. 4.1c, adds further information into the structure of radar echoes. This plot is derived from 694, 3 km CAPPI data

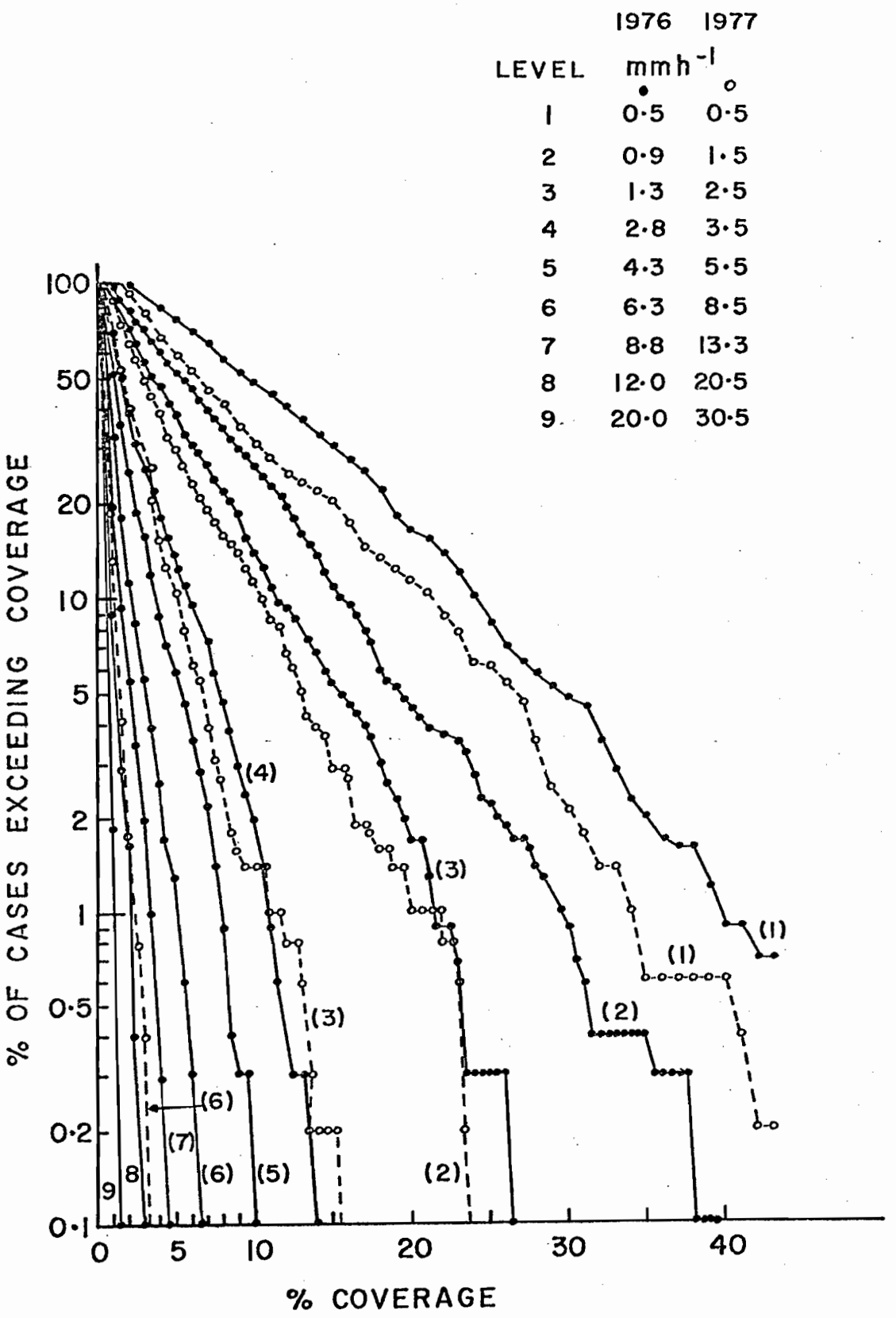

Fig. 4.1c. Cumulative frequency distribution of rainfall rate thresholds exceeding a certain size.

obtained during the 1976 test. More exhaustive work for Montreal storms using radar and raingages has been reported by Marshall and Holtz (1970), Zawadzki (1975), Drufuca and Zawadzki (1975) and Drufuca (1977). Comparison with their results is not attempted on account of differences in resolution between raingage data at a point and 3 km data averaged over a 36 km^2 grid. A general exponential decay is observed with echo size for all intensities, with the greater rate of decay being experienced by the higher levels. For nearly all the rainfall rates, the slope exhibits an observable downward "kink" beyond the 2% cumulative probability level. This effect is likely due to averaging over the relatively large 36 km^2 grid, which decreases the occurrence of the higher rainfall rates which may be of a scale smaller than 36 km^2. The low probability of occurrence of the higher levels is a determining factor on the inability of an extrapolating technique to forecast their location to within a few grid lengths. Some curves are provided for 1977 data. While differences in the calibration of both years renders exact comparison difficult, the reduced size of echoes in 1977 is evident.

b) Speed and Direction Distribution

The distribution of speeds portrayed in Fig. 4.2 shows that the most probable pattern speed, (38% of the cases), occurs in the 40-60 km h^{-1} range. A definite difference can be observed between the two summers; 38% of the storms in 1976 had speeds greater than 50 km h^{-1}, but 63% exceeded that magnitude in 1977. In fact, the average speed is calculated to be 45 and 54 km h^{-1} respectively. Fig. 4.3, displaying the distribution of azimuthal directions and corresponding speeds reveals a further contrast between the two summers. In 1977, the spread in azimuthal directions was confined to a predominant W-E motion, with moderate and fast speeds directly from the W or WSW. For example, 45% of all precipitation patterns in 1977 originated from a sector between 240 and 284 degrees, travelling at a speed varying

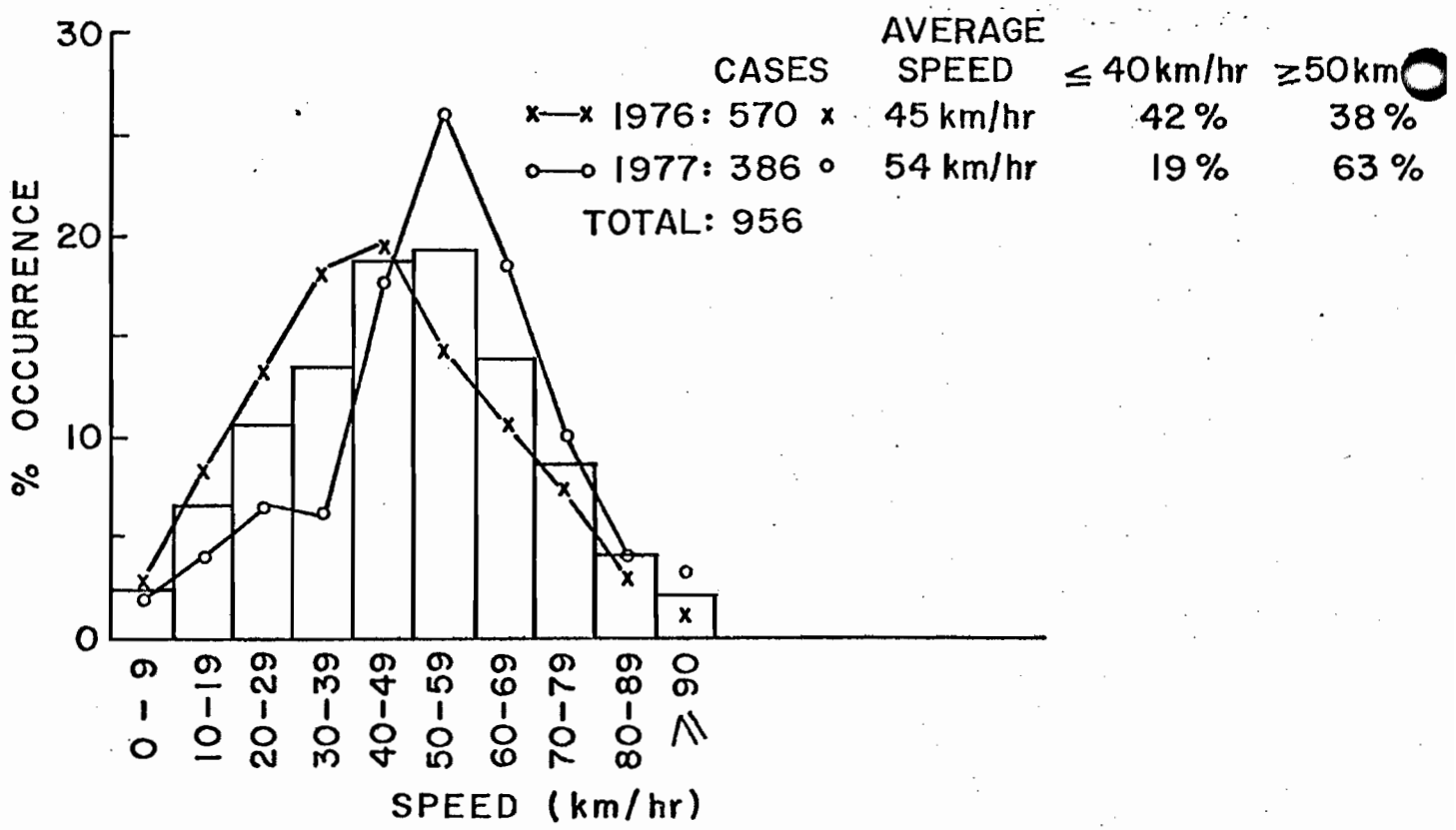

Fig. 4.2. Distribution of precipitation pattern speeds.

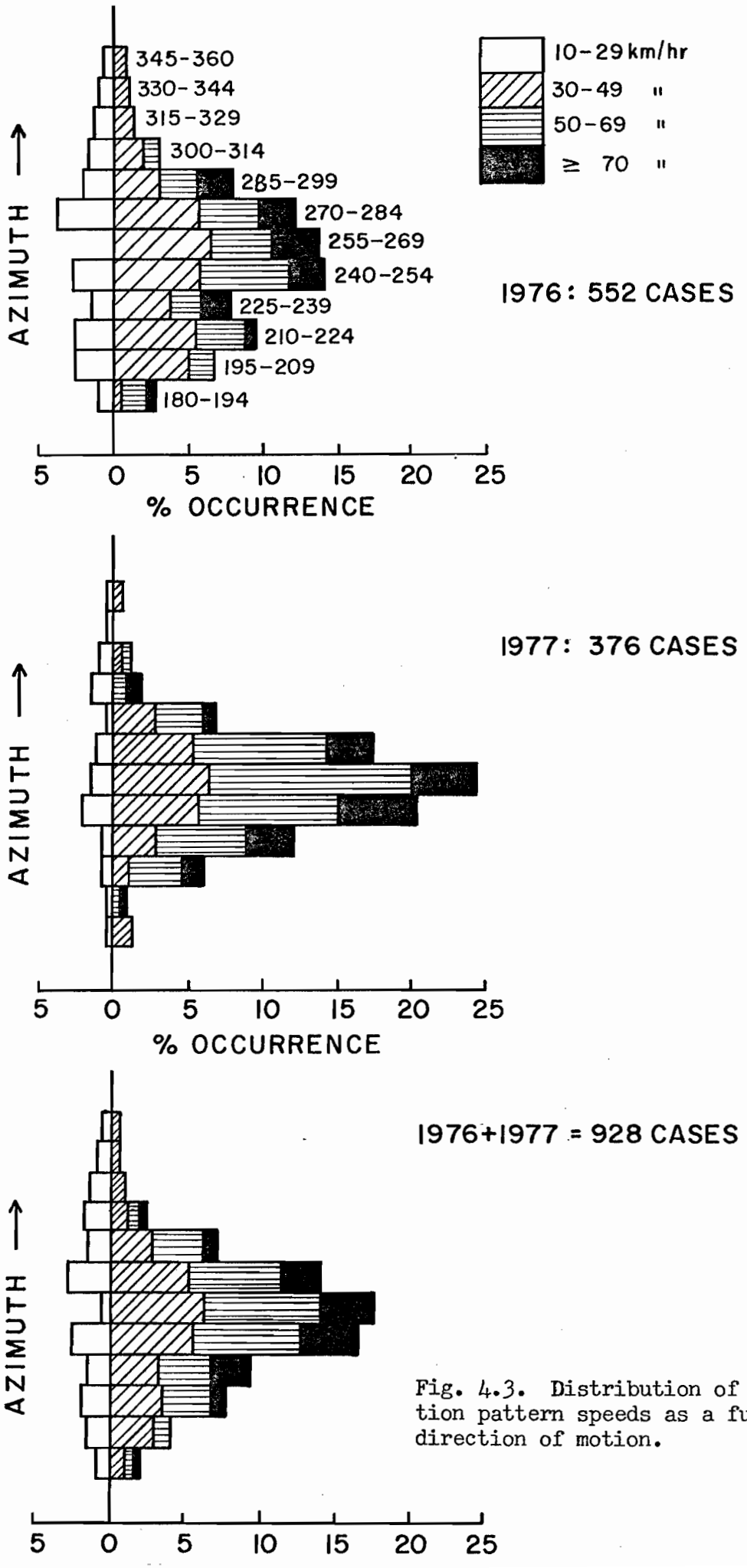

Fig. 4.3. Distribution of precipitation pattern speeds as a function of direction of motion.

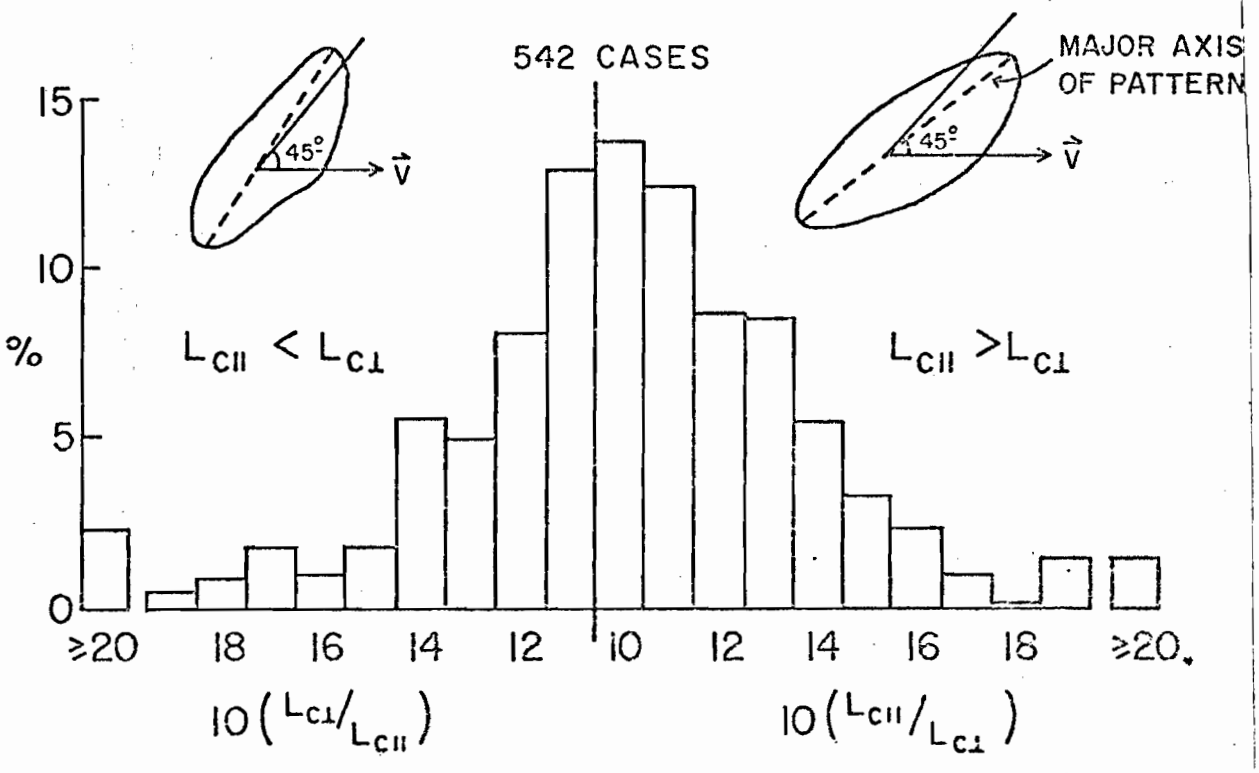

Fig. 4.4. Distribution of echo pattern orientation along directions orthogonal to the direction of motion.

between 40 and 70 km h^{-1}. The wider distribution of azimuths for the summer of 1976 indicates a more disturbed circulation accompanying weather systems. In particular, the secondary peak from the SW and the more prominent occurrence of NW motion would suppose motion of weather echoes in the warm sector of a low passing north of the radar site, followed by storms accompanying the cold front passage immediately to the rear of the low centre. Synoptic maps for 1977 revealed that many cold front passages were associated with purely westerly motion since the cold front was relatively far removed from the low centre, and hence devoid of a vigorous northwest push at its rear.

c) Orientation of Patterns

The preferred orientation of weather patterns in relation to their motion, in particular in directions parallel and perpendicular to their displacement, has been investigated. The technique consists of calculating the autocorrelation coefficient γ_A along the desired direction and noting the lag at which it decays to a value of $\frac{1}{e} \approx 0.37$. This distance is known as the characteristic pattern length L_c. Assuming an exponential decay of γ_A with distance,

i.e.,

$$\gamma_A = e^{-\lambda L}, \text{ then } 0.37 = e^{-\lambda L_c}$$

L_c can be easily obtained by calculating γ_A for a few lags along the chosen directions and deriving an average value for λ. The ratio of L_c parallel ($L_{c\parallel}$) and perpendicular ($L_{c\perp}$) to the motion is plotted in Fig. 4.4. Note that the parameters are interchanged when $L_{c\parallel} > L_{c\perp}$ in order to avoid distortion of the curve. Over 60% of the 542 cases of the 1976 season analyzed display an orientation which is preferentially aligned in their direction of motion. However, the more significant aspect of this distribution

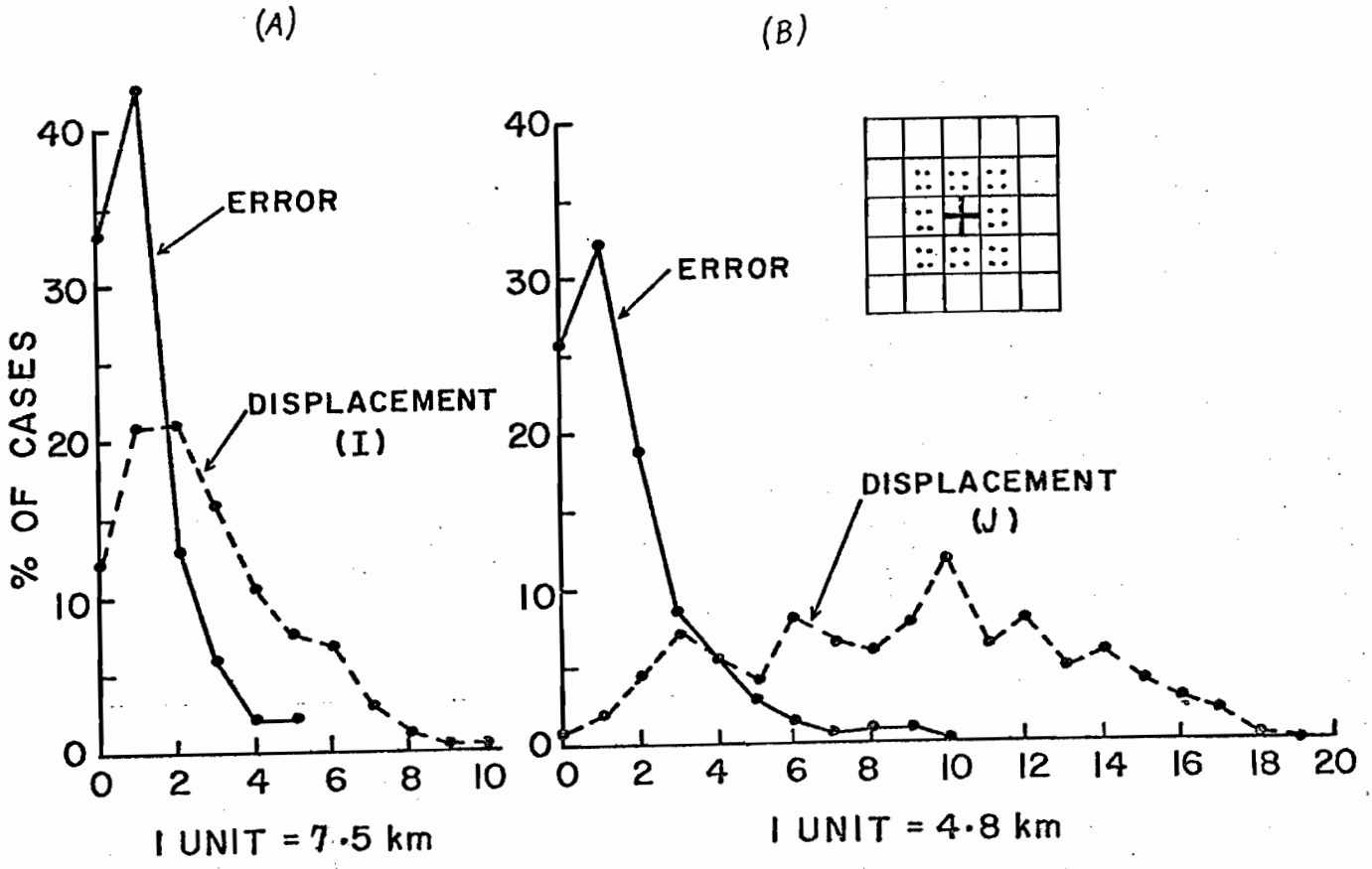

Fig. 4.5. Distribution of the 1 h forecast error and displacement along the north-south (a) and west-east (b) directions for both years combined.

is that it contains relatively few patterns with marked elongations, that is, with ratios greater than 1.5 along directions parallel or perpendicular to their motion.

4.2 Spatial Error of Forecast Displacement

The distribution of speeds with direction for magnitudes under 30 km h^{-1} is presented to the left of the axis in Fig. 4.3. This consideration is necessary since the coarse spatial resolution of the map, particularly in the I or north-south direction forces the distribution into preferred directions like 270°, while certain intervals, for example 255° - 269°, are mathematically impossible. Quantization of direction can be minimized by a reduced grid size which can be achieved by limiting the (64 x 100) matrix to a range of 200 km rather than 240 km, thus improving the grid area by about 30%. However, the useful far range detection capability of the radar would have been ignored. In 1977, a technique was introduced which reduced this quantization problem by computing pattern motion in fractions of a grid length by way of a 9-point interpolation of the cross-correlation coefficients around γ_{max}.

The need for improving the north-south resolution becomes more apparent when the spatial errors for 1-hour forecasts are examined. The distribution in both the I, north-south, and J, west-east, direction of the error and actual absolute motion in grid lengths is depicted in Figs. 4.5a and 4.5b. The average of the absolute motion in grid lengths for the 735 verifying cases is found to be (2.7 I, 8.8 J). Their distribution is given by the dashed lines. Thus, the I and J resolution represent 37% and 11% respectively of the average absolute displacement, implying that an error of one grid length entails a significant percentage error for a one-hour forecast.

The peak which occurs at 1 grid length error can thus be attributed to a quantization effect, which is more severe in the I direction. A separate examination of the 1977 cases revealed that while this effect was reduced by the introduction of fractional grid length displacements, it still persisted. Parameters describing the spatial errors for both 1976, 1977 and both years combined are presented in Table 4.1 and defined in Fig. 4.6. For forecasts longer than one hour, the actual motion has been computed from the vector sum of the one hour displacements recorded during the real-time test. The predicted displacement is an appropriate constant of the latest one hour displacement.

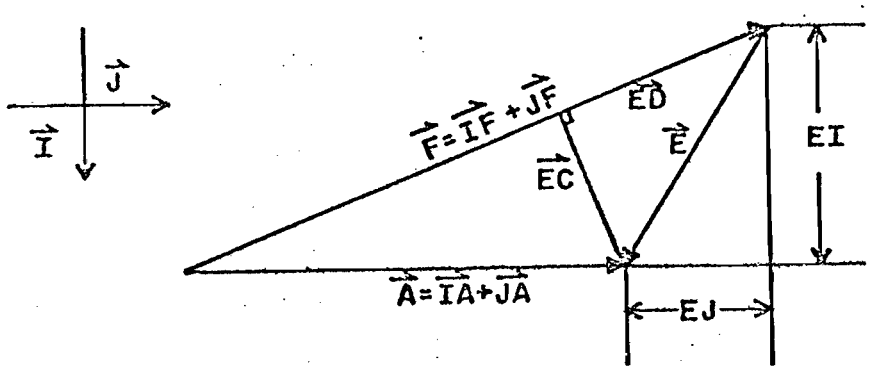

$\vec{F}$: FORECAST VECTOR
$\vec{A}$: ACTUAL MOTION
$\vec{E}$: SPATIAL ERROR
$\vec{EC}$: CROSS-RANGE ERROR
$\vec{ED}$: DOWN-RANGE ERROR

$$\vec{A}=\vec{F}+\vec{E}$$
$$\vec{E}=\vec{EI}+\vec{EJ}=\vec{EC}+\vec{ED}$$
$$EI=|\vec{IF}-\vec{IA}|$$
$$EJ=|\vec{JF}-\vec{JA}|$$

$$EI' = EI \text{ IF } EI > 1 \qquad = 0 \text{ IF } EI \leq 1$$

$$EJ' = EJ \text{ IF } EJ > 1 \qquad = 0 \text{ IF } EJ \leq 1$$

$$\overline{EI} = 100\,\frac{\Sigma EI}{\Sigma IA} \qquad \overline{EJ} = 100\,\frac{\Sigma EJ}{\Sigma JA}$$

$$\overline{EI'} = 100\,\frac{\Sigma EI'}{\Sigma IA} \qquad \overline{EJ'} = 100\,\frac{\Sigma EJ'}{\Sigma JA}$$

$$\overline{E} = 100\,\frac{\Sigma E}{\Sigma A} \qquad \overline{E'} = 100\,\frac{\Sigma\sqrt{(EI')^2+(EJ')^2}}{\Sigma A}$$

Fig. 4.6. Definition of the spatial error E and other related parameters.

Length of forecast (hrs)	Year	No. of forecasts	$\overline{EI}$	$\overline{EJ}$	$\overline{EI'}$	$\overline{EJ'}$	$\overline{E'}$	$\overline{E}$	$\overline{A}$ (km)
	76	434	40.9	20.6	25.7	16.4	21.5	28.3	46.5
1	77	301	40.0	17.4	22.8	13.9	17.9	27.7	54.9
	76+77	735	40.4	19.0	24.5	15.2	19.8	26.2	49.9
	76	350	43.0	19.9	37.7	18.5	26.1	27.8	93.9
2	77	238	41.0	16.7	33.7	15.6	21.8	23.8	109.1
	76+77	588	42.2	18.4	36.1	17.2	24.2	25.8	100.0
	76	284	43.2	19.6	40.7	18.9	26.6	27.2	142.4
3	77	186	40.8	17.2	37.1	16.8	22.8	23.4	162.1
	76+77	470	42.3	18.5	39.4	18.0	25.0	25.6	150.1
	76	231	42.2	19.3	40.9	18.9	26.2	26.5	190.9
4	77	148	43.0	17.3	41.4	17.0	24.1	24.3	215.3
	76+77	379	42.6	18.5	41.2	18.1	25.4	25.6	200.3
	76	189	41.8	19.9	40.9	19.6	26.6	26.8	241.0
5	77	118	49.9	18.4	49.0	18.2	26.6	26.7	271.0
	76+77	307	44.7	19.3	43.8	19.1	26.6	26.8	252.5

Table 4.1 Parameters describing the difference between forecast and actual displacement, that is, the spatial error for the two year experiment.

The table shows that, in general, the 1977 forecasts resulted in slightly reduced percentage errors, particularly for forecasts less than 5 hours. This is probably a consequence of the narrower speed and direction distribution in 1977 as shown in Figs. 4.2 and 4.3. Note that the overall error $\overline{E}$ is independent of the length of the forecast, ranging in the neighborhood of 26% for both years combined. If errors of one grid length are excluded, as expected, marked differences are noted in the one-hour forecasts. For example, the average spatial error in the I and J direction is found to be 40.4% and 19.0% respectively. It drastically falls to 24.5% and 15.2% with the above consideration, reducing the total error $\overline{E}'$ to less than 20%. Such differences can be explained with the insert of Fig. 4.5b. If we equate a perfect spatial forecast with the ability of hitting the centre of the target, and assume the rms error to be large compared with the grid size, i.e., of the order of 2 or 3 grid lengths, it is evident that there are eight times as many chances of missing it by one grid length than there are of hitting it. In conclusion, Table 4.1 indicates that the major source of error in storm displacement forecasts is derived from the determination of the north-south component of velocity. An error reduction will be achieved if the average magnitude of this component for one hour displacements is increased to about 5 times the grid length. This goal is impeded by the aspect ratio of output devices which, for the sake of conformality, necessitate a larger grid length along the north-south direction. In addition, the north-south component is usually of smaller magnitude in a predominantly westerly circulation. A finer grid length, as may be obtained by increasing the number of rows of the map matrix, would solve the problem but it may be rejected by core and time constraints of a minicomputer as well as by transmission considerations. However, if successful, the magnitude of the errors in the J, west-east direction, assures us of a total error of less than 20%.

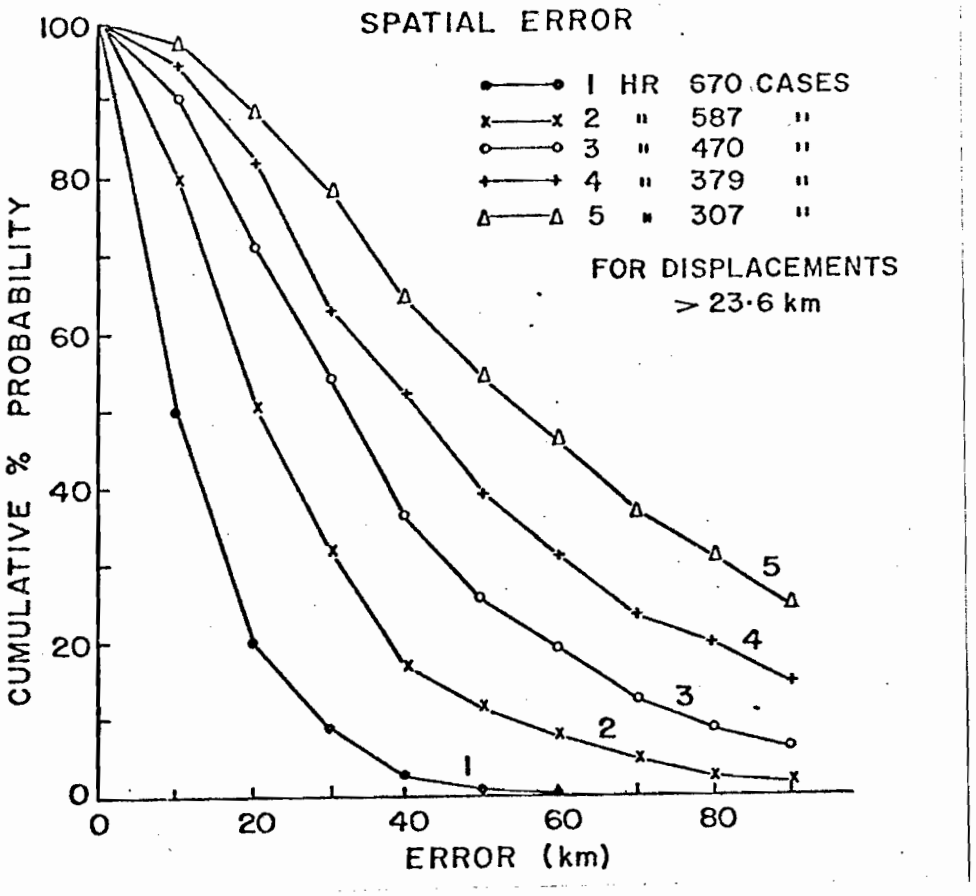

Fig. 4.7a. Probability distribution, derived from 1976 and 1977 data, of the spatial error exceeding specified values for 1–5 h forecasts.

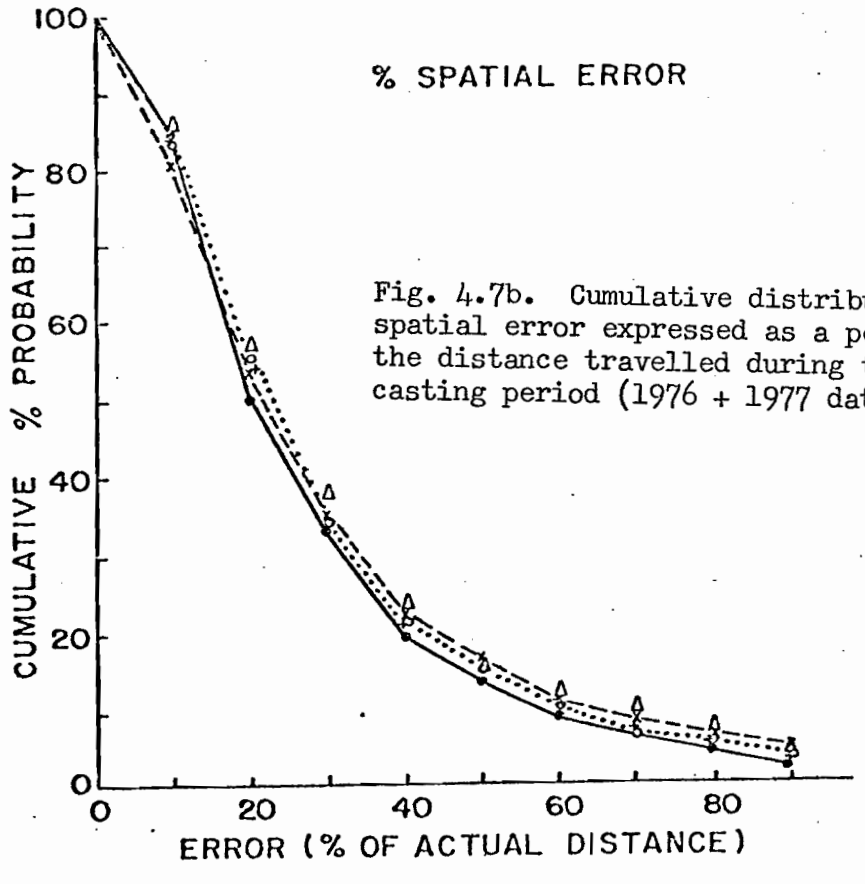

Fig. 4.7b. Cumulative distribution of the spatial error expressed as a percentage of the distance travelled during the forecasting period (1976 + 1977 data).

The cumulative distributions of the average error and of its orthogonal components ED and EC (see Fig. 4.6) parallel and perpendicular to the direction of motion as a function of the forecast length provide a more appropriate analysis of the spatial error. In order to minimize quantization effects caused by the relative magnitude of the displacement and the grid size, only cases for which the actual motion is greater than 24 km are included. Since the forecasting concept is based on constant linear motion, the spatial error is a measure of the departure from linearity of weather systems displacement. The probability distribution of the spatial error exceeding specified values for one to five hour forecasts is shown in Fig. 4.7a. Fig. 4.7b presents the cumulative distribution of the spatial error in terms of the percentage of the distance travelled during the forecasting period. For 1 h forecasts, there exists a 50% probability that the error be greater than 10 km and a 10% probability that it exceeds 30 km. For a 2 h forecast, the 10 and 30 km limits correspond to the 80 and 30% probability levels. Quite evident is the rapid increase in the probability of the large magnitude errors, i.e., > 30 km, as the forecast length is extended. However when expressed as a percentage of the distance covered, the result is relatively independent of the forecast length, Fig. 4.7b, with a 33% probability of the error being over 30% of the total distance. This statement defines the rms error. Hence, taking an average speed of 50 km h^{-1}, a 30% rms error corresponds to 2I or 3J grid lengths per hour. It is equivalent to a deviation of about $\pm$ 12° in direction and $\pm$ 20% in speed. This is comparable with the accuracy of forecasting larger scale weather patterns and is generally regarded as acceptable.

Sets of graphs for the cross-range and down-range components of the spatial error are given in Figs. 4.8a and 4.9a. In Fig. 4.8a the points are nearly symmetrically distributed on both sides of the centre axis, thus

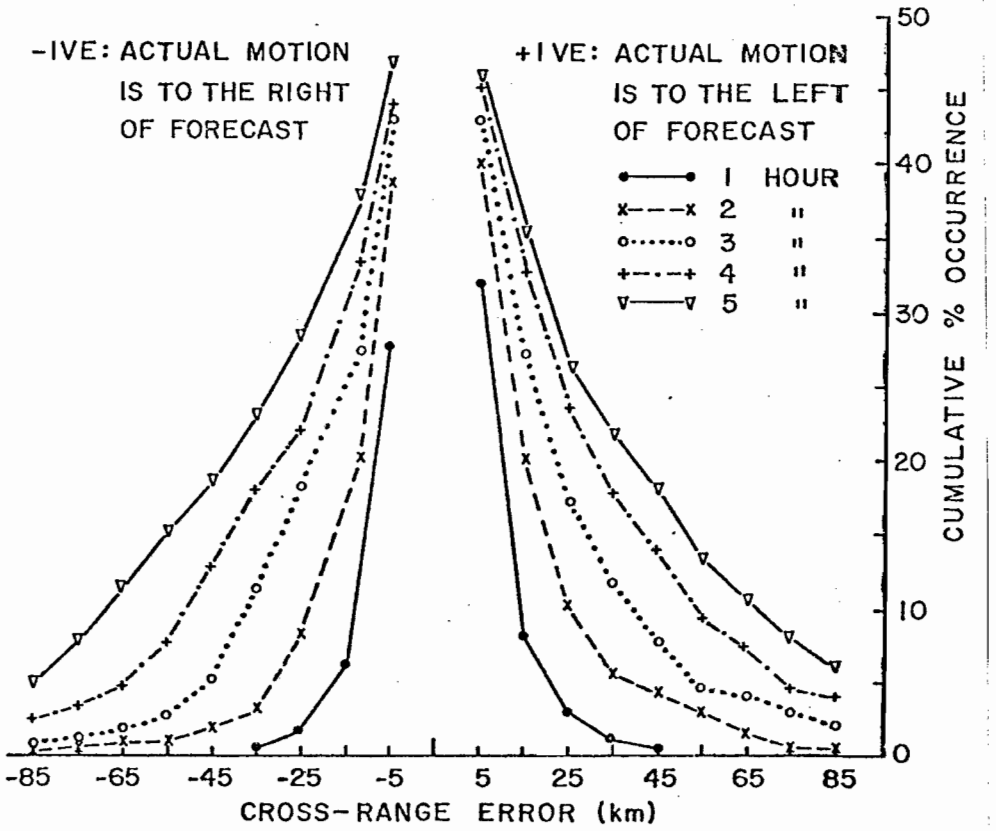

Fig. 4.8a. Cumulative distribution of the cross-range error exceeding specified values.

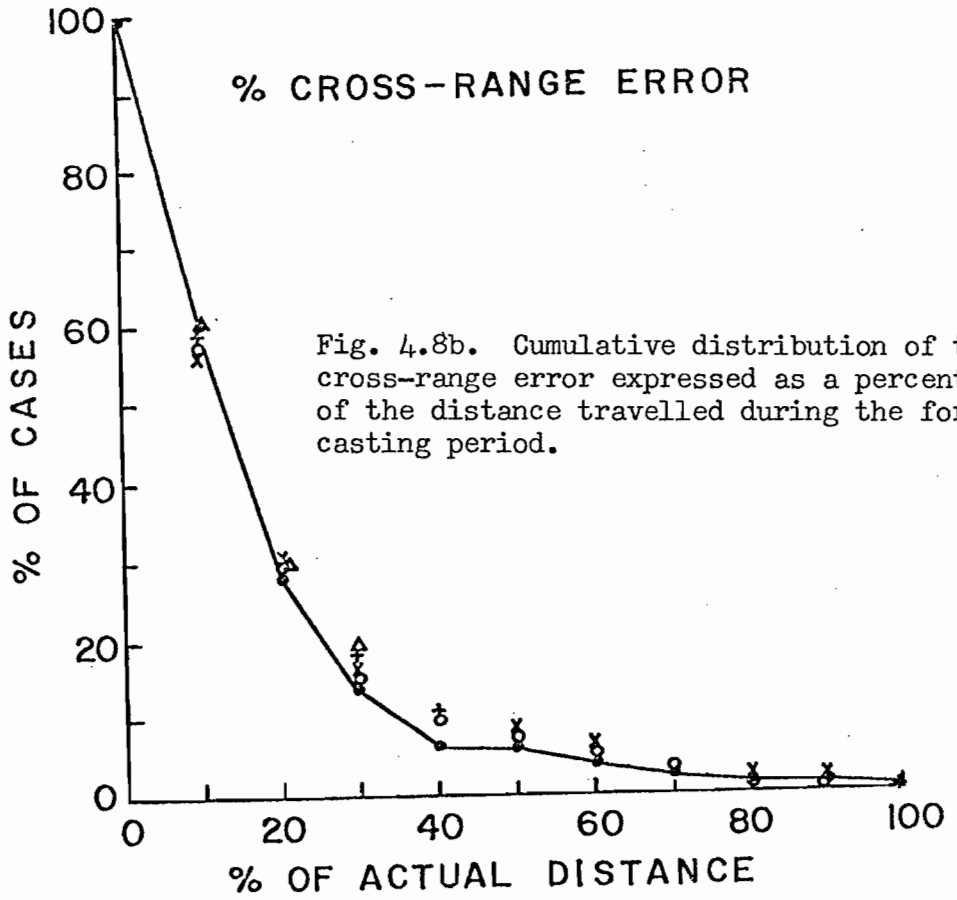

Fig. 4.8b. Cumulative distribution of the cross-range error expressed as a percentage of the distance travelled during the forecasting period.

discounting any discernible tendency. Again, its expression as a percentage, Fig. 4.8b, is independent of the forecast length. This figure proves to be a verification reference for the arbitrary choice of the 16° arc as the basis for sector forecasts exemplified in Fig. 3.3b. From the value of tan $8^{\circ} = 0.14$, the sector forecasts accounted for all expected cross-range errors with absolute values of less than 15%. Figure 4.8b discloses that this choice includes nearly 60% of all cases. Note that the magnitude of the cross-range error is more critical than that of the down-range error in determining whether a particular storm area will eventually pass over a forecast location. The down-range error affects only its time of arrival, while a cross-range error greater than the scale length of the forecast feature will result in a false alarm or unexpected rain.

Fig. 4.9a reveals a definite tendency for motions slower than forecast, particularly for longer forecast lengths. A possible explanation for this effect is sketched in Fig. 4.9b.

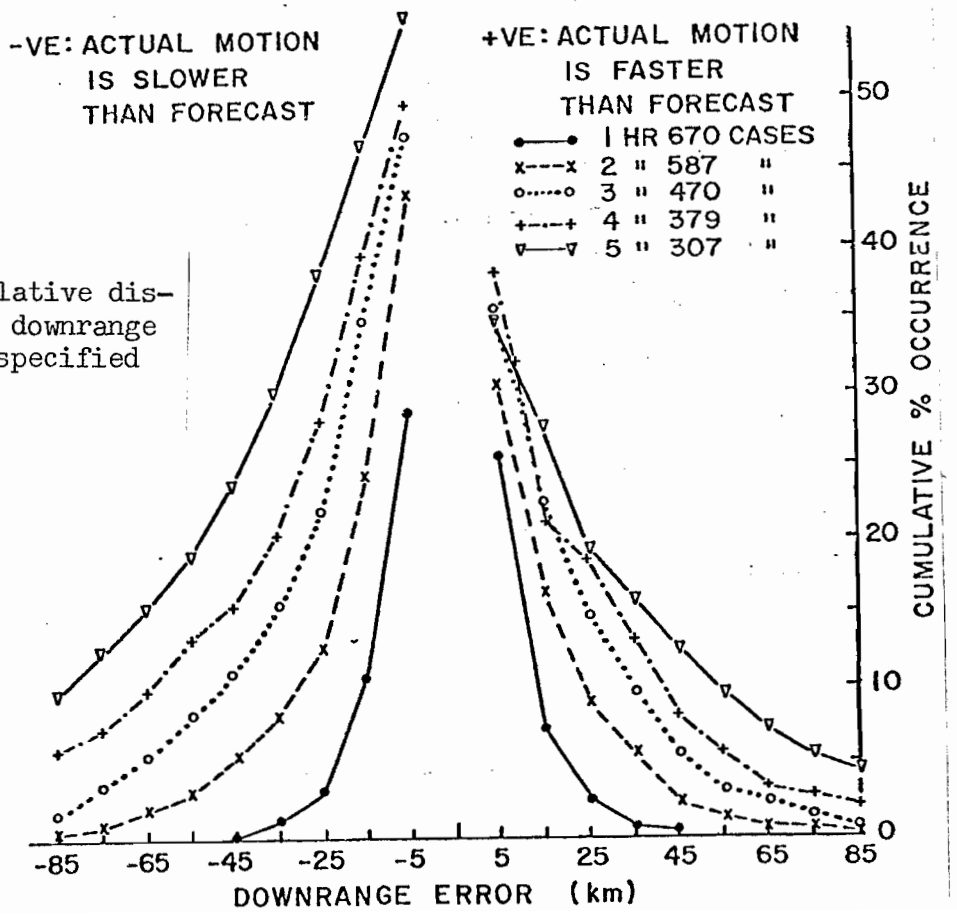

Fig. 4.9a. Cumulative distribution of the downrange error exceeding specified values.

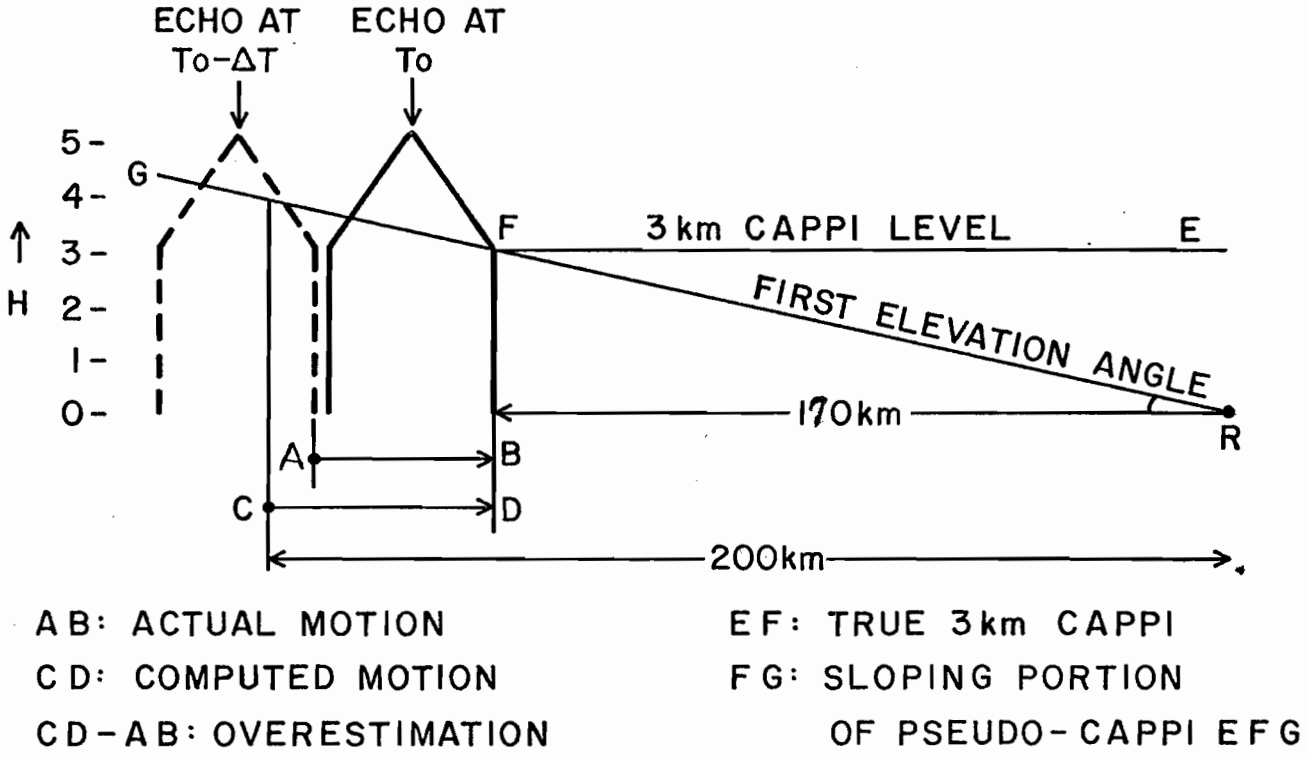

Fig. 4.9b. Possible explanation for the observed tendency to overestimate the speed of precipitation patterns.

With an elevation of 0.6° as the first rotation, our digital maps cease to be a true 3 km CAPPI beyond a range of 170 km. Thus, assuming a decrease in precipitation area with altitude, the height dependence of the data between 170 km, and 205 km, denoting the limit of the area of cross-correlation, forces a comparison between precipitation elements at two different levels, resulting in an overestimation of the speed which becomes apparent when extrapolated to longer forecast periods. Similarly, the storm appears to accelerate as it recedes from radar range at the opposite boundary, but this effect does not enter into the verifiable statistics. While this assumption needs to be confirmed by a detailed investigation of pertinent cases, it corroborates with personal experience during the two-year real-time test.

4.3 Forecast Verification of Rainfall Intensities

Though the degree of linearity of the motion of weather patterns is a first indication of the successfulness of the forecasts, it does not provide a direct comparison between the predicted rainfall intensity at a station from the 3 km CAPPI and that actually experienced at the ground. This analysis has been carried out for part of the 1976 data by personnel of the Quebec Weather Office, Marois (1977). The forecast time of arrival and intensity of rainfall as provided by the SHARP output of Figs. 3.3a and 3.3b were compared with the actual meteorological observations. The report, based on data from a limited number of stations (6), concluded that the forecast products delivered by SHARP constituted a useful input to a forecast office. The details of this analysis, however, will not dealt with here.

Since the quantity of ground measurement is very small and can produce only a partial verification, each grid area of the (64 x 100) matrix can be considered as a verifying location using radar data. Thus, with the help of

the computer, the number of verifying events can be increased to a more statistically significant number. One drawback must be accepted; namely that comparisons between forecast and actual precipitation can be accomplished only between two 3 km CAPPI maps. Existing discrepancies between the precipitation intensity at radar beam height and the ground are thus ignored; likewise, any inexactness resulting from the estimation of rainfall rate from the relationship $Z = 200\ R^{1.6}$ is neglected. These are summarized in Wilson and Brandes (1979).

Before undertaking any verification procedure solely from radar data, it is mandatory to determine the range dependence of the data and the regions where ground echo, or the shadow of nearby obstacles render the data unreliable. This can be achieved by summing the intensity levels at each grid point of available 3 km CAPPI data. Hourly maps of 1976 summer data with at least 2% coverage and devoid of anomalous propagation were used for this purpose. In order to derive a meaningful pattern of radar echoes distribution, locations of high reflectivity ground echo are blotted out, and the remaining portion of the map is scaled into 15 divisions, Fig. 4.10. The "M" contour outlines ground echo, especially prominent along the Green Mountains in the SE. The immediate vicinity is often also contaminated by ground returns, but of a less persistent or intense nature. Other zones include the Adirondacks to the south, Mount Royal to the east, and one grid area to the north due to a peak of the Laurentian hills. Four examples of shadow effects can be noticed; the most conspicuous is a twin shadow cast in the northwest beyond 150 km by two hills on adjacent sides of the Lake of Two Mountains, at about 15 km from the radar. In the south, the Adirondacks also create a broad shadow starting at about 200 km with a narrower extension toward nearer ranges. The presence of a tall building, a few feet higher

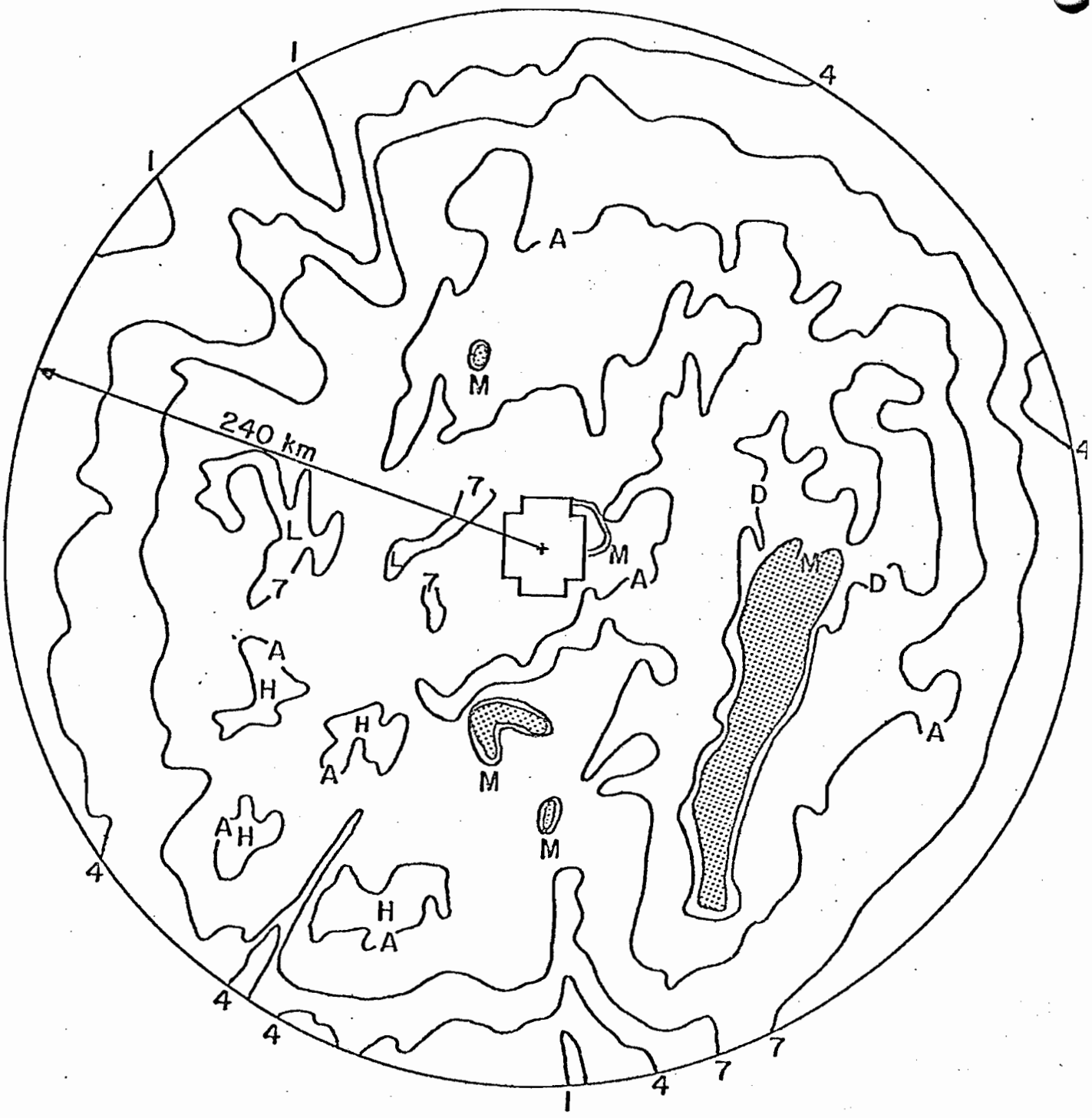

Fig. 4.10. Average dBz pattern arbitrarily scaled into 15 divisions, 1 to F, derived from 725 hourly 3 km CAPPI maps from summer 1976.

than the radar tower but less than 2 km away at azimuth 215°, projects a needle-like shadow in that direction starting at about 150 km. Finally, Mount Royal, 20 km distant, generates a smaller shadow at far ranges in the ENE.

In directions free from shadow effects, instrumental range dependence is not noticeable until distances beyond 200 km. It coincides with the limit within which a range correction is applied on the data by radar hardware. It also represents the distance at which beam filling effects become significant. Toward the west, the direction from which weather echoes enter the radar coverage, range effects begin at about 170 km due to the presence of a "human" element in any radar installation whereby weather patterns are already surprisingly well within range by the time the radar hardware and the recording computer are both in operation.

The parameter being summed here is logarithmic intensity levels (dBZ), but a similar procedure for rainfall yielded essentially the same pattern. There exists a prominent echo region around the southeast mountains extending up to the northeast, another relative maximum in the north, and a few intense patches in the southwest. A definite minimum occurs just west of the radar.

Using the output of Fig. 4.10, areas affected by ground echo, mountain shadows and far ranges are subjectively excluded to yield a mask, (see Figs of sect. 4.4), delineating the domain of unblemished data quality around the radar. This problem-free area totals 3097 grid points. Hence, all verifications and data analysis presented here include data totally outside the masked region.

The parameter commonly used for verification purposes is the Critical Success Index. The CSI was used as an objective evaluation of the techniques

		OBSERVED	
		VALUE LESS THAN THRESHOLD	VALUE EQUAL TO OR GREATER THAN THRESHOLD
FORECAST	VALUE LESS THAN THRESHOLD	W	Y
	VALUE EQUAL TO OR GREATER THAN THRESHOLD	Z	X

Table 4.2. Illustration of parameters used in the definition of CSI.X, hits: Y, misses; Z, false alarms (adapted from Donaldson et al (1975)).

for predicting severe weather events in Donaldson et al (1975). In the present work, it is applied to the direct comparison, with respect to a chosen threshold level T_L, of the forecast, I_{FOR}, and observed, I_{OBS}, precipitation intensities at each grid location of 36 km^2 in area of two 3 km CAPPI maps. A "hit", (X in Table 4.2), is scored when $I_{OBS} \geq T_L$ and $I_{FOR} \geq T_L$. A "miss" Y is obtained when the actual intensity is equal to or greater than the threshold following the prediction of a value below the threshold, that is, $I_{OBS} \geq T_L$ and $I_{FOR} < T_L$. Conversely, a "false alarm" (Z) consists of a forecast above or equal to the threshold which does not materialize at observation time, that is, $I_{FOR} \geq T_L$ and $I_{OBS} < T_L$. Finally, values which are forecast and verified to be below the threshold (W), are not included in the computations. Thus, CSI is defined as

$$CSI = 100 \frac{(\ X\ )}{X+Y+Z}$$

Two additional scores can also be defined in assessing the usefulness of a forecast product; they are the Probability of Detection and the False Alarm Ratio, expressed as

$POD = 100\ (\frac{X}{X+Y})$ for $I_{OBS} \geq T_L$, it expresses the percentage of all the forecast levels which are greater than or equal to T_L.

$FAR = 100\ (\frac{X}{X+Z})$ for $I_{FOR} \geq T_L$, it expresses the percentage of all the observed levels which are greater than or equal to T_L.

These introduce a practical aspect to a forecasting technique. For example, if it is essential to predict as many events as possible above a prescribed threshold, regardless of the number of false alarms, a technique yielding a high value for POD, which is independent of Z, is required. Conversely, if false alarms provoke undue concern, and misses are tolerated, a forecast technique ought to be verified in terms of FAR. It is seen that the CSI combines elements from both considerations.

A computer program has been implemented comparing the forecast and actual rainfall intensity at each of the 3097 grid areas of every map. We shall first concern ourselves with the verification of one hour forecasts of the 1976 test. The result of each comparison pair is totalled in a contingency table from which the above parameters can be easily calculated. However, not all the 552 forecasts produced should be verified. The onset of anomalous propagation cannot be considered as observational data. Restrictions have also been applied requiring at least 2% coverage at both forecast and verifying times. With these limitations, 424 forecasts were verified. The resulting truth table, showing the number of occurrences for each possible pair of intensities, is presented in Table 4.3. The parameters X,Y,Z and W are delineated for threshold 5.

OBSERVED

FORECAST	.	1	2	3	4	5	6	7	8	9	A	B	C	D
.	19401	29223	10593	12329	3306	2309	1246	794	554	181	70	87	10	2
1	29331	9719	4768	5766	1363	836	578	196	108	27	11	6	1	0
2	10957	5085	3153	4235	1108	634	275	192	98	18	5	8	1	2
3	11818	6473	4688	8033	2464	1749	702	379	200	49	9	5	1	1
4	2737	1582	1871	2755	1037	845	369	227	131	27	6	4	0	0
5	1802	991	913	1985	788	761	357	261	127	29	9	1	3	0
6	830	458	341	965	454	406	219	174	98	19	6	1	1	0
7	488	247	239	589	274	289	151	132	86	14	4	2	0	0
8	238	139	101	358	177	158	83	109	56	18	11	3	1	0
9	105	47	31	89	47	43	37	35	21	5	5	2	0	0
A	22	17	4	30	12	15	10	11	6	4	0	1	0	0
B	17	5	7	14	10	8	4	6	6	3	0	1	0	0
C	4	2	3	2	0	1	1	0	1	1	0	0	0	0
D	2	1	0	1	1	1	0	0	0	0	0	0	1	0
E	1	0	0	0	0	0	0	0	0	1	0	0	0	0
F	0	0	0	0	0	0	0	0	0	0	0	0	0	0

W = 4688, X = 6, Y = 108, Z = 4

Table 4.3. Truth table from 424 verifiable forecasts in 1976 showing the number of occurrences of each intensity level matching.

The special case of a zero matching with a zero is included only if the zero at verifying times has at least 2 of its sides bounded by grid areas with precipitation. However, this number does not enter into any computations. Perfect forecast would be achieved if all pairs lay along the diagonal. One should not be surprised or disturbed at the significant scatter about this diagonal.

A technique has been developed which takes into account possible spatial errors of the order of 1 to 2 grid lengths. The four adjacent grids are scanned by the CSI program and the rainfall intensity which best approximates the forecast intensity is identified as the matched value. This concept has been expanded to incorporate larger verifying areas consisting of (3x3), (3x5) and (5x5) matrices centred on the original grid area, Fig. 4.11.

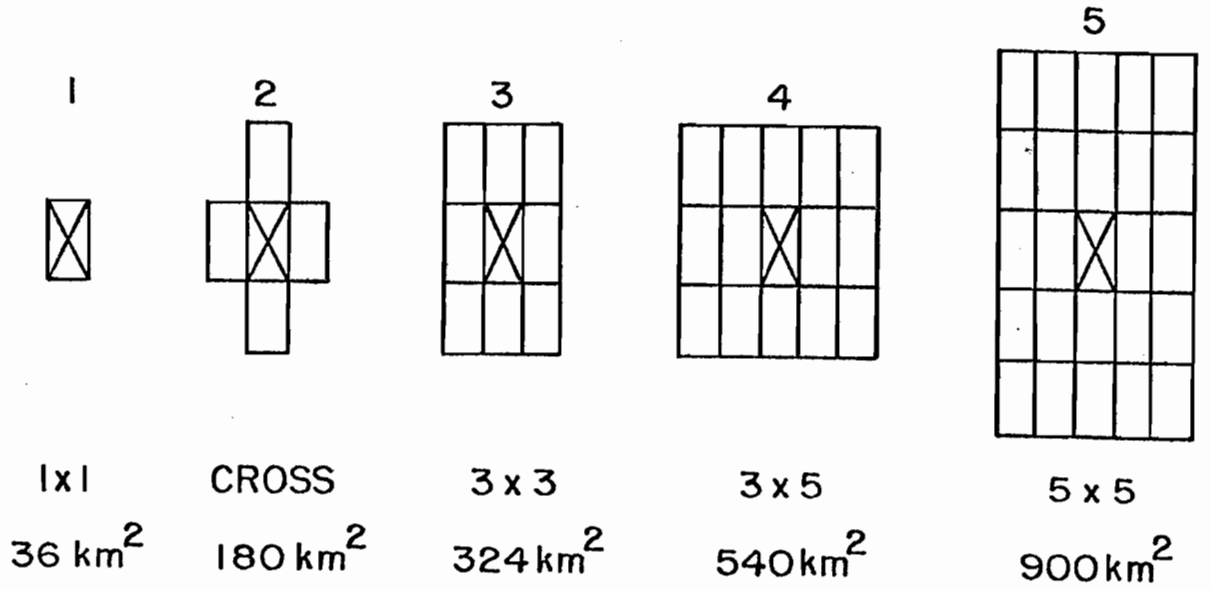

Fig. 4.11. Size and shape of the five verifying areas.

The number of chances of exact matching with the forecast value is increased from 1 to 5, 9, 15 and 25. Hence, the much-improved numerical values are to be expected. Tables similar to those of Table 4.3 but for the larger verifying areas reveal a marked shift toward the diagonal and away from

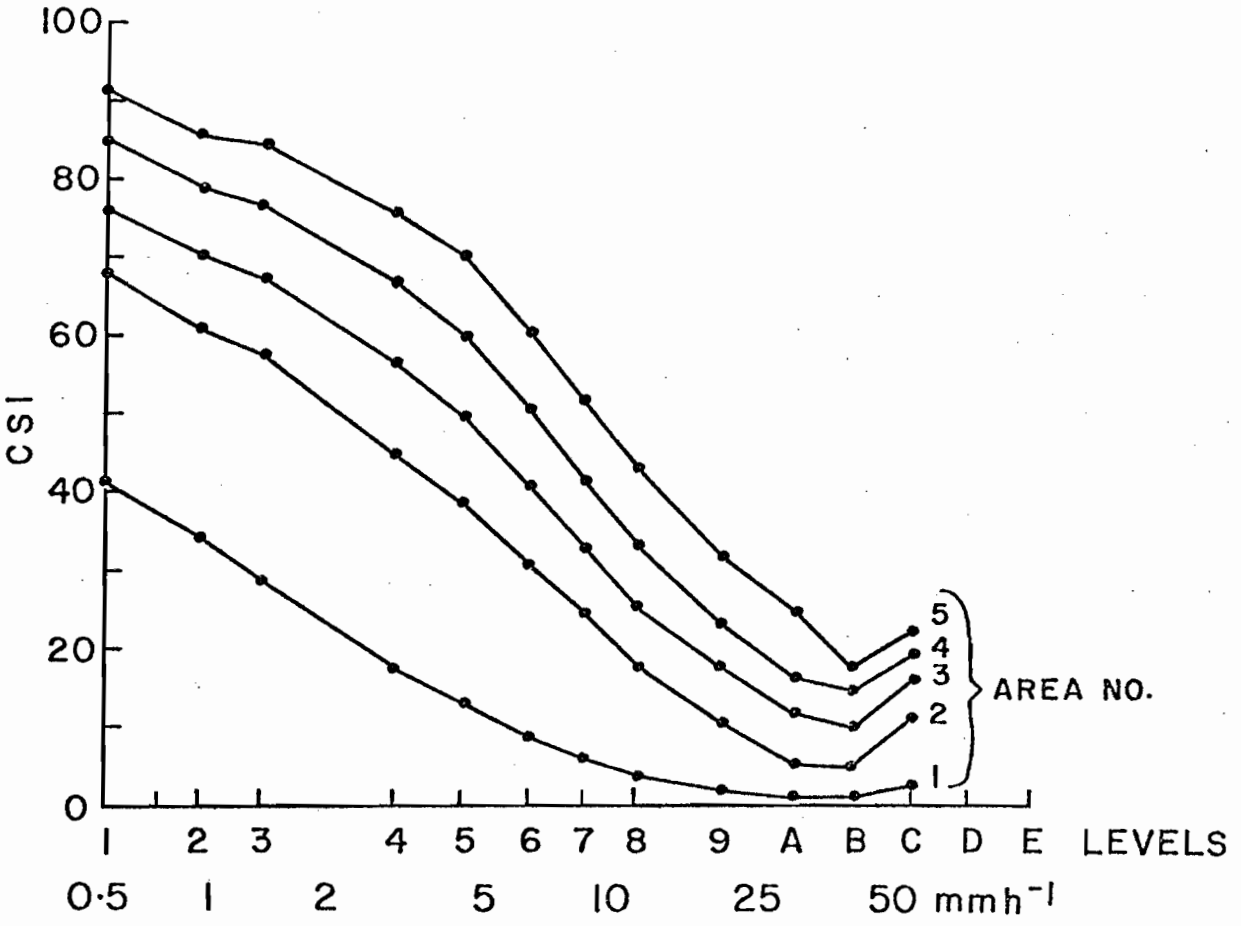

Fig. 4.12. CSI (Critical Success Index) as a function of rainfall rate with the verifying areas as a parameter. (1976 data)

poor matchings. This indicates that whereas the verifying basic grid unit may not contain a value of the same intensity as was forecast, the probability of finding one in the immediate neighborhood is greatly enhanced. In this context, a "near miss" or "false alarm" is scored as a hit.

The dependence of CSI on the rainfall and size of the verifying area is illustrated in Fig. 4.12.[1] It demonstrates that the CSI scores decrease linearly with the logarithm of the rainfall rate. The general levelling of the scores for area #1 beyond 10 mm h^{-1} probably reflects that the typical size is down to one grid area. Even under the unlikely assumption of persistence for 1 h, the chances of achieving a "bull's eye" forecast are small with an rms error of about 30% of the mean displacement. In fact, the rms error for the motion of intense echoes is likely larger, since they usually have motions different than that of the overall pattern. It is thus realized that a more practical degree of success can be achieved if flexibility is permitted in terms of acceptable motion deviations. This is demonstrated by the higher scores for larger verifying areas. When the CSI scores for each intensity level are plotted against the logarithm of the verifying area as the independent parameter, there results a good linear relationship.

The low CSI scores at high rainfall rates are influenced by their relative probability of occurrence as well as their small scale. Thus, if a high rainfall rate occurs at a low probability, the chances of accurately forecasting it are dictated to a greater extent by its lifetime or probability of reoccurrence, than by the degree of accuracy of its forecast motion.

---

[1] Differences between 76 and 77 scores are so small as to be totally accountable to calibration fluctuations between the two summers.

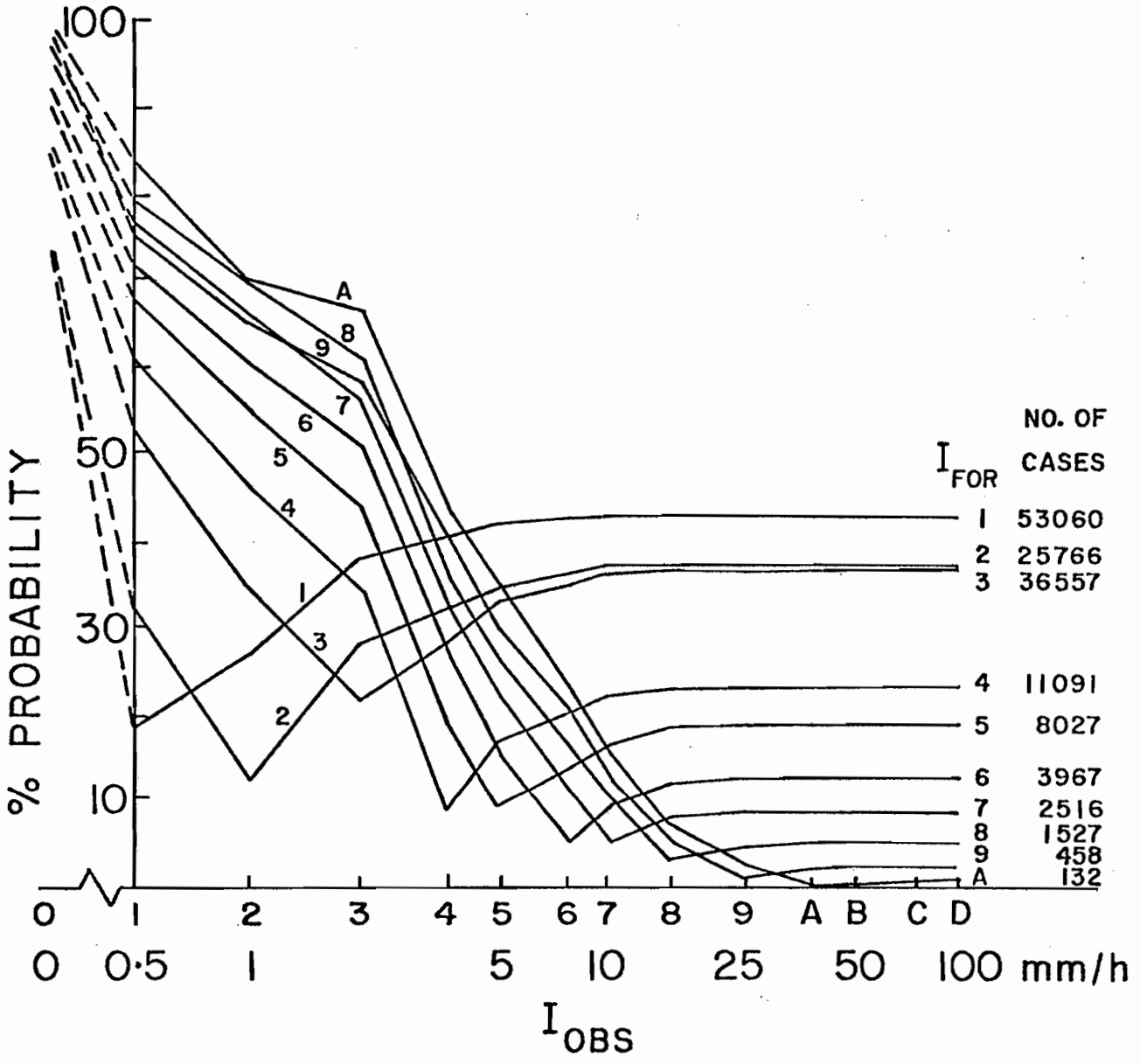

Fig. 4.13. Probability of the observed intensity level I_{OBS} as a function of the forecast level I_{FOR} for any intensity spread ΔI about I_{FOR}. The total number of forecasts for each intensity level I_{FOR} is also given (1976 data).

The CSI has the property that an error of any magnitude which underestimates the rainfall rate is given a positive contribution while any overestimation decreases the score. For any rainfall event, it is more likely that the rate will decrease (overestimation) in view of the relative frequency of occurrence of the various rainfall rates, refer to Fig. 4.1c. Thus, in order to counteract this particular bias in the definition of CSI, an additional type of flexibility could be introduced whereby forecasts which over- or underestimate the rainfall level are equally weighted. The result of this attempt is illustrated in Fig. 4.13 which essentially portrays a more vivid visual representation of Table 4.3. Denoting the forecast and observed intensity level by I_{FOR} and I_{OBS}, and the difference between them by ΔI, the following probabilities can be deduced from each curve:

(a) $P_1(I_{FOR})$ as the probability that $I_{OBS} = I_{FOR}$; $\Delta I = 0$.

(b) $P_2(I_{FOR}, \Delta I)$ as the cumulative probability, including P_1, that $I_{OBS} \leq I_{FOR} - \Delta I$; $\Delta I = 0,1,2,3$ etc.

(c) $P_3(I_{FOR}, \Delta I)$ as the cumulative probability, including P_1, that $I_{OBS} \geq I_{FOR} + \Delta I$; $\Delta I = 0,1,2,3$ etc.

For example, 9% of the 11091 forecasts of intensity level 4 were verified exactly as predicted. About 46% verified with levels 2 to 4, while 20% were matched with the higher levels 4 to 6, that is, $P_1(4) = 0.09$, $P_2(4,2) = 0.46$ and $P_3(4,2) = 0.20$. From these, we can derive $P(I_{FOR},\Delta I)$ as the probability that I_{OBS} be within ΔI levels from I_{FOR}. Since P_1 is included in both P_2 and P_3, $P(I_{FOR},\Delta I) = P_2 + P_3 - P_1$. In our particular example, $P(4,2) = 0.57$. The marked tendency for all levels to verify with the lower ones is well exemplified in Fig. 4.13 since $P_2 > P_3$ for all curves. Note that since the intensity levels were approximately logarithmically spaced, the range of ΔI in mm/h is different either side of the verifying

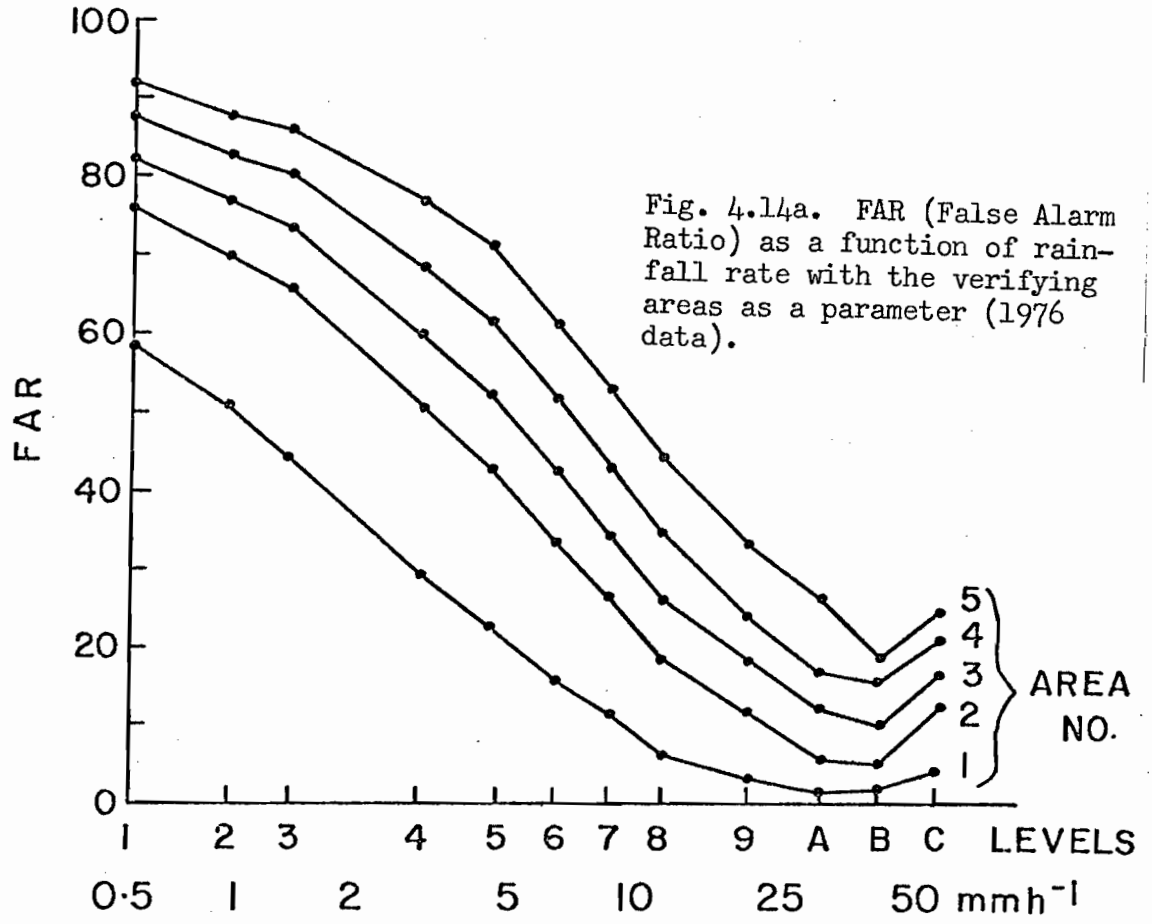

Fig. 4.14a. FAR (False Alarm Ratio) as a function of rainfall rate with the verifying areas as a parameter (1976 data).

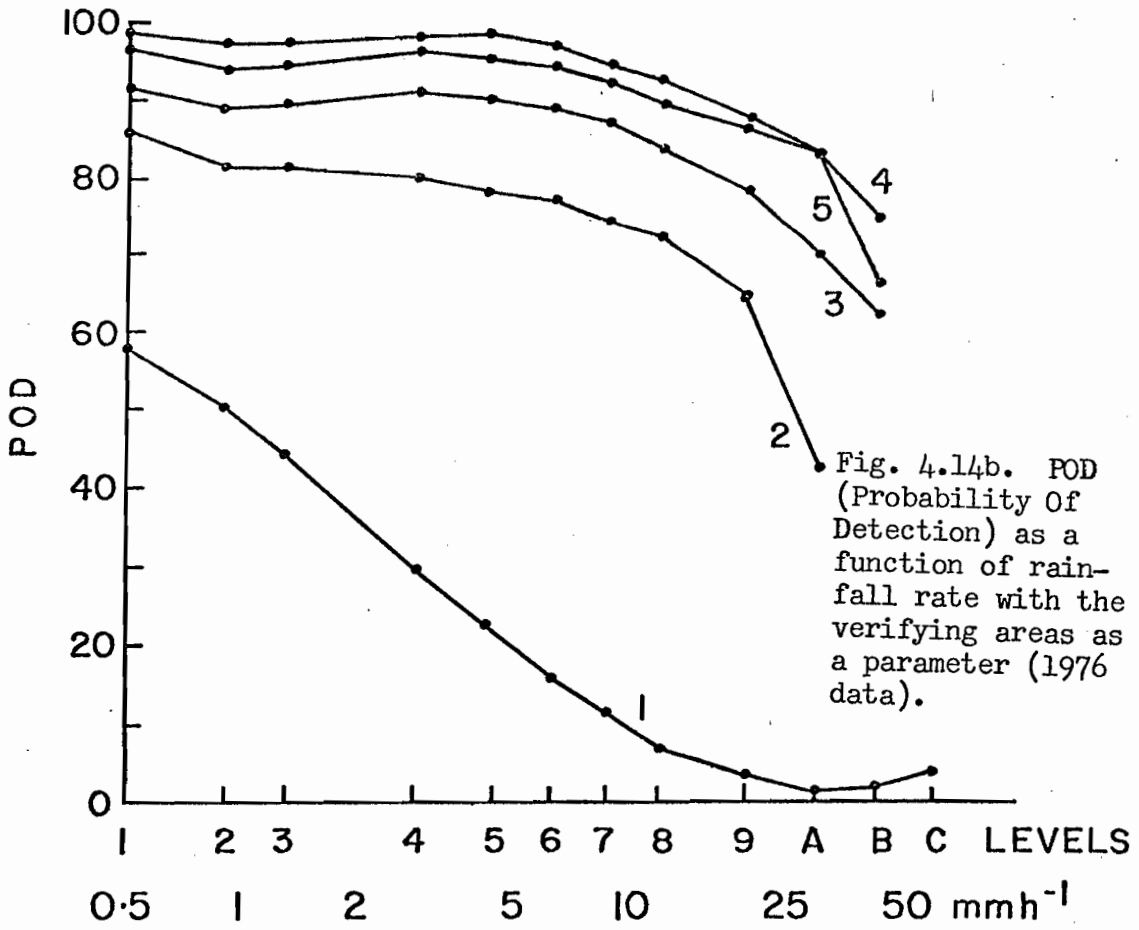

Fig. 4.14b. POD (Probability Of Detection) as a function of rainfall rate with the verifying areas as a parameter (1976 data).

level, affecting the form of the curves. Also, due to a programming oversight, level 3 is wider than required by the logarithmic law. As a result, $P_1(3)$ is larger than the neighbouring values. One fact brought into sharp focus by both Figs. 4.12 and 4.13 does remain: the fundamental limitation of the status quo assumption, particularly at the upper end of the rainfall scale where the short lifetime of cells reduces the precision of the forecasts.

The behaviour of the FAR curves, Fig. 4.14a, exhibits a similar trend to those of the CSI of Fig. 4.12, but with larger scores on account of their mathematical formulation. A different behaviour is observed in the POD curves, Fig. 4.14b, particularly for verifying grid sizes other than the #1 area. This behaviour is due to the fact that as the verifying area is expanded, the number of misses (Y) is drastically smaller than the number of false alarms (Z). Once again, the explanation lies in the distribution of the relative probabilities of the various intensity levels; if a comparison is made between a predetermined level and a number of random levels, there is a greater probability that the nearest be of a lesser than of a greater value. On account of this severe bias, the POD curves for the verifying areas other than #1 do not express the intended meaning of probability of detection.

The decrease in accuracy verified over area #2 as the forecasts are extended beyond one hour is examined in Fig. 4.15. Here, the CSI scores for the various rainfall intensities form a family of curves plotted versus the logarithm of the forecast length. Note that the number of cases diminishes from 400 to 200 as the forecast verification period is increased from 1 to 5 hours. In addition, the geographical area over which the forecasts are verified is also reduced, and is generally shifted toward the

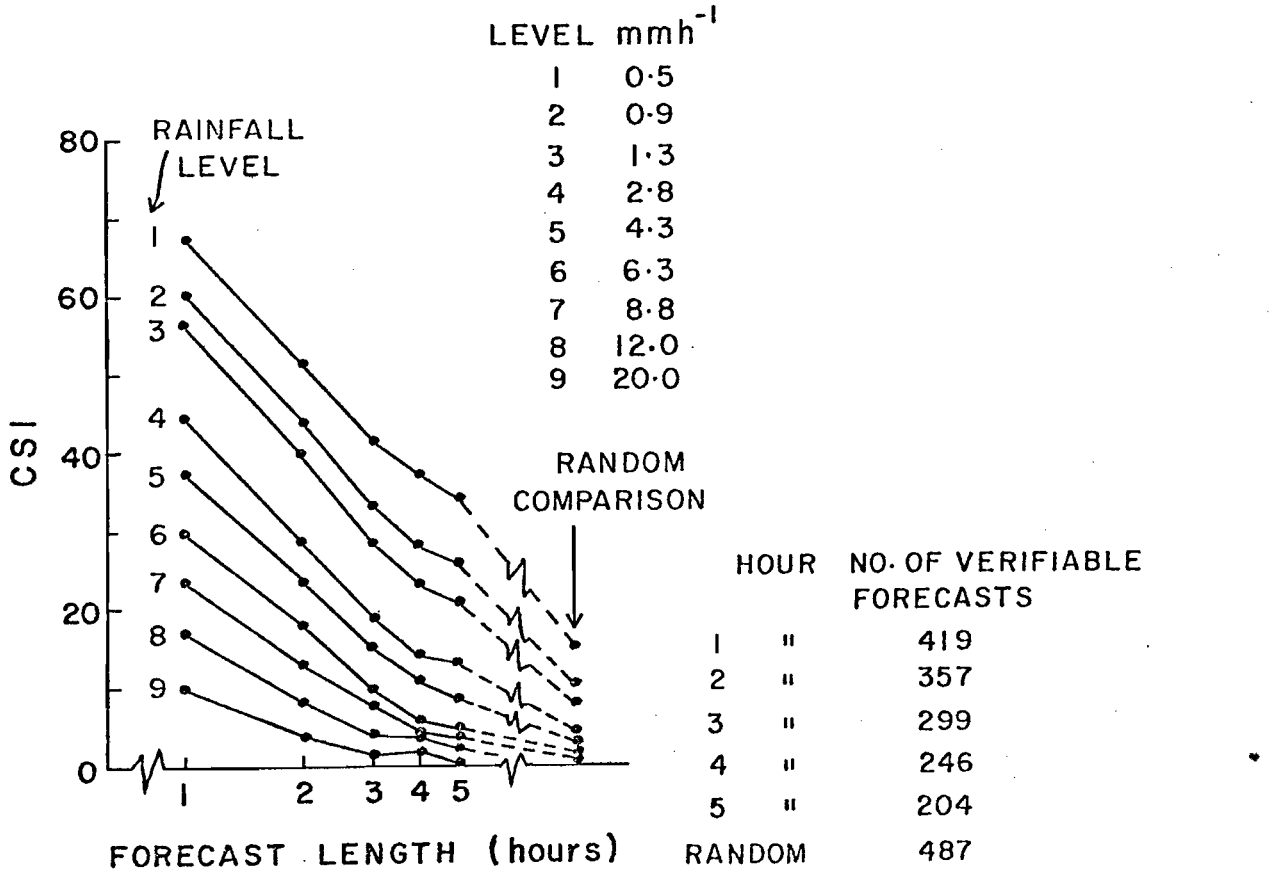

Fig. 4.15. CSI scores of various rainfall rate levels as a function of the logarithm of the forecast length in hours verified over area #2 (1976 data).

east, since both the predicted and observed rainfall intensities must be within radar range. Fig. 4.15 reveals that the CSI scores decrease approximately exponentially with the length of the forecast for periods of up to 3 hours. This rate of decrease is faster for the lower rainfall rates. For example, a loss of 25 points is observed for the lower levels between 1 and 3 hour forecasts while during the same period the loss is about 10 points at the upper end of the rainfall scale. Beyond the three hour period, a reduction in the rate of decrease is experienced by all levels, but particularly levels ≥ 4, where the slope of the curves is nearly flat between the 4 and 5 hour interval. This behaviour implies that, under the status quo assumption, the limit of the forecast skill of rates greater than 3 mm h^{-1}, as verified by area #2, does not exceed 3 or 4 hours. When the verifying area is increased, curves similar to Fig. 4.15 have shown that the skill is extended both in time and for greater rainfall rates, with the opposite effect for area #1.

It is interesting to derive the lowest limit of CSI scores which indicates the total absence of a forecast skill. This is obtained by comparing two maps separated by such a large time interval as to render them essentially independent or random. This result is simulated by partitioning the entire 76 data set of summer CAPPI maps with at least 2% coverage into 2 parts, copying both parts into another tape in reverse order, and performing a sequential comparison with the original data set. This procedure ensured that maps being compared differ in time by at least one month. The CSI scores for this type of comparison are presented at the right side of the plot in Fig. 4.15. The average echo coverage over Montreal is about 11% (see Fig. 4.1c). Thus, if radar echoes were randomly distributed over the entire range, there would be a 1.2% chance of an exact overlap of two

positive intensities, or 5 x 1.2 = 6% when compared over area #2. The CSI score for level 1 of nearly 15 should not be surprising since radar echoes are not randomly distributed but are clustered in patches and, as seen in Fig. 4.10, more likely to occur at nearer ranges or in preferred regions. Note however, that a value of γ = -0.001 was derived from the "hits" matrix of the random comparison, indicating a total absence of correlation between the maps. As was concluded above, the relatively small differences between the "random" scores and those of forecasts beyond 4 hours point to the limiting extent of the skill of the forecast procedure.

While CSI, FAR and POD scores provide an assessment of the expected quality of a forecast, the usefulness of these parameters does not necessarily lie in their absolute value, but rather as comparators between different forecast techniques, or as "barometers" for evaluating various alternatives within one general technique. In our case, accepting a cross-correlation procedure followed by a steady-state extrapolation applied to the entire radar map as the basic technique, a comparison in terms of CSI scores has been derived for the forecasts issued during the 1976 real-time test with simulated forecasts made with the following five predictors.

1) Optimum vector, that is, the predicted displacement is made equal to the actual motion during the verifying interval.

2) 700 mb wind; the predicted vector is equal to the latest available 700 mb wind speed and direction. This level has been chosen since it has been quoted in the literature as being more representative of precipitation pattern velocities, (Newton and Katz (1958) and Harper and Beimers (1958)). The data are from the Maniwaki station, 200 km northwest of the radar.

3) Constant motion; all patterns are extrapolated by the same amount of 45 km h^{-1} from 260 degrees azimuth, which corresponds to the average velocity for the 1976 data.

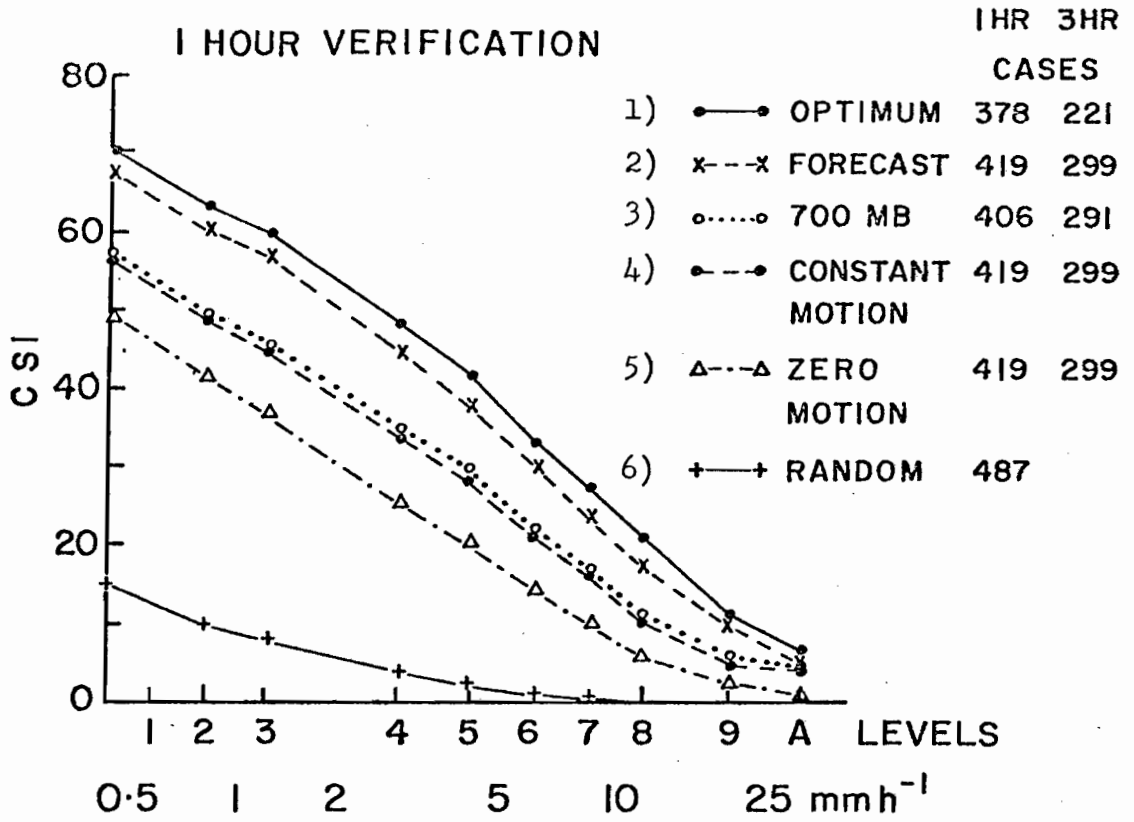

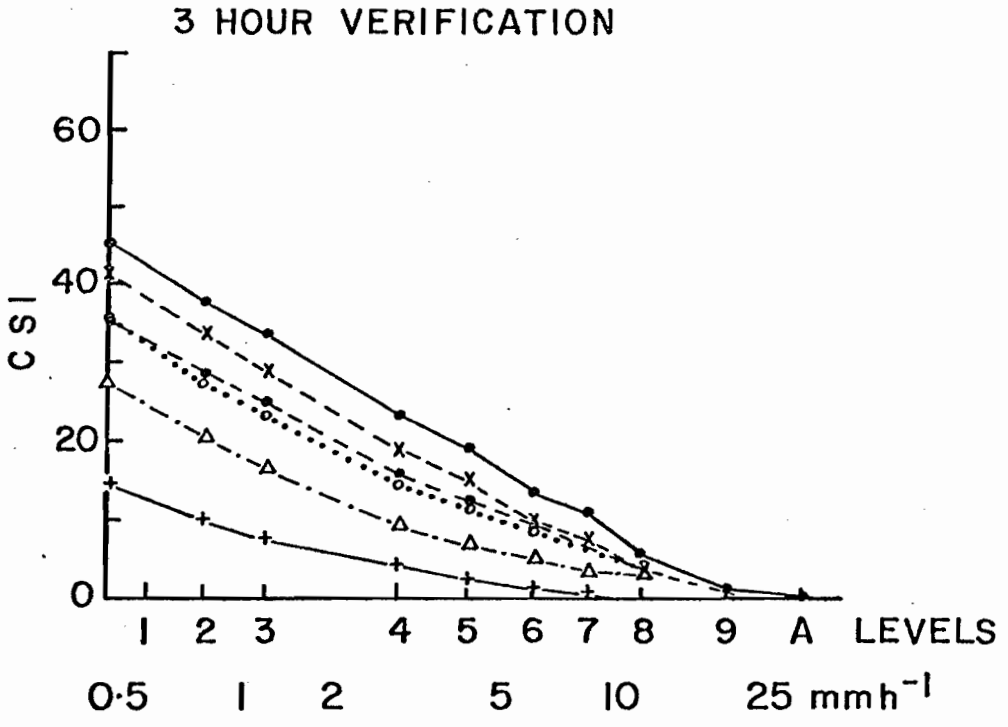

Fig. 4.16. CSI scores as a function of rainfall rate for various predictors verified over area #2 (1976 data).

4) Zero velocity; this choice is equivalent to the assumption of persistence in space and time applied to rainfall rates.

5) Random Correlation as defined earlier.

The results for area #2 are representative of the others and are shown in Fig. 4.16a and 4.16b. An immediate conclusion which can be drawn from the one hour forecasts is that the score would have been only marginally increased if the overall motion of the weather systems had been perfectly forecast. This implies that the major portion of forecastability loss is attributed to the rearrangement and restructuring of weather patterns as they undergo development or decay during the forecast length, a direct consequence of the "status quo" assumption. The difference between curves 5 and 1 represents the accuracy gained through knowledge of the pattern motion. For a given forecast situation, this gap is reduced by a slow pattern motion and by a large scale length. The simulated experiment also shows that this gap varies between 20 and 10 CSI units from the lower to the upper rainfall rate scale. A reasonable guess as exemplified by curves 3 and 4 account for nearly 40% of this difference. An additional 40% is acquired by the "now-casting" technique adopted in the real-time experiment. It is understood that the absolute differences between the various predictors are heavily dependent on the length of the verifying period, as the curves would nearly coincide for very short forecasting periods. In the limit of very long intervals, they will approach the random curve. Their behaviour for an intermediate forecast duration is typified in Fig. 4.16b. It is seen that the curves representing 700 mb and the constant motion are still coincident but are closer to the experimental curve. This observation implies that the predictor derived from the 1 h motion prior to the forecast imparts undesirable short term deviations to a 3h displacement. The latter is thus increasingly better estimated by the climatological or "smoothing" predictors of curves 4 and 3.

As expected, a wider gap exists between the optimum and experimental curve. However, the difference between the former and the zero motion curve is not as large as anticipated. This is surprising since, in view of the suppression of motion before comparison, major discrepancies were expected between curves 1 and 5 at longer forecasting periods. The explanation lies partly in the large scale length of many echo patterns encountered during the 1976 season. In addition, in cases of smaller storm areas, for which the knowledge of motion is crucial in obtaining a good comparison, the drastic transformation of their intensity structure after 3 h diminishes the optimum scores, thus reducing the impact of motion information.

An important conclusion to be drawn from Fig. 4.16b is that the accuracy of the high intensities is independent of the predicted displacement as revealed by the closeness of curves beyond 10 mm h^{-1} or at higher rates for 1 h forecasts. Again, it signals the limit of any forecasting skill for these rates. It is evident that since the evolution and erratic motion of convective elements exhibit a period shorter than 1 h, the chances of accurate forecasts beyond this period are severely reduced.

4.4 Geographical distribution of storm growth and decay

The SHARP test provided an ideal data base for the determination of the geographical distribution of development and dissipation of summer storm systems.

A preliminary study on this topic reported in Bellon and Austin (1978) concentrated on cases of "excessive" development or dissipation. These terms were defined as a difference between the forecast and actual rainfall of at least 4 intensity levels. This criterion can be expressed as follows:

$DIF = A(I,J,T + \Delta T) - F(I,J,T + \Delta T)$ where

$A(I,J,T + \Delta T)$ is the actual intensity at grid point (I,J) at time of verification $(T + \Delta T)$ and $\Delta T = 60$ minutes.

$F(I,J,T + \Delta T)$ is the forecast intensity distribution obtained as $F(I,J,T + \Delta T) = A(I - IF, J - JF, T)$ where (IF,JF) is the forecast displacement computed by cross-correlating the map $A(T)$ with $A(T - \Delta T)$. Then $DIF \geq 4$ denotes a drastic development and $DIF \leq -4$ denotes a drastic dissipation. The analysis consisted in obtaining the geographical distribution of the number of developments and dissipations. The outcome revealed a fairly large point to point variability with the number of occurrences of development or dissipation ranging from 2 or 3 to about a dozen. Nonetheless, clusters of higher and lower values could be distinguished. For a preliminary assessment of the results, the number of "decays" was subtracted from the number of "developments" and an equally weighted nine-point smoother was applied to the difference field. The results bear a significant correlation with terrain features. In particular, enhancements over upslope areas and decreases over lakes are noted which are consistent with simplistic explanations. However, before these results may be used to improve the operational procedure, the data set must be expanded in order to counteract the influence of a specific year with particular climatological characteristics. Moreover, the reported analysis suffers from the fact that it is limited to only extreme differences in rainfall levels and hence is biased toward certain storm categories and unrepresentative of an entire summer season. Note that by focussing our attention on cases for which $|DIF| \geq 4$ is equivalent to limiting the analysis to convective situations with relatively higher intensity levels which are less likely to occur. As can be estimated from Table 4.3, the number of pairs included represents only about 15% of the total. This drawback was initially circumvented by modifying the program to include all comparisons for which $|DIF| \neq 0$. However, it is more appropriate to express differences in predicted and observed values in terms of rainfall rather than intensity levels. Thus, the analysis described earlier has been duplicated

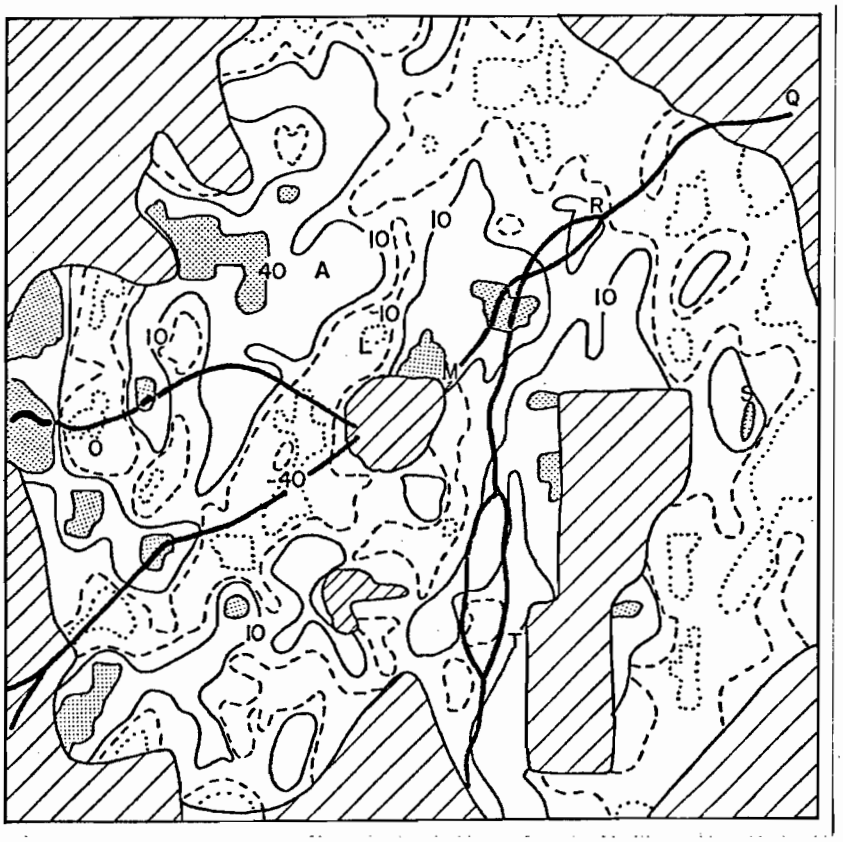

Fig. 4.17a. Geographical distribution of the rainfall flux difference for the summer of 1976. For geographical locations, refer to Figs. 4.17c and 2.3.

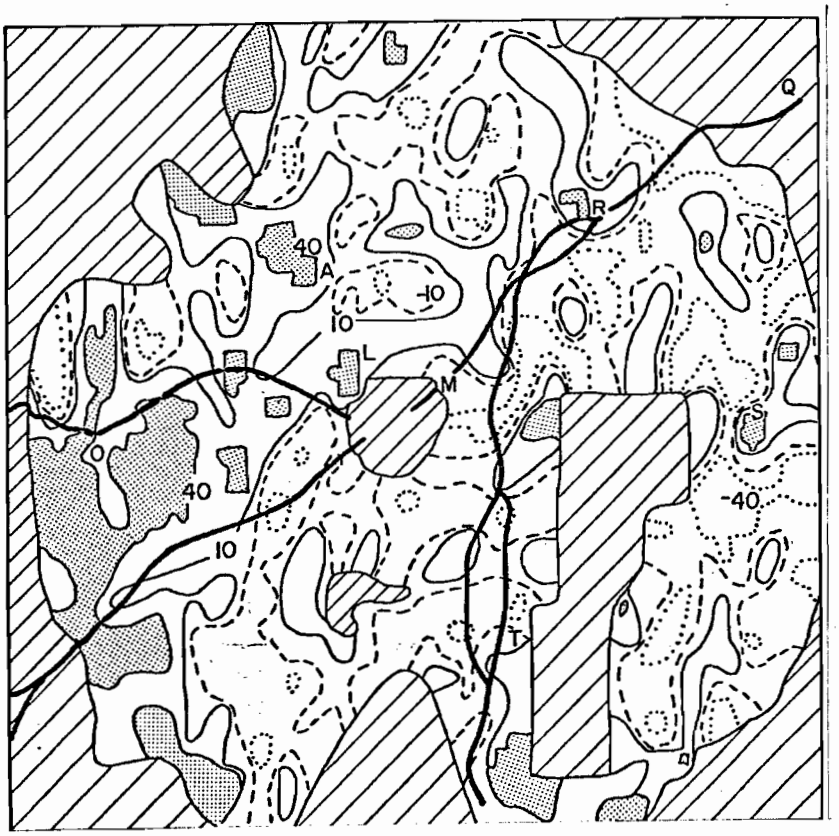

..... - 40%

------ - 10%

_____ + 10%

shaded + 40%

Fig. 4.17b. As in Fig. 4.17a for summer 1977.

with rainfall flux difference as the comparative parameter; that is for each grid area (I,J), the following parameter was computed:

$$100 \frac{\Sigma \text{ actual rainfall} - \Sigma \text{ forecast rainfall}}{\Sigma \text{ actual rainfall}}$$

The denominator is also required to total at least 20 mm of rainfall. The results are further refined by using the actual displacement (IA,JA) between A(T) and A(T + ΔT) rather than the forecast displacement (IF,JF) obtained from A(T - ΔT) and A(T). This choice eliminates differences caused by a deviation in storm trajectory and includes only storm development. The results for 1976 and 1977 are shown in Figs. 4.17a and 4.17b respectively. A geographical overlay is outlined in order to bring into greater perspective potential orographic influences. First of all, it should be noted that the negative values at far ranges near the eastern boundary, as well as some positive numbers neighbouring the western boundary are the expected outcome of an instrumental range dependence of the data. Since the 1976 analysis is based on 405 verifications while the 1977 analysis is the outcome of only 322, the latter appears to be more "noisy". Features which persist from year to year are few. Regions of positive areas remain near Ste-Agathe, west of the Adirondacks and Green Mountains. This result would confirm the existence of an upslope effect on the west side of hilly areas in a predominantly westerly circulation. The other development-prone regions northeast of the Montreal area in 1976 and around Three-Rivers and Sherbrooke in both years cannot be related to obvious topographical causes. The more pronounced regions of negative influence include an area east of the radar in 1977, and in 1976, various centres around Ottawa, a narrow corridor running parallel to the east side of the Laurentians and a wider band southwest of the radar. Note that the region of dissipation near Ottawa has been replaced by a positive tendency

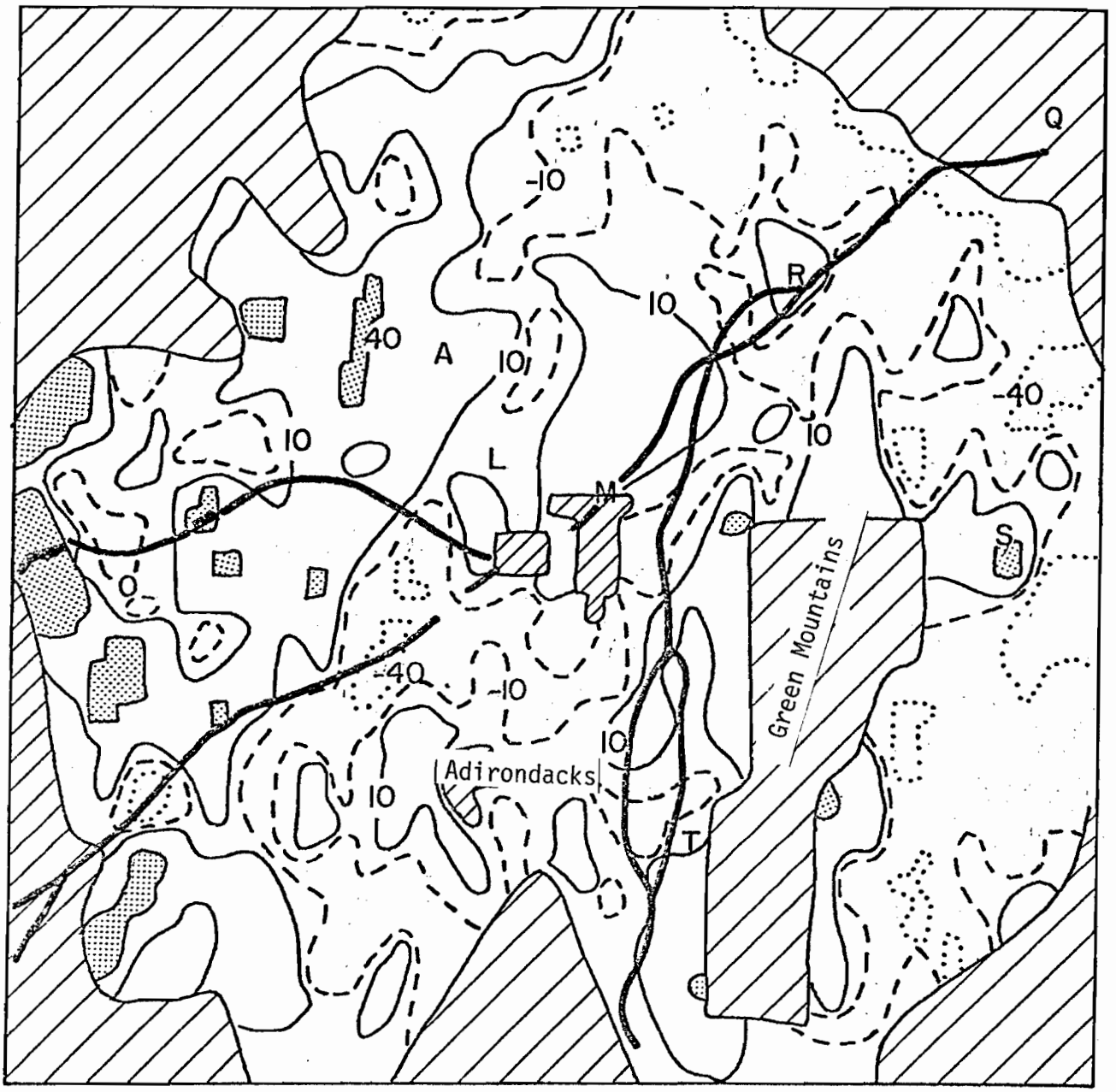

Fig. 4.17c. As in Fig. 4.17a for summers 1976 and 1977 combined

O: OTTAWA
A: STE. AGATHE
M: MONTREAL
R: THREE-RIVERS
Q: QUEBEC
T: BURLINGTON
S: SHERBROOKE
L: MIRABEL

in 1977. In view of the absence of any orography in that region, this opposite trend is clearly a random effect of two independent data sets. The accumulation of yearly results of this type will eventually smooth out non-orographic effects until only terrain-linked features are observable. This is shown in Fig. 4.17c which is the combined result of both years. Being based on 727 comparisons, this figure displays a smoother appearance due to the cancelling of opposite trends; hence the area enclosed by ± 40% contours is significantly reduced. The size and magnitudes of features which persist during both years have also been sharply reduced.

An attempt has been made to stratify the results of Fig. 4.17c in terms of direction of motion of the precipitation patterns. The 727 comparisons have been sub-divided as follows

CATEGORY	DIRECTION OF MOTION	NO. OF CASES
SW	180° - 239°	211
W	240° - 284°	401
NW	285° - 360°	115

The differences between these categories, however, were not readily explained by the various directions of motion since orographic effects shown in 4.17c have been noted to be relatively minor. Differences could as easily have been ascribed to different sampling of the 727 cases. Thus, the W situation comprising the largest number of cases exhibited a greater resemblance to the combined result of Fig. 4.17c. Conversely, the NW case displayed an intricate pattern with a high degree of fluctuations caused by too few cases. Influences which could be explained solely from wind directions like upslope and downslope effects were few; a slightly positive trend on the southwest side of the Adirondacks and a negative on the north side was observable on

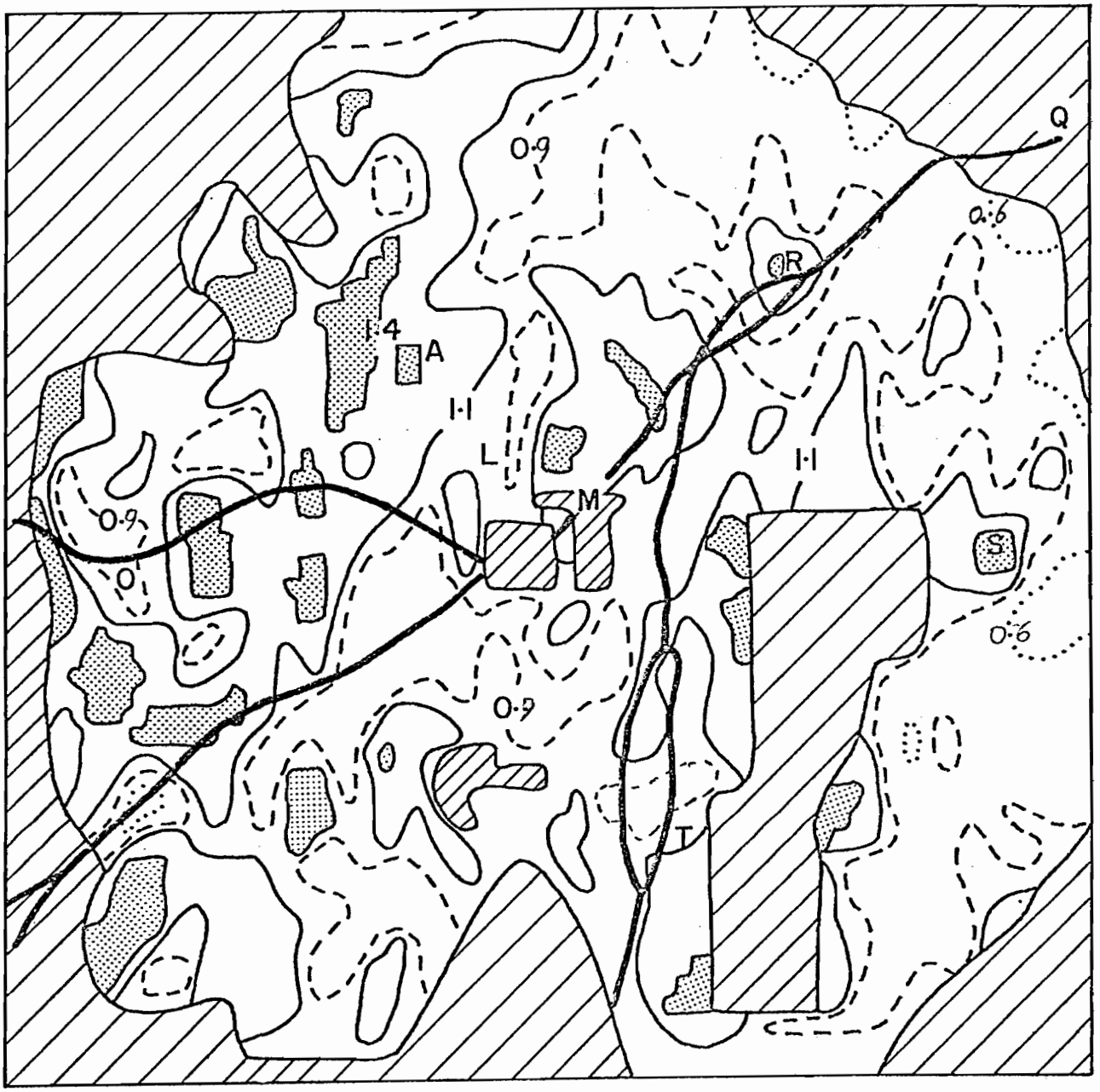

Fig. 4.18. Geographical distribution of the A/F ratio derived from the 1976 and 1977 data sets combined.

	A/F
.....	0.6
- - -	0.9
———	1.1
shaded	1.4

the SW situation while the reverse tendency was more prominent for the NW situation. Others were of an unexplained nature; for example, Ottawa was surrounded by a negative influence for both the SW and NW situations, but was slightly positive during westerly motion. The Sherbrooke area yielded a positive-negative-positive behaviour while northeast of Montreal, the trend was negative, moderately positive and highly positive for the SW, W and NW situations respectively. It was concluded that little knowledge was gained by this form of stratification and that the addition of more cases in each category will further alter the distributions presented in these figures. This is because the year to year variation is more dominant than the one dependent on direction of storm motion.

In spite of the relatively weak trend shown in Fig. 4.17c it was incorporated into a forecasting scheme to determine if any improvement can be detected when forecasts are verified in terms of the CSI parameter. Essentially, the procedure consists in applying the statistics from the 1976 and 1977 combined data set to the 1979 data sample.

The parameter portrayed in Fig. 4.17c, namely

$$\text{net rainfall difference} = \frac{\text{actual rainfall - forecast rainfall}}{\text{actual rainfall}}$$

is not directly suitable. In order to predict the actual rainfall at $(T + \Delta T)$ from the present unmodified rainfall at (T), (which otherwise becomes the forecast rainfall), we need the simple ratio

$$A/F = \frac{\text{actual rainfall}}{\text{forecast rainfall}}$$

The geographical distribution of the A/F ratio derived from the 1976 and 1977 data sets combined is shown in Fig. 4.18. From the similarity of its definition with the net rainfall difference, the distribution bears a close resemblance to that of Fig. 4.17c.

Some of the 1979 summer data in the form of 3 km CAPPI's from July and August were used as a test base. A total of 372 one-hour comparisons were performed. At first, the forecast rainfall rate was left unchanged by setting A/F = 1 at all geographical locations (I,J). The resulting CSI scores, Table 4.4 are similar in magnitude and exponential behaviour as those computed from the 1976 data.

RATE MM H^{-1}	A/F = 1	A/F = f(I,J)	DIF
Trace	41.4	41.4	0.0
0.5	37.0	36.9	-.1
1.5	27.7	27.3	-.4
2.5	17.7	17.3	-.4
3.5	12.2	12.4	+.2
4.5	10.0	10.1	+.1
5.5	8.5	8.6	+.1
7.5	6.5	6.4	-.1
9.5	5.5	5.7	+.2
11.5	4.3	4.5	+.2
13.5	3.2	2.9	-.3
15.5	2.5	2.4	-.1
17.5	2.3	2.1	-.2
19.5	2.2	2.0	-.2
21.5	1.7	1.5	-.2

Table 4:4 CSI (Critical Success Index) for 1979 data using the 'status quo' assumption (A/F = 1.0) in comparison with the one obtained by allowing a modification of the predicted rainfall rate in accordance with the A/F distribution of Fig. 4.18 which is based on 1976 and 1977 data sets.

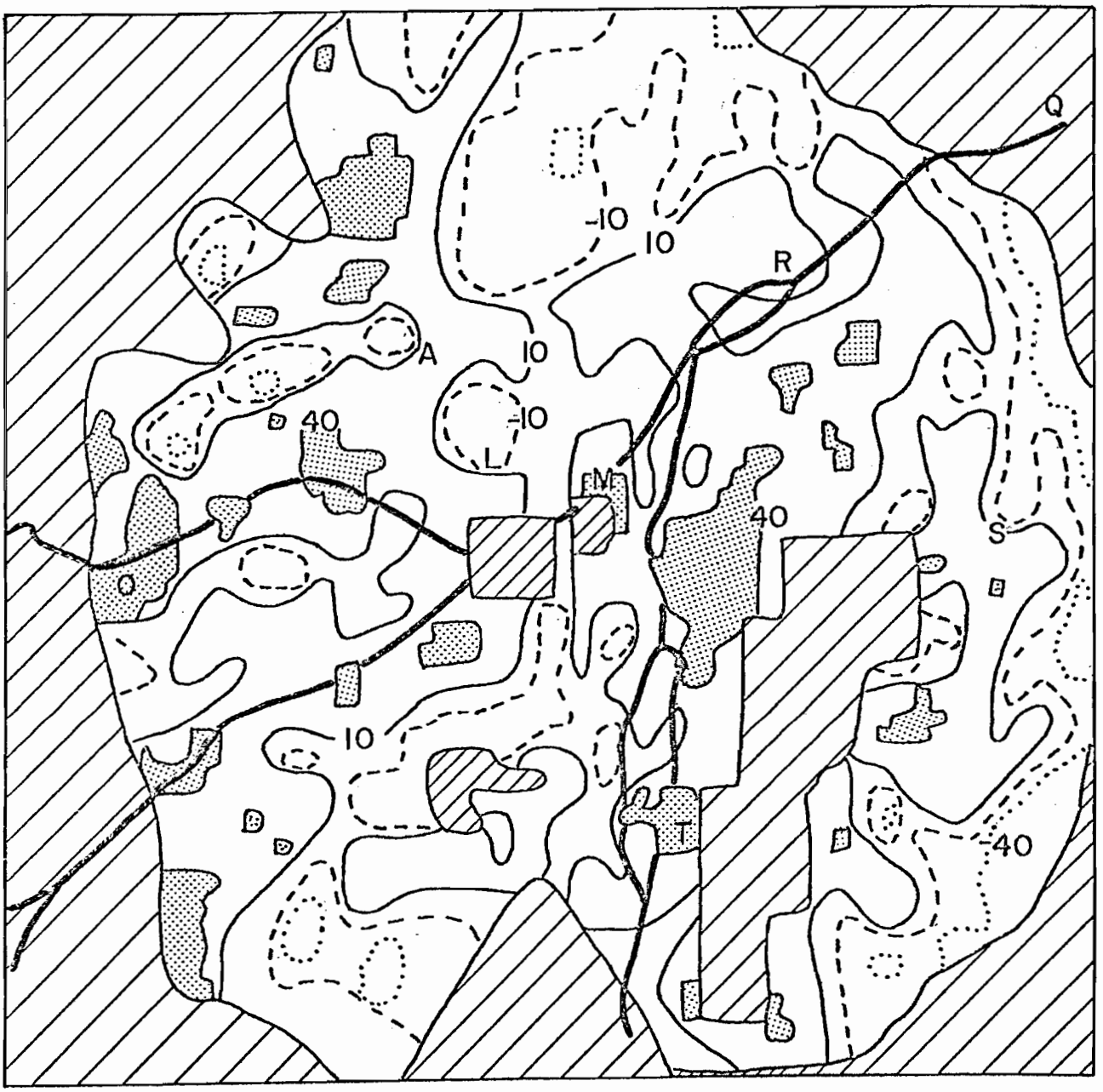

Fig. 4.19. Geographical distribution of the rainfall flux difference for 1979 data derived with A/F = 1.0.

The experiment is then repeated by allowing a modification of the predicted rainfall rate as follows. Each rainfall rate R(I,J,T) observed to move to (I + IF,J + JF) at time (T + ΔT) is multiplied by the ratio A/F(I + IF,J + JF) to obtain the modified rainfall rate R'(I',J',T');

$$R'(I',J',T') = R(I,J,T) * \frac{A}{F}(I',J')$$

where $T' = T + \Delta T$, $I' = I + IF$, $J' = J + JF$

and (IF,JF) is the observed displacement. In real time operation, the term "observed" displacement will be replaced by the "forecast" displacement.

It is seen that the magnitudes of the Critical Success Index remain essentially unaltered differing by less than 0.5 units from the'status quo' result. There are three main reasons for this result:

a) The A/F ratios are relatively close to unity. In fact, as can be verified from Fig. 4.18, $A/F \geq 1.4$ or $A/F \leq 0.7$ over only a small percentage of the geographical area under verification. Thus, the number of rainfall rates experiencing a significant change is minimal.

b) Truncation effects further reduce the number of modifications. Nearly 90% of all rainfall rates in Montreal (Bellon and Austin 1977) are less than or equal to 3 mm h^{-1}. These require A/F ratios which depart substantially from unity in order to induce a modification. For example, if R = 2 mm h^{-1} and A/F = 1.2, R' = 2.4 is truncated to R' = 2.

c) The fundamental explanation for the absence of a significant improvement in the magnitudes of the CSI parameter is that the trend derived from the 1976 and 1977 summers does not reflect the behaviour observed in 1979. To verify this assumption, the net rainfall difference defined earlier has been computed for the 1979 season, Fig. 4.19. Comparison with Fig. 4.17c, which can be considered as the predictor in the experiment described above, reveals many contrasts. For example, the region west of Ste-Agathe, characterized in Fig. 4.17c by development is under a negative influence in 1979. Opposite

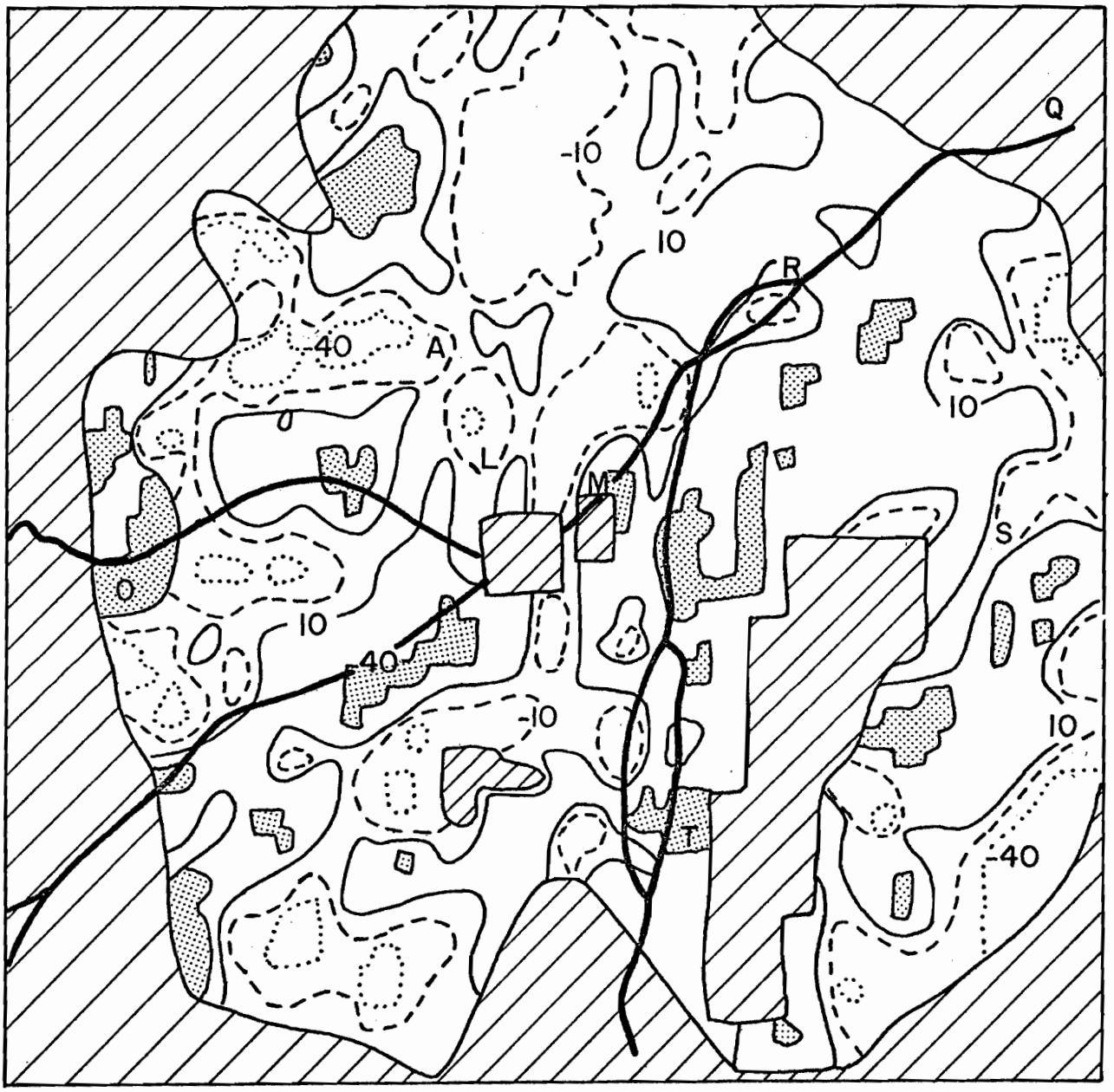

Fig. 4.20. Geographical distribution of the rainfall flux difference for 1979 data derived by applying the A/F distribution of Fig. 4.18.

trends are also present around Ottawa and southwest of the radar. Thus, when the modifying algorithm is applied as

$$R' = R(T) * (A/F)$$

the deviation from the actual rainfall is enhanced rather than reduced. This is shown in Fig. 4.20 which displays the rainfall difference between the actual and modified rate. Note the emergence of the -40% contour west of Ste-Agathe and the larger area enclosed by the +40% contour southwest of the radar. Deviations are diminished mainly east of the radar near the Green Mountains where the persistence of an upslope effect enabled a reduction of the positive deviation.

It is the belief of the author that the assimilation of preferred behaviour of rain patterns which enables a forecasting technique to depart from the "status quo" assumption, based on a statistical map of average orographic effect, would improve the accuracy of the forecasts only slightly in the Montreal region. However, in other parts of the world, the enhancement of a precipitation system is of significant proportions and the non-inclusion of orography will constitute a useless product (e.g., South Wales in Britain as described by Browning et al (1974) and (1975).

CHAPTER V

THE ROLE OF 2 KM CAPPI'S

From the early days of the operation of SHARP, it became evident that, in cases of light precipitation, the lowering of the CAPPI level would result in a more appropriate representation of the rainfall distribution at the ground. During the 1977 SHARP test, this notion has been put into practice for nearly 50 hours of operation (see Table 3.2) when 2 km real time maps were sent when radar echoes were not seen to penetrate sufficiently the 3 km level. At the end of the summer, the 2 km level was also employed in a pattern recognition technique and forecasts were issued. This approach was likewise extended for winter snowstorms. However, it was realized that the 60 minute interval between correlated maps was too large, particularly for cases of extensive radar echo coverage with a uniform intensity distribution. This situation arises frequently during spring and fall rainstorms and winter snowstorms. In these instances, the calculated motion was nearly zero due to the absence of recognizable features persisting for at least one hour.

The purpose of the study reported in this chapter is thus twofold:

1. To analyse the radar echo intensity distribution between the 2 and 3 km levels for light precipitation in summer in order to determine the gain in precipitation detectability derived at the lower height. As a frame of reference, some cases of convective character are also included in order to establish the 3 km level as a suitable CAPPI height for typical summer weather. The vertical distribution of radar reflectivity between the 2 and 3 km levels for extensive precipitation patterns in fall and winter snowstorms is also examined.

2. To investigate whether a reduction in the time interval between maps being correlated eliminates errors encountered in the attempted real time test. A general approach to be followed for forecasts at the 2 km

level and with a shorter time interval can thus be formulated, taking into account additional difficulties arising from quantization effects and the increased probability of ground echoes.

In order to obtain an appropriate data set for both of these goals, a program has been written which produces 2.0, 2.5 and 3.0 km CAPPI maps, at every 30 minutes, for desired sequences of weather, and outputs them into one magnetic tape for convenient analysis. The range of the maps is restricted to 180 km, with a unit grid area of (6.0 x 3.6) km^2. Included were 26 sequences of 1977 weather, totalling 250 hours or 500 maps for each of the three heights.

Category	No. of sequences	No. of 30-min. maps
1) light summer precip.	10	200
2) convective summer precip.	8	80
3) winter snowstorms	5	135
4) extensive fall precip.	3	85
	26	500

Table 5.1: Type and quantity of data used in the study reported in this chapter.

5.1. Vertical Distribution of Rainfall

As a consequence of our radar antenna elevation program (refer to Fig. 2.5), the 1977 data from the three chosen levels are independent only within a range of 150 km. All comparisons are thus limited to inside this range. As was done in a similar procedure in the verification of 3 km forecasts, all maps of the 2 km level are summed in order to locate and mask areas affected by ground echoes, anoprop, and shadowing effects. After obtaining the distribution of intensities over grids denoting reliable data, the analysis consists of computing the total flux F for each height as follows:

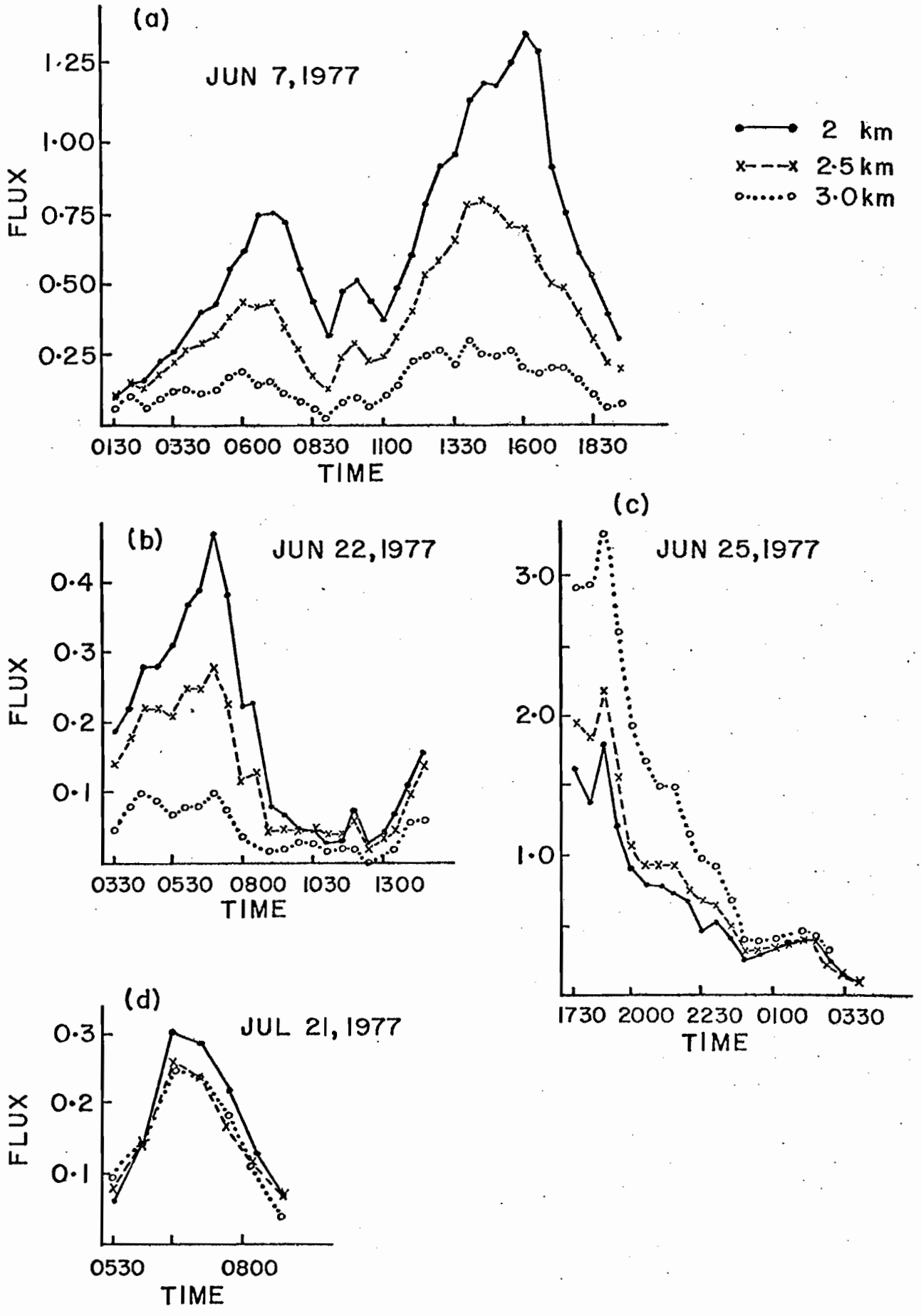

Fig. 5.1 The variation of the flux F with time and height for selected sequences of light summer precipitation.

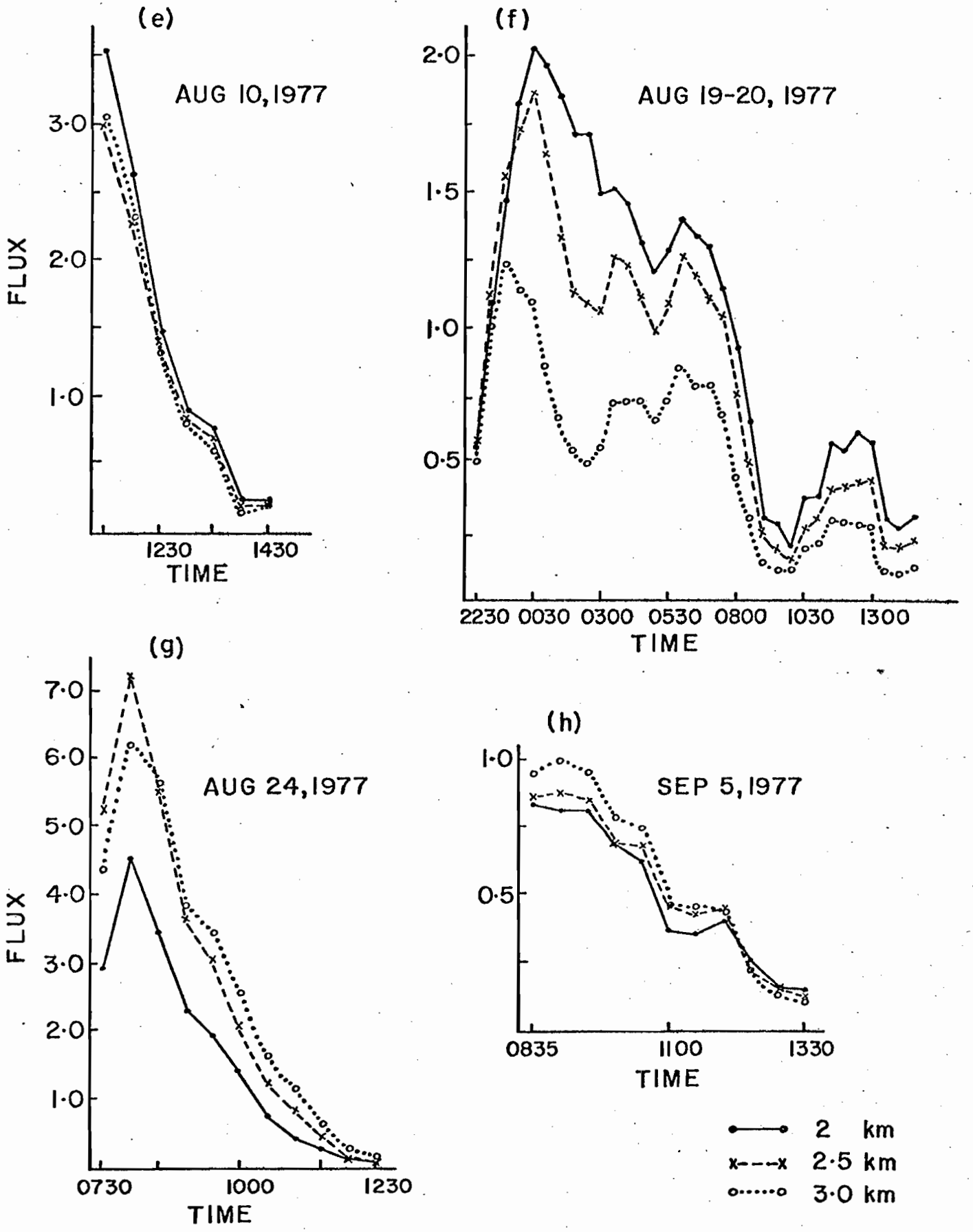

Fig. 5.1 The variation of the flux F with time and height for selected sequences of light summer precipitation.

$F = K \sum_i D(I_i)R(I_i)$ where

$D(I_i)$ = number of occurrences of intensity level I_i

$R(I_i)$ = rainfall rate corresponding to intensity level I_i (mm h^{-1})

K = constant needed to reduce the result in units of cubic hectometers of water per 5 minutes (hm^3/5 min.) $K = 0.0018$.

Analysis in terms of F can be supplemented by means of vertical cross-sections.

5.4.1 Light Summertime Precipitation

The variation of F with time and height for selected sequences is plotted in Figs. 5.1a to 5.1h. Some sequences have been omitted on account of the disruptive influence of anomalous propagation at the lower levels which did not manifest itself by visual inspection of 3 km CAPPI's. The behaviour of F with time should not be considered important here since the peaks and troughs are not necessarily associated with development and dissipation. They are rather mainly the direct consequence of radar patterns entering the 150 km range, being at times affected by the mask, and then leaving through the opposite boundary. Instead, of primary concern is the vertical spread of its magnitude among the three levels. Note that in cases (a), (b) and (f), the flux through the 3 km level is considerably reduced. On the other hand, in (c) and (g), the opposite effect is observed. Only (d), (e) and (h) offer little height variation. It becomes immediately apparent that these differences are associated with the level of the bright band occurring near the 0° isotherm. This fact is well illustrated by means of vertical cross-sections.

Figs. 5.2a to 5.2g represent vertical cuts through precipitation areas along lines as indicated on the corresponding CAPPI maps. The rainfall rates associated with the alphanumerics on the CAPPI maps and on the cross-sections are listed in Table 5.2.

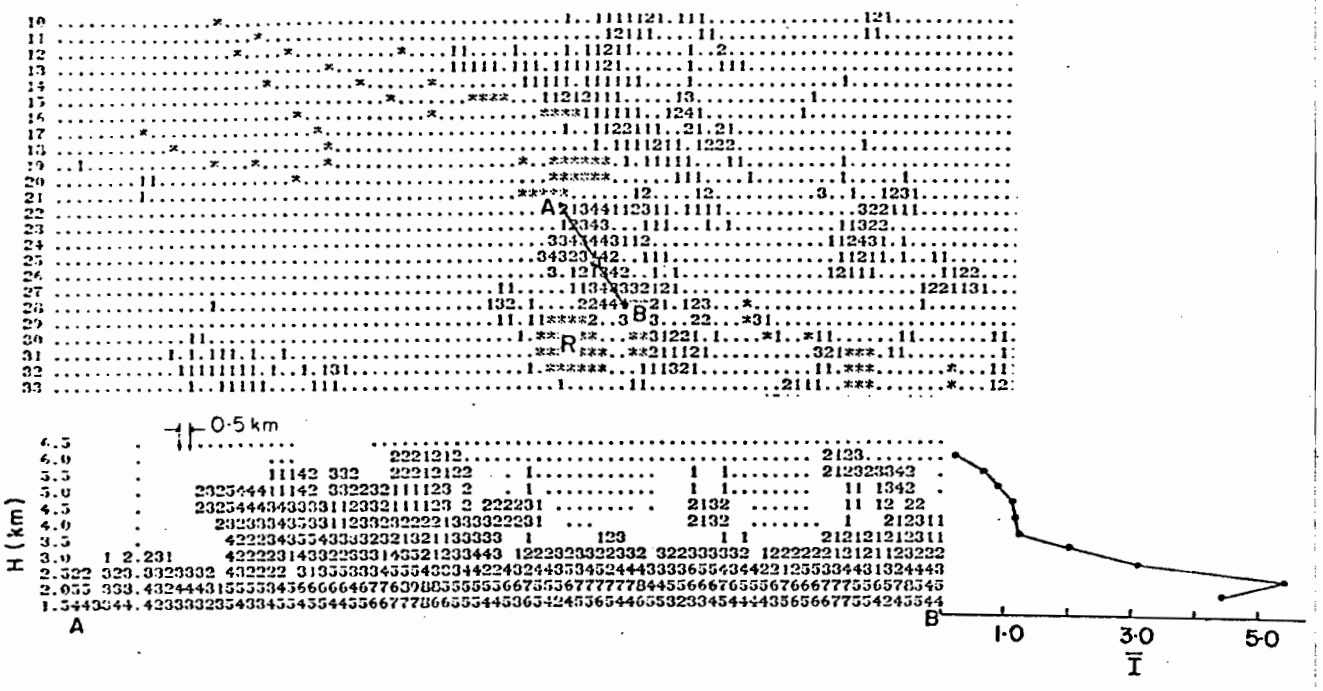

5.2a : 15:30, 7-June - 77

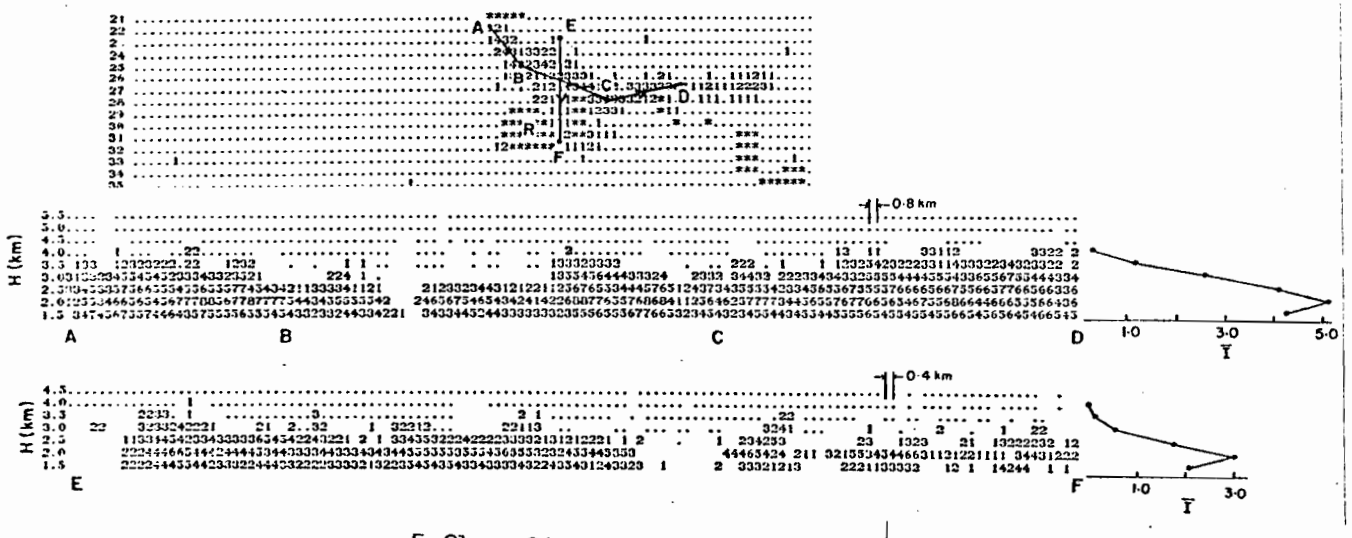

5.2b : 09:00, 22 - June - 77

5.2c : 18:30, 25 - June - 77

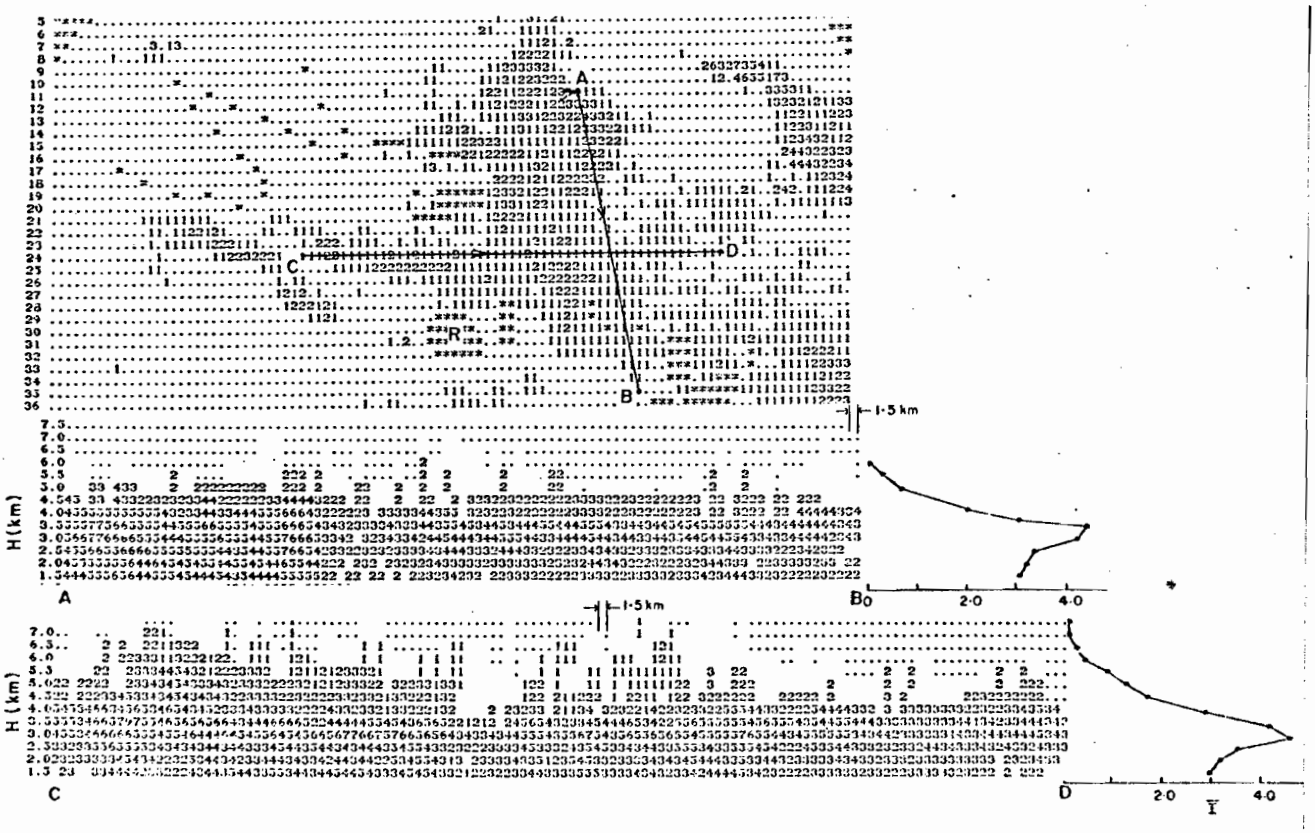

Fig. 5.2. Vertical cross-sections through precipitation areas along lines as indicated on the corresponding CAPPI maps.

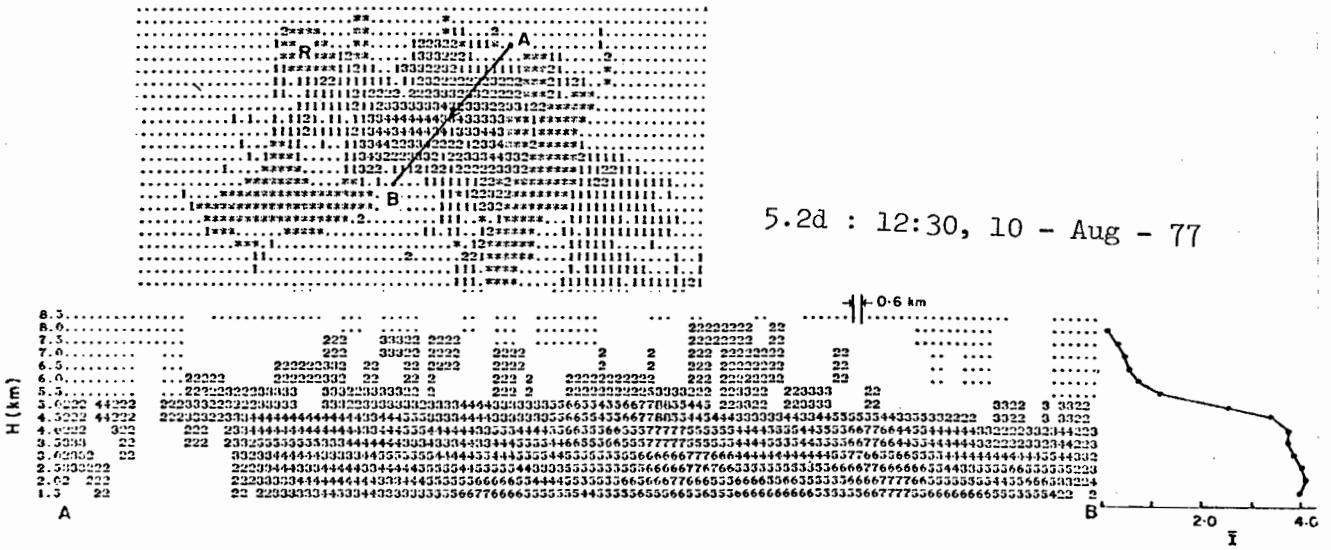

5.2d : 12:30, 10 - Aug - 77

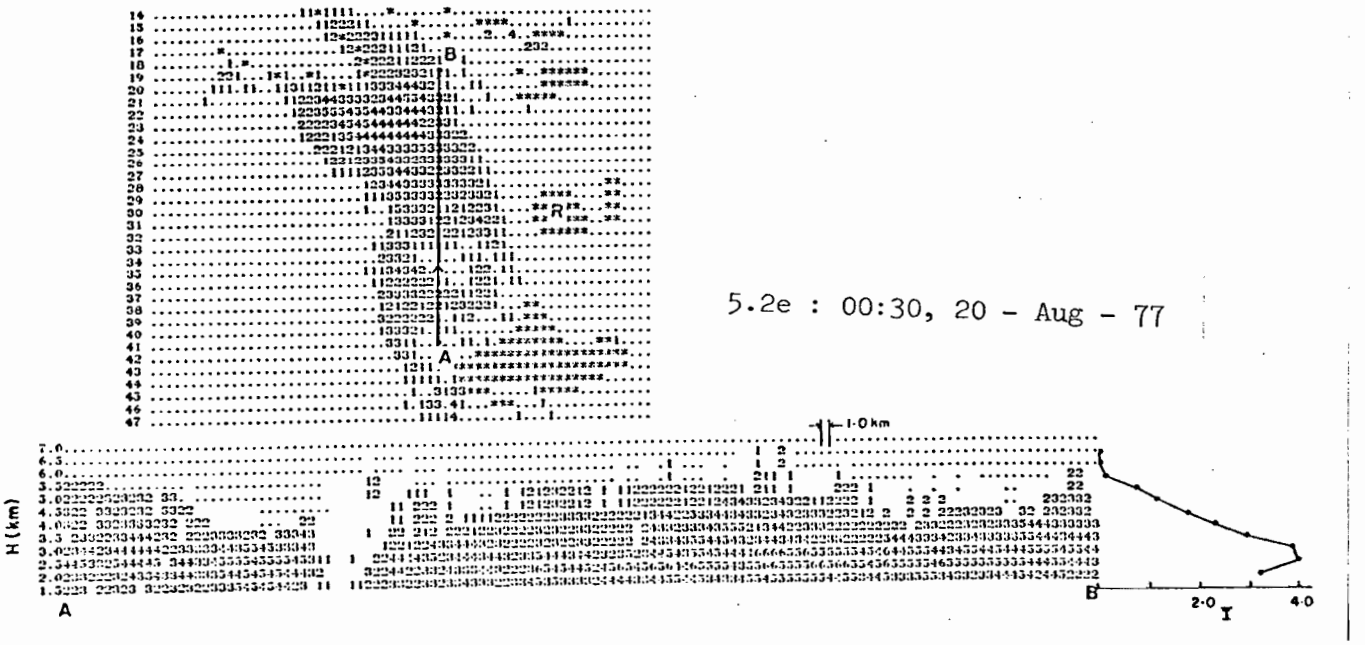

5.2e : 00:30, 20 - Aug - 77

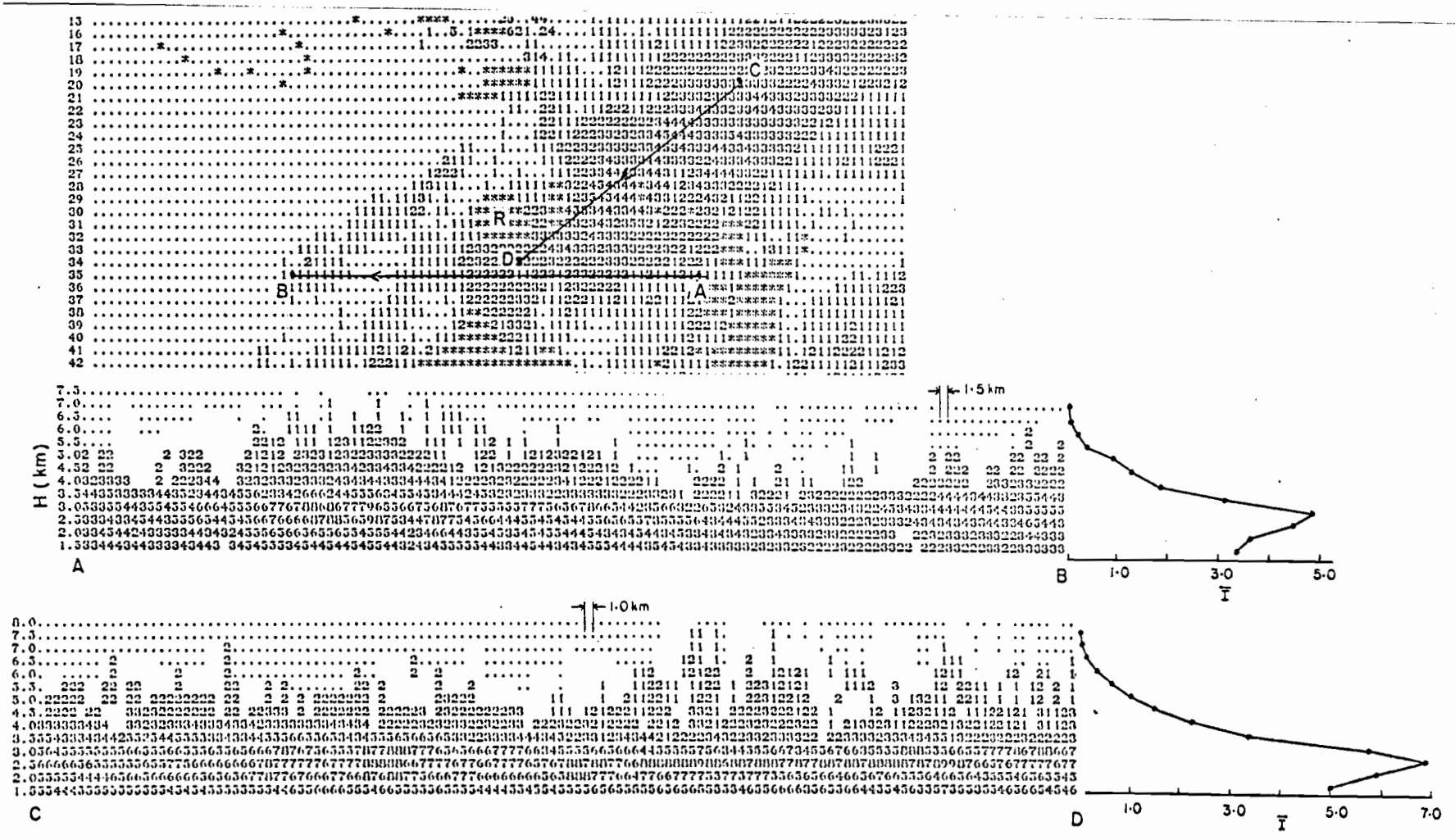

5.2f : 08:00, 24 - Aug - 77

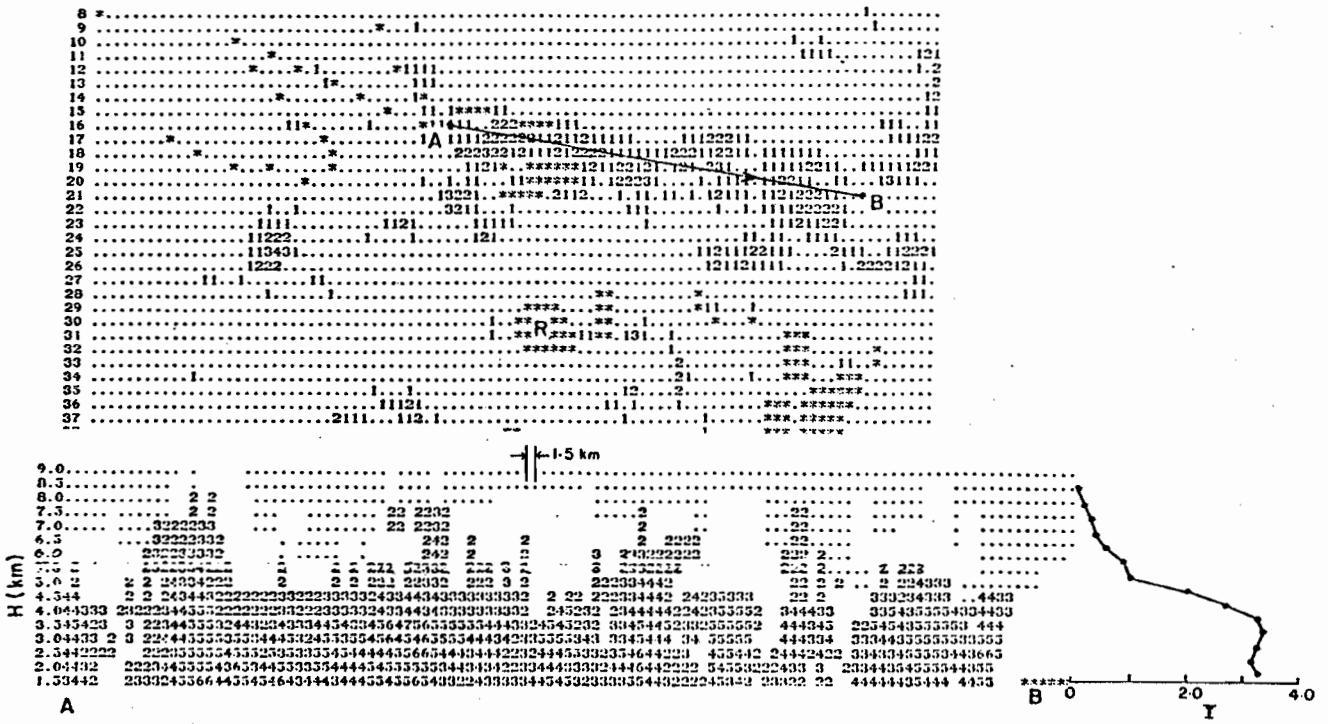

5.2g : 08:35, 5 - Sept - 77

CROSS-SECTIONS							CAPPI's	
	DBZ		rainfall rate $Z=200R^{1.6}$ ($mm\ h^{-1}$)		snowfall rate $Z=2000R^{2}$ ($mm\ h^{-1}$)		rainfall rate or snowfall rate	
α	LT	UT	LT	UT	LT	UT	LT	UT
1	11	15	0.18	0.32	0.8	1.3	1(0.5)	1(1.5)
2	15	19	0.32	0.56	1.3	2.0	2(1.5)	2(2.5)
3	19	23	0.56	1.00	2.0	3.2	3(2.5)	5(4.5)
4	23	27	1.00	1.78	3.2	5.0	5(4.5)	8(7.5)
5	27	31	1.78	3.16	5.0	7.9	8(7.5)	13(12.5)
6	31	35	3.16	5.62	7.9	12.6	13	20
7	35	39	5.62	10.00	12.6	20.0	20	30
8	39	43	10.00	17.80	20.0	31.6	30	40
9	43	47	17.80	31.60	31.6	50.0	40	50
A	47	51	31.60	56.20	50.0	79.3	50	75
B	51	55	56.20	100.00	79.3	126.0	75	100
C	55	59	100.00	178.00	126.0	200.0	100	150
D	59	63	178.00	316.00	200.0	316.0	150	200
E	63	67	316.00	562.00	316.0	500.0	200	300
F	≥67		≥562.00		500.0		300	

α: alphanumeric character
LT: lower threshold
UT: upper threshold

Table 5.2. Correspondence between alphanumerics and rainfall rates in 1977. Snowfall rate is in $mm\ h^{-1}$ of dry snow.

Note that on account of hardware design the intensity levels 1 and 2 of the raw data, that is, in the cross-sections, occur only within 60 and 120 km respectively.[1] Moreover, only heights above 1.0 km should be considered since at approximately that level, ground echo suppression is performed to reduce tape consumption. It should be pointed out that since the coordinates of linear height versus distance of these cross-sections are derived from an original display with coordinates of antenna elevation number versus distance, rows are repeated when the 0.5 km height increment is less than the resolution of the original raw data. This occurs especially at higher heights. The average intensity level for each 0.5 km layer is calculated in order to bring into sharper focus any vertical gradient of reflectivity. This method of representation clearly underlines the presence of a bright band and the flat top of the radar echo, characteristic for this type of non-convective precipitation. Although the averaging process reduces the overall difference, a detailed examination of the cross-sections reveals that the increase in reflectivity between the bright band and the neighbouring layers may vary between 2 and 3 intensity levels (8 to 12 dBZ or a factor of 3 to 5 in rainfall rate). Figs. 5.3a and 5.3b show that the enhancement of rainfall rates due to the bright band is quite drastic and also could spread over nearly the entire radar coverage.

---

[1] This range dependence of reflectivity intensity is circumvented in the production of summer CAPPI maps by including levels 3 and above. Since a significant portion of winter precipitation is at levels 1 and 2, they are included in CAPPI production, but, at times, generate artificial echo features capable of disrupting a pattern recognition technique.

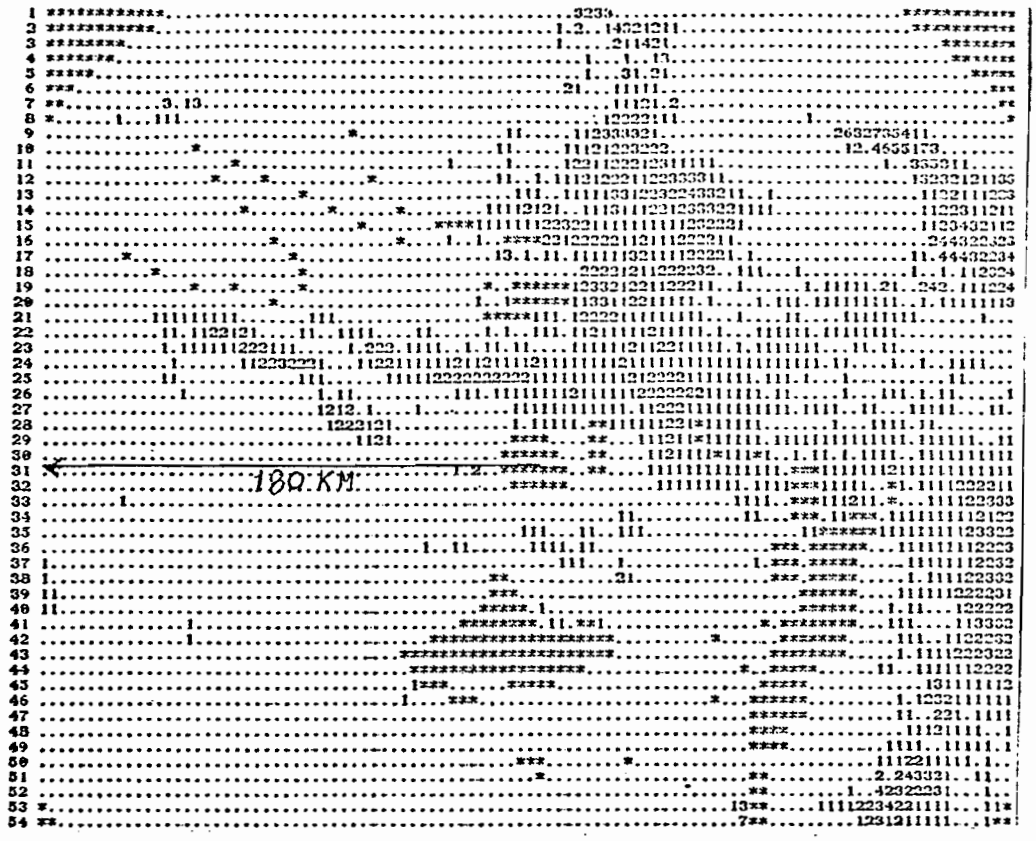

Fig. 5.3a. 2 km CAPPI map at 1830 EST 25 June 1977.

Fig. 5.3b. 3 km CAPPI map at 1830 EST 25 June 1977.

In cases (a) and (b), the low level of the precipitation requires that a 2 km CAPPI be used. An underestimation is observed even in regions where the echo top manages to reach the 3 km level, since a 3 km CAPPI actually consists of a slice between 2.7 and 3.3 km.

It is seen that the distribution of the reflectivity values at the bright band is a better estimation of conditions at the surface than that at the 3 km level. Moreover, the enhancement at the bright band is capable of raising the precipitation rate above the lowest detectable threshold and thus provide a more complete assessment of the area of precipitation at the surface.

In other instances, the appropriate course of action to be taken is less straightforward. Avoidance of a bright band in an operational environment involves a shift to a higher level which may reduce echo coverage or brings the CAPPI to a lower level contaminated by anomalous propagation or an unacceptable increase in ground echo returns. The desirable solution may be to maintain a constant level and by means of cross-sections in real time, the presence, behaviour and significance of the bright band and other vertical gradients, can be monitored constantly in order to compensate for the increase or decrease of rainfall rates at the pre-chosen level. The importance of the availability of vertical cross-sections as a primary tool for decision-making is thus readily realized. A recent technique developed by Collier et al (1980) may also be used in differentiating between bright band and convective showers in the same radar display.

5.1.2 Convective summer precipitation

As was anticipated, the flux gradient at the lower levels of a convective storm is relatively weak, with only occasional marginal increases of less than 10% around the 3 km level. In fact, as shown below, the total

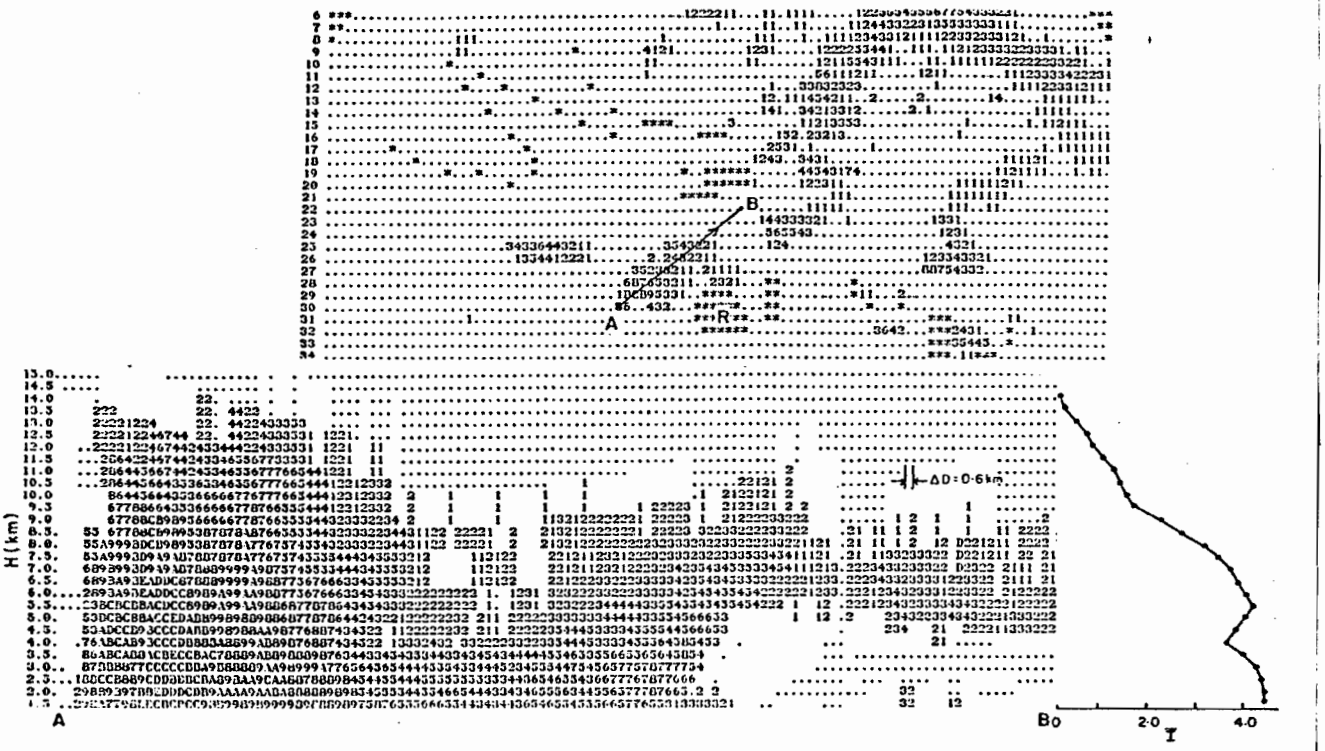

5.4a : 16:00, 4 - Aug - 77

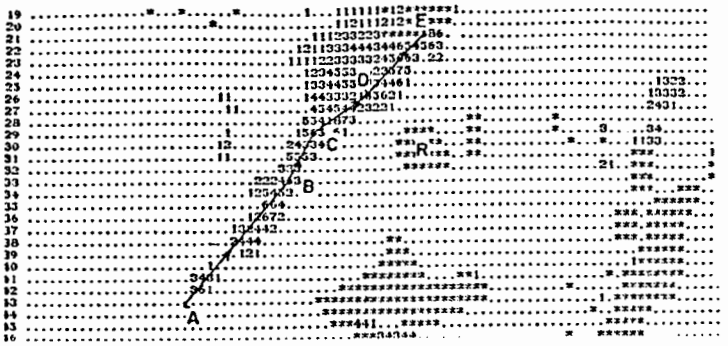

5.4b. 16:30, 29 - Aug - 77

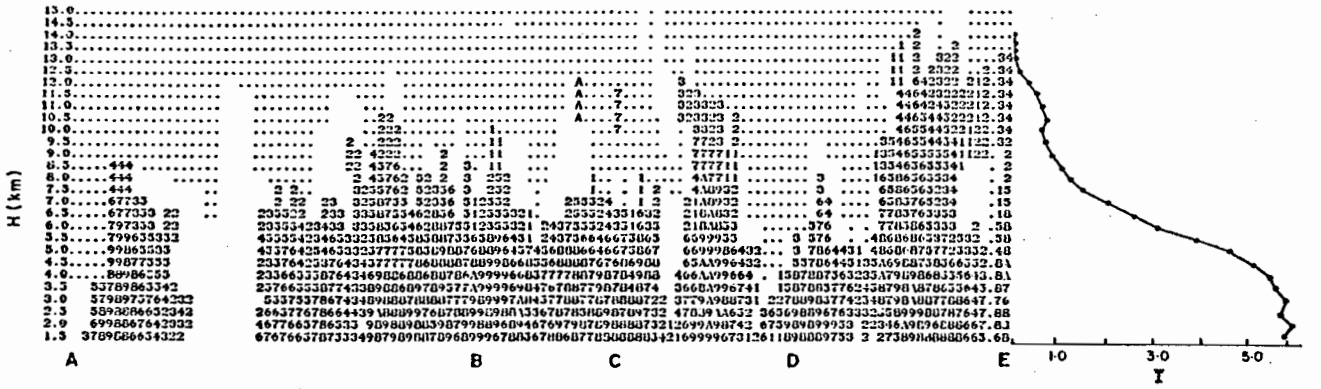

Fig. 5.4. Vertical cross-sections through precipitation areas along lines as indicated on the corresponding CAPPI maps.

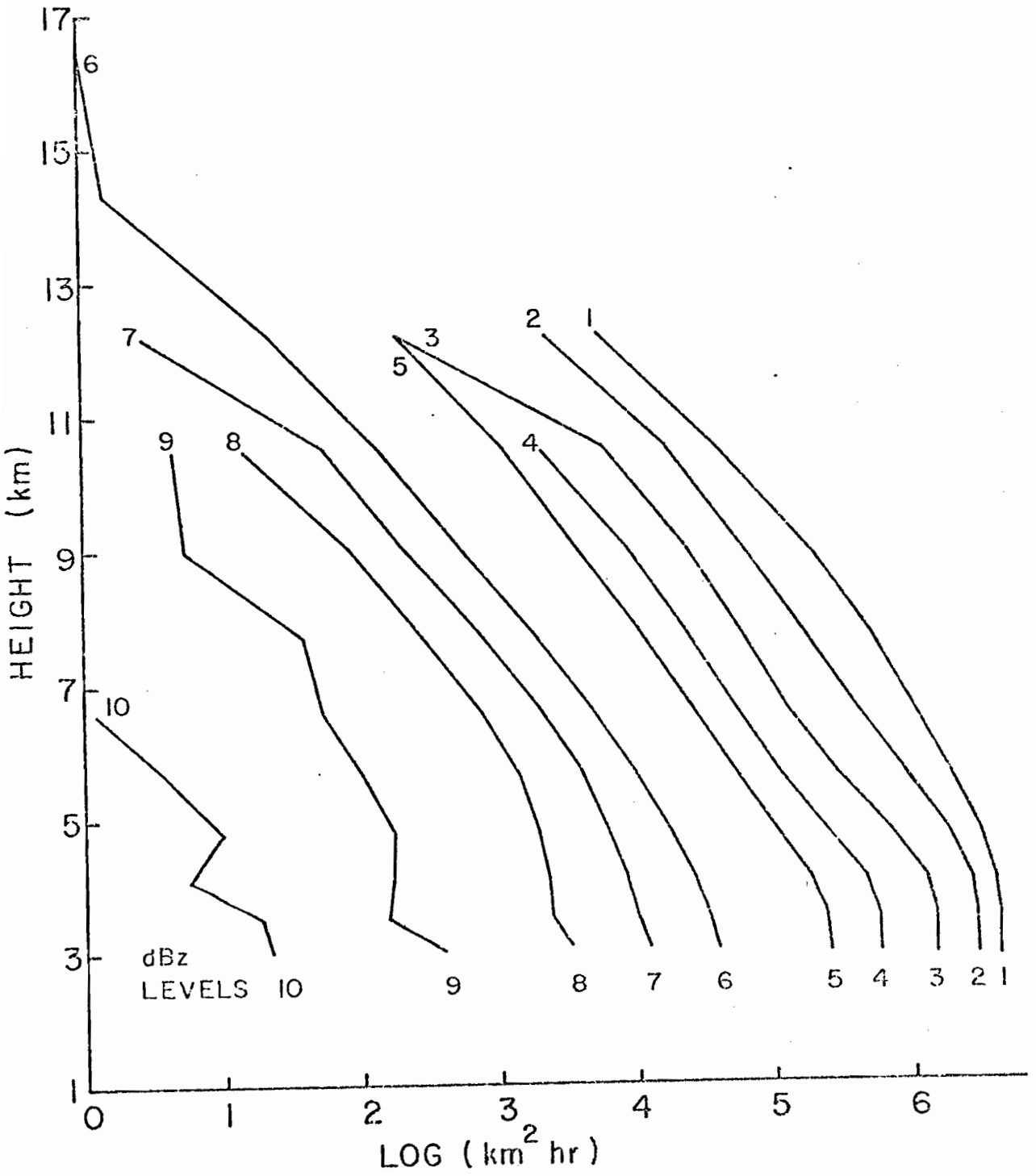

Fig. 5.5. Vertical distribution (above 3 km) of the areal extent of the indicated intensity levels. The data base for this graph consists of 340 hours of convective weather in June, July and August 1976. The rainfall rates corresponding to the intensity levels are given in Table 5.2 under "cross-sections". The area under intensity level i also includes the areas of levels 1 to (i − 1). Curves are terminated at a height at which noise contaminated the data base. (From Kilambi and Marshall (1978), private communication.)

flux at 3 km for all 80 maps in this category is identical to that at 2.5 km and shows only a modest increase of 3.3% compared to that at 2.0 km.

Height (km)	2.0	2.5	3.0
Total flux (hm^3/5 min)	171.5	176.7	177.4
%	96.7	99.6	100.0

Table 5.3: Distribution of flux for convective weather at three levels.

These differences are so small as to clutter a flux diagram: hence, these have not been presented. However, the cross-sections provided in Figs. 5.4a and 5.4b further corroborate the above statement. The choice of a 3 km CAPPI, which avoids the pitfalls of one at 2 km, namely, enhanced ground echo and anomalous propagation is thus fully justified for typical summer weather.

A related research at the Stormy Weather Group on the convective precipitation flux for all heights above 3 km is summarized in Fig. 5.5. It is an extension of previous investigations by Marshall and Holtz (1970), who used an attenuating wavelength and photographic data. Similar studies are summarized by Konrad (1978) who also reports constant echo area up to a height of 4 km for the mid-Atlantic region.

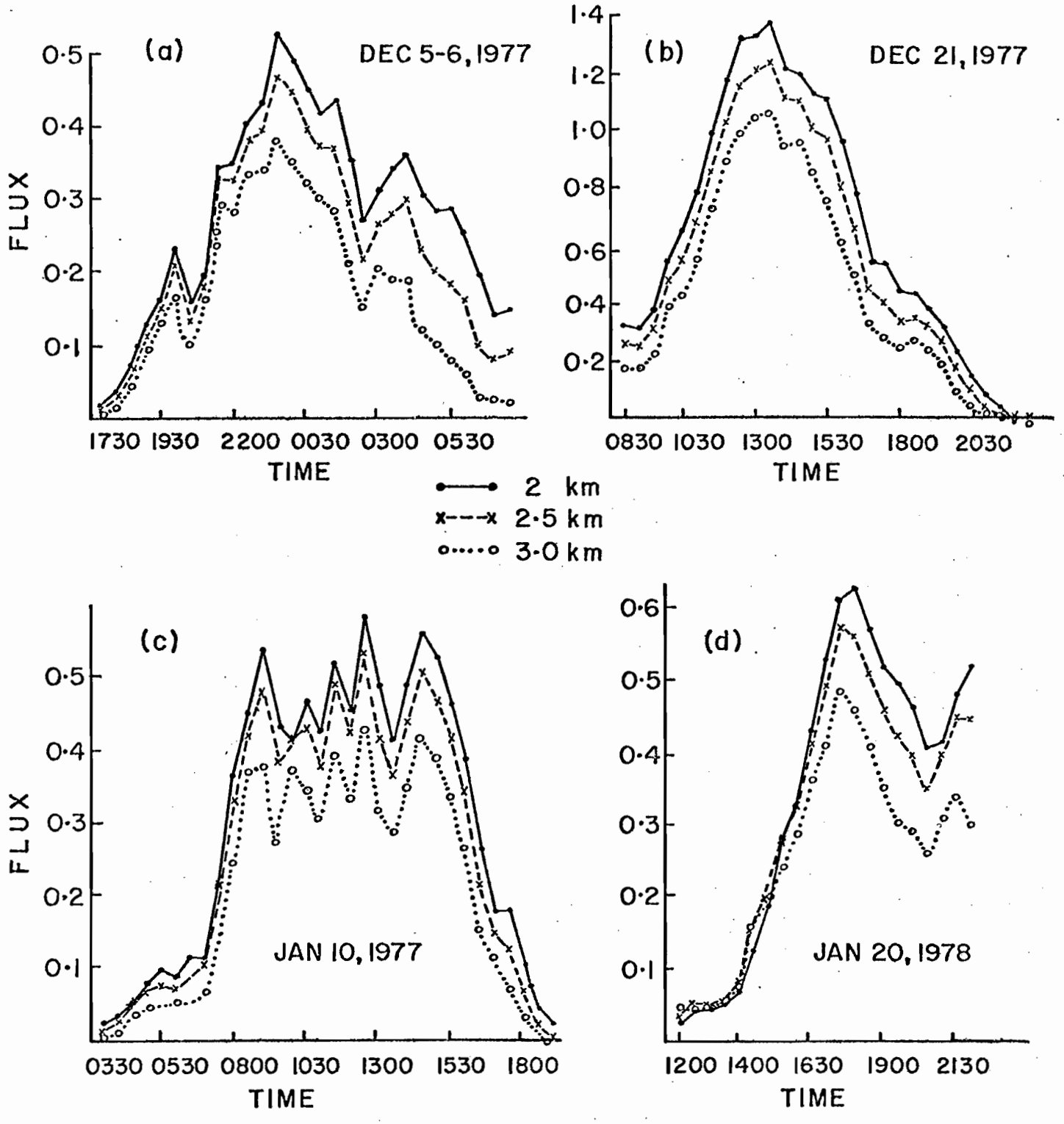

Fig. 5.6. The variation of the flux F with time and height for selected sequences of snowstorms.

5.1.3 Snowstorms

The total flux through the three levels under consideration for the five snowstorms studied is given below.

Height (km)	2.0	2.5	3.0
Total flux (hm^3/5 min)	55.1	48.6	39.4
%	100	88.2	71.5

Table 5.4: Distribution of flux for intense winter snowstorms.

It is seen that, on the average, the 3 km level embodies an underestimation of about 30% with respect to the 2 km height. As illustrated in Figs. 5.6a to 5.6d, this discrepancy is evident after the early stages of each snowstorm passage and this behaviour exhibits little variation from storm to storm.

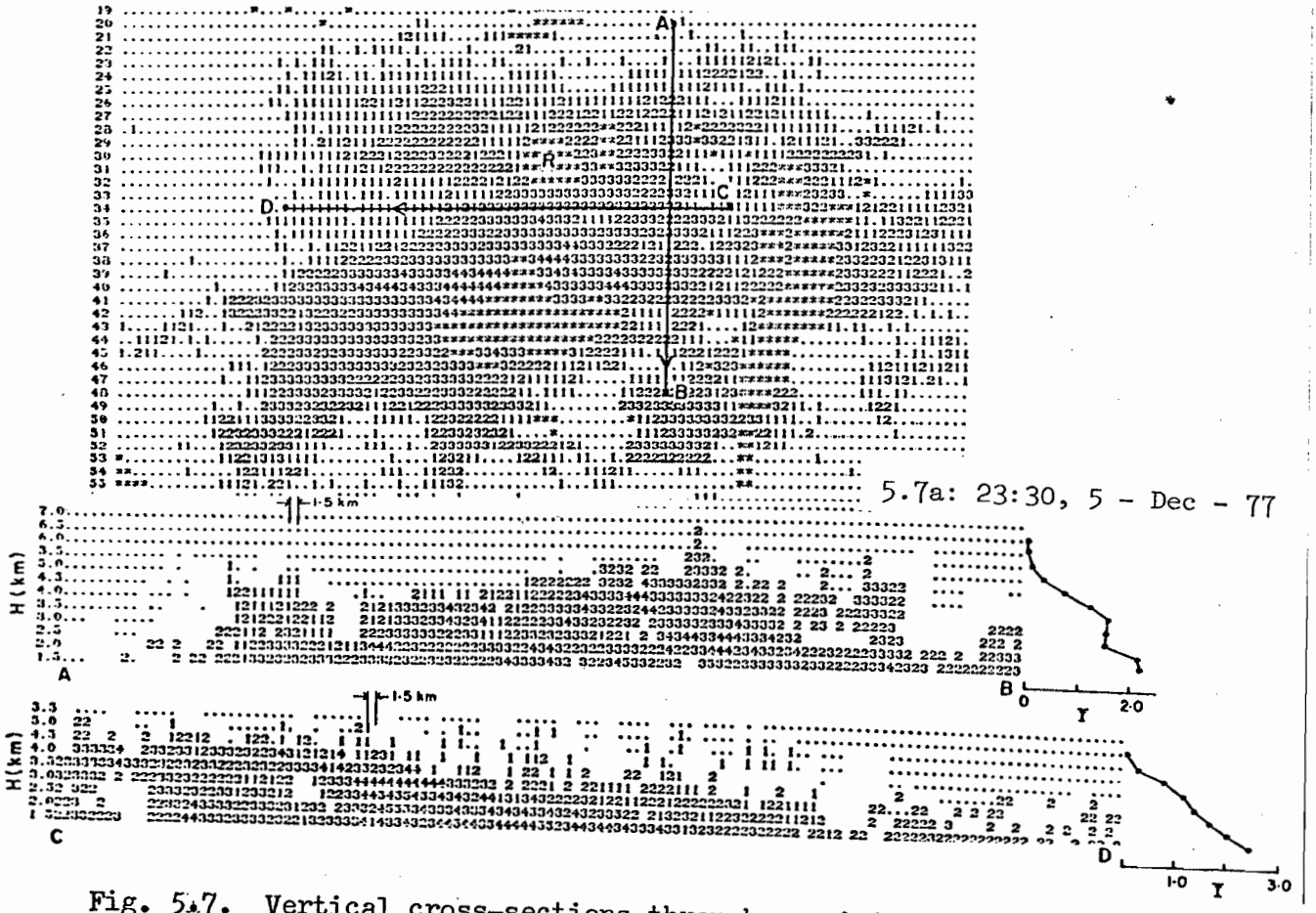

Fig. 5.7. Vertical cross-sections through precipitation areas along lines as indicated on the corresponding CAPPI maps.

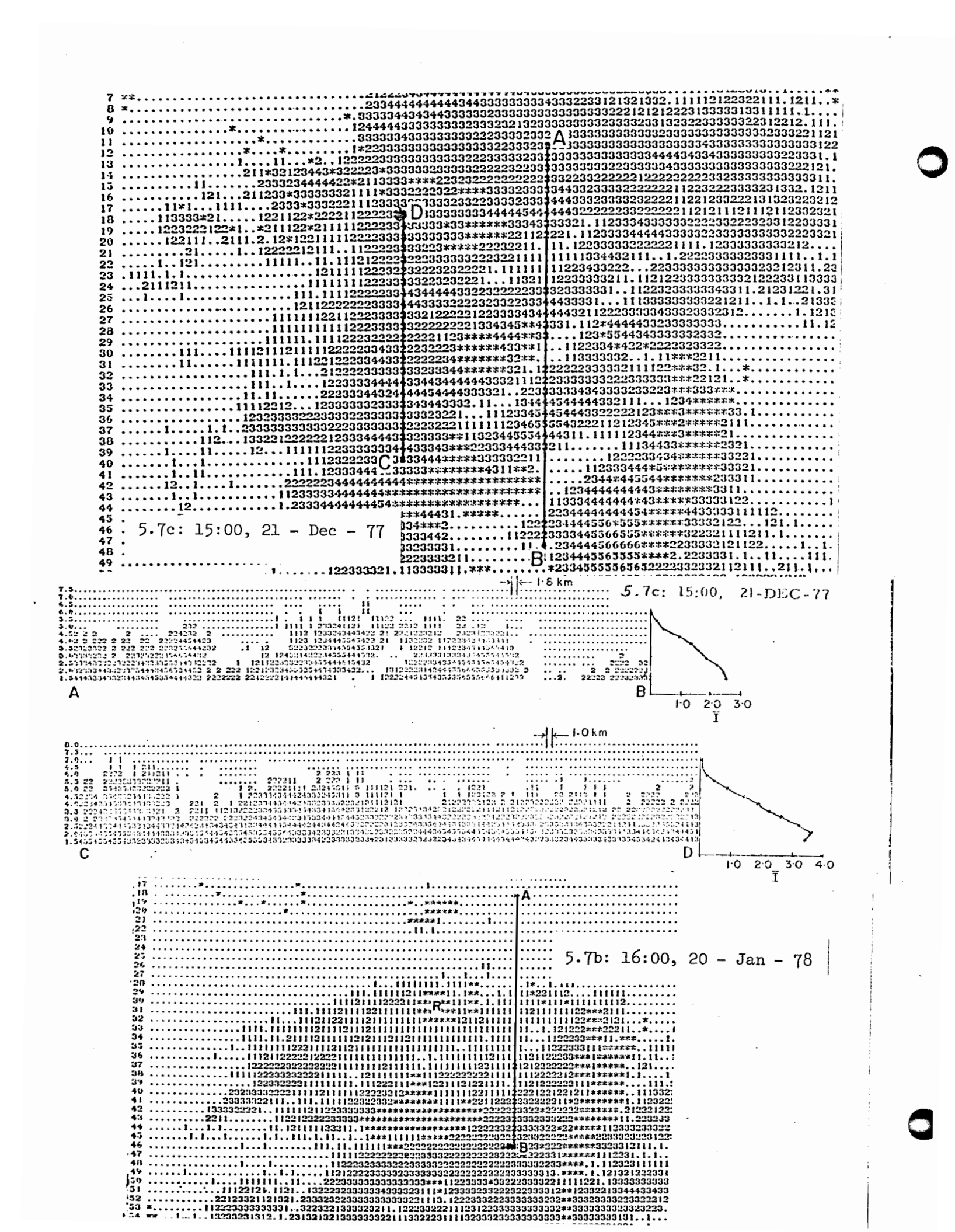
5.7c: 15:00, 21 - Dec - 77
1·6 km
5.7c: 15:00, 21-DEC-77
A
B
1·0
2·0
3·0
Ī
1·0 km
C
D
1·0
2·0
3·0
4·0
Ī
5.7b: 16:00, 20 - Jan - 78

The cross-sections of Figs. 5.7 offer a further example of the gradual decrease of radar echoes with height. In most cases, the highest radar return is near the 6 km level. Although the horizontal reflectivity gradient is generally weak, the presence of some convective elements with higher intensities can be found as in Fig. 5.7c. It is above these regions that the highest turrets are observed. Fig. 5.7b illustrates a common feature of an approaching snowstorm, namely the presence of an overhang, protruding as much as 30 km beyond the precipitation at 1.5 km. Evaporation of light snow through dry air is likely its cause. In Fig. 5.7a_2, the top of the snowstorm is sloping upward from a W-E direction toward the centre of the incoming low centre.

It should be noted that these cross-sections are examples of vigorous winter snowstorms associated with a deep low off the eastern seaboard. The vertical distribution of reflectivities for cases of local snowflurries or for snow from continental lows is expected to show more pronounced differences. While examples were not available, it is believed that the maximum height attained will be significantly lower, barely penetrating the 3 km level. The use of a 2 km CAPPI is thus mandatory in these circumstances. In fact, its adoption is generally recommended for all snow situations since its main drawback in the form of anoprop is totally absent in winter on account of the lack of strong vertical moisture gradients. However, because of the light snowfall rate and low heights, detectability at far ranges remains a problem, Carlson and Marshall (1972).

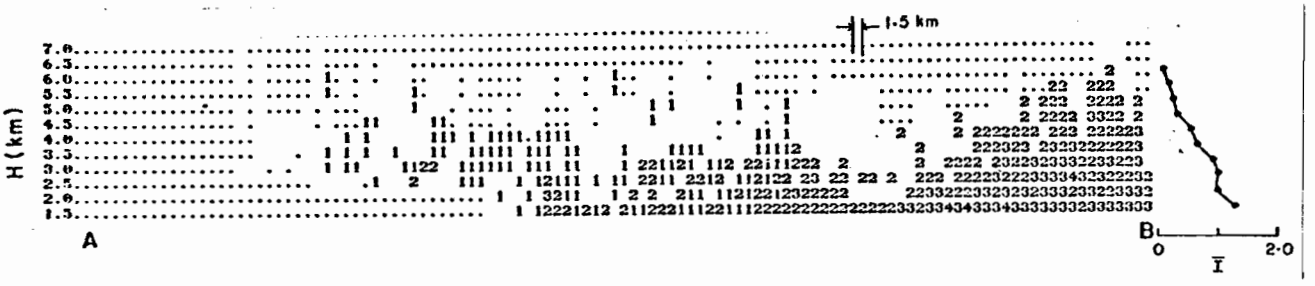

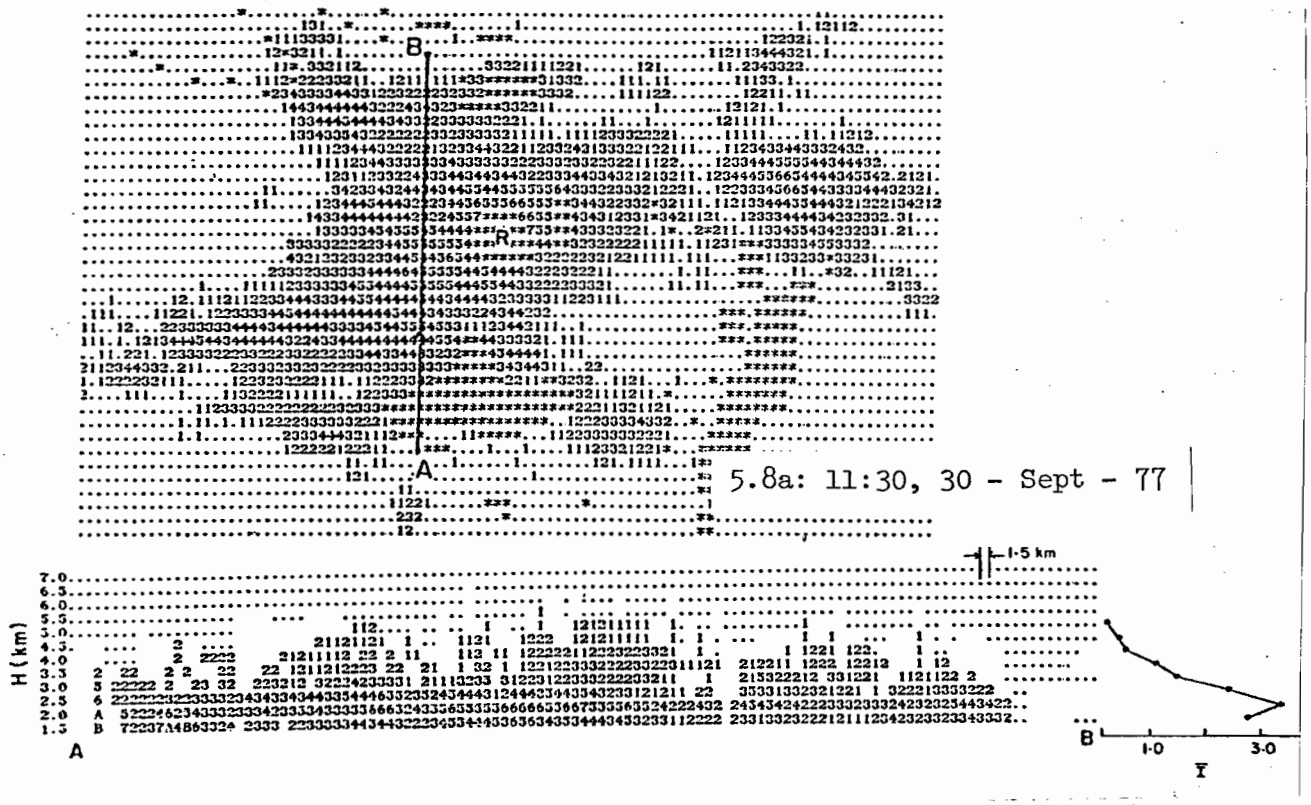

5.8a: 11:30, 30 - Sept - 77

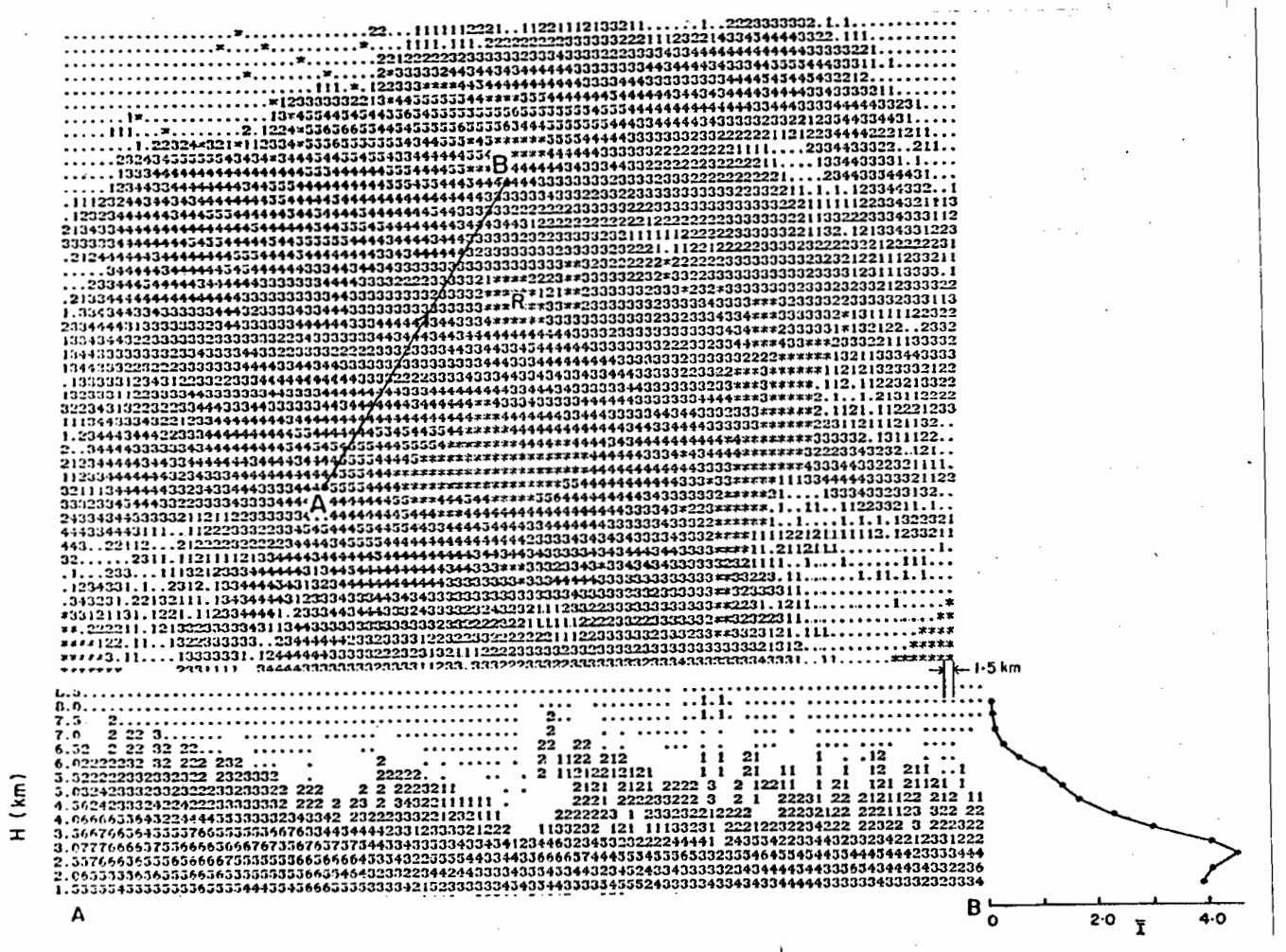

5.8b: 16:05, 1 - Oct - 77

5.1.4 Extensive Fall Precipitation

The three cases of fall weather analysed revealed characteristics similar to those of light summer rain. The bright band can occur at any height, but is often at 2 km. The knowledge of its location from cross-sections is thus necessary in order to determine whether the measurements from the chosen CAPPI level are taken in a layer of snow, rain or in the vicinity of the bright band. Some examples are provided in Figs. 5.8.

5.8c: 09:00, 4 - Nov - 77

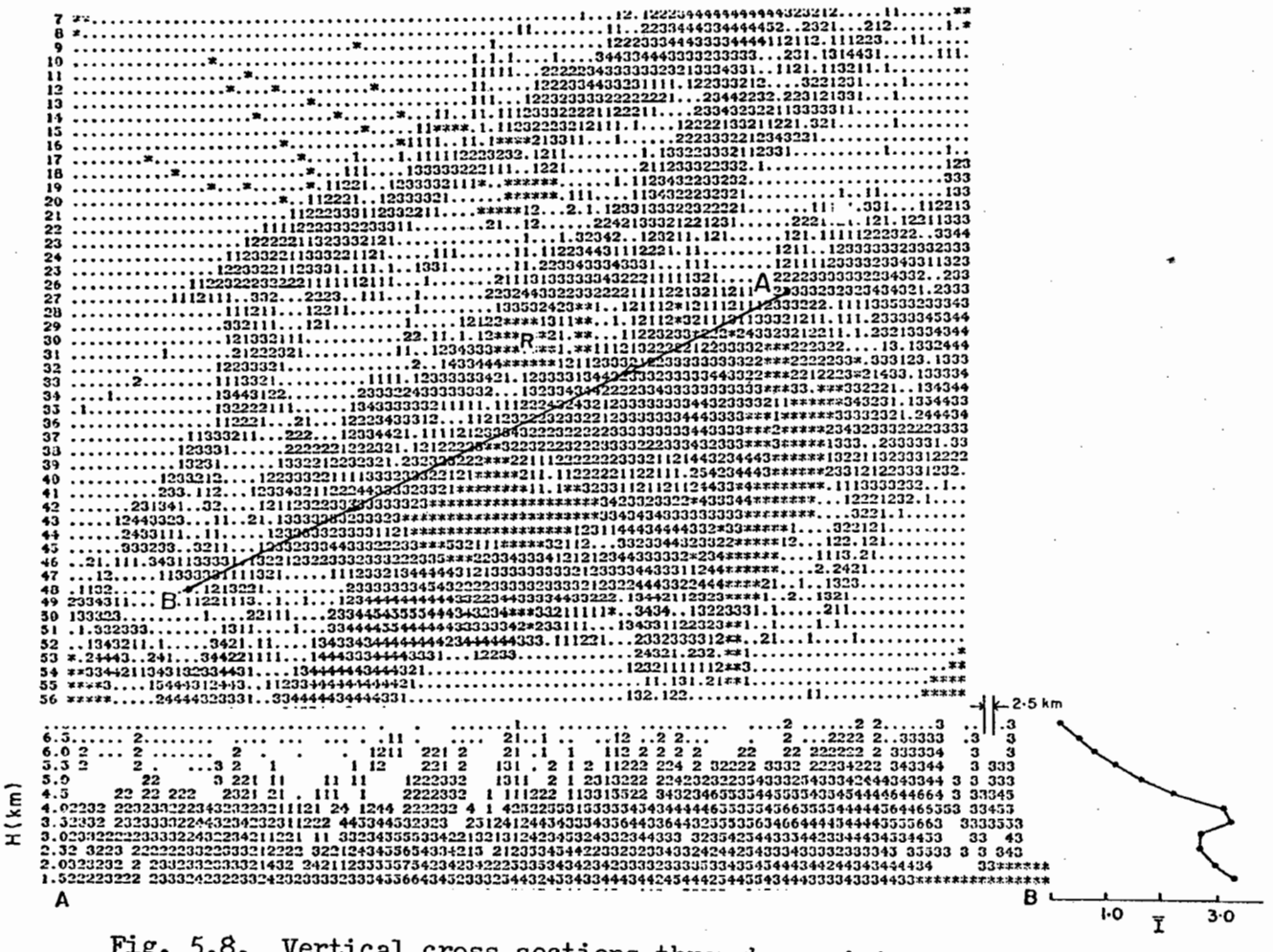

Fig. 5.8. Vertical cross-sections through precipitation areas along lines as indicated on the corresponding CAPPI maps.

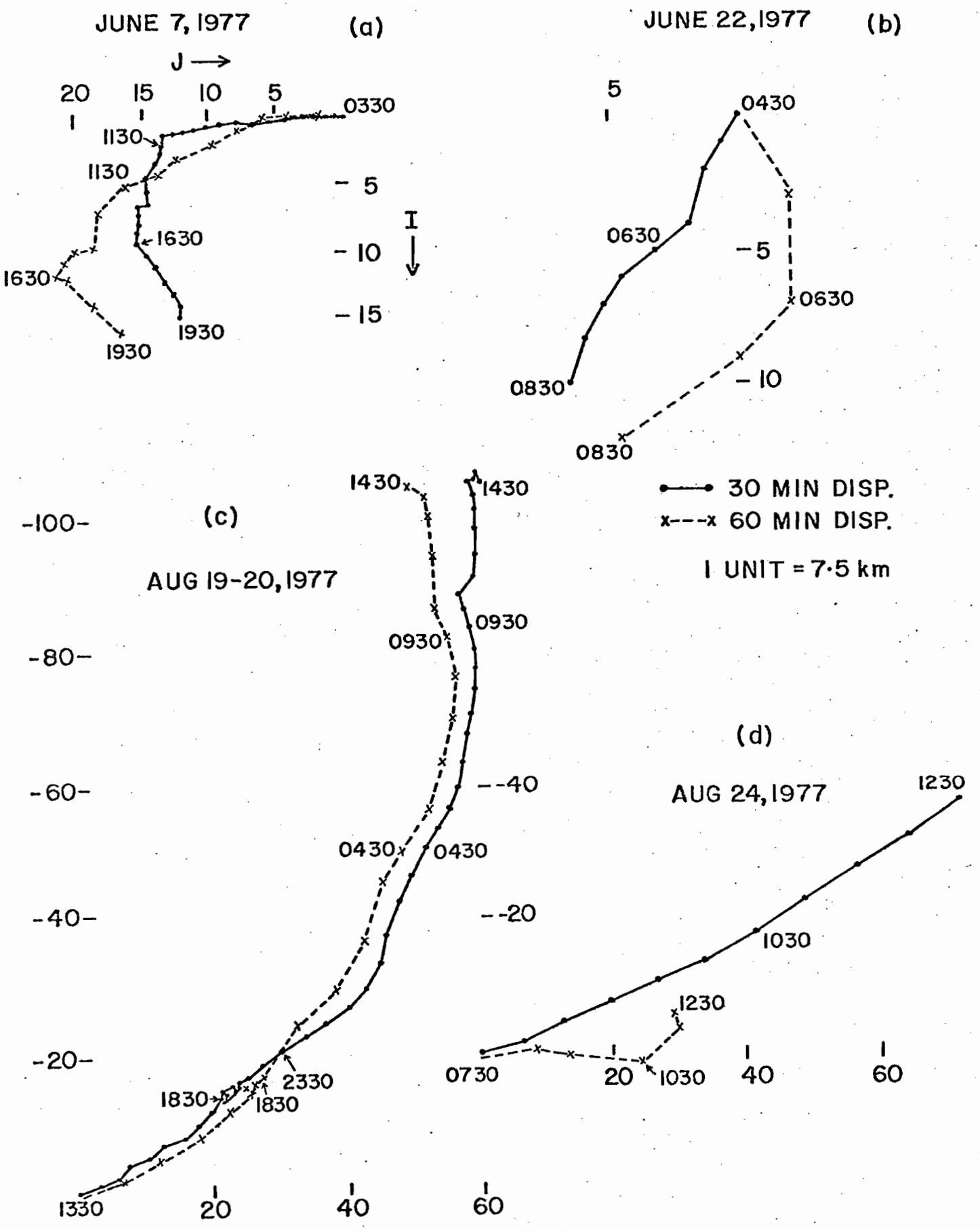

Fig. 5.9. Trajectories of light summer precipitation derived using 30- and 60-minute displacements.

5.2 Effect of Time Interval on Computed Pattern Displacement

The data set described above also permitted the comparison of 30-and 60-minute displacement of pattern sequences. Since the cases analysed are relatively few, instead of providing the results in the form of statistical parameters like average percentage error, error distribution or standard deviation, the trajectory obtained from the vector summation of the interval displacement is plotted. In this form of presentation, any differences are more easily conveyed to the eye than the magnitude of some parameter, and the occurrence of significant variations are quickly identified and investigated from the corresponding digital maps. In this method of comparison, undue emphasis should not be placed on the gap between the end point of the trajectories, but rather on partial vectors comprising shorter time intervals of arbitrary segments, since an erroneous displacement in one time interval will affect the position of all subsequent trajectory points.

5.2.1 Light Summertime Precipitation

Figs. 5.9a to 5.9d exemplify the main characteristic differences associated with a shorter time interval. In (a), it is seen that the exceptionally slow moving nature of the pattern, that is, of the order of one grid length, entails quantization effects on the 30-minute trajectory, forcing it primarily into a E-W or N-S direction, instead of in a general NE direction. This effect is experienced even at the reduced grid length chosen. In order to compute displacements in fractional grid lengths, interpolation of the cross-correlation coefficients centred about γ_{max} has been performed with moderate success. The longer time interval results in displacements larger than the unit length in both cartesian directions and thus reflect more truthfully the physical motion. Note that this trajectory is typical for the passage of an east-coast low, which is accompanied by the counterclockwise shift of the

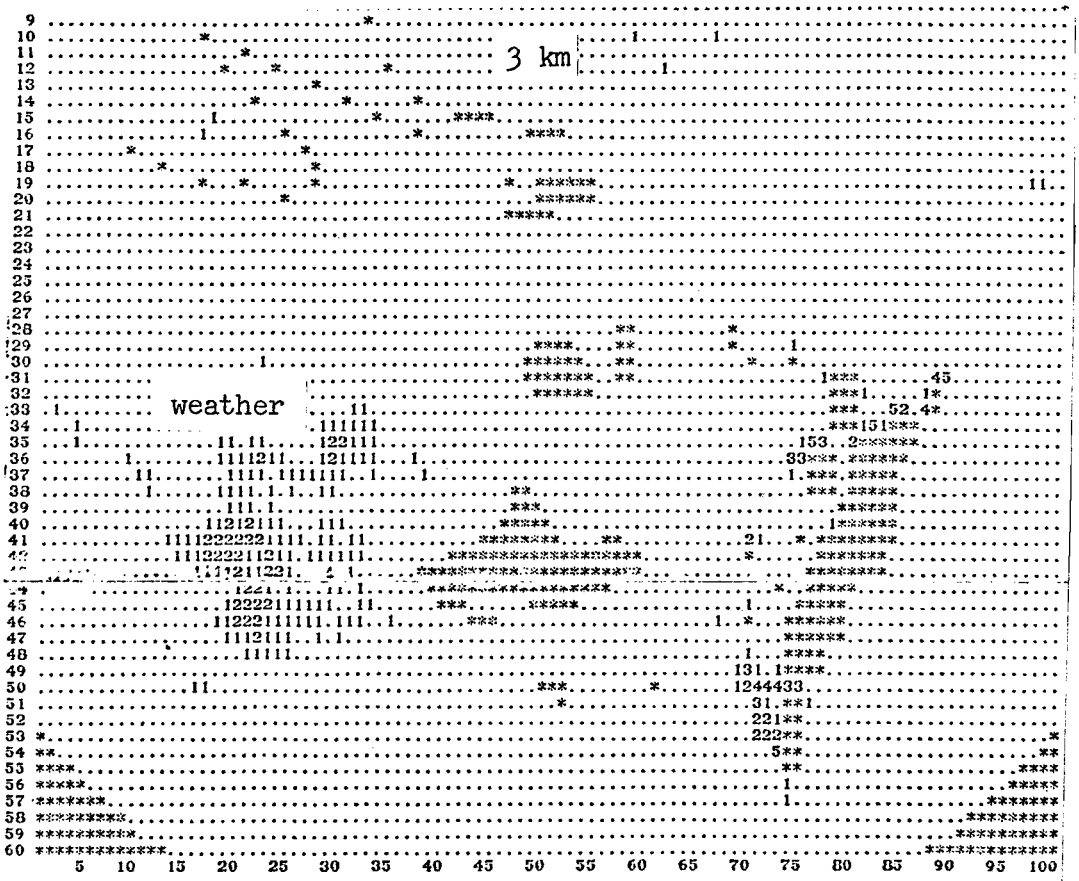

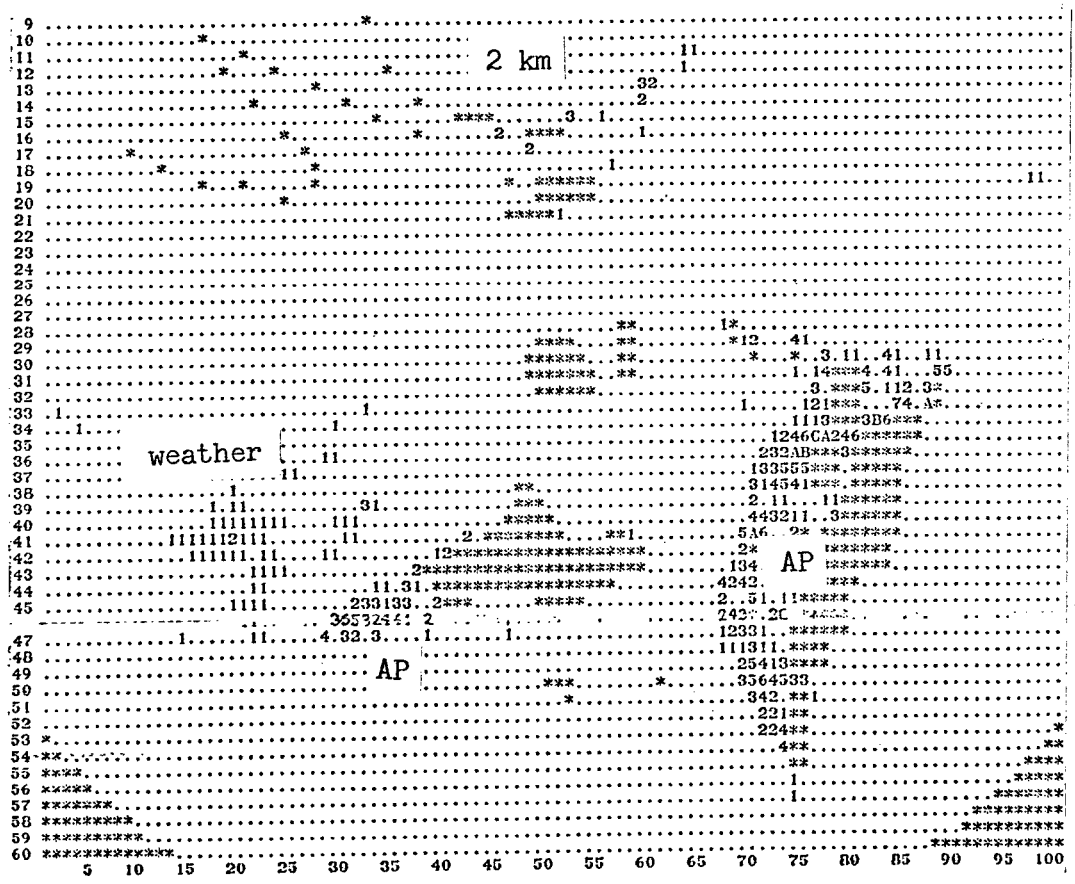

Fig. 5.10. CAPPI's at 2 and 3 km at 0030 EST 4 July 1977 depicting the extent of anoprop echoes at the lower height.

circulation around from the east, northeast, north and northwest. It is realized that the changes in direction are not as abrupt as portrayed in the computed trajectory and their linear extrapolation into a two-hour forecast entails gross directional errors. The legality of the SHARP "refusal" to issue forecasts on these occasions is readily comprehended.

Fig. 5.9b and d display a marked contrast between the 30- and 60-minute trajectories. This result is more typical of summer light weather, whether isolated and of low coverage as in (b) or extensive and widespread as in (d). The differences are readily attributed to the fact that such patterns are so ephemeral in appearance that their motion escapes the perception of a pattern recognition technique, (and at times even of the human eye) when they are set 60 minutes apart.

Fig. 5.9c, while showing good agreement between the two time intervals, confronts us with a vexing problem facing 2 km forecasts, namely, the increased probability of anomalous propagation. The correlation algorithm locks onto these strong and persistent echoes, and the motion of precipitation patterns, if present, is ignored. Since anoprop at 2 km is far more extensive and spatially variable than at 3 km, its recognition and elimination is rendered more difficult. The CAPPI's at 2 and 3 km of Figs. 5.10 clearly depict the magnitude of this problem. In all cases, it was eliminated by performing the cross-correlation algorithm at the 3 km level.

5.2.2 Convective Summer Storms

Tests performed on typical summer patterns by varying the time interval of correlation and CAPPI height revealed no significant differences except in cases of anoprop at 2 km. This result confirms the choice of a 3 km CAPPI and a 60-minute interval for the SHARP project as adequate. Ideally, it is the opinion of the writer, that the shortcomings of a 30- and 60-minute interval are such that both can be overcome by the adoption of a

45-minute interval in conjunction with a grid length used here. This conclusion was also reached by Wilk and Gray (1970) in analyzing motion forecast of echo centroids. This interval may in fact be more appropriate for a wider range of precipitation, ranging from severe to widespread, light weather patterns.

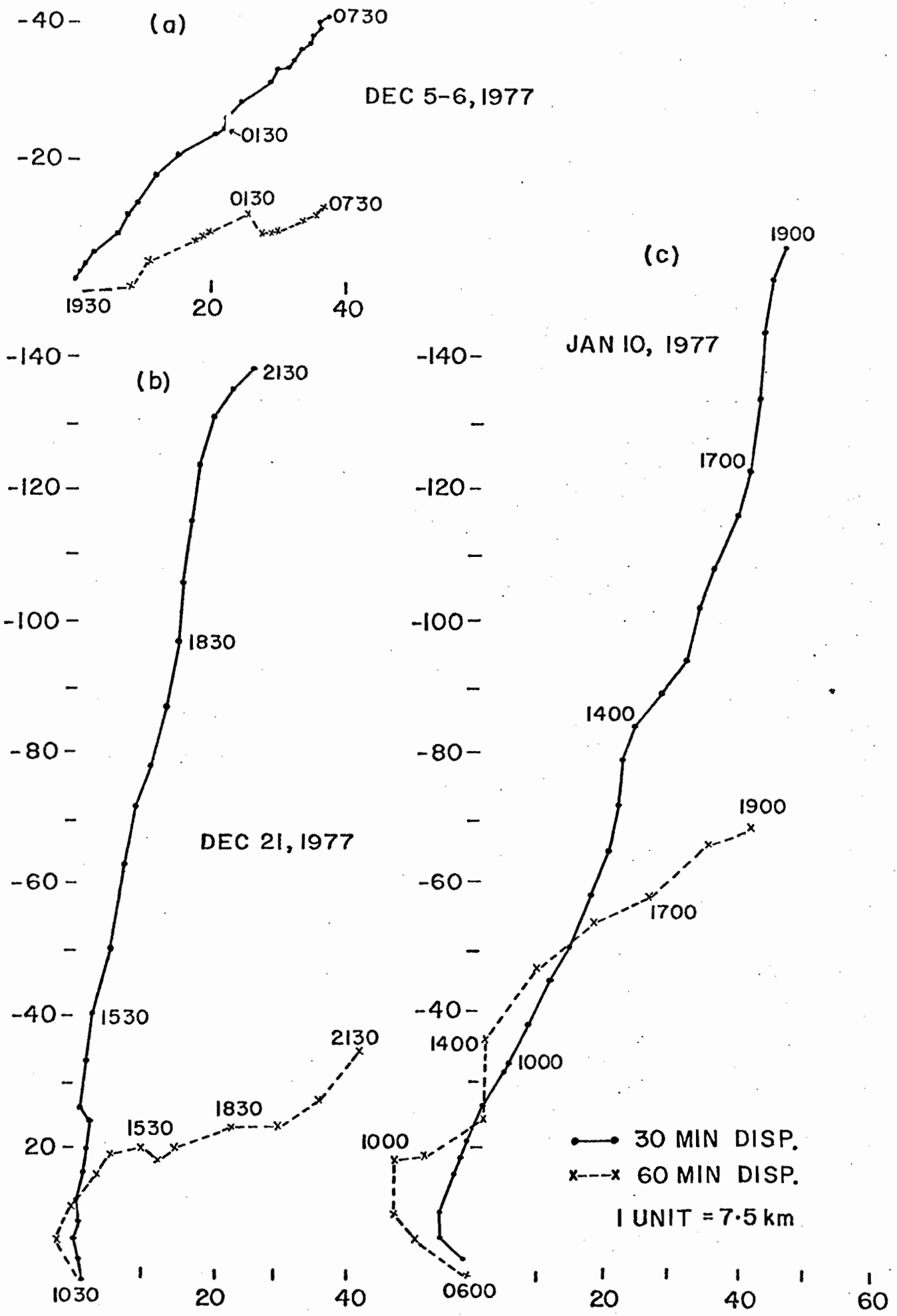

Fig. 5.11. Trajectories of snowstorm precipitation sequences derived

5.2.3 Snowstorms

As stated earlier, the computed displacement of snowstorm patterns 60 minutes apart did not correspond to reality and the real-time forecast test had to be abandoned since time allocation on our minicomputer facility to other users did not allow a shorter interval. Figs. 5.11a to c typify the remarkable gap between trajectories derived from the 30- and 60-minute displacements. A detailed analysis of the maps involved revealed that a 30-minute trajectory is a more accurate representation of the actual motion. It is seen that, in general, a 60-minute trajectory underestimates the velocity of a snowstorm system. In particular, the northward movement of the storm is well captured by the shorter time interval but barely manifests itself in the 60-minute motion. Again, the particular configuration of radar echoes of snowstorms in the form of extremely large patches of weather occupying nearly the entire radar screen, (Fig. 5.7), and characterized by a uniform distribution of intensities which are more prone to range dependent effects than rain, seriously disrupt a pattern recognition technique. Pattern speed is mainly evident by the movement of features at its outer edges. Under conditions of high velocity, they need to be examined 30 minutes apart. Unlike the approach of a rainstorm in spring or fall, which often consists of easily recognizable edges, the onset of a snowstorm is usually preceded by a light snowfall area whose motion at far ranges is difficult to assess. This difficulty stems from its low height, the shadowing effect of mountains in the south and southeast, and finally, to the radar limitation mentioned earlier, whereby the lower reflectivities can be recorded only at closer ranges. Under these conditions, the appearance of the approaching snowstorm often takes the shape of a "crescent" with no apparent motion. Only when the heavier snowfall rates begin to be detectable is any reliable motion computed. Fortunately, the

latter is the significant parameter one would want to forecast. Hence, the trajectories provided do not include non-physical displacements in the early stages of a storm appearance.

5.2.4 Extensive Fall Precipitation

In two of the three sequences analyzed, the differences between the 30- and 60-minute trajectories were relatively minor. Contrary to expectations, the other case consisting of nearly 100% coverage, seems to be better represented by the longer time interval. However, it is realized that an erroneous estimation of velocity represents a serious setback upon extrapolation only when the forecast element is of relatively small scale. In cases of extensive echo coverage, similar to Fig. 5.8b, where the reflectivity intensity is nearly isotropic, it can be maintained that the actual displacement is of little consequence on the predicted intensities for many stations on the map.

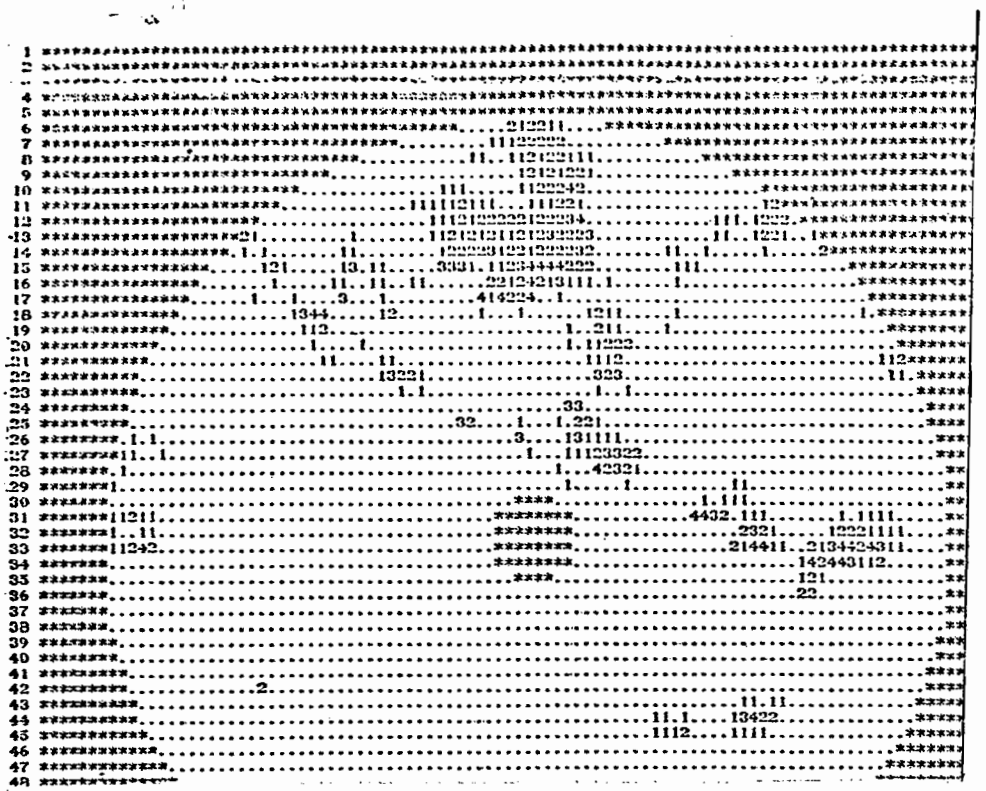

Fig. 6.1. Precipitation pattern corresponding to F(T - ΔT) in the development and dissipation program.

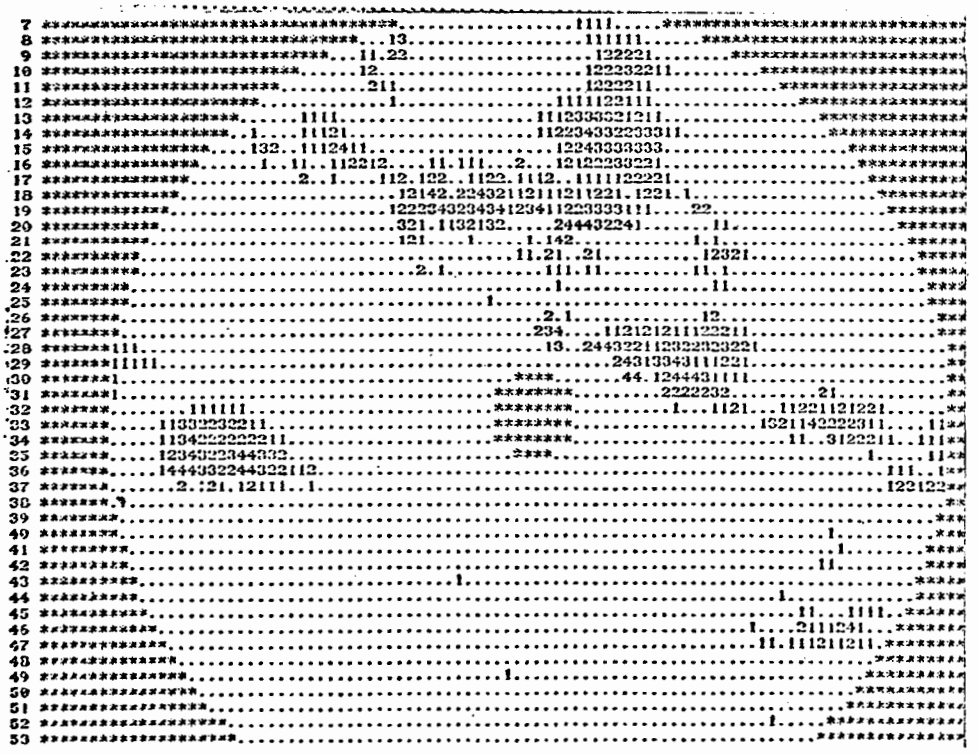

Fig. 6.2. Precipitation pattern corresponding to F(T) in the development and dissipation program.

CHAPTER VI

REFINEMENTS TO THE BASIC TECHNIQUE

6.1. Development and dissipation

6.1.1 Description

In the real time operation of SHARP, the simple method of "nowcasting", that is, of extrapolating the present radar echo pattern F(I,J,T) unaltered in shape and structure to its predicted displacement has been adopted. Thus, the intensity distribution of the forecast map $F_F(I',J',T')$ is identical to that of F(I,J,T) but displaced by the forecasted lag (ID,JD) so that

$$I' = I+ID \qquad J' = J+JD \qquad T' = T+\Delta T \qquad \Delta T = 60 \text{ min.}$$

It is recognized that this steady state approach does not reflect the true "state of affairs" in the atmosphere since intensification and dissipation of radar echoes is normal occurrence. However, it was felt, that even if one particular tendency was observed during the cross-correlation interval $(T - \Delta T,T)$, persistence of that tendency would not necessarily continue until $(T + \Delta T)$, and any tampering with the observed data will only lead to marginal success at the cost of contaminating the original data. Preliminary work on relatively few cases using manually digitized data, confirmed the above suspicion. However, there is a need to further substantiate these results using a statistically large data sample.

A program has been written capable of identifying the intensity and areal changes which have been experienced during the time interval $(T - \Delta T,T)$ of a radar pattern, and of projecting these changes into the future by operating equivalent modifications on F(I,J,T) to derive the modified $F_{mod}(I',J',T')$. After determining the lag displacement (ID,JD) between $F(T - \Delta T)$ and F(T), a (3 x 5) sub-array, - or $(22.5 \times 24)_{km}^2$ area -centred on each F(I,J,T) element is compared with the corresponding neighbourhood of the pattern $F(I-ID, J-JD, T-\Delta T)$. The comparison domain has been chosen large enough so as to eliminate high resolution fluctuations. With an areal

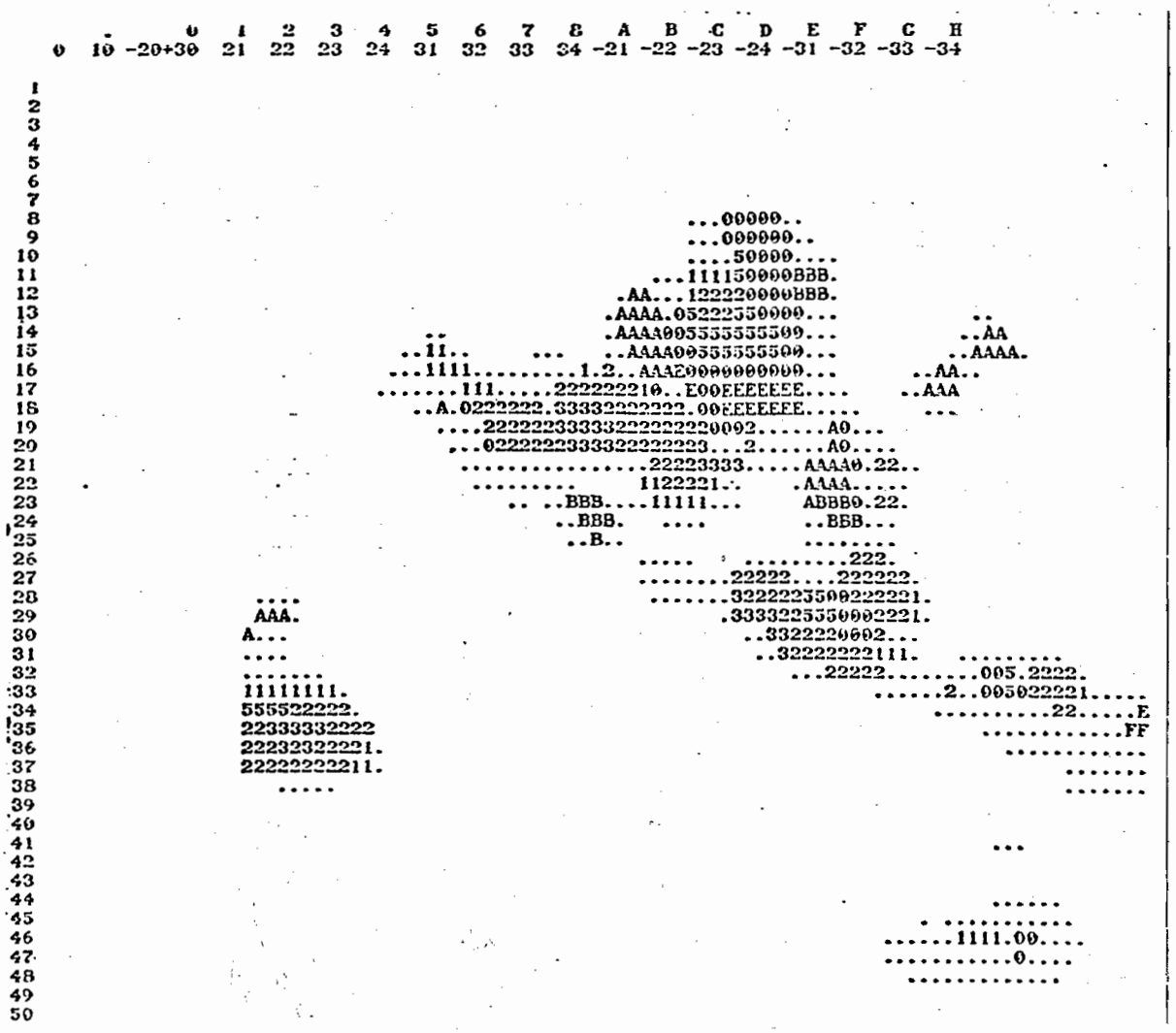

Fig. 6.3. Tendency matrix between F(T - ΔT) and F(T) of Figs. 6.1 and 6.2.

The correspondence of the alphanumerics with the numerical classification of pattern trends of Table 6.1 is shown below

blank	0	A	-21
·	10	B	-22
0	-20 or +30	C	-23
1	21	D	-24
2	22	E	-31
3	23	F	-32
4	24	G	-33
5	31	H	-34
6	32		
7	33		
8	34		

resolution of 36 km^2, it seems unwise to assume the continuation of an observed trend down to this small scale for a period of one hour. A significant proportion of the grid by grid differences is statistically random, due to the fine structure gradient of a storm. Thus the future evolution of the pattern will not be related to these differences. For a similar reason, prior to the comparison, the intensity resolution of the data has been degraded to five levels, i.e., 0 to 4.

On the "tendency" map, Fig. 6.3, the outcome of each comparison is represented by an alphanumeric symbol denoting a signed two digit number, the first digit indicating a particular trend category, the second expressing the magnitude of that trend (Table 6.1).

In the table below, x is a function of (F_2-F_1), where $F_2 \equiv F(T)$ and $F_1 \equiv F(T-\Delta T)$, and is calculated so as to reflect the magnitude of the trend in a scale of Ø to 4. Each category requires a minimum number of occurrences

Category	Definition	Two digit code	Number of occurrences	$F(T-\Delta T)$ or F_1	$F(T)$ or F_2	Selection criteria
Ø	insufficient data	ØØ	NØØ	-	-	NØØ>Ø.6(N)
3a	intensity increase	+3x	NPP	+ive	+ive ($F_2>F_1$)	NPP>Ø.5(N)
3b	intensity decrease	-3x		+ive	+ive ($F_2<F_1$)	
2a	areal growth	+2x	NØP	Ø	+ive	NØP>Ø.5(N) and NØP>2NPØ
2b	areal decay	-2x	NPØ	+ive	Ø	NPØ>Ø.5(N) and NPØ>1.5NØP
			Ttl=N$\leq$15			
1	indeterminate	10: used when none of the above is satisfied.				

Table 6.1: Numerical classification of pattern trends.

in order to characterize a given grid point. Selection of categories is performed in the order they appear in Table 6.1. Thus, if more than 60% of the points surrounding any (I,J) grid of F(T) involve zero matching, the "tendency" matrix at (I,J) is set to zero, i.e., TD(I,J) = ∅. If at least 50% of the pairs in the corresponding (I,J) neighborhood show matching of two positive values, then TD(I,J) = ± 3x. Hence, +31 implies an intensification of one unit of intensity and -32 means that a decrease of "2" has pervaded in the neighborhood of a particular grid point. Similarly, if 50% of the pairs are such that F(T)>∅ and F(T - ΔT) = ∅, a certain growth in the form of areal expansion has been located and is indicated by TD(I,J) = +2x. Thus, TD(I,J) = +23 denotes that F(T) has increased its area at that point by virtue of the appearance of an average intensity value of "3". If TD(I,J)= -21, the trend is one of decay, i.e., on the average, the intensity level "1" is disappearing. If none of the minimum number of occurrences defining a category is satisfied, a fourth category, TD(I,J) = 10, is used to indicate an undefined tendency which will involve no eventual modifications. This situation is predominant around the perimeter of a rain pattern, or characterizes the perishable, unforecastable information of small scale echoes.

When the "tendency" map has been obtained, it serves as input to the program to bring about appropriate modifications to F(T) according to the interpretation of TD as summarized in Table 6.2.

F(T)	TD 31	32	33	34
0	1	2	3	3
1	2	3	3	4
2	3	3	4	4
3	3	4	4	4
4	4	4	4	4

F(T)	TD -31	-32	-33	-34
0	0	0	0	0
1	1	0	0	0
2	1	1	0	0
3	2	1	1	0
4	3	2	1	1

Table 6.2: Intensity values assigned to F_{mod} as a function of F(T) and TD for category 3.

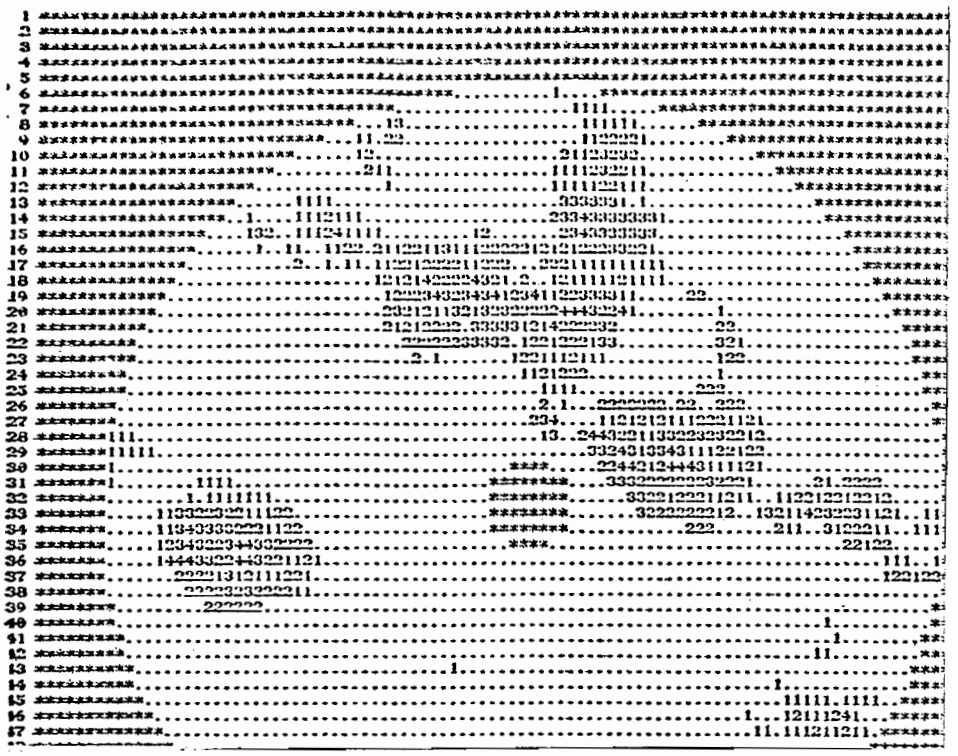

Fig. 6.4. Precipitation pattern corresponding to $F_{mod}(T)$

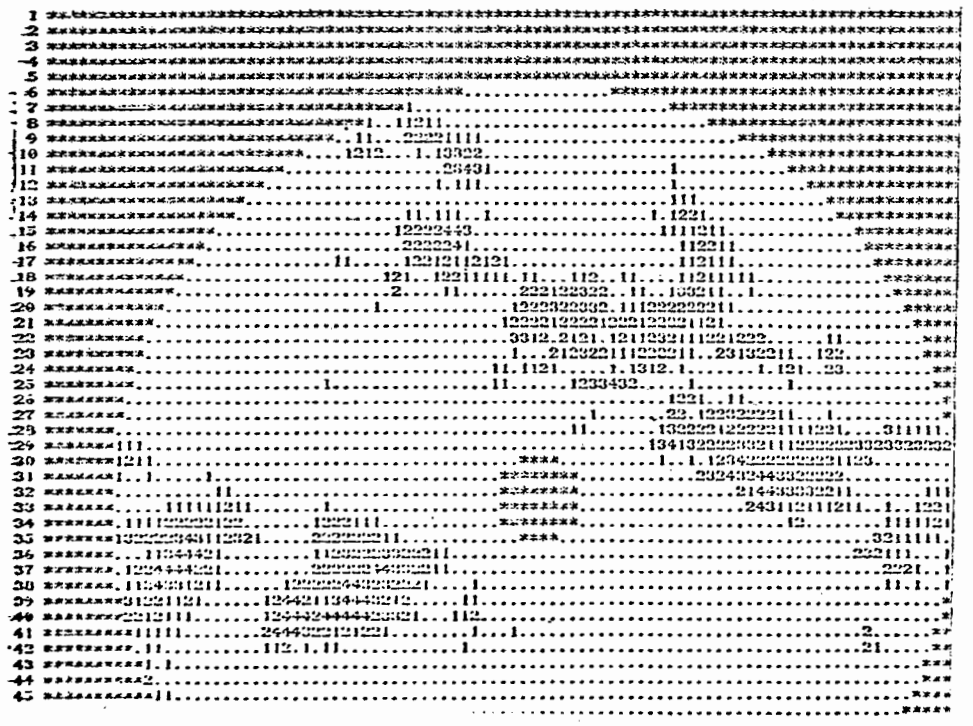

Fig. 6.5. Actual precipitation pattern $F(T + \Delta T)$ at verifying time.

No action is taken on F(T) if the magnitude of the tendency code is zero, since it defines a very weak trend. From Table 6.2, if F(T) = 2 and TD = +31, F(T) becomes $F_{mod}(T) = 3$. Similarly, if TD = -31, $F_{mod} = 1$. Care is taken that no intensity becomes negative or greater than the upper threshold of 4. Whenever category "2" is encountered, the modifications are performed as follows. If TD(I,J) = -2x, a subroutine searches in the immediate neighbourhood of (I,J) for a grid point of value x and replaces it by a $\emptyset$, thus duplicating the observed change by reducing the remaining echo area. Similarly, if TD(I,J) = +2x, a routine substitutes an intensity x for a zero in the (I,J) neighbourhood. The order of the search is performed in a cyclical manner of ever increasing distance from the (I,J) grid until the restricted neighbourhood represented by a (5 x 5) array is explored. If the search fails to come up with the desired intensity level, one or two additional attempts are performed with a different intensity, but keeping the eventual change in proportion to the first try. In order to avoid multiple modifications to take place at the expense of a single element, a special check ensures that any element of F(T) is altered only once. Not all searches are successful, in which case the grid point is left untouched. This effect is desirable since it is the equivalent of a smoother, dampening in the forecast the observed changes which took place between $F(T - \Delta T)$ and F(T). Note that since a search for a zero to replace it by a positive intensity, (category 2a), has a higher probability of success than its counterpart, partial removal of this bias is accomplished by increasing the selection criteria for category 2a with respect to those of 2b as noted in Table 6.1.

The resultant modified pattern denoted by $F_{mod}(I,J,T)$, (see Fig. 6.4) is then translated by its forecast lag to become the predicted map $F_{mod}(I',J',T')$. It is then cross-correlated with the actual precipitation configuration $F(I,J,T+\Delta T)$, (see Fig. 6.5), yielding a maximum cross-correlation coefficient

which will be denoted by γ_{mod}. Other parameters like CSI_{mod}, FAR_{mod}, and POD_{mod} are also derived from the "HITS" matrix of each comparison. The magnitude of each of the four parameters is compared with the one obtained from the correlation of the unchanged $F(I',J',T')$ with $F(I,J,T + \Delta T)$. They are symbolized by γ_{sq}, CSI_{sq}, FAR_{sq}, and POD_{sq}. The larger will dictate which of the forecast distribution bears a closer resemblance to the actual pattern and hence determines the more advantageous approach.

6.1.2 Results

The above technique has been applied to all one-hour verifiable forecasts of 1976 and 1977 summers. Their number totalled 753. The truth tables for both the "status quo" and storm development program are given in Table 6.3.

(a) SQ

$\gamma = 0.560$

FORECAST \ OBSERVED	0	1	2	3	4
0	1744216	87699	22757	6462	2108
1	82990	62403	22234	3868	957
2	19694	24551	22794	5652	1527
3	3624	4720	6730	3246	1250
4	1055	1124	2148	1474	1000

(b) MOD

$\gamma = 0.569$

FORECAST \ OBSERVED	0	1	2	3	4
0	1739443	82821	20658	4825	1795
1	85201	65125	23355	4048	1020
2	21862	23777	20522	5218	1492
3	5005	7604	9912	4112	1522
4	1185	1276	2278	1558	1006

	CSI		FAR		POD	
LEVEL	MOD	SQ	MOD	SQ	MOD	SQ
1	44	42	61	61	61	58
2	29	29	44	46	46	44
3	15	15	23	26	31	26
4	8	8	14	15	15	15

Table 6.3. Truth tables of the forecast and observed patterns derived using (a) the "status quo" and (b) the storm development program.

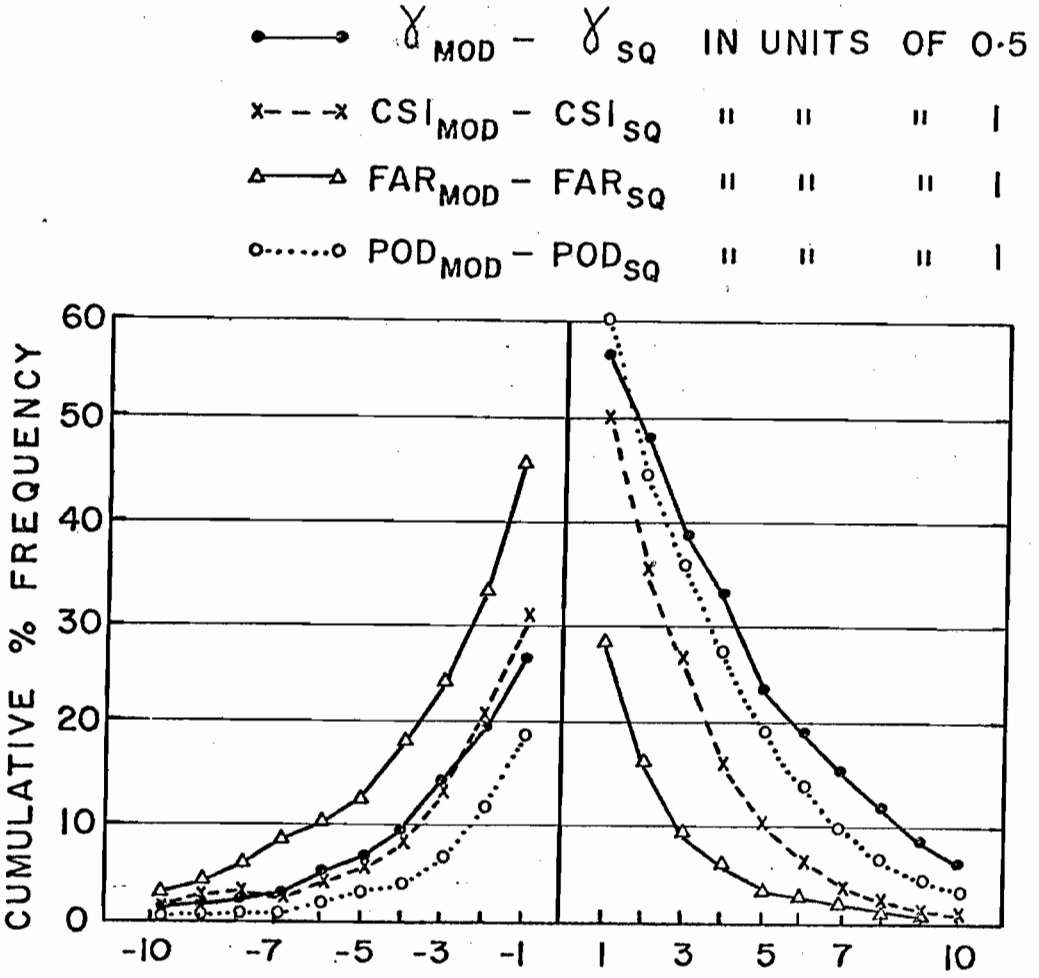

χ	$\chi \leq -1$	$-1 < \chi < 1$	$\chi \geq 1$
$\gamma_{MOD} - \gamma_{SQ}$	19·5	32·3	48·2
$CSI_{MOD} - CSI_{SQ}$	30·7	18·7	50·6
$FAR_{MOD} - FAR_{SQ}$	46·7	24·8	28·5
$POD_{MOD} - POD_{SQ}$	19·0	20·6	60·4

Fig. 6.6. Cumulative frequency distribution of the algebraic difference of parameters derived from the "status quo" and storm development program.

As can be more clearly realized from the parameters from each contingency table, the differences, if any, are minor. In general, the number of misses is slightly reduced at the expense of an increase in the number of false alarms. The probability of detection POD and the false alarm ratio FAR behave accordingly. The only significant difference occurs at the intensity level 3. The cross-correlation coefficient, derived from each table in the fashion of section 2.2, which may be considered as a summary of the overall experiment, limits the improvement to less than 2%. Considering that it is based on a large data sample, this value can be statistically valid but its magnitude may not justify the use of the technique on a routine basis. It is conceivable that an adjustment of the parameters defining the observed trend during the past history of a pattern as well as the varying of the procedure for applying the observed trend in the form of pattern changes may lead to results other than those obtained in this test. From another point of view, it may be argued that the present procedure may be utilized if the user is interested in increasing the probability of detection without concern for the false alarm ratio.

The distribution of the algebraic difference of the parameters being discussed is presented in Fig. 6.6. It reveals that in 60% of the forecasts, the probability of detection for intensity level 1 resulted in an improvement of at least 1, i.e., for i = 1, $(POD_{mod} - POD_{sq}) \geq 1$. In only 20% of the cases was the above value negative. $(CSI_{mod} - CSI_{sq})$ exceeded 5 units 10% of the time while the probability of $(CSI_{mod} - CSI_{sq}) \leq -5$ was 5%. Similarly, the false alarm ratio was improved by 5 or more units only 3.5% of the times while the chance of the opposite effect reached the 12% probability level. In nearly all cases, the differences are restricted to less than 10 units, a small interval if we consider that the parameters are expressed on a scale of 0 to 100.

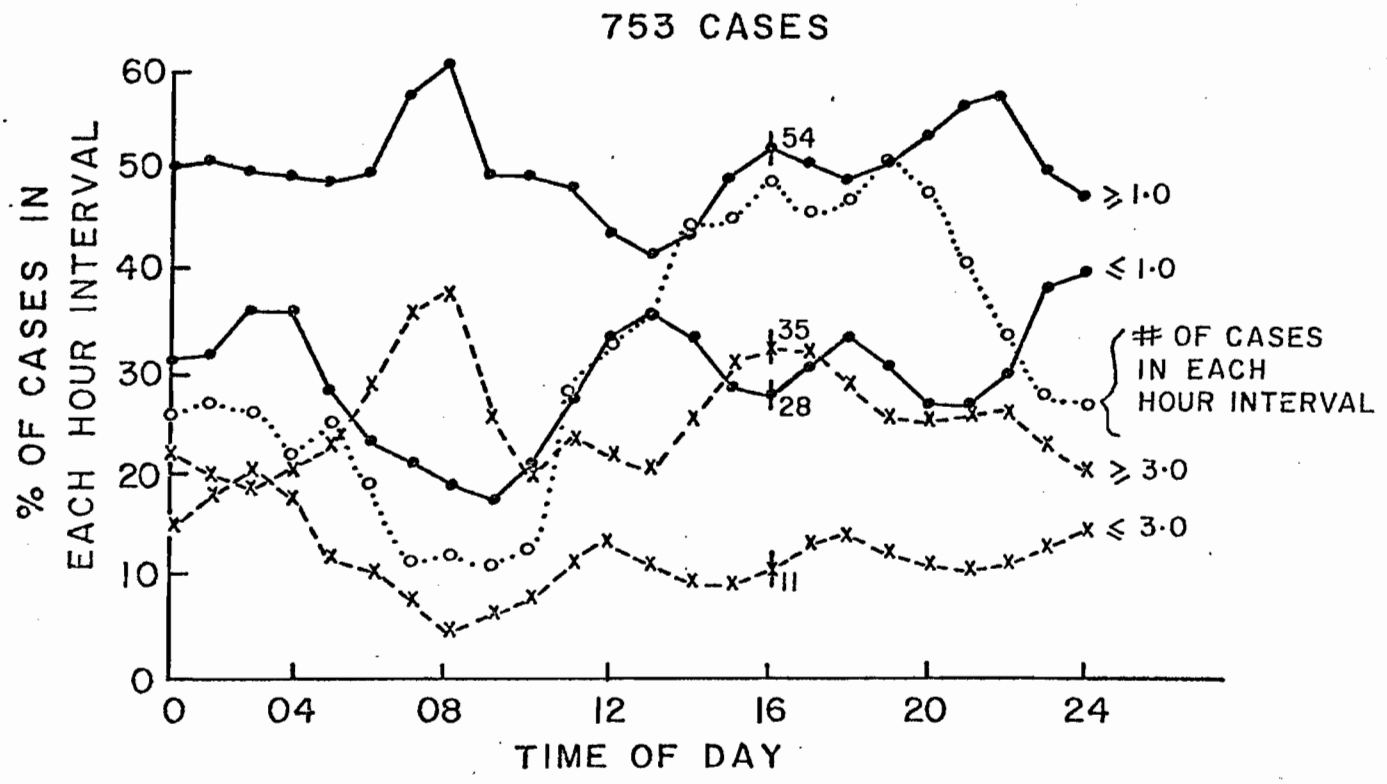

Fig. 6.7. Diurnal trend of differences of CSI scores from the two techniques.

An attempt has been made to subdivide the results in a form suitable for discerning any diurnal trends. Fig. 6.7 provides a representative outcome of this analysis for CSI. These curves should be interpreted as follows. In 54% of the forecasts verified at 1600 EST, which totalled 50, $(CSI_{mod}-CSI_{sq}) \geq 1$. This expression was negative 28% of the cases. A positive and negative difference of 3 units was experienced 35% and 11% of the times respectively. It is observed that the widest difference, i.e., improvement, occurs during the early morning hours (0500 - 0900) and in late afternoon and evening (1500 - 2200). The first interval is probably associated with persistence of a dissipation trend while a proper extrapolation of a well established growing weather system may account for the relative success during late afternoon. The minimum around noon could be explained by the difficulty in determining the early stages of echoes development when they undergo unpredictable restructurization as mid-morning solar heating becomes sufficiently strong to initialize a reversal of the nocturnal trend.

An examination of the temporal distribution of the verification results in each weather sequence revealed that the long lasting weather systems display a better improvement in forecast quality. It has also been observed that the storm modification technique yields better or worse forecasts in succession, that is, there is a temporal continuity in the sign of any parameter $(P_{mod} - P_{sq})$. Thus, if the technique described here yielded better results for the past few hours, the probability of success during the next forecast is enhanced.

6.2 Determination of Differential Motion.

6.2.1 Description

The idea of determining the differential motion of echoes within sub-areas of a map has been approached in terms of its application toward the improvement of point forecasts. Hence, local predictions would be based on the motion of

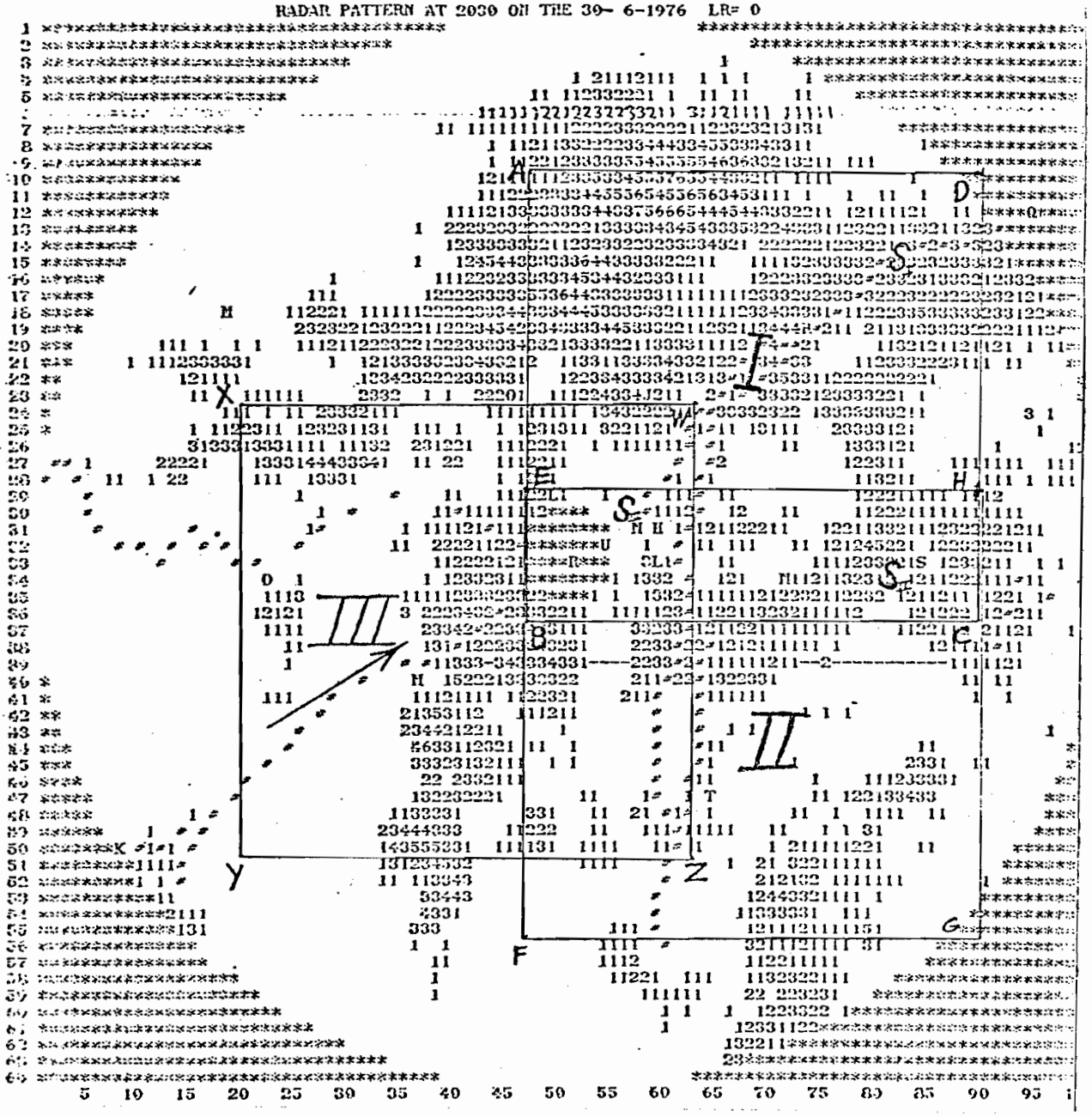

Fig. 6.8. Size and location of the three subareas used in the differential motion program.

rain patterns approaching a given station rather than on the motion of the overall pattern over the entire map. No attempt has been made to isolate, track and forecast individual echo patches on account of the complexity of such a program and of the lack of forecastability of the smaller echoes. Moreover, unlike the situation in continental North America, the occurrence of scattered, isolated air mass storms, for which such a technique would be most applicable, is the exception rather than the rule in the Montreal area.

As shown in Fig. 6.8, the (64 x 100) digital map has been arbitrarily subdivided into three smaller arrays, their dimensions being (27 x 43) units or (203 x 206) km^2 in area. Assuming a SW motion as indicated by the arrow, a station "S" would be located near the NW corner. Initially, the entire map was partitioned into five (21 x 33) sub-areas, but preliminary results immediately revealed the need to enlarge them in order to be capable of a better determination of storm movement.

The procedure consists of first scanning each of the three sub-areas for sufficient data to warrant the necessity of a forecast. It so, the displacement of echoes over the entire radar map is computed and used as a first guess for the displacement in each of the sub-areas. On account of the smaller scale of the sub-areas, it is desirable to compute 30-, as well as 60-minute displacements. Thus the program has been tested only on part of '76 data consisting of approximately 330 hours of the longer sequences of weather originally used for an hydrological study and hence available at 5 minute intervals.

After obtaining the motion vectors for each area, the discrepancy between the individual vector displacements and the overall motion has been computed. The degree of linearity of motions within each sub-area has also been determined in order to assess its persistence and role as a useful predictor.

	30 min.					60 min.				
	Default			Restricted		Default			Restricted	
sub-area	no. of cases	E'	E	no. of cases	E	no. of cases	E'	E	no. of cases	E
I	531	20.5	33.0	351	31.7	260	26.4	32.5	162	29.5
II	515	26.9	39.1	355	32.5	254	31.4	36.4	148	30.7
III	584	21.1	33.2	398	27.4	279	25.9	31.1	180	28.4
average		22.8	35.1		30.5		27.9	33.3		29.5

Default: $\gamma > 0.1$
Restricted: $\gamma > 0.3$

Area > 10 units (~0.86%)
50 units < area < 400 units or
4.3% < area < 34.4%, NBD < 40

Table 6.4. Deviations of the computed echo displacements inside the three subareas of dimensions (27 x 43) from the motion of the entire echo system within 200 km radius inside the (64 x 100) matrix. E and E' are defined as in Fig. 4.6.

	30 min. forecasts from 30 min. history					60 min. forecasts from 60 min. history					60 min. forecasts from 30 min. history				
	Default			Restricted		Default			Restricted		Default			Restricted	
Area	# of cases	E'	E	# of cases	E	# of cases	E'	E	# of cases	E	# of cases	E'	E	# of cases	E
all	615	6.3	20.0			288	20.6	27.1			585	16.3	21.6		
I	490	17.8	30.5	296	29.6	223	38.0	42.5	120	40.9	459	27.3	31.6	245	31.5
II	470	27.6	39.7	312	36.9	215	40.2	44.9	115	40.8	435	35.5	39.7	270	36.6
III	542	23.1	35.5	341	32.1	242	33.8	38.7	138	34.3	509	31.9	36.5	287	27.9
Average of I, II, III:		22.8	35.2		32.9		37.3	42.0		38.7		31.6	35.9		32.0

Table 6.5. Differences between predicted and actual displacement vectors for echoes in each subarea and for the overall pattern. The "default" and "restricted" conditions are as defined on Table 6.4.

6.2.2 Results

Table 6.4 provides statistics about the scatter of the individual velocities about that of the overall displacement. The main parameters characterizing each computation are the magnitude of the cross-correlation coefficient γ, area A of echoes in grid areas and the number NBD of echo elements touching the boundaries. If all cases, irrespective of the value of the above parameters, are included in the comparison, the average error E, as defined in Fig. 4.6, is 35 and 33% for 30- and 60-minute displacements respectively. These differences are large but, as shown by E', are partly due to quantization effects from the relatively large grid area of the data set. However, in some of the cases examined, it has been observed that the pattern recognition algorithm was not able to compute the proper motion when the sub-areas involved were of extensive coverage. We have dealt with this problem in Chapter V in conjunction with snowstorms or rainstorms in the fall. However, because of the reduced dimensions of the areal subdivisions, a similar effect often occurs in summer. When the maximum echo coverage is limited to about 35%, and the requirements for other parameters are made more restrictive, some improvement is observed with differences being reduced to 30% of the overall motion.

Table 6.5 summarizes results derived when the computed displacement is used as a predictor for 30- and 60-minute forecasts. Note in passing that the 60-minute forecasts, from 30-minute history, yield significantly improved results than those derived from 60-minute history. This result confirms statements made in Chapter V. The average error E and E' for the overall forecasts is in conformity with results of Table 4.1, that is E = 27% and E' = 21% for 60-minute forecasts based on 60-minute history. If 30-minute predictors had been used, E = 22% and E' = 16%. However, the vector linearity of sub-areal motion fails to yield errors E of less than 35%. Some error reduction, of about 4%, is obtained under restricted conditions. It is

			30 min. forecasts			60 min. forecasts		
no. of sub-areas	area dimensions	area size (km^2)	approx. no. cases	E'	E	approx. no. cases	E'	E
5	(21x33) =	(157x158)	460	31	44	195	50	54
3	(27x43) =	(203x206)	500	23	35	227	38	42
1	200 km radius		615	6	20	288	21	27

Table 6.6. Variation of error in the predicted displacement as a function of the size of the subarea.

believed that this lack of continuity is caused by spuriously computed motions and by the failure of genuine differential motion to persist over a small area. There exists a close relationship between the success of the experiment and the size and number of sub-areas, the time between cross-correlated patterns, length of verifiable forecasts and the grid length used. Table 6.6 exemplifies the dependence of vector linearity on size of sub-areas. It is evident that the error is minimized with an increase in the size of areas. Clearly, a pattern recognition technique cannot be successfully applied to a small domain on account of fast motion of echoes in and out of boundaries and, in general, of the lack of recognizable features which can persist for successive time intervals. In addition, radar echoes are given artificial shapes by being cut out by boundaries, an effect which is not as serious when the entire map is correlated.

A grid point by grid point comparison between the actual and forecast intensity pattern, with the latter being derived by extrapolation of the overall motion and of the individual displacements, has been performed. On account of the lack of linearity of the motion within each sub-area, the results, in the form of "HITS" matrices, indicate that no benefits are to be derived when differential motion vectors are computed and subsequently used in producing a forecast. The examination of some cases supportsthe suspicion that it is detrimental to determine motion of sections of large weather patterns. They ought to be treated as an entity since an arbitrary sectioning creates spurious features which bear no relationship to motion. This effect is mainly responsible for the large difference of 30% between the overall and individual displacements reported earlier. In cases when scattered echoes are present over the map, a differential motion program is likely to yield improved forecasts if the computed velocities do indeed persist inside the respective sub-areas. However, the data set used was biased in

the sense that it contained a considerable number of large scale patterns and relatively fewer cases of widely scattered storms suitable for the success of the technique. It could also be mentioned that a verification in terms of "HITS" should be restricted to the downstream section of the sub-area near the neighbourhood of station "S", since verification at its opposite side is dependent on motion of echoes which has not been determined (Fig. 6.8).

In concluding, this experiment has shown that

i) for the grid length and time interval used, the extrapolation error of each predicted sub-areal displacement decreases as the size of the array is increased,

ii) the determination of proper motion of echoes occupying nearly the entire sub-area may be in error on account of the absence of recognizable features and of the disruptive influence of boundaries creating artificial shapes,

iii) when correctly computed, motion within sub-areas may not persist till veryifying time since it may consist of short-term accelerations of echo sub-structures which do not possess a long forecastability period,

iv) the use of a differential motion technique should be avoided when the characteristic pattern length is large. Automatic distinction between these situations and those consisting of smaller, isolated echoes can be performed by means of the decay curve of the auto-correlation coefficient,

v) since in Montreal, summer convection is often caused by the passage of large scale low pressure centres, or frontal systems, the associated rain patterns are usually of large extent, and travel in one direction. Storms of the air mass type, less frequent in Montreal, would be more apt for the differential motion technique described here. However, for the larger areas considered in the satellite experiment of Chapter VII, the adoption of a single motion vector is obviously incorrect. Hence, this procedure has been successfully applied there.

vi) verification in terms of "HITS" of all forecasts using the individual and overall vector motion revealed small differences, in favor of forecasts made using the overall vector.

vii) the data set used was biased toward heavy coverage and of a grid length larger than desirable.

CHAPTER VII

APPLICATIONS OF COMBINED RADAR AND SATELLITE DATA SETS

7.1 Rain Determination Procedure from Satellite Imagery

Unlike the techniques of other researchers which require, to a greater or lesser degree, the need of human intervention (e.g. Stout et al. (1979), and particularly, Scofield and Oliver, (1977)) and which concentrated primarily on regions of active convection, our goal is to develop a fully automated rain delineation procedure which includes all types of precipitation. The basic algorithm toward this aim has been formulated, tested and verified over radar range by Lovejoy and Austin (1979a). Their technique is particularly suitable for those latitudes in which summer rainfall is mainly influenced by a westerly circulation. In these climates, the major contribution to summer rainfall is from relatively extensive rain areas associated with frontal zones connected to low pressure systems, rather than from highly localized intense storms of the air mass variety as in the tropics. The technique has also been used successfully in the GATE area of the tropical Atlantic. The main drawback is its limitation to daylight hours.

7.1.1 Type of Data

The data used in this work consist of SMS/GOES-E images archived at 30 minute intervals by the University of Wisconsin - Madison. Photos of the visible (0.7 μm wavelength) and infrared (11.5 μm) channels are available at a resolution which corresponds to approximately (1.5 x 0.75) km^2 at 45° latitude. However, the magnetic tapes were recorded with a scale factor of 2 or 4, resulting in resolution of about (6 x 3) km^2. Infrared data are independent only at a resolution of about 8 km. The subroutines essential for the navigation of the satellite data, Smith and Phillips (1972), were also provided. These perform the transformation from satellite coordinates,

DATE	PERIOD (Z)	NO. of MAPS
1 June 1977	1730 - 2000	6
2 June 1977	1730 - 1900	4
29 June 1977	1300 - 1730	10

TABLE 7.1 Summary of the satellite data used in this work.

referred to as (line, element), into earth coordinates of latitude and longitude (ϕ,λ).

The intensity range of the recorded satellite imagery is 0-255. The infrared count, c_{IR}, is related to the temperature T of the emitting cloud by the conversion formula

$$T = 330 - \frac{1}{2} c_{IR} \qquad c_{IR} \leq 176$$

$$T = 418 - c_{IR} \qquad c_{IR} > 176$$

The height of the cloud can then be inferred from a tephigram or by assuming a standard atmosphere. The relation between visible counts, c_{VIS}, and cloud thickness is more intricate and uncertain on account of radiation geometry, Mosher (1975). The three-dimensional structure of the cloud, its composition and solar zenith angle are the main factors influencing the computed thickness. Since we require only relative magnitudes, the simple assumption of a sufficiently large, flat cloud, with a crude correction for time of day enables us to use the visible data in its recorded range.

Since successive maps are needed to compute pattern displacement, this work is based on data from only three days in June 1977 when sequences were available as summarized on Table 7.1. Corresponding radar data were obtained from the McGill Weather Radar described earlier. These were in the form of 3 km CAPPI maps extending up to a range of 200 km and digitized in levels providing the average rainfall rate over (4×4) km^2 grid areas.

a) Map Projection of Satellite Data

On account of the inflexibility of satellite display system, one is often obliged to remap other data sets, e.g. radar data, on to satellite coordinates. Since in this work, a pattern recognition technique is applied to two successive satellite pictures, it is desirable to use maps showing minimal areal and directional distortion. Moreover, since comparisons will

Photo Size Category	No. of lines /Photo	No. of elements/line	Scale Factor	Resolution at 45°lat (km^2)	Edge of Photos in (ϕ,λ)
1	490	672	2	(3 x 1.5)	(52,83) (52,67) (39,81) (39,67)
2	240	672	4	(6 x 3)	(52,92) (52,60) (39,88) (39,64)
3	490	672	4	(6 x 3)	(64,100) (64,52) (34,86) (34,64)

Table 7.2. Size of infrared and visible digital data available on tape.

Map Number	Matrix Dimensions (Row X Column)	Grid Area (km^2)	Map Size(km) N-S	Map Size(km) W-E	Coordinates of NW Corner ϕ λ	Standard Parallels ϕ_1	Standard Parallels ϕ_2
# 1	(184x132)	(8x8)	1472	1056	(52,83)	41.5	50.0
# 2	(92 x 66)	(16x16)	1472	1056	(52,83)	"	"
# 3	(187x255)	(8x8)	1496	2040	(52,91)	"	"
# 4	(94 x128)	(16x16)	1504	2048	(52,91)	"	"
# 5	(190x150)	(16x16)	3040	2400	(60,98)	38.5	55.5

Table 7.3 Characteristics of digital cartesian satellite map sizes.

be performed between the satellite-derived rain maps and synoptic charts, whether as part of a research analysis, or, in real-time by a forecaster on duty, it is convenient to produce products on equivalent map projections. This will facilitate the comparison on both the human and computer level. In mid-latitudes, a conic projection of the Earth, true at two standard parallels, has been most commonly used by meteorologists. A description of the derivation of the transformation equations from (ϕ,λ) to cartesian (x,y) appears in Appendix A.

b) Construction of Cartesian Satellite Images

Each photo on tape is only a sector of the field of view of the satellite scanners. Hence, the (line, element) pair of the first datum of each photo as well as the scale factor is required for proper navigation. As indicated on Table 7.2, the satellite pictures are of 3 size categories. On account of daily fluctuation of navigation parameters, the above photo boundaries are only approximate and subject to minor variations even between successive photos. Thus for the purpose of standardizing digital displays, the following 5 map sizes can be generated from the same computer program by simply varying the "map number" input. (See Table 7.3).

Map #2 has been primarily used during the trial runs of early development work, since it implies economy in both computer time and core (and hence in $!). Most of the analysis reported here is based on map #3, since its size and resolution is most appropriate for application to a forecasting system for eastern Canada. Also, its matrix dimensions of (187 x 255) will fit well into a TV screen. If a coarser resolution of (16 x 16) km^2 of the same area is sufficient, map #4 will satisfy the output constraints of conventional line printer or teletype margins. Map #5 comprises nearly the full coverage recorded for each photo. Finally, if only size category 1 is available (see Table 7.2), map #1 is chosen, which includes most of the populated regions of Ontario and

Quebec. However, its limited E-W extent does not provide a long lead time for weather systems approaching from the west. At any rate, if the raw satellite data are available over the desired part of the earth's surface, then additional map categories, which satisfy particular requirements of a local or operational nature, can be obtained at will by simply varying the defining parameters of Table 7.3.

It is seen from Table 7.2 that a typical digital picture consists of (490 x 672), or 329,280 (line, element) pairs. A straightforward procedure would consist of using the navigation subroutines to transform each pair into (ϕ,λ) and to subsequently apply equations 4 and 5 of Appendix A to compute the (x,y) cartesian coordinates. This method may be sketched as follows:

$$\text{(line, element)} \rightarrow \begin{array}{c}\text{navigation}\\ \text{subroutine}\end{array} \rightarrow (\phi,\lambda) \rightarrow \begin{array}{l}x = f(\phi,\lambda)\ \text{eq.(4)}\\ y = f(\phi,\lambda)\ \text{eq.(5)}\end{array} \rightarrow (I,J)$$

where I is the row and J the column number of the map array obtained by applying a scale factor to (x,y) and choosing an arbitrary origin. However, the transformation from (line, element) to (ϕ,λ) is complicated and hence time consuming. Tests on an IBM-370 computer have demonstrated that it can perform only 275 transformations per second. Considering the area of map #3, approximately 20 minutes of CPU time are required to operate on all 330,000 raw data points of each photo. This already unacceptably high computation time does not include subsequent steps necessary before obtaining a pair of digital satellite images. An alternate, more efficient procedure was essential, particularly in view of its eventual implementation in a slower mini-computer environment.

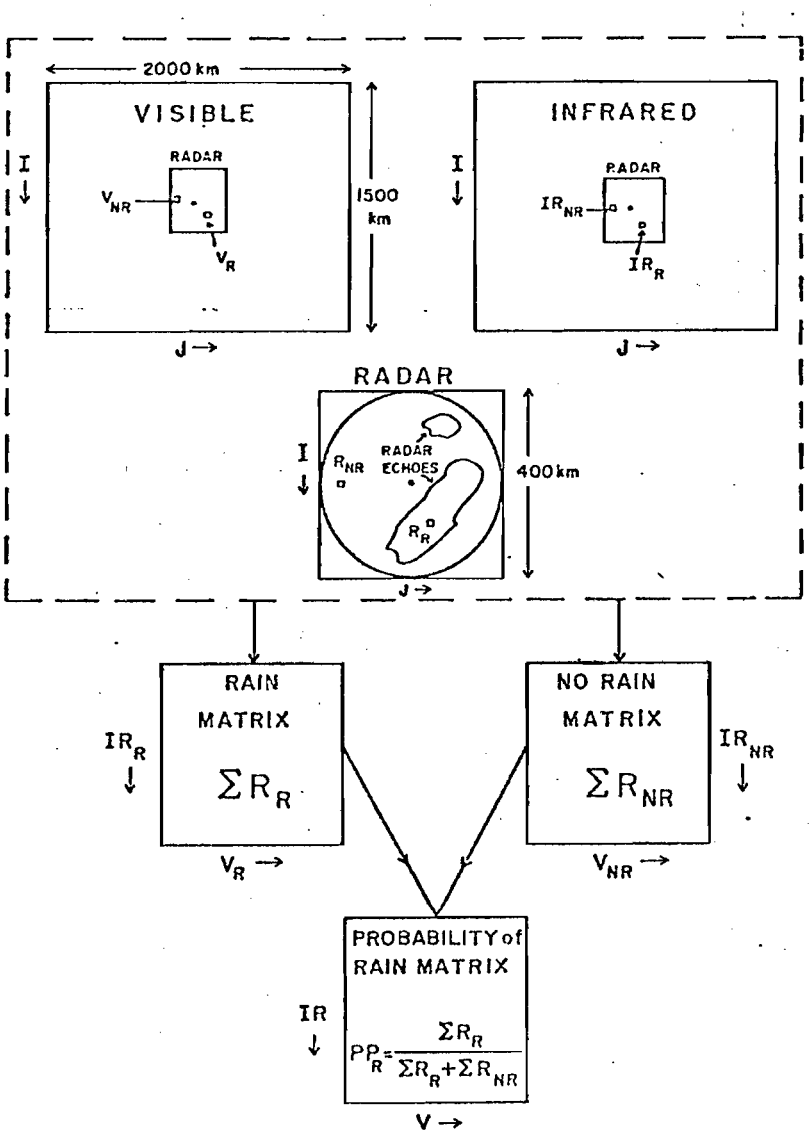

Fig. 7.1 Sketch illustrating the procedure in deriving probability of rain from satellite visible and infrared imagery colocated with radar data.

Using the relatively simple inverse relationships $\lambda = f(x,y)$ and $\phi = f(x,y)$ as given in eqs. 6 and 7 of Appendix A, a (ϕ,λ) pair is computed at every 80 km, i.e., 10 grid points. This (ϕ,λ) pair serves as input to the navigation subroutines yielding a (line, element) pair at those points. The number of calls to the complex navigation routines has thus been reduced by at least a factor of 100. Since the variation of line and element numbers within an 80 km interval is very uniform, a linear interpolation scheme is employed to compute the (line, element) pairs for each (I,J) of the map array. The entire process takes about 20 seconds for map #3 and correspondingly less for the others. The complete production of an (187 x 255) satellite image from raw data requires approximately 100 seconds of CPU time on an IBM 370. Details of the satellite-imagery program can be found in Bellon (1979). Since a printer-plotter is available at the McGill Radar site, images were transferred to magnetic tape, read by the minicomputer facility at the radar, and plotted with uniform shading as illustrated in figures of this chapter.

7.1.2 Description of Basic Satellite Rain Technique

The fundamental algorithm consists of obtaining two bivariate frequency distributions from visible and infrared images, colocated with simultaneous radar data in order to discriminate between raining and non-raining clouds. The major steps of this procedure are sketched in Fig. 7.1. The visible counts are normalized by assuming that the brightest 5% of the data correspond to infinitely thick clouds and observing the variation of this brightness level as a function of the time of day.

A visible and infrared digital picture and the corresponding radar map form the data base. The radar enables us to identify the raining R_R from the non-raining R_{NR} points. For each R_R, the corresponding datum V_R on the

Fig. 7.2. Digital GOES-East visible satellite image of Eastern Canada at 1830Z, 2 June 1977, as produced by a continuous tone printer-plotter. The darker shades designate higher visible counts.

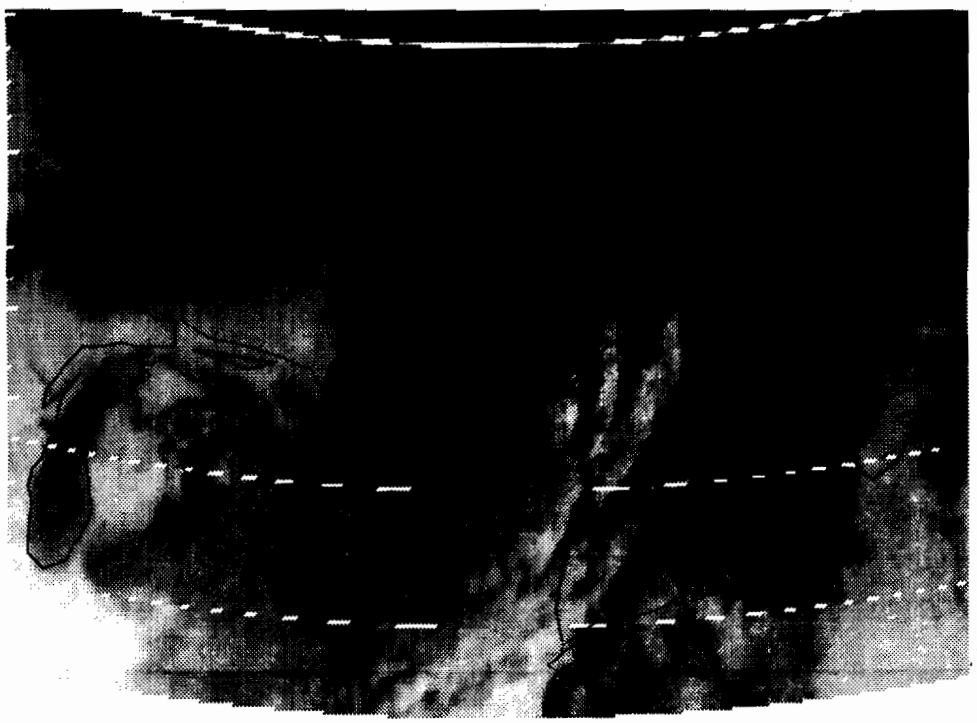

Fig. 7.3. Infrared image at 1830Z, 2 June 1977. The darker areas indicate higher IR counts, i.e., colder temperatures.

visible and IR_R on the infrared image are located. The set (IR_R, V_R) becomes the subscripts of a contingency matrix in which all the R_R points are accumulated. Similarly, the pair (IR_{NR}, V_{NR}) provides the coordinates of the "no-rain" matrix for all the radar echo-free points R_{NR}. These two arrays in infrared-visible space are then combined to yield a percentage probability of rain distribution as a function of infrared and visible values, expressed as

$$PP_R(IR,V) = 100 \times \frac{R_R(IR,V)}{R_R(IR,V) + R_{NR}(IR,V)} \qquad \text{eq. 7.1}$$

$R_R(IR,V)$ is the number of occurrences of rain with associated (IR,V) magnitudes and the denomination represent the total number of points in each (IR,V) interval. The above empirical relationship, derived from (IR,V) values within radar range is then assumed to apply over the entire domain of the satellite image to yield a "satellite rain" or P_{RS}[1], map. Thus, the underlying assumption in extracting rain information from satellite data is that clouds that are both thick, i.e., of intense visible brightness, and high, i.e., cold as inferred from the infrared counts, possess a greater probability of producing rain. This entire process is now illustrated by means of actual data.

Figs. 7.2 and 7.3 are the digital GOES visible and infrared images at 1830Z on June 2, 1977, as produced by a continuous tone printer-plotter of a minicomputer at the radar facility. The darker areas in Fig. 7.2 designate higher visible counts (thicker and/or highly reflective clouds), while those on the infrared picture indicate that the top of the emitting cloud is of high altitude. The white areas denote absence of data or locations where one or more lines of the raw data has been removed by a filter routine.

---

[1] P_{RS} : Probability of rain from satellite

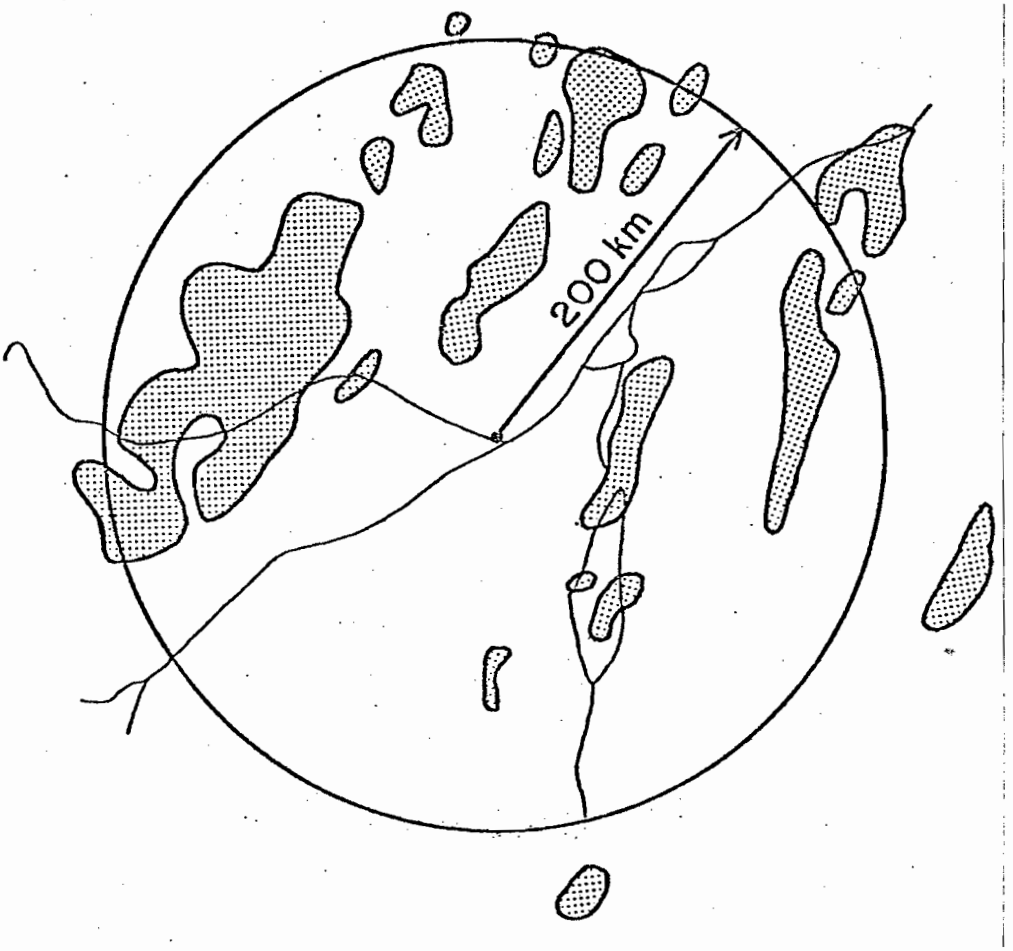

Fig. 7.4. Outline of the 0.5 mm h^{-1} contour from the digital radar rainfall map at 1830Z 2 June 1977.

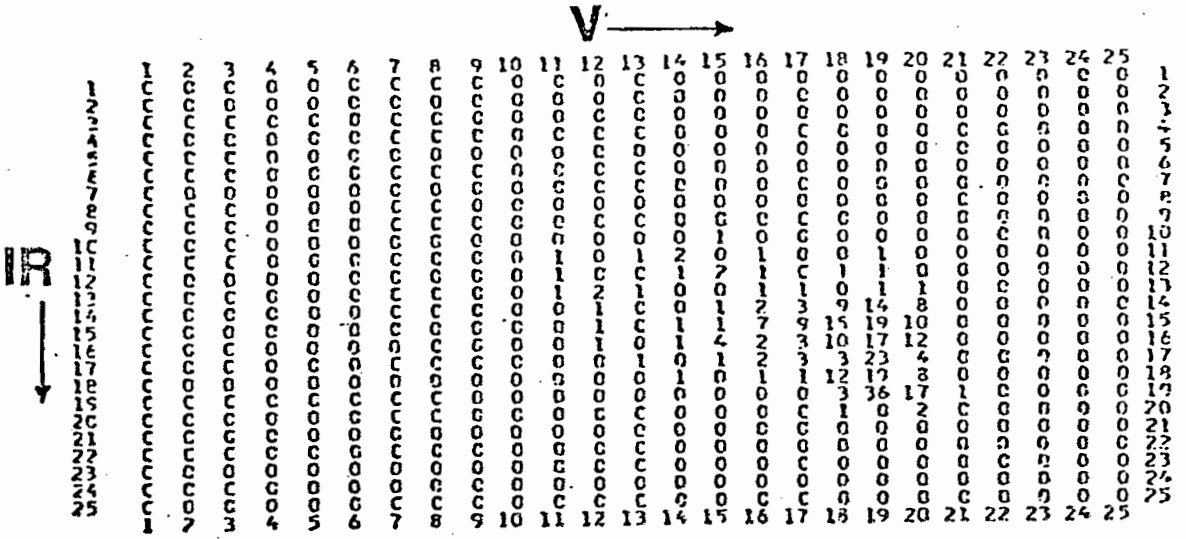

Table 7.4a. Bivariate frequency distribution in visible and infrared space of the "rain" grid areas for 2 June 1977 at 1830Z.

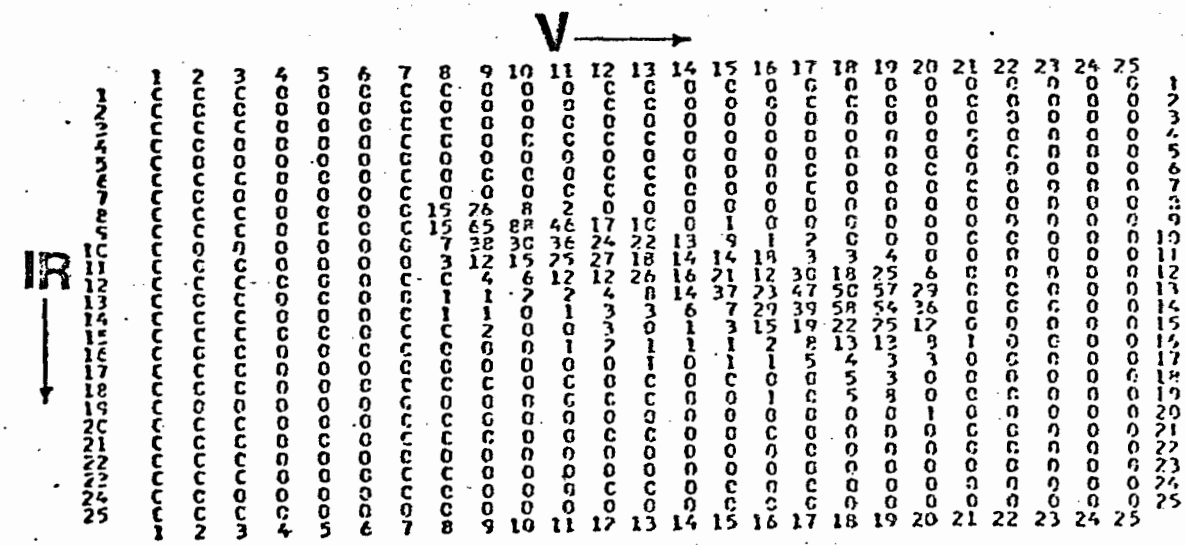

Table 7.4b. Bivariate frequency distribution in visible and infrared space of the "non-raining" grid areas for 2 June 1977 at 1830Z.

The geography consists of a dark outline if the background is light and reverses to a white line on a black background. The synoptic conditions will be discussed in a later section. The echoes observed by the McGill radar are shown in Fig. 7.4. Note that only radar information within a range of 200 km and which is not contaminated by ground clutter, mountains or shadowing effects is incorporated in the analysis - refer to section 4.3. This data set which is available in a (4 x 4) km^2 resolution is first degraded into a (50 x 50) array in a coarser (8 x 8) km^2 grid to facilitate comparison with the satellite maps. There are 4 radar data values per satellite grid area. An element of the (50 x 50) array is arbitrarily defined as rain if it contains at least 2 data values above the radar threshold of 0.5 mm h^{-1}. The frequency distribution of the raining and of the non-raining points is presented in Tables 7.4a and 7.4b respectively. Note that the visible and infrared scales have been reduced to 25 levels (i.e., 10 counts per level according to the relation level = 1 + count/10) in order that a sufficient number of (8 x 8) km^2 radar values, N(IR,V), fall inside each (IR,V) interval to justify the statistics of Table 7.4c. This table provides the percentage probability of rain $PP_R(IR,V)$. For example,

$$PP_R(17,19) = 100 \frac{R_R(17,19)}{R_R(17,19) + R_{NR}(17,19)} = 100 \frac{23}{23+3} = 88$$

means that there exists an 88% chance of rain if

$$160 \leq c_{IR} \leq 169 \quad \text{and} \quad 180 \leq c_{VIS} \leq 189$$

Similarly, $PP_R(15,16) = 100(\frac{7}{7+15}) = 32$

Note that it is impossible for N(IR,V) to be sufficiently large for all (IR,V) intervals; for example, among others, the (16,21) and (19,21) pairs yielding PP_R values of 0 and 100 respectively. Likewise, PP_R magnitudes of

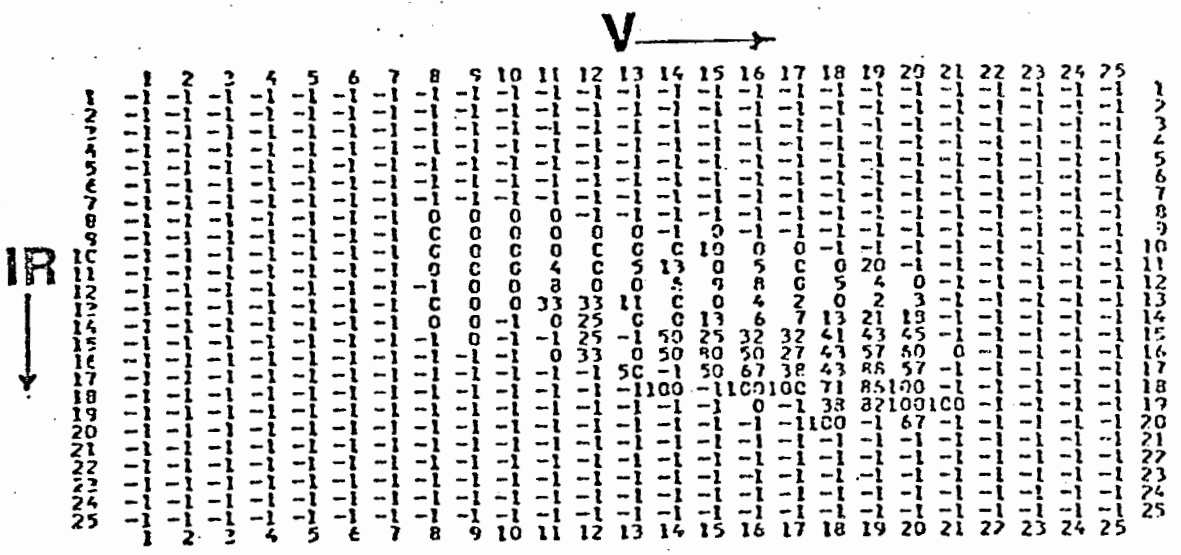

Table 7.4c. Percentage probability of rain distribution as a function of infrared and visible values. "-1" indicates no data.

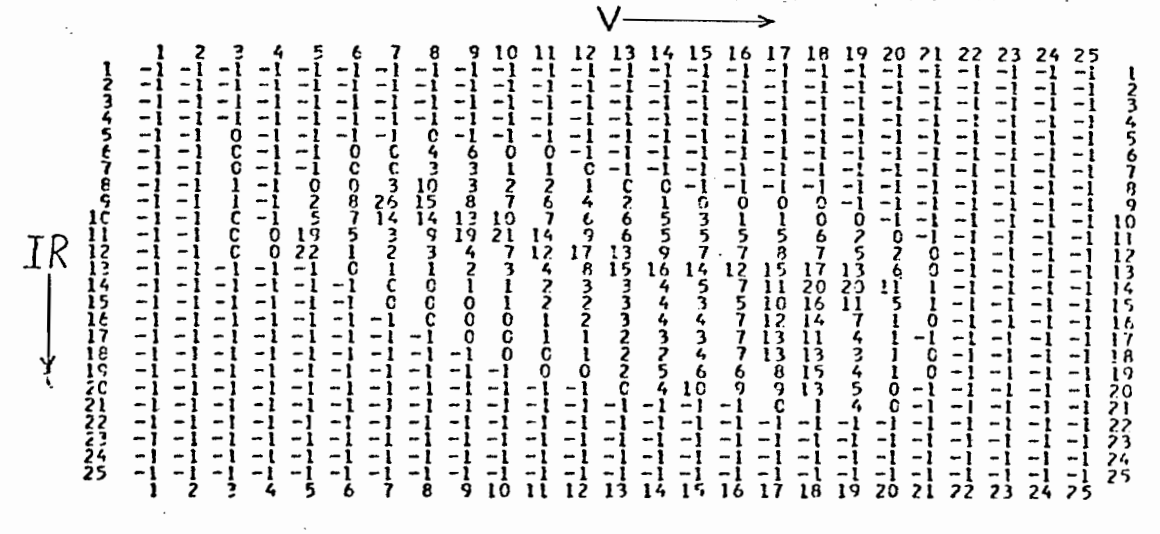

Table 7.4d. Frequency distribution in units of 0.1 % of visible-infrared pairs over the entire satellite map at 1830Z 2 June 1977. The total number of visible-infrared pairs is 45157. "-1" indicates that the particular (IR,V) pair does not occur.

50, 33 and 25, or multiples of the last two, are caused by the same reason. Moreover, as evidenced by Table 7.4d, there are certain (IR,V) combinations present over the entire satellite map which do not, or cannot, occur in the distribution which is limited to within radar range. An obvious example is the body of water in the cloud free regions of the Great Lakes and Atlantic Ocean whose IR-V distribution is approximately bounded by

$$9 \leqslant IR \leqslant 12 \quad \text{and} \quad 5 \leqslant V \leqslant 6$$

Of more significant concern to a rain determination scheme is the occurrence of very high infrared and visible values, or other potentially rain producing pairs, which are not encountered within radar range. An additional consideration is that the scatter in Table 7.4a is partly caused by a slight mismatch between radar and satellite maps, or simply by an insufficient sample, which is particularly serious at low echo coverage. Thus, after careful scrutiny of numerous $PP_R(IR,V)$ matrices, the following arbitrary criteria have been automatically implemented into the procedure.

a) $PP_R = 0$ if $PP_R(IR,V) < 10$

Removes noise in all $PP_R(IR,V)$ caused by map mismatch, statistical fluctuations or other unexplained causes.

b) $PP_R = 0$ if $IR < 13$ or $V < 16$

Eliminates spuriously high PP_R values at low (IR,V) intervals, which, as seen on Table 7.4d, may include a large number of points.

c) $PP_R = 40$ if $IR \geqslant 19$ and $V \geqslant 19$ and the (IR,V) pair does not occur within radar range. For example, referring to the (21,19) pair, 0.4%, or about 180, grid points, found over the entire satellite map are assigned a 40% probability of rain.

Neighbouring percentages in Table 7.4c would imply a higher probability. However, regions under this criterion, in addition to consisting of very tall cumulonimbus towers, may also be associated with nearby thick anvils.

Radar cross-sections of these anvils have shown that they may be active in generating hydrometeors which, however, do not necessarily reach the ground as precipitation. It is conceded that the automated procedure described in this report cannot cope with a Cb situation as adequately as the one developed by Scofield and Oliver (1977), which, with human assistance and much finer resolution in space and time, concentrates principally on areas of intense convective activity where the anvil problem is likely to occur. However, the type of precipitation around 45°N latitude, with fewer cases of isolated vigorous convection, and a larger proportion of widespread rainfall, is amenable to an automated procedure, Wylie (1979).

d) Interpolation in (IR,V) space. If IR $\geq$ 15 and V $\geq$ 19, i.e., thick but relatively low clouds occur over the satellite map but not near the radar, an interpolation over neighbouring (IR,V) pairs is performed using Tables 7.4a and 7.4b.

e) Spatial Smoothing.

After assigning a PP_R (IR,V) value over the entire satellite map on the basis of Table 7.4c and the criteria listed above, a 5-point smoother with double weight on the centre grid is applied. This step has the effect of adding spatial information, removes noise and yields easily recognizable PP_R contours. It is not desirable for precipitation scales of a few grid lengths as is the case with isolated convective storms. However, this smoother has been applied to all maps because of the good spatial correlation determined from radar studies between the observed rain at one point and the probability of its existence some distance away ($\sim$ 10 km).

It is understood that the criteria described above are subject to modification as more cases will be examined in a minicomputer environment. Numerous trial runs can then be tested with varying parameters or with refinements of the basic technique with relatively minor costs.

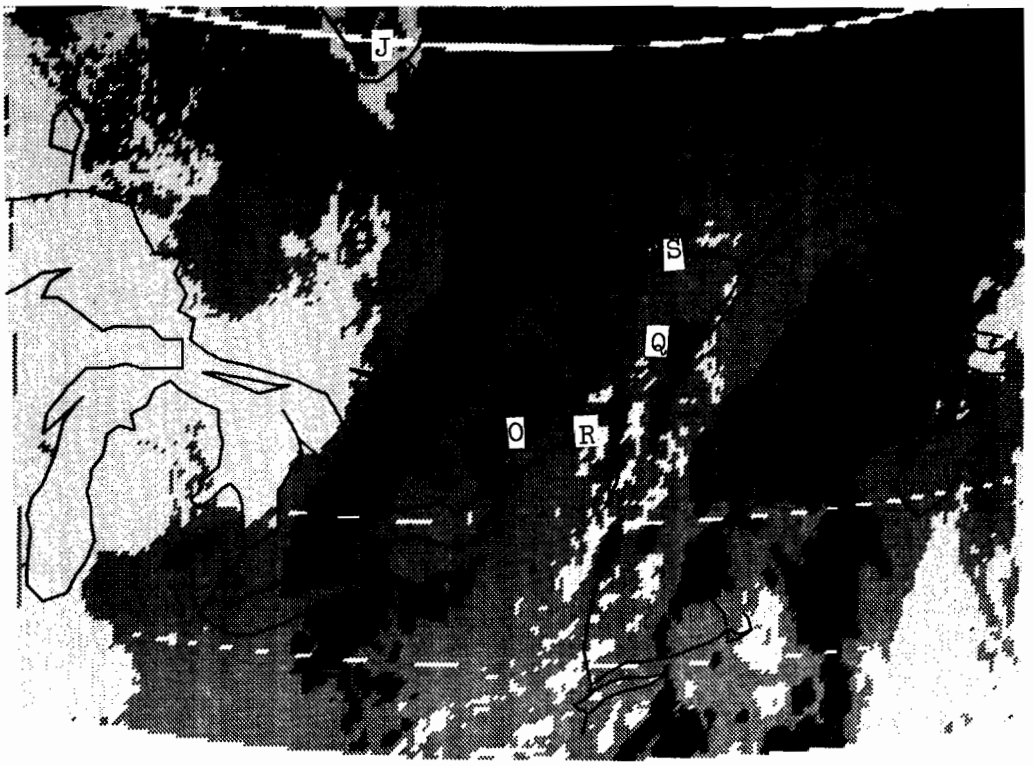

Fig. 7.5. Smoothed probability of rain map at 1830Z 2 June 1977, derived from GOES visible and infrared images of Figs. 7.2 and 7.3, and from the radar data of Fig. 7.4.

R: Radar Q: Quebec O: Ottawa
S: Saguenay and Lake St. John J:James Bay

The ultimate result, that is, the spatially smoothed probability of rain map from GOES visible and infrared images is presented in Fig. 7.5. Five shades or levels can be distinguished:

level	Characteristic
1	clear skies defined as $c_{VIS} < 90$
2	cloudy skies defined as $c_{VIS} \geq 90$ and $PP_R < 10$
3	$10 \leq PP_R < 30$
4	$30 \leq PP_R < 50$
5	$PP_R \geq 50$

The cirrus and stratus components of the infrared and visible pictures are effectively removed by the bivariate frequency distribution technique. For example, the high infrared values over and south of the Gulf of St. Lawrence, north of the Saguenay estuary up to Anticosti Island could be classified as rain producing clouds by a single infrared threshold technique. However, the visible counts over this region reveals them to be relatively thin, probably cirrus fields. Hence, Fig. 7.5 indicates no probability of rain. Similarly, clouds with a relatively high solar brightness but lower infrared counts, i.e., of low altitude, are correctly categorized as non-raining. Instances can be found by comparing Figs. 7.2, 7.3 and 7.5 particularly in Southern Michigan and along the wide cloud band aligned from just east of James Bay to west of Lake Erie. It may be observed that along this band, the high infrared values exhibit a better correspondence with the rain areas of Fig. 7.5 than does the visible picture. Note that the radar echoes of Fig. 7.4 are independently reproduced by the P_{RS} map of Fig. 7.5.

In Lovejoy and Austin, (1979a), a single PP_R threshold was chosen from visible-infrared space in order to separate raining from non-raining zones. Their method consists in choosing an appropriate PP_R value from Table 7.4c such that the rain coverage, resulting from the satellite data within radar

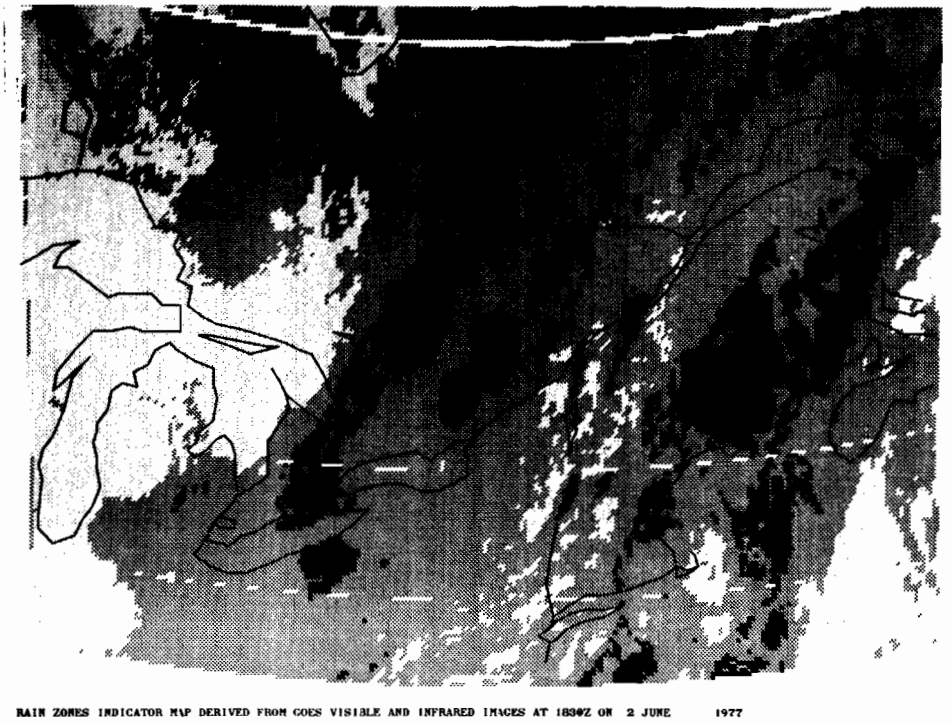

Fig. 7.6. Non-smoothed rain map at 1830Z 2 June 1977, derived from GOES visible and infrared images and radar data. The PP_R contour separating raining from non-raining areas is 45.

range, would be equal to that detected by radar. This normalization procedure is usually obtained with a value of $PP_R \approx 45$. Fig. 7.6 exemplifies a map obtained with this technique. However, this report will concentrate on the PP_R technique of eq. 7.1. Note that no special normalization scheme needs to be devised since multiplication of the areas of Fig. 7.5 within radar coverage by their corresponding probabilities, followed by integration will automatically yield the same[1] coverage perceived by the radar.

---

[1] Spatial smoothing and the subjective criteria established may cause the satellite and radar coverage to differ slightly.

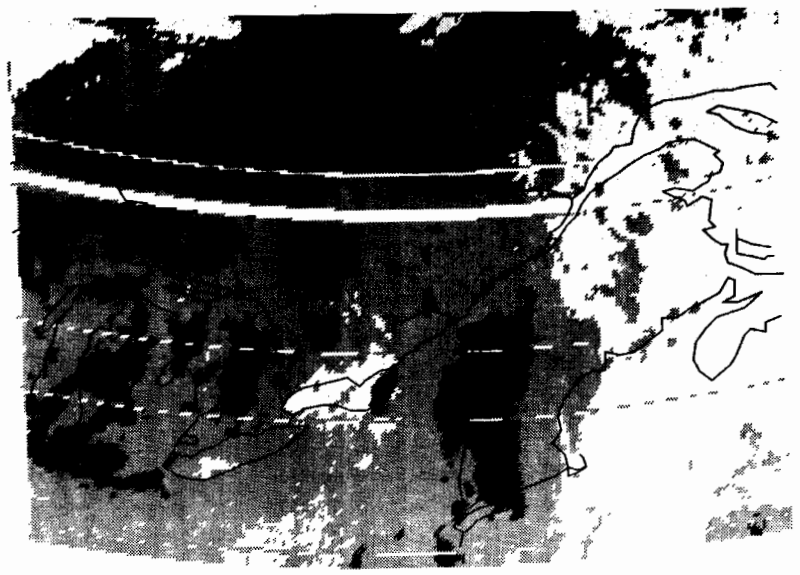

Fig. 7.7. Sequence of probability of rain maps from 1st June 1977.

7.2 Motion and Synoptic Verification of Satellite Rain Areas

In order that satellite rain maps be used as input to a SHARP-like forecasting scheme, the technique described must produce P_{RS} rain zones which are sufficiently consistent in time so as to be trackable by a pattern recognition algorithm. This task can be achieved with the available data and compared with upper level winds. However, the more crucial verification between P_{RS} areas over the entire map and the actual precipitation could not be rigorously carried out in this work on account of the lack of suitable ground truth data. A comparison is thus performed with surface synoptic observations. It is imperative that a more detailed analysis be planned between satellite rain areas and other radar data (e.g., Woodbridge Radar near Toronto) and raingage information. For longer sequences, hydrology accumulation maps independently derived from satellite, radar and raingage will provide an ideal inter-comparison.

The three available sequences are now examined on an individual basis within the context of this chapter.

7.2.1 Case 1 (June 1, 1977)

The six half-hourly P_{RS} maps forming the sequence of June 1, 1977 are portrayed in Fig. 7.7. The surface synoptic chart at 1800Z as analyzed by the Quebec Forecast Office, is given in Fig. 7.8. It shows a depression in central Quebec with a cold front trailing across through the northern Great Lakes. A low pressure system with a trowel, originating from the Mississippi Valley, and advecting warm, moist air, is converging toward the descending cold front.

The PP_R zones of Fig. 7.7 can be considered consistent over the 2 1/2 h period. The patch SSE of Montreal is associated with the advancing warm front. With the exception of a developing Cb just east of Lake Ontario, the

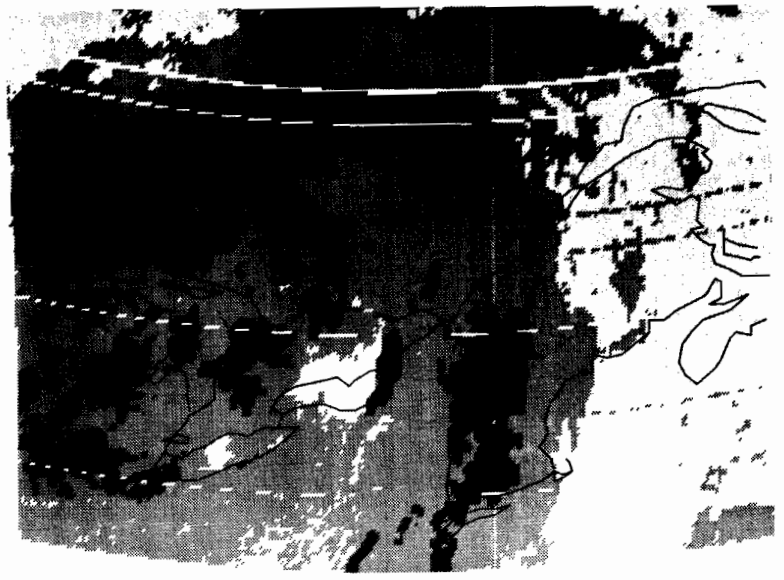

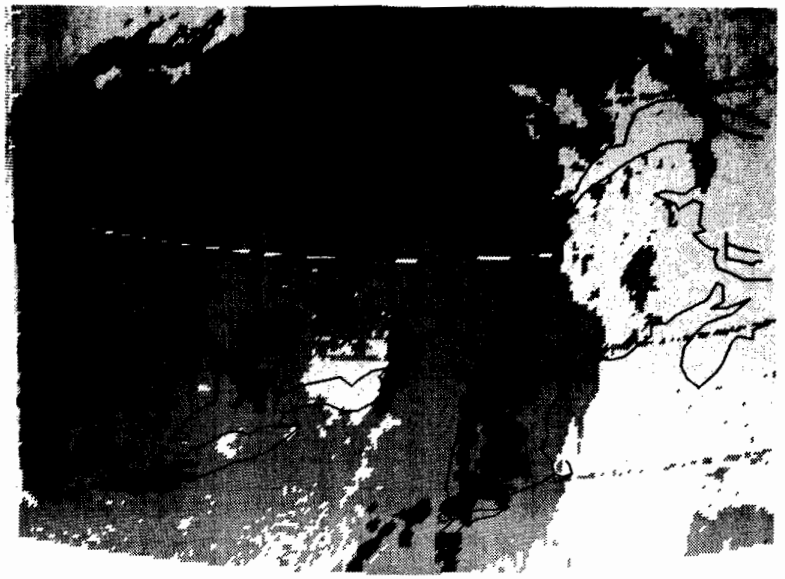

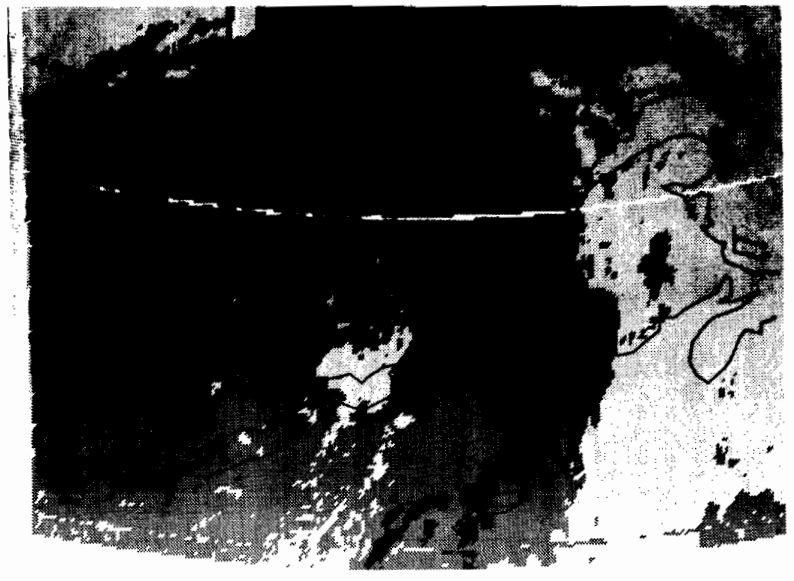

Fig. 7.7. Sequence of probability of rain maps from 1st June 1977.

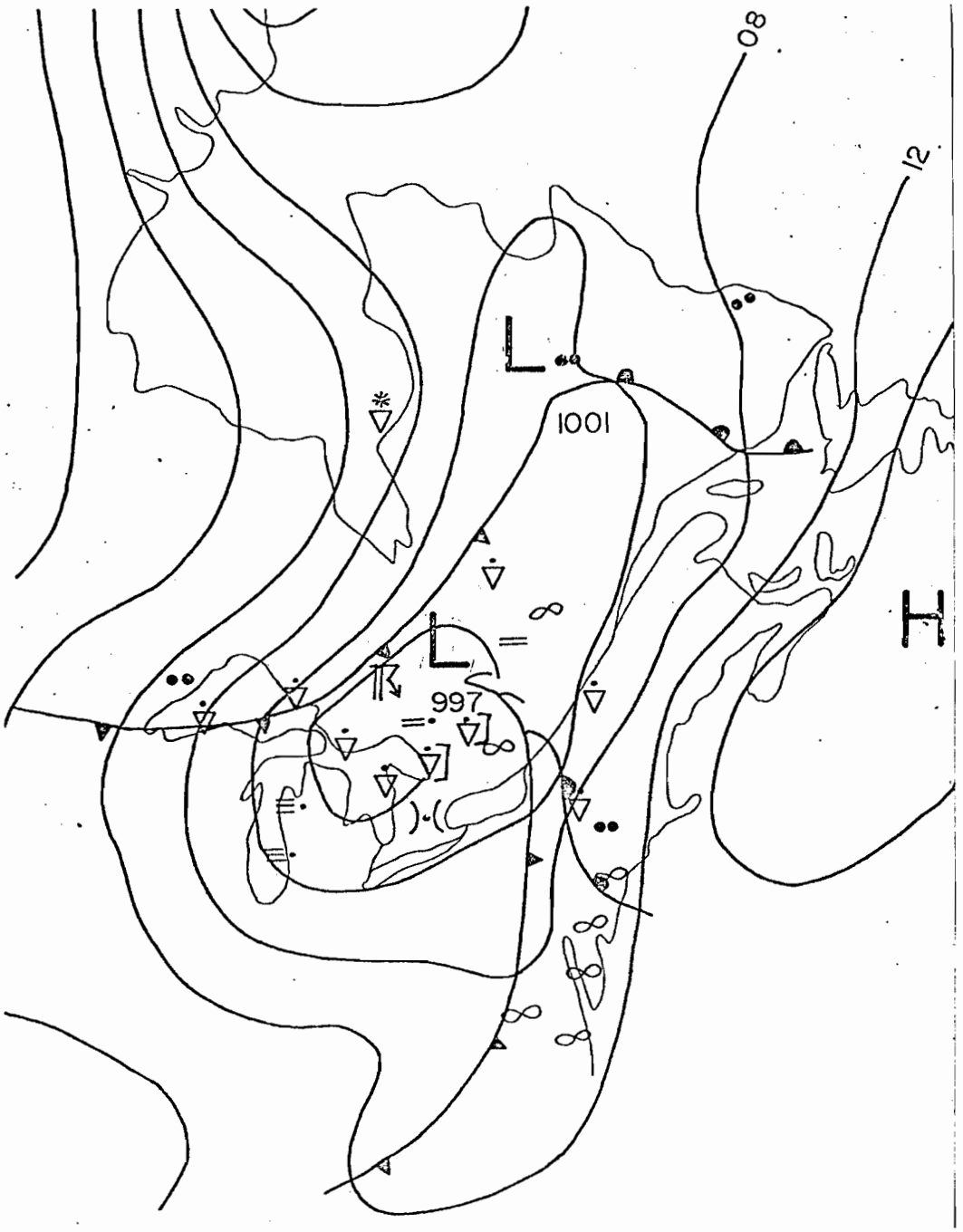

Fig. 7.8. Surface synoptic chart at 1800Z, 1st June 1977, as analyzed by the Quebec Forecast Office.

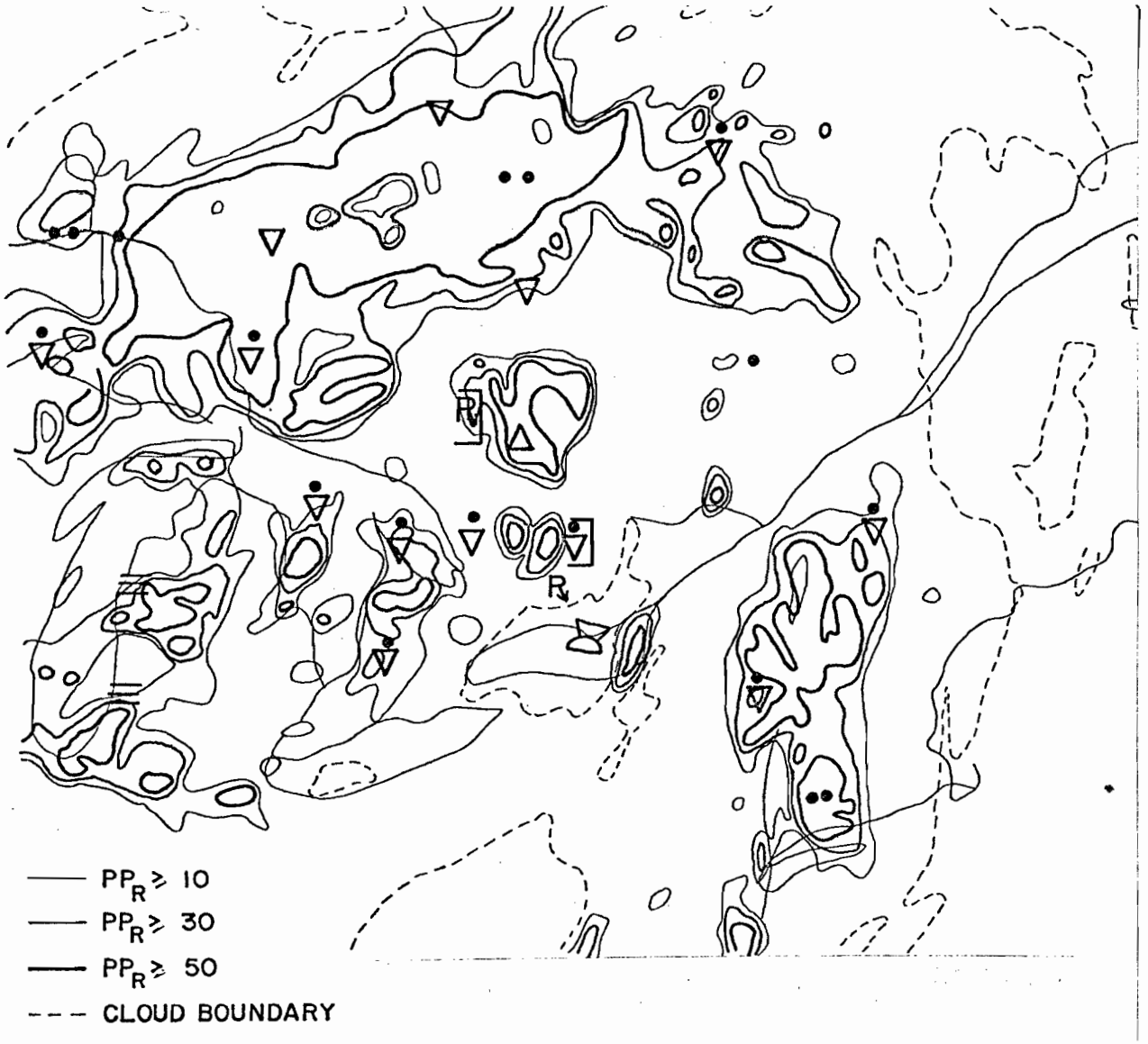

Fig. 7.9. Pertinent surface observations from Fig. 7.8 superimposed over probability of rain contours from the 1800Z map of Fig. 7.7.

southern cold front is relatively inactive. The configuration of the rain pattern north-west of the Saguenay region seems to denote the presence of a warm front. While it is not analyzed on the synoptic chart, a steep temperature gradient, from high 20's to the teens, is observed at the surface. The rain area with a circular shape northwest of Ottawa coincides with the location of the low pressure centre. The scattered showers of probable convective nature extending to southern Lake Michigan are associated with a lagging trough over the Great Lakes. The more extensive rain area is found at, or behind, the arctic cold front. It is assumed that the rain band from east of James Bay to north of Lake Superior, consists of light, continuous precipitation typical of the more northerly latitudes. Note that after 1900Z, the PP_R values undergo a general decrease and the patterns appear to be breaking up. This may be a genuine diurnal or synoptic effect. Other possible causes may be the crude normalization of visible data and an insufficiency of radar echoes within range to provide reliable statistics. In section 7.3, a "general" relationship of eq. 7.1 will be derived to counteract the latter problem.

In Fig. 7.9, the significant surface observations are superimposed on PP_R contours of the 1800Z P_{RS} map. We are reminded that a strict comparison cannot be performed on account of drastic differences in the temporal and spatial scale between the satellite data and the synoptic charts. For example, surface observations at each station are valid for a 3 h period preceding map time; they are scarce in the northern latitudes, and some observations have not been assimilated into the display chart. Nonetheless, the comparison in Fig. 7.9 is acceptable. Some discrepancies are apparent east of Lake Michigan where PP_R areas fail to be substantiated by surface observations, but the 2400Z chart shows widespread rain over this region. From this observation, it may be inferred that while the PP_R zones may not locate regions which are presently precipitating, they point out areas with future potential for precipitation.

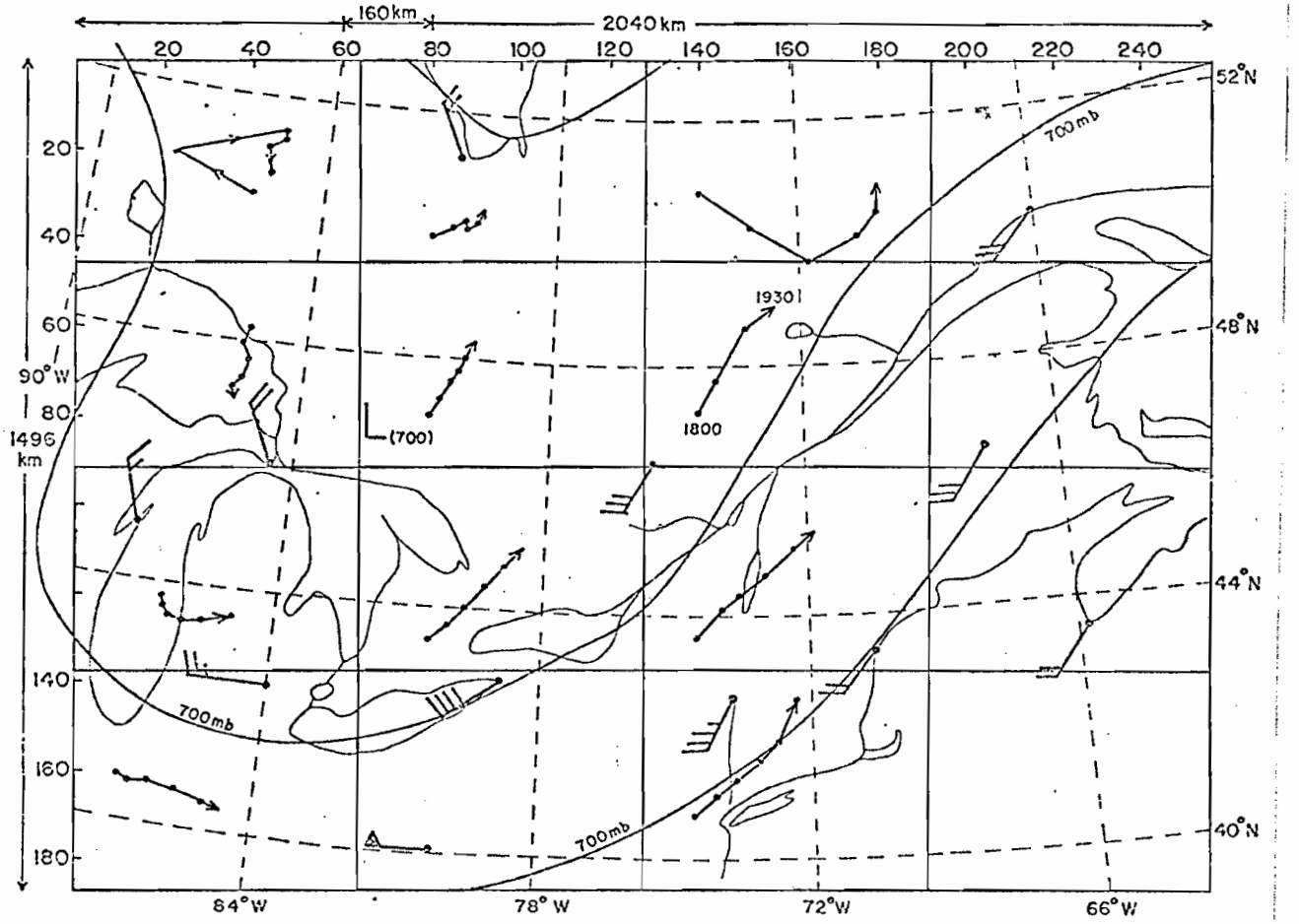

Fig. 7.10 Trajectories derived over each subarea with sufficient "satellite echo" coverage for 1730-2000Z 1st June 1977.

It is immediately apparent that, to determine the motion of the PP_R zones, a pattern recognition technique must be applied to sub-areas of the entire map. This course of action was also adopted in Chapter VI in resolving the differential motion of radar echoes. Hence, the (187 x 255) matrix has been sectioned into 16 sub-areas. Each consists of a (46 x 64) array, or 368 x 512 = 188,000 km^2. The SHARP program operated successfully in real time over an area of about 132,000 km^2. Tracking of radar echoes over this area has revealed a fairly uniform motion. A larger area has been chosen for tracking of satellite rain zones since, as was expected, they are less consistent and exhibit less continuity in time than radar echoes. Equally important is the need for a proper balance between the temporal and spatial resolution and the characteristic scale length of the patterns. A minimum of 1 % coverage computed from zones for which $PP_R \geq 30$ is required before attempting the pattern recognition technique. The weighting in computing the cross-correlation coefficient is as follows:

$PP_R \geq 50$	2 (weighting)
$30 \leq PP_R < 50$	1 "
$PP_R < 30$	ϕ "

The results of the tracking program for the sequence of case 1 are summarized in Fig. 7.10. The half-hourly displacements, computed in fractions of grid lengths to avoid quantization effects, have been summed to form a trajectory for each sub-area. Unless otherwise indicated, each begins at 1730Z and terminates at 2000Z. The 700 mb analysis for 2400Z, with the radiosonde wind data, has been added for visual comparison. Fig. 7.10 shows that the PP_R zones on the southern section of the map have been correctly followed, yielding a displacement which compares favourably with the 700 mb wind. Speeds of the order of 50 and 60 km h^{-1} correlate well with 700 mb wind speeds found ahead of the 700 mb trough.

In this region, the linearity in both speed and direction augurs well for a short term forecasting system based on pattern extrapolation. Behind the arctic front, or closer to the 700 mb centre, lower speeds are calculated in accordance with upper level data, but, as exemplified by sub-area (3,1) which includes Michigan, the expected passage of an upper front must be taken into account when performing a forecast by pattern advection.

A disturbing aspect of Fig. 7.10 is the trajectories in the northern portion of the map. It is obvious that the first two calculated displacements for sub-areas (1,1) and (1,3) constitute spurious motion. These are caused by the absence of easily recognizable features, or by the creation of artificial ones arising from the arbitrary sectioning of patterns into sub-areas, or by a high percentage coverage as in (1,2). It has been pointed out in Chapter VI that a coverage greater than 40% is as detrimental to a pattern recognition technique as insufficient coverage, by underestimating the actual motion and hence being subjected to quantization effects. An additional explanation for the erratic motion in sub-areas (1,1) and (1,3) is that the rain determination algorithm, derived from radar data near 45°N latitude, may not be as stable in northern latitudes, yielding rain zones with edges which appear to advance or recede at unreasonable speeds. However, as was the case in the real-time operation of SHARP, certain criteria can be introduced which will reject apparently unacceptable displacements. These criteria consist of:

a) increasing the necessary minimum coverage of 1%

b) decreasing the allowable maximum coverage

c) comparing with previously acceptable motions

d) determining the number of data along sub-areal boundaries

e) rejecting extreme speeds.

A simple decision scheme, based on the number of "penalty points" accumulated for the violation of the above criteria, removed the unrealistic motions of Fig. 7.10. In cases of uncertainty, a reasonable guess, like the 700 mb wind velocity if available, may be adapted.

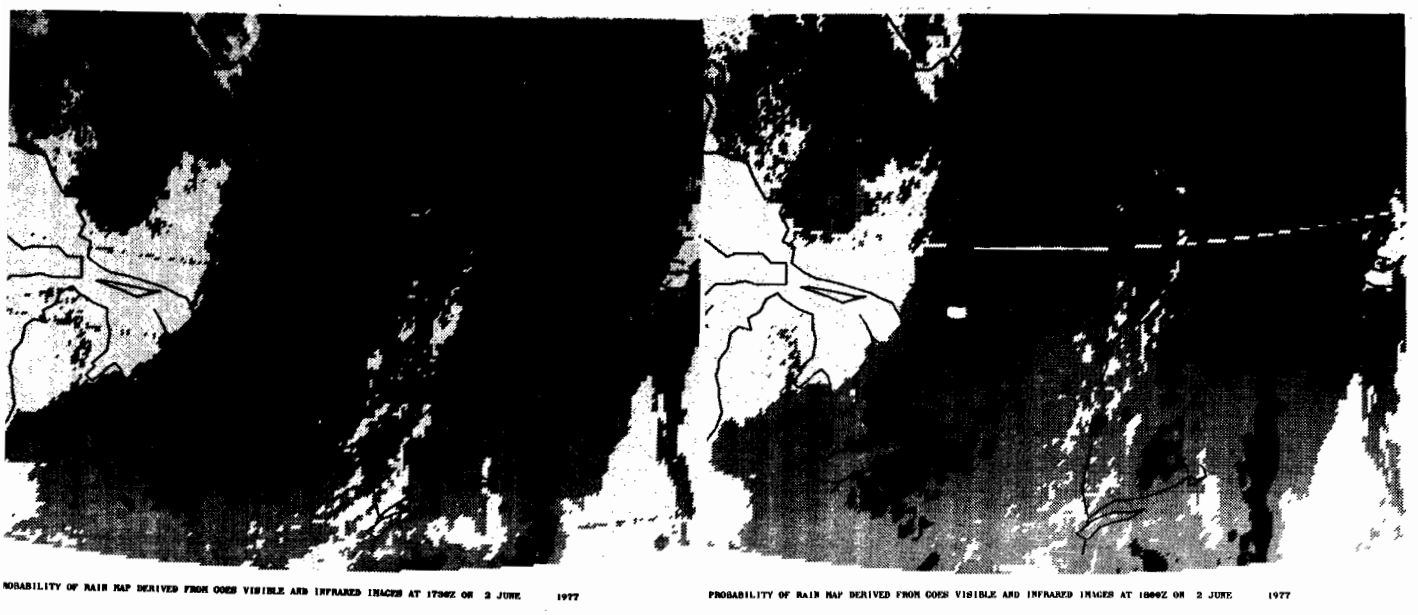

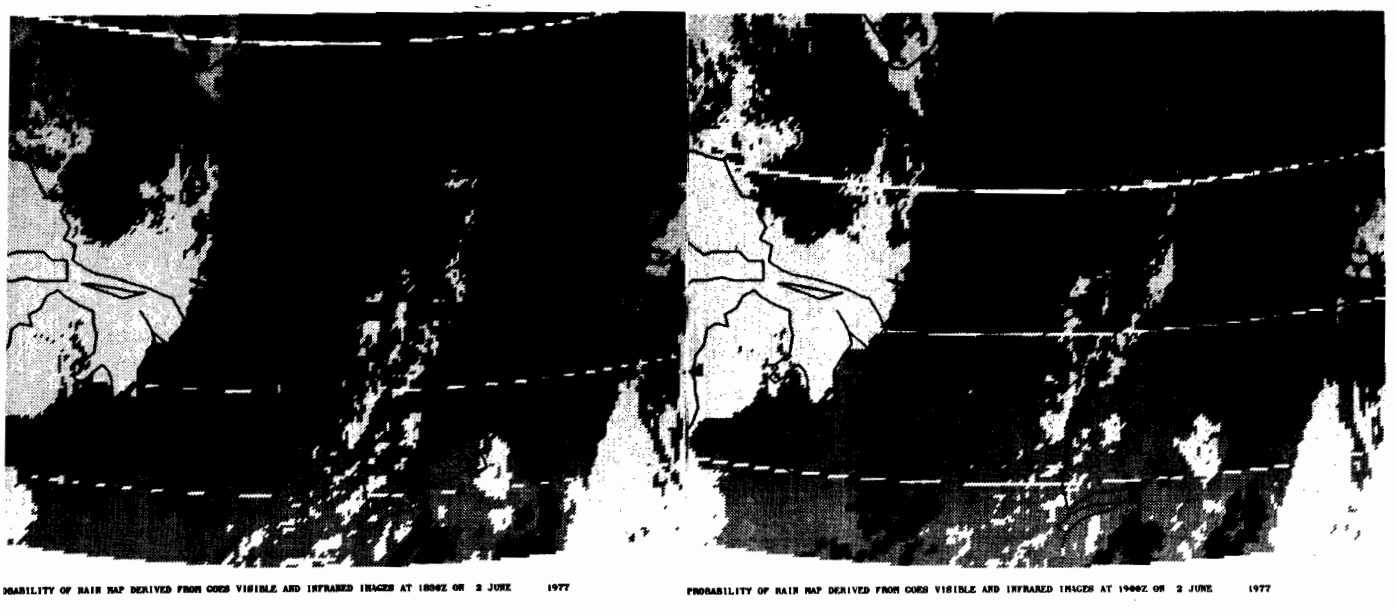

Fig. 7.11. Sequence of 2 June 1977.

7.2.2 Case 2 (June 2, 1977)

The P_{RS} maps of this sequence are illustrated in Fig. 7.11. The 1800Z surface analysis, Fig. 7.12, shows that the cold front, which 24 hours earlier was stretching from James Bay to north of Lake Superior, has descended in a rotational movement south of Lake Erie and Lake Ontario. The depression which originated from the SW is completely amalgamated into the cold front which is now of a more convective character. Smaller disturbances, analyzed on subsequent charts, have also developed along the front. The wave crest associated with the SW low has meanwhile moved into Maine and New Brunswick (from the 12Z analysis). The rain bands associated with these two principle systems are well delineated in Fig. 7.11. More precisely, Fig. 7.11 reveals that two lines are associated with the cold front. The first one, elongated from north of Lake St. John through Ottawa and south of Lake Erie, coincides with the arctic front position. In addition, a wider and more continuous band of precipitation is located 300 km behind it. In the relatively clear area between the precipitation over Ontario and near the Maritimes, intense solar heating induced the formation of localized thunderstorms arranged in short lines just east of Montreal and near Quebec City. The formation, development and displacement of these convective storms can be observed from the P_{RS} maps. It may be pointed out that in such cases when the convective activity is confined to a relatively small scale, the 5-point smoother on an (8 x 8) km^2 grid reduces considerably both the area and the magnitudes of the higher PP_R values.

Fig. 7.13 offers the crude verification between surface synoptic observations and the P_{RS} map at 1800Z. The inadequacy of such verification is evidenced by the lack of surface reports of the thunderstorm activity in the region just discussed, although merely in its infancy stage by 1800Z.

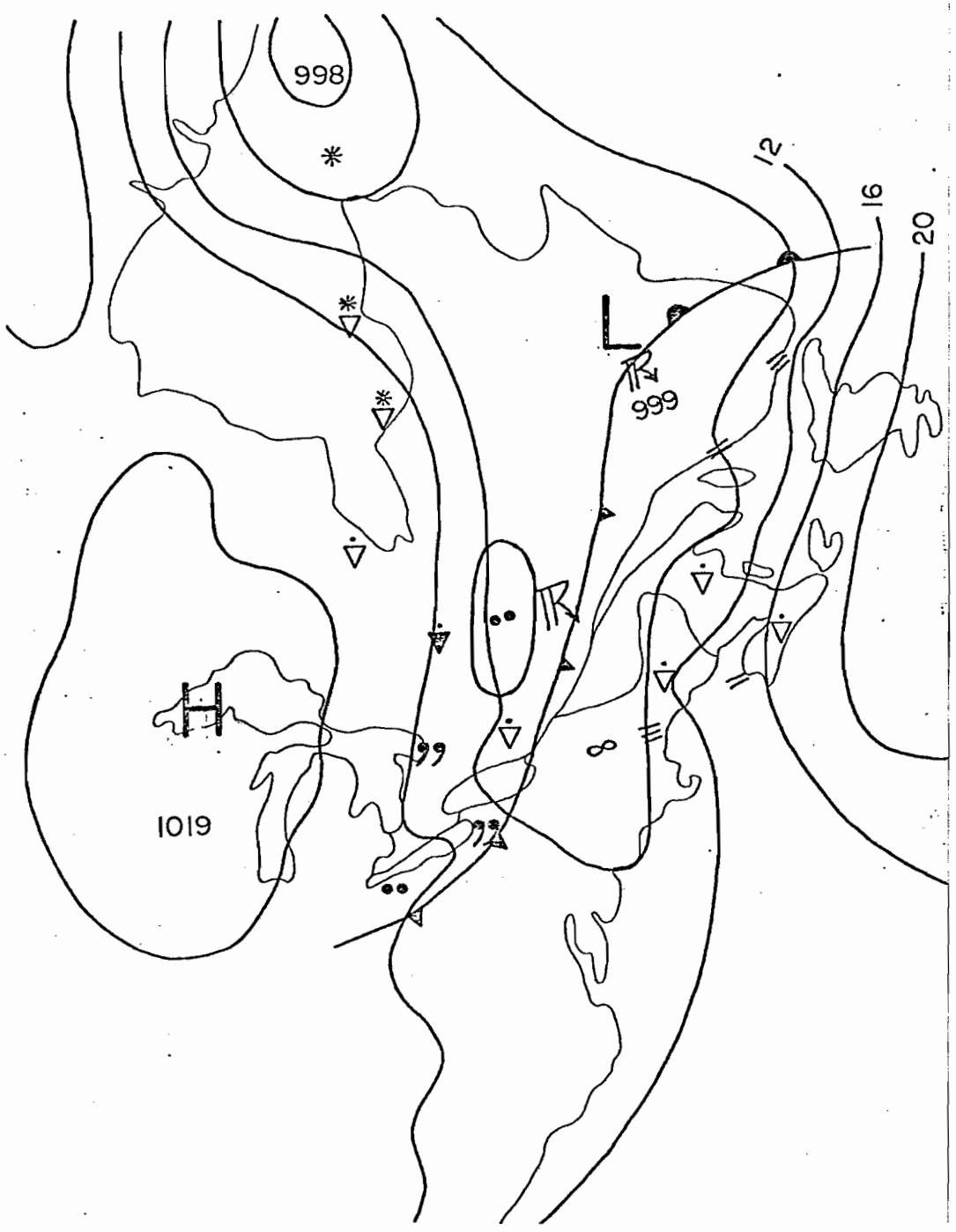

Fig. 7.12. Surface synoptic chart at 1800Z, 2 June 1977, as analyzed by the Quebec Forecast Office.

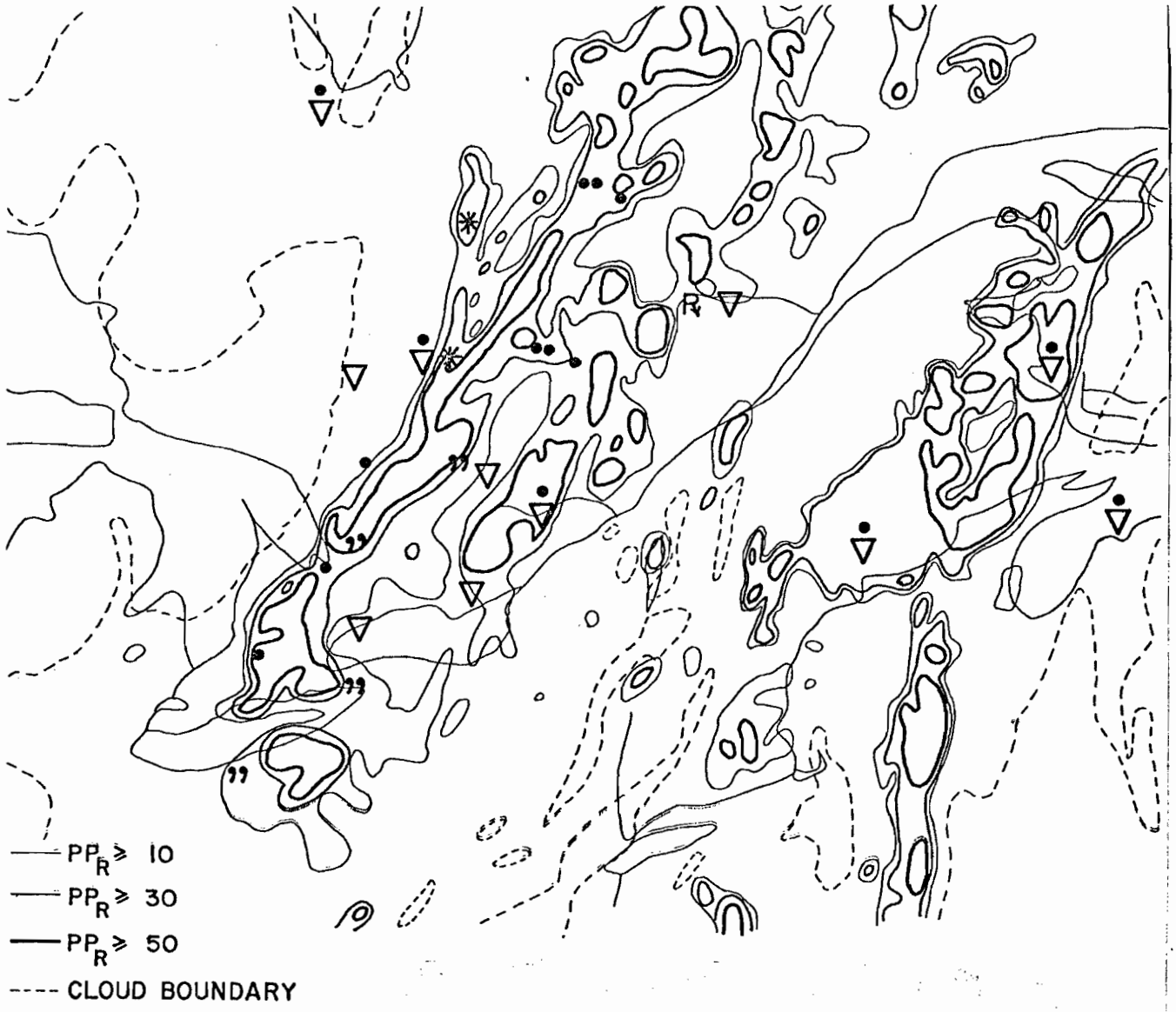

Fig. 7.13. Pertinent surface observations from Fig. 7.12 superimposed over probability of rain contours from the 1800Z map of Fig. 7.11.

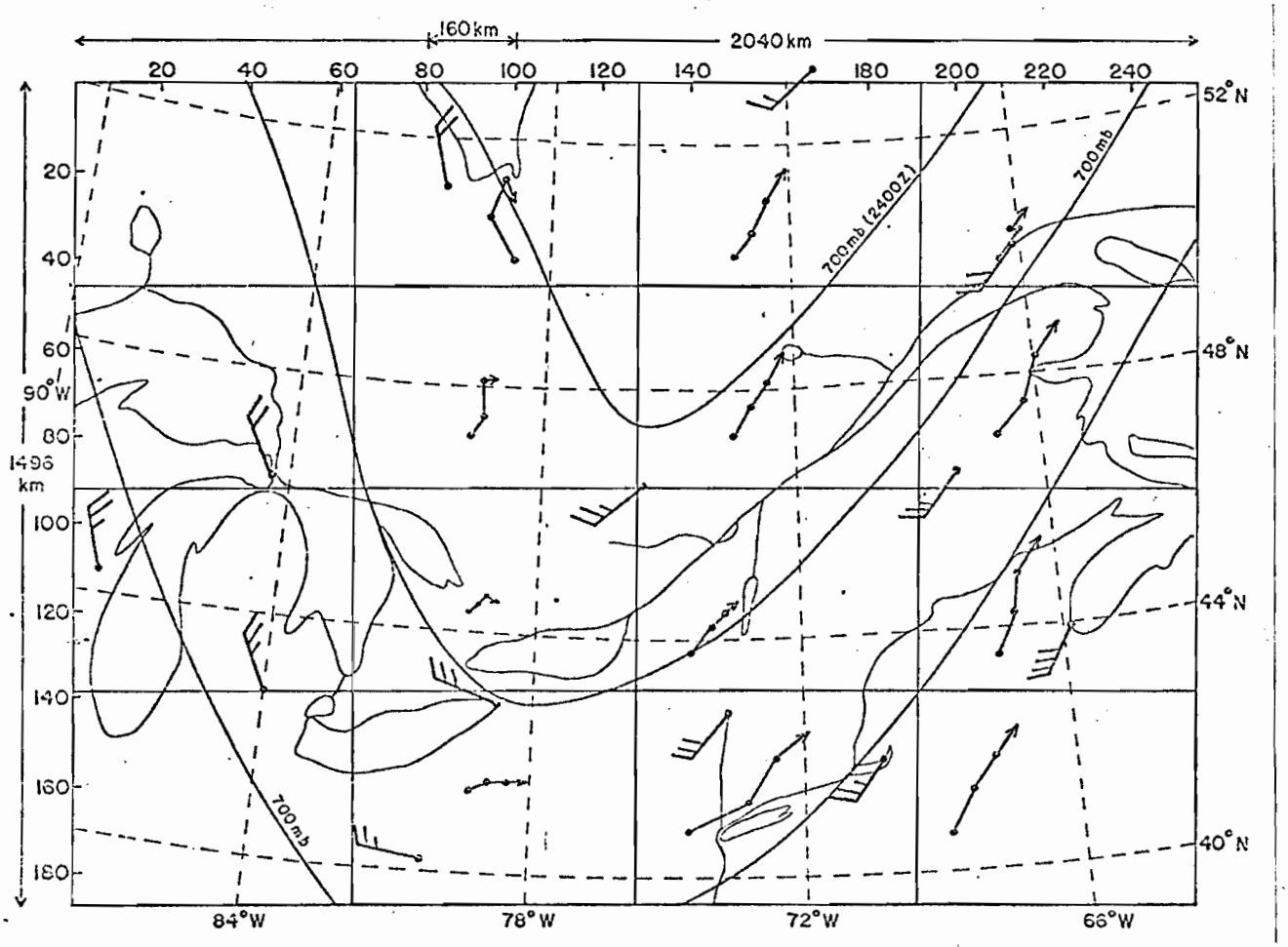

Fig. 7.14. Trajectories for 1730-1900Z 2 June 1977.

Reports of Cb activity first appeared on the 2100Z map. Fig. 7.13 can again be considered as an acceptable comparison of satellite rain data and observation of surface precipitation. There are two instances, in Halifax and Moosonee on James Bay, where surface observations of rain fail to be present on the 1800Z P_{RS} map. However, in both cases, because of the presence of on-shore winds, they are certainly showers of low altitude triggered by this local effect. Note, nonetheless, that a 10 to 30% probability of rain is computed for the area near Halifax on the 1730Z map.

The trajectories from the 4 half-hourly maps have been derived as described earlier. Correlation with the 700 mb wind speed, shown in Fig. 7.14, is excellent, with a notable exception occuring in box (1,2) near James Bay. Some of the discrepancies near the 700 mb through are caused by the time difference between the trajectories and the radiosonde data. Attention is directed to the line of precipitation over the Atlantic east of Cape Cod with a trajectory toward Nova Scotia - see box (4,4). The extent of this precipitation zone will likely be incomplete, even as determined by a weather radar situated on the southernmost tip of Nova Scotia. However, the sequence of Fig. 7.11 and the trajectory display of Fig. 7.14 can provide an adequate forecast for the arrival and duration of precipitation over that province.

7.2.3 Case 3 (June 29, 1977)

This case study consists of the longest sequence, 1300Z to 1730Z. However, the longitudinal extent of the satellite data, Fig. 7.15, is approximately half the size of maps seen so far. Hence, the P_{RS} displays are presented on a map size #1 of Table 7.3. The synoptic situation at 1700Z depicted in Fig. 7.16 is characterized by a deep low pressure system east of James Bay with a cold front as indicated. Fig. 7.15 illustrates very well

DERIVED FROM GOES VISIBLE AND INFRARED IMAGES AT 1300Z ON 29 JUNE

DERIVED FROM GOES VISIBLE AND INFRARED IMAGES AT 1400Z ON 29 JUNE

DERIVED FROM GOES VISIBLE AND INFRARED IMAGES AT 1600Z ON 29 JUNE

DERIVED FROM GOES VISIBLE AND INFRARED IMAGES AT 1730Z ON 29 JUNE

Fig. 7.15. Sequence of 29 June 1977.

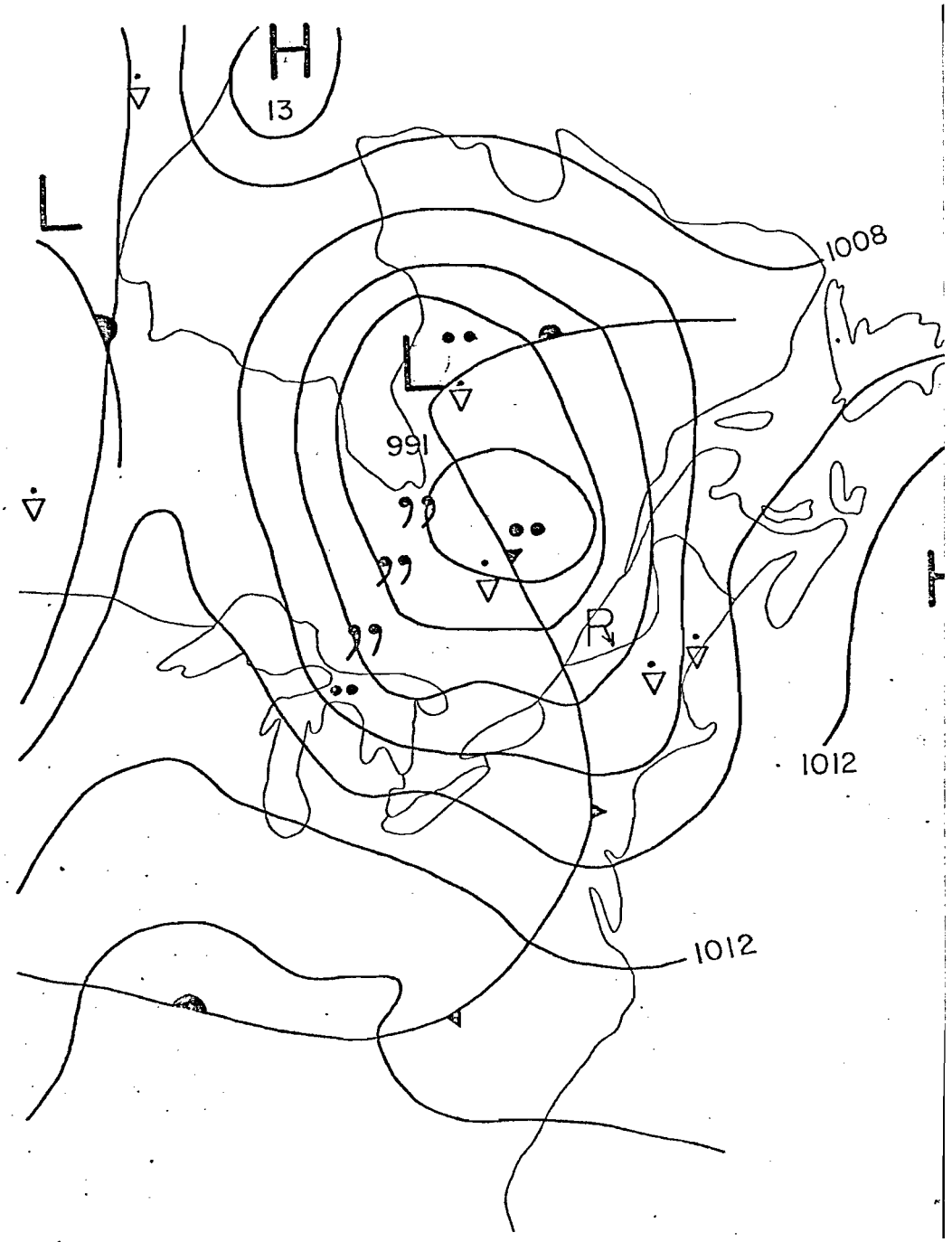

Fig. 7.16. Surface synoptic chart at 1700Z, 29 June 1977, as analyzed by the Quebec Forecast Office.

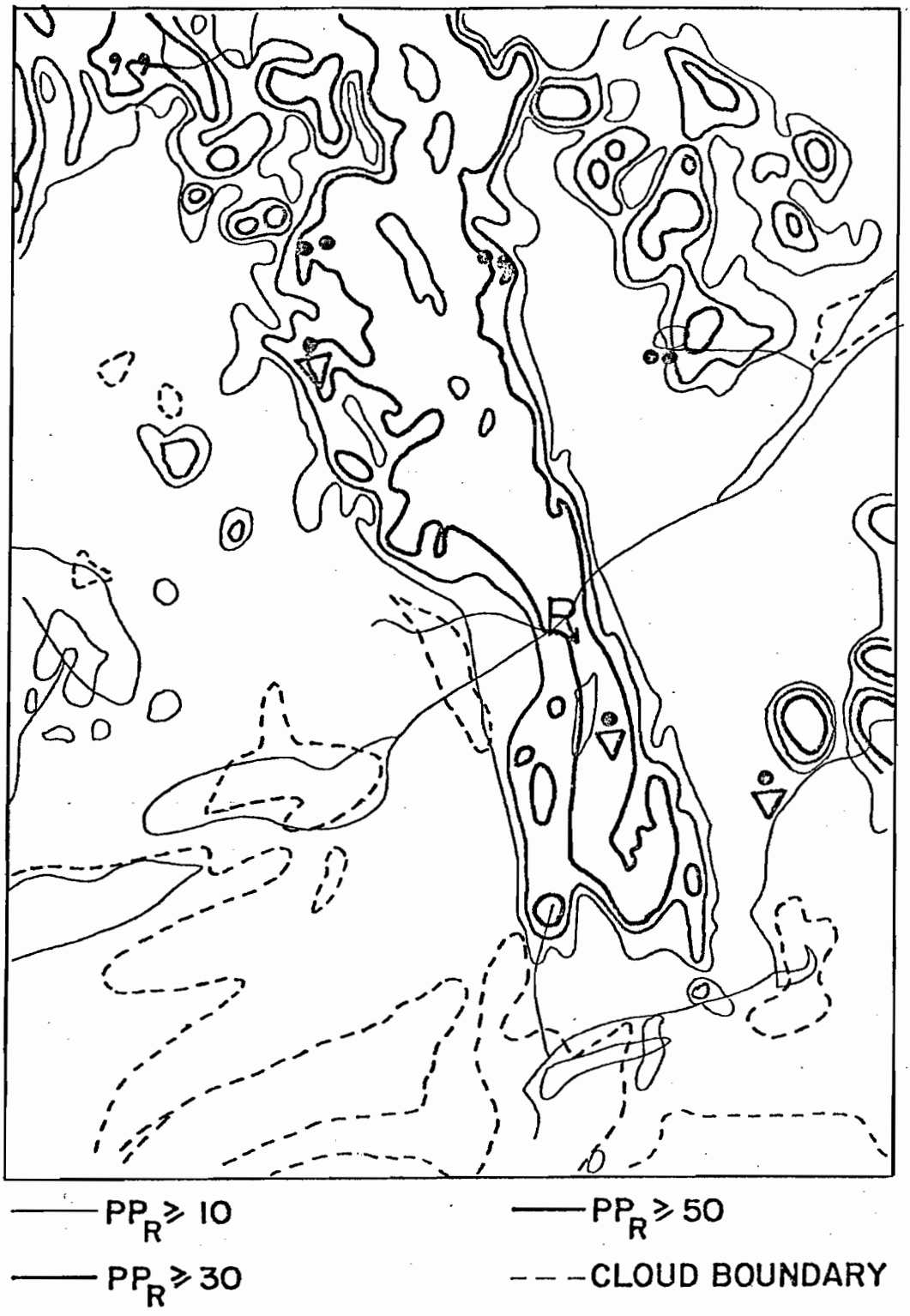

Fig. 7.17. Pertinent surface observations from Fig. 7.16 superimposed over probability of rain contours from the 1700Z map of Fig. 7.15.

the passage of the rain area over Montreal. This main band precedes the cold front and limits its activity to latitudes north of New York City. In this simple case, the comparison with surface observations, Fig. 7.17, is very good. The showers in the vicinity of Maine are correctly identified on the P_{RS} maps. The difference in resolution between satellite and synoptic maps is brought into sharp focus by the synoptic analysis near the Saguenay Region. Both satellite and surface reports indicate precipitation near Lake St. John and at a station about 200 km to the WNW. While in the synoptic analysis rainfall is assumed between the two sites, the satellite data disproves it.

A trough with a line of precipitation extending from the low centre to the junction of Lake Superior and Lake Huron is analyzed on the surface chart. On account of the limit of the western boundary of the P_{RS} maps, only the northern portion of this precipitation lines is discernible. However, some instability developed in the afternoon ahead of this trough line which manifested itself by the appearance of the 10 to 30% PP_R contour by 1600Z on the P_{RS} maps. This precipitation does not reach radar range until 1830Z.

The map of trajectories in Fig. 7.18 is limited to 8 sub-areas of (46 x 66) grid areas each. The 700 mb data are from 1200Z. Vectors in the southern latitudes are from a WSW or SW direction while motion just ahead of the depression is southerly. Note the shift in the motion in box (2,1) following the passage of the cold front. Since the length of this sequence permitted it, the trajectories were computed using both hourly and half-hourly intervals. As observed in Chapter VI, the north-south component of the displacement is at times underestimated using the hourly displacements, particularly in cases of extensive echo coverage. This effect is particularly evident in sub-area (1,1) and (2,1). Hence, from these considerations, if practical in real time, it is advisable to track satellite rain zones with a 30 minute interval.

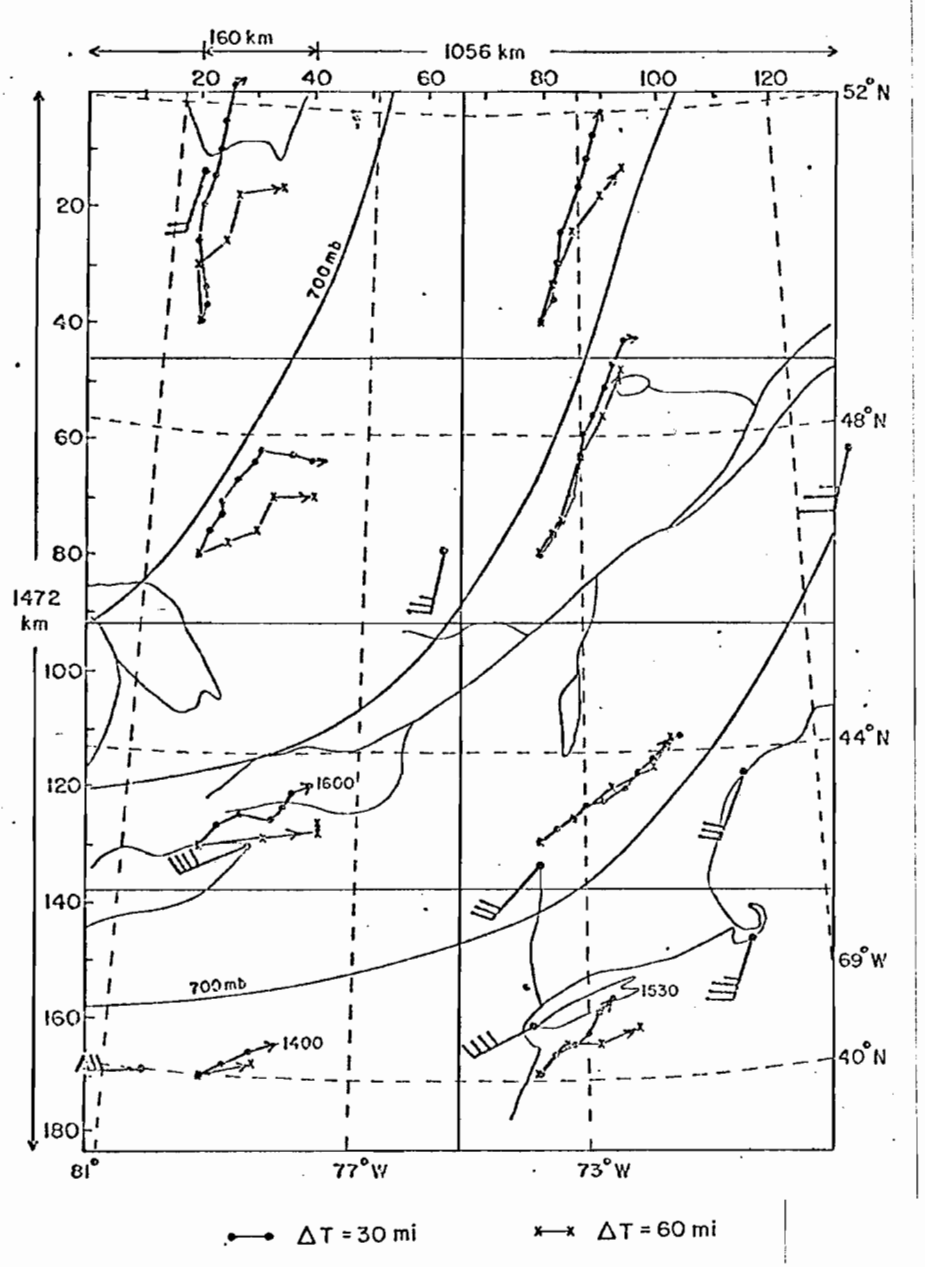

Fig. 7.18. Trajectories for 1300-1730Z 29 June 1977.

A prototype model called RAINSAT which produces P_{RS} maps and computes the displacement of the rain areas is currently being tested on a mini-computer. Implementation of a real-time experiment is scheduled for the summer 1981.

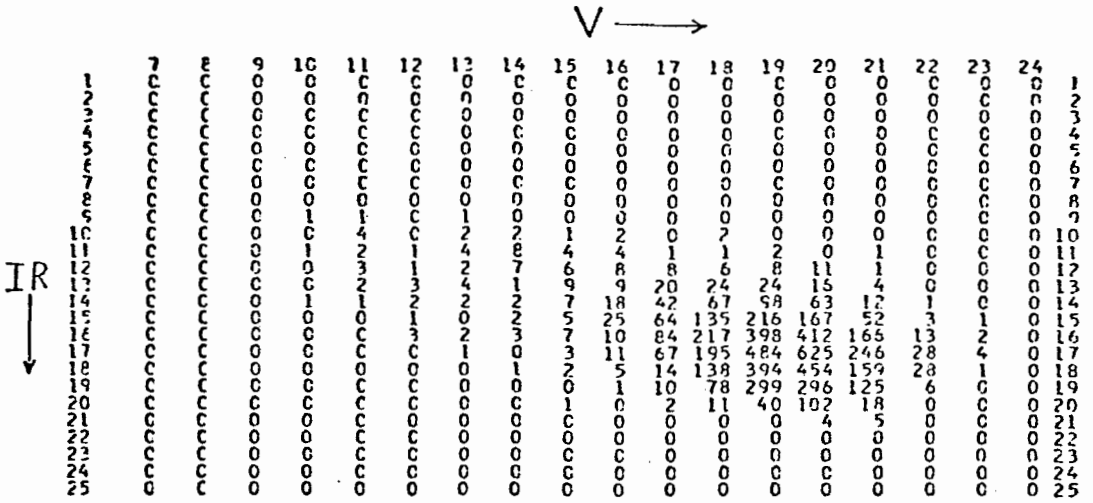

Table 7.5a Cumulative bivariate frequency distribution in visible-infrared space of the "rain" grid areas for the 20 available maps.

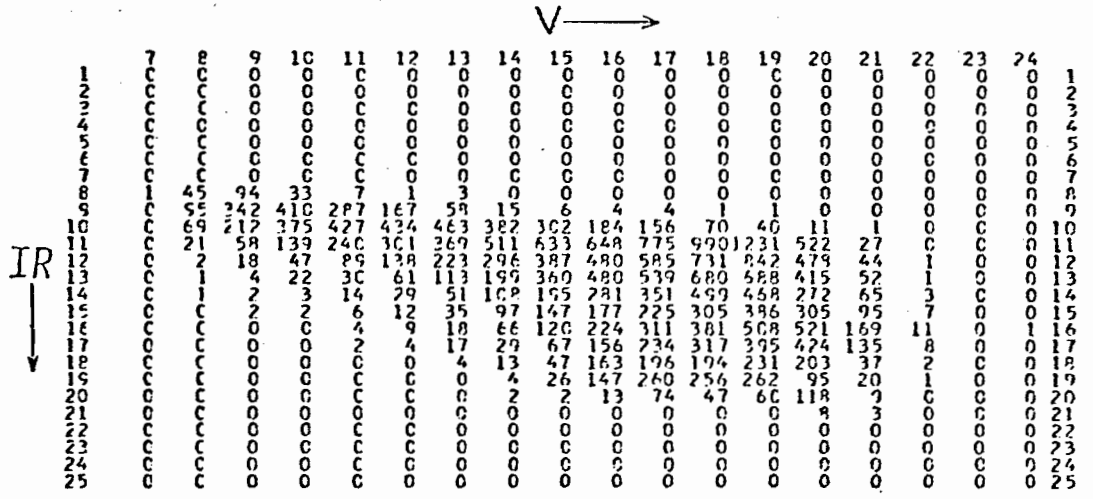

Table 7.5b Cumulative bivariate frequency distribution in visible-infrared space of the "non-raining" grid areas for the 20 available maps.

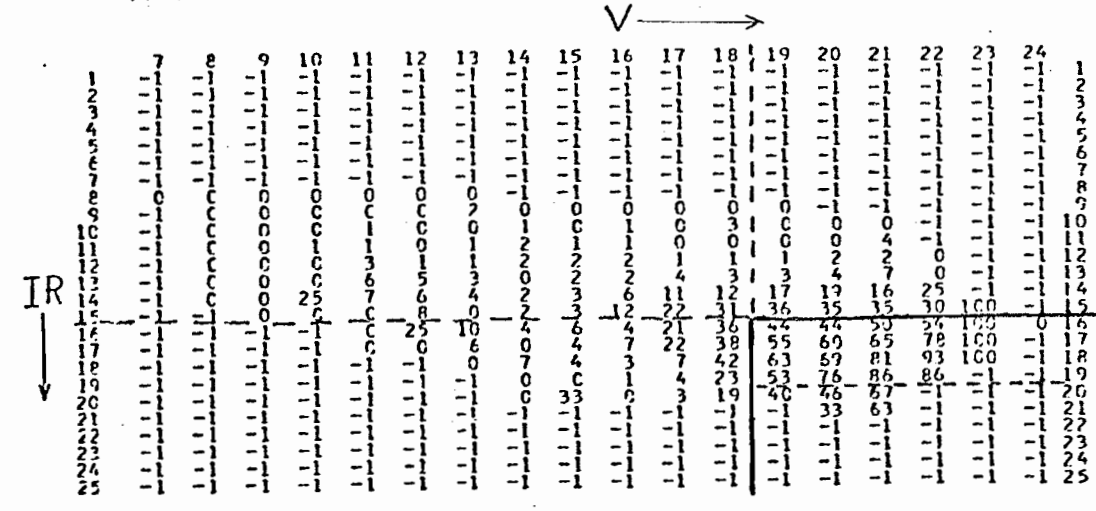

Table 7.5c "General" percentage probability of rain distribution as a function of infrared and visible values. "-1" indicates that the corresponding (IR,V) pair did not occur throughout the entire data

7.3 General Statistics and Hydrological Verification

7.3.1 Derivation of a "General" $PP_R(IR,V)$ Relationship

The production of P_{RS} maps requires the simultaneous availability of visible and infrared satellite and radar rainfall data. The amalgamation of these three data sets permitted the derivation of the empirical relationship of eq. 7.1, which is optimized or updated for each map time. Each relationship is strictly valid within radar range, the supposition being then made that similar meteorological conditions enable us to extend it to the entire satellite area. An equivalent assumption may be invoked to enable a temporal extension of $PP_R(IR,V)$ in order to preclude the need of radar data for each satellite picture. This course of action becomes a necessity when radar data are simply not available, or the grid areas with echoes within radar range are insufficient in number to extract a truly reliable statistical relationship as exemplified in tables 7.4. At first glance, a 6 to 8% coverage will ensure a satisfactory number of (8 x 8) km^2 rain areas for Table 7.4a.

The goal of a general formula can be achieved by accumulating statistics according to the technique described in section 7.1 for all the 20 available map times. This procedure yields the "rain", "no-rain" and percentage probability of rain matrices in Tables 7.5a, 7.5b and 7.5c respectively. Note that the (IR,V) pairs included in the dotted line for $c_{IR} \geq 190$ possess PP_R values which are lower than those for warmer temperatures. As mentioned earlier, this may be explained by the fact that this neighborhood describes the characteristics of moderately thick anvils which generate precipitation which does not necessarily fall through the 3 km level. This has the observed effect of lowering the PP_R values and initiated the formulation of the third criterion in section 7.1.

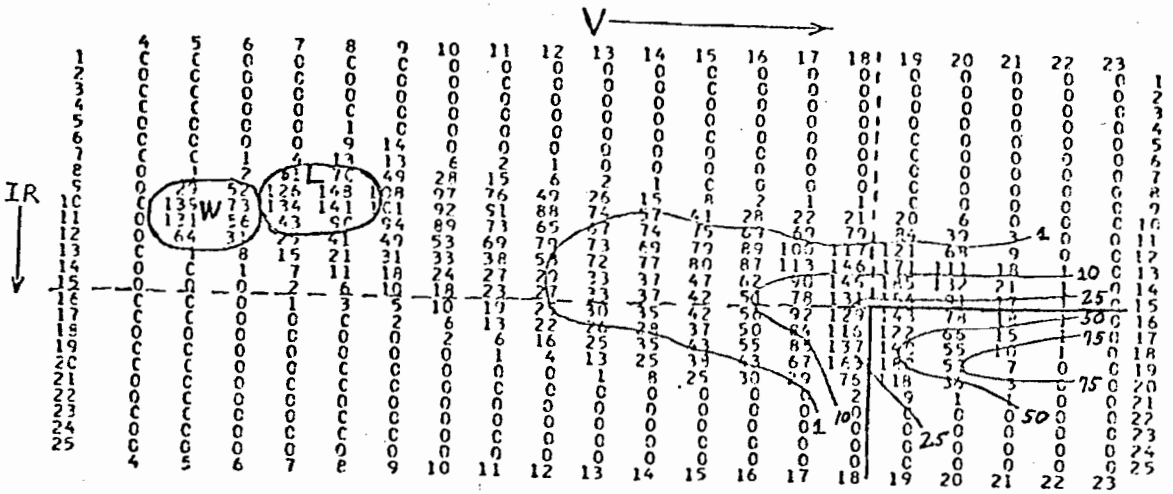

Table 7.5d Cumulative frequency distribution of visible-infrared pairs for the 20 available maps. One unit corresponds to 0.01% of 675398. ~~"-1" indicates absence of data.~~ The water and land characteristics are denoted by the W and L contour respectively.

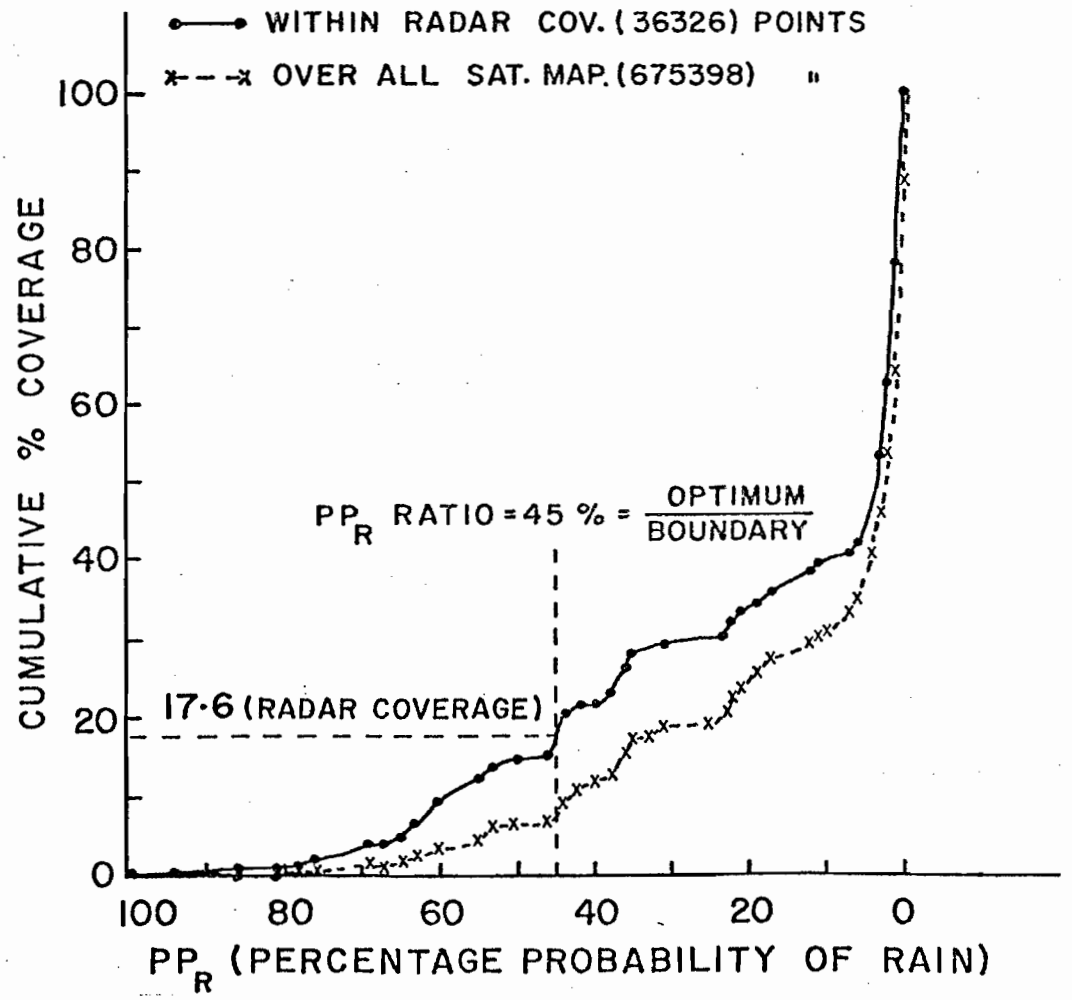

Fig. 7.19. Cumulative "satellite echo" coverage as a function of the percentage probability of rain.

Appropriate contours from Table 7.5c are superimposed on the visible-infrared frequency distribution, Table 7.5d, of the 20 satellite maps. It enables us to visualize the percentage of the satellite photo included by a particular PP_R value as well as demonstrating the virtue of the algorithm in discarding as rain certain (IR,V) pairs. Note that one unit of this contingency table is equivalent to 0.01% of the total number of grid points (675398). On this frequency distribution, the distinguishing features of water and land are noticeable, the latter being more reflective and generally warmer in the summer season. The considerable number of (IR,V) pairs for which $1 \leqslant PP_R < 10$ effectively indicate the non-raining clouds. Conversely, starting from $PP_R = 100$, the progressively larger number of clouds which will be considered as raining can be determined as PP_R is decreased. The result is depicted in Fig. 7.19. It can be seen that 70% of the area is characterized by $PP_R < 10$. However, it appears that $PP_R = 15$ or 20 is a more appropriate lower limit for the possibility of rain since around this PP_R interval the curve begins to slope upward drastically, indicating the start of the more numerous non-raining clouds. Thus, an improved choice of contours for P_{RS} maps would be 20, 30, 40, and 50. A similar curve for points within radar range (200 km) is also provided. It permits the determination of the PP_R value which divides the data into two categories, namely raining and non-raining. The average percentage coverage over radar range for the 20 maps at the 8 km resolution is

$$\% \text{ cov} = 100 \frac{R_R}{R_R + R_{NR}} = 100 \left(\frac{6384}{36326}\right) = 17.6\%$$

From the graph, it corresponds to $PP_R = 45$. This value yields a coverage of 8% over the entire satellite map.

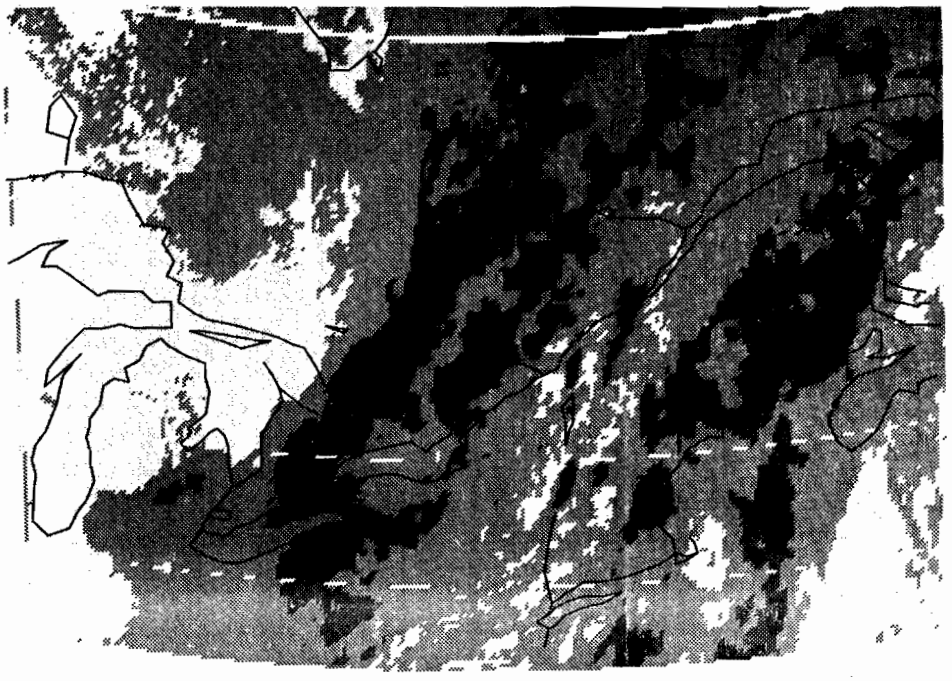

Fig. 7.20. Smoothed "general" probability of rain map at 1830Z 2 June 1977, derived from GOES visible and infrared images and from the empirical relationship of Table 7.5c.

Returning to Table 7.5c, it can be seen that the $PP_R = 45$ contour can be simplified by the combination of a visible and infrared threshold which includes the data bounded by the dark heavy line. The total number of points in it constitute a 10.5% coverage, slightly higher than the previously obtained value of 8%, mainly because it enclosed the "anvil component", particularly 1.2% of the data from the pair (20,19) for which $PP_R = 40$. In terms of counts, this approximate double-threshold, rain boundary is defined by

$$c_{VIS} \geqslant 180$$

$$C_{IR} \geqslant 150 \qquad \text{or } 255°K\ (-18°C)$$

The infrared threshold compares favourably with a value of 257.5 K obtained by Wylie (1979) for the Montreal area. However, a single infrared threshold does not eliminate the "cirrus component" of clouds delineated on Table 7.5c, defined as

$$c_{VIS} < 180 \text{ and } c_{IR} \geqslant 150$$

A total of 17.6% of the data would be incorrectly classified as rain using a single infrared threshold. A similar computation reveals that 12.5% of the data would be incorrectly classified as rain from the "stratus component" if a visible threshold of $C_{VIS} \geqslant 180$ is taken. This is the contribution from the relatively warm, but highly reflective stratus clouds. However, the author believes that the development of the probability of rain technique avoids the pitfalls of a single and even double threshold approach by attributing the relevant magnitudes of Table 7.5c. As initially stated and intended, the advantage of the "general" $PP_R(IR,V)$ relationship of Table 7.5c over the "particular" relationship exemplified on Table 7.4c is that the former does not require simultaneous radar and satellite data. This is achieved at the cost of sacrificing the optimum relationship for the specific time in question.

MAP LEVELS		"Particular" 2	3	4	5	TOTAL (No. of Data per Level)
"General"	2	95.8	3.1	0.6	0.5	338795
	3	30.3	50.2	13.8	5.7	80027
	4	2.9	21.4	47.0	28.7	78671
	5	0.5	1.9	29.7	68.0	38737

Table 7.6a Contingency table between the levels of the "general" and "particular" P_{RS} maps, with the "general" levels acting as the normalization basis.

MAP LEVELS		"Particular" 2	3	4	5
"General"	2	92.4	15.5	3.3	2.8
	3	6.9	58.8	18.0	8.3
	4	0.6	24.7	60.0	41.0
	5	0.04	1.0	18.7	47.9
TOTAL		351346	68256	61621	55007

Table 7.6b Contingency table between the levels of the "general" and "particular" P_{RS} maps, with the "particular" levels acting as the normalization basis.

The differences between them are in the form of lower PP_R magnitudes at higher (IR,V) pairs on account of the smoothing introduced by the larger data sample. Fortunately, for the same reason, most of the spuriously high PP_R values at the lower (IR,V) pairs are eliminated without recourse to subjective criteria.

An example of a smoothed "general" probability of rain map derived with the help of Table 7.5c is provided in Fig. 7.20. When compared with the equivalent P_{RS} map in Fig. 7.5, the dampening effect of the "general" algorithm is evident but the principal features are maintained. Note the reduction of the $PP_R \geq 50$ contour and the creation of a "hole" over Maine. However, this example displays greater than average differences. A comparison between the "particular" and "general" P_{RS} maps is presented in the contingency Tables 7.6a and 7.6b.

These tables compare the levels 2 to 5 as defined in section 7.1. For example, there is a total of 78671 points at level 4, i.e., $30 \leq PP_R < 50$, on the 20 maps derived using the "general" relationship of Table 7.5c. When overlapped with maps derived with the help of simultaneous radar data, 2.9%, 21.4%, 47% and 28.7% of these points correspond to level 2, 3, 4 and 5 respectively. Table 7.6b provides the same information, but with the "particular" points acting as the normalization basis. It is seen that 52% of the 55007 points of level 5 are suppressed, 41% become level 4, while 15.5% of the 68256 points of level 3 are declassified to level 2 for which no probability of rain is attributed. This explains the formation of the "hole" referred to earlier. The smoothing effect is also apparent by the smaller total of data for levels 4 and 5 in the "general" P_{RS} maps and by the converse result for levels 2 and 3.

Since the three available sequences constitute typical summer weather in the Montreal vicinity, the empirical relationship of Table 7.5c may be employed for similar meteorological conditions. Given a sufficiently large data base, analogous functions can be obtained for less convective situations in spring and fall. Radar data for other sites will eventually form the basis of parallel relationships for other geographical locations. At this moment, it cannot be ascertained to what extent these refinements will improve the ground truth verification of the "general" P_{RS} maps derived so far, nor is it possible to define a tolerable difference which will render superfluous the constant need of radar data.

7.3.2 Derivation of Rainfall Rate Information from Probability of Rain Maps.

In Lovejoy and Austin (1979a), an effort was made to separate light ($\leqslant 2$ mmh^{-1}) from "heavy" (> 2 mmh^{-1}) precipitation rates by examining the characteristics of the bivariate frequency distribution of the corresponding visible and infrared data. While the "occurrences of "heavy" rain were invariably shifted towards the high I.R., high visible end of the diagram, the shift was so small that when the probability of them coming from the same population was determined, the probability was almost always at least 80% that the samples had come from the same population."

However, following the production of P_{RS} maps, it became apparent that the higher PP_R contours were enclosed by the lower in a similar way that the core of higher rainfall rates in a shower is surrounded by lighter precipitation as viewed by the radar. This observation suggests that in part the lack of success of Lovejoy's rainfall rate discrimination technique was that the analysis was performed solely in "visible-infrared space" and it omitted to take into consideration the spatial information contained in the distribution

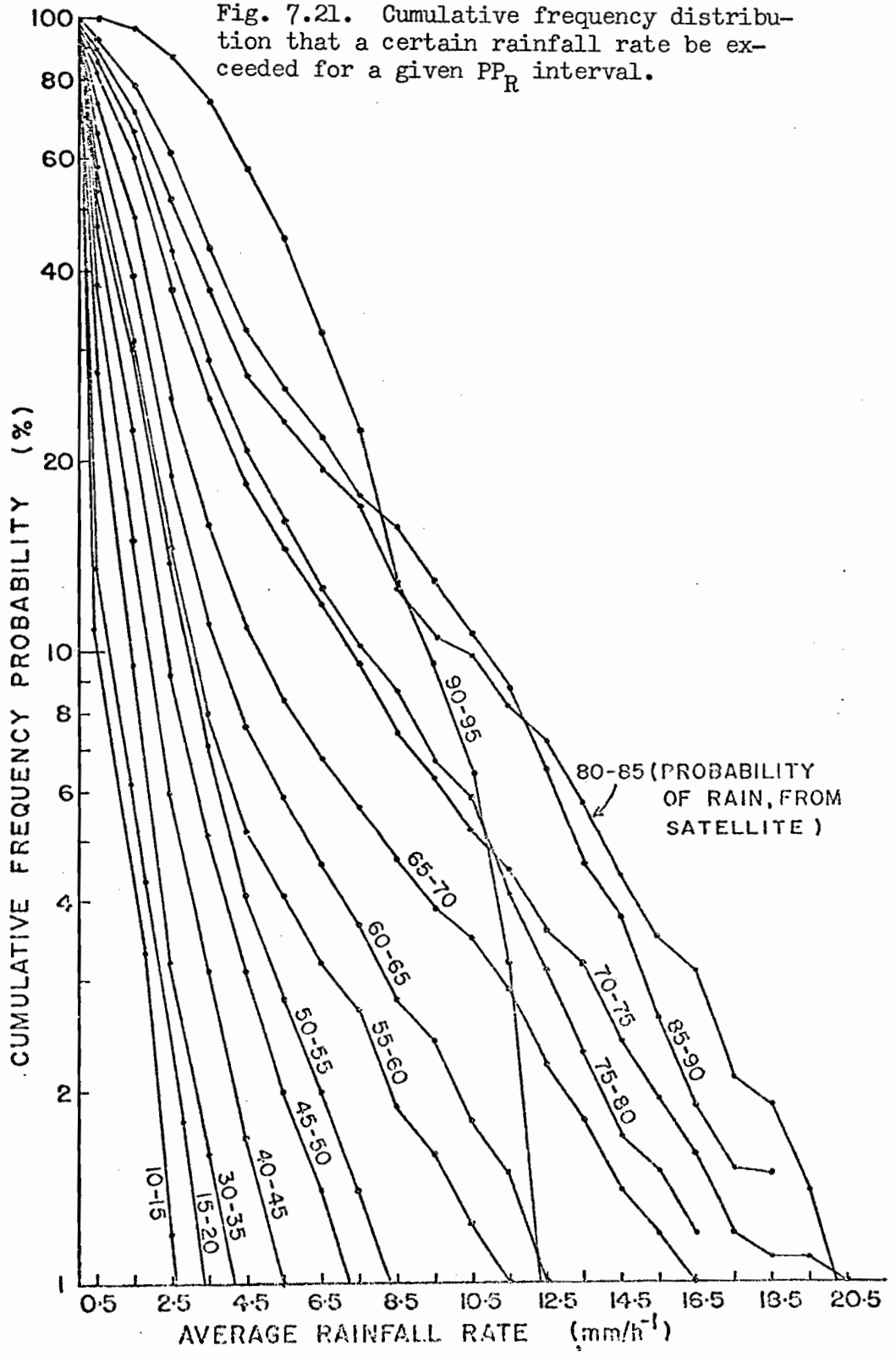

Fig. 7.21. Cumulative frequency distribution that a certain rainfall rate be exceeded for a given PP_R interval.

of rainfall rate as typified by a "concentric" storm model. Thus, a preliminary comparison between radar rainfall rates and PP_R values was attempted. The "general" relationship of Table 7.5c was applied to readily available data from Lovejoy's work to produce P_{RS} maps at (4 x 4) km^2 resolution. This comparison was limited to a range of 180 km since the accuracy of radar measured rainfall rates decreases beyond this range. Since the navigation of satellite imagery is accurate within 10 km, spatial adjustments between the two data sets were performed to obtain the best match. The comparison from each satellite and radar grid point is accumulated in a contingency table with intervals of 5 in PP_R and of 1 mmh^{-1} in rainfall rate. The result is displayed in Fig. 7.21 which provides the cumulative frequency probability distribution that a certain rainfall rate be exceeded with a given PP_R interval. For example, considering $60 \leqslant PP_R < 65$, there is a 40% chance that the rainfall rate exceeds 1.5 mmh^{-1}, a 12% chance that it is greater than 3.5 mmh^{-1} and a 2.4% chance that it is above 9.5 mmh^{-1}. While the heavier rainfall rates, say > 5 mmh^{-1}, are undoubtedly associated with the higher PP_R intervals, the cumulative probability is low, generally < 10%. At higher cumulative probability levels, about 40 or 50%, the interval $30 \leqslant PP_R \leqslant 90$ is constrained to rainfall rates between 0.4 and 3.5 mmh^{-1}. The "cross-over" at the higher PP_R intervals is caused by the lack of a sufficient data sample.

The principal statistics of this comparison are defined and presented on Table 7.7.

For each PP_R interval, an average rainfall rate RF can be computed. When the relationship which includes the no-rain points is plotted on semilog paper, Fig. 7.22, an exponential behaviour is apparent over nearly the entire $10 \leqslant PP_R \leqslant 90$ interval. It is also seen that the dynamic range in RF extends from 0.2 to $\sim$ 5 mmh^{-1}, or a factor of 25. This interpretation of curve (1) is misleading since, by definition, a PP_R value of 20 contains 80% non-raining

INTERVAL	PP_R LIMITS	INCLUDING "ZEROES"					EXCLUDING "ZEROES"			
		N_1	%	VOL (%)	RF_1	RMS	N_2	%	RF_2	RMS
1	10- 15	2877	6.7	1.2	0.18	552	311	1.7	1.70	155
2	15- 20	3367	7.8	1.7	0.22	380	459	2.5	1.59	105
3	20- 25	2582	6.0	1.8	0.30	302	502	2.8	1.53	99
4	25- 30	2162	5.0	1.9	0.37	307	492	2.7	1.61	117
5	30- 35	3494	8.1	3.5	0.43	243	971	5.3	1.55	96
6	35- 40	4544	10.5	5.7	0.53	220	1541	8.5	1.58	99
7	40- 45	4698	10.9	7.1	0.65	205	1802	9.9	1.68	100
8	45- 50	4171	9.7	8.8	0.90	176	1974	10.8	1.91	97
9	50- 55	2975	6.9	8.0	1.15	158	1593	8.7	2.15	93
10	55- 60	3569	8.3	11.0	1.31	166	2087	11.4	2.25	110
11	60- 65	2415	7.9	13.4	1.67	156	2257	12.4	2.53	113
12	65- 70	2091	4.9	10.8	2.21	159	1539	8.4	3.00	126
13	70- 75	1247	2.9	8.9	3.03	135	1024	5.6	3.69	115
14	75- 80	1034	2.4	7.7	3.19	112	892	4.9	3.69	97
15	80- 85	567	1.3	5.4	4.05	109	509	2.8	4.52	99
16	85- 90	260	0.6	2.7	4.43	94	242	1.3	4.75	87
17	90- 95	31	0.1	0.4	5.48	51	31	0.2	5.48	51
18	95-100	2	0.0	0.0	5.98	34	2	0.0	5.98	34

Table 7.7. Principal statistics of the comparison between PP_R intervals from the "general " PR_S maps and radar rainfall rates, both on a 4km grid.

N_1: Total number of radar areas per PP_R limit including the echo free areas.

VOL: Percentage contribution ot the total water volume from each PP_R interval.

RF_1: Rainfall rate (mm h^{-1}) per PP_R interval including the echo free areas.

N_2: Total number of radar areas with a rainfall rate $\geq$ 0.5 mm h^{-1} per PP_R interval.

RF_2: Rainfall rate (mm h^{-1}) per PP_R interval from radar areas exceeding the threshold of 0.5 mm h^{-1}.

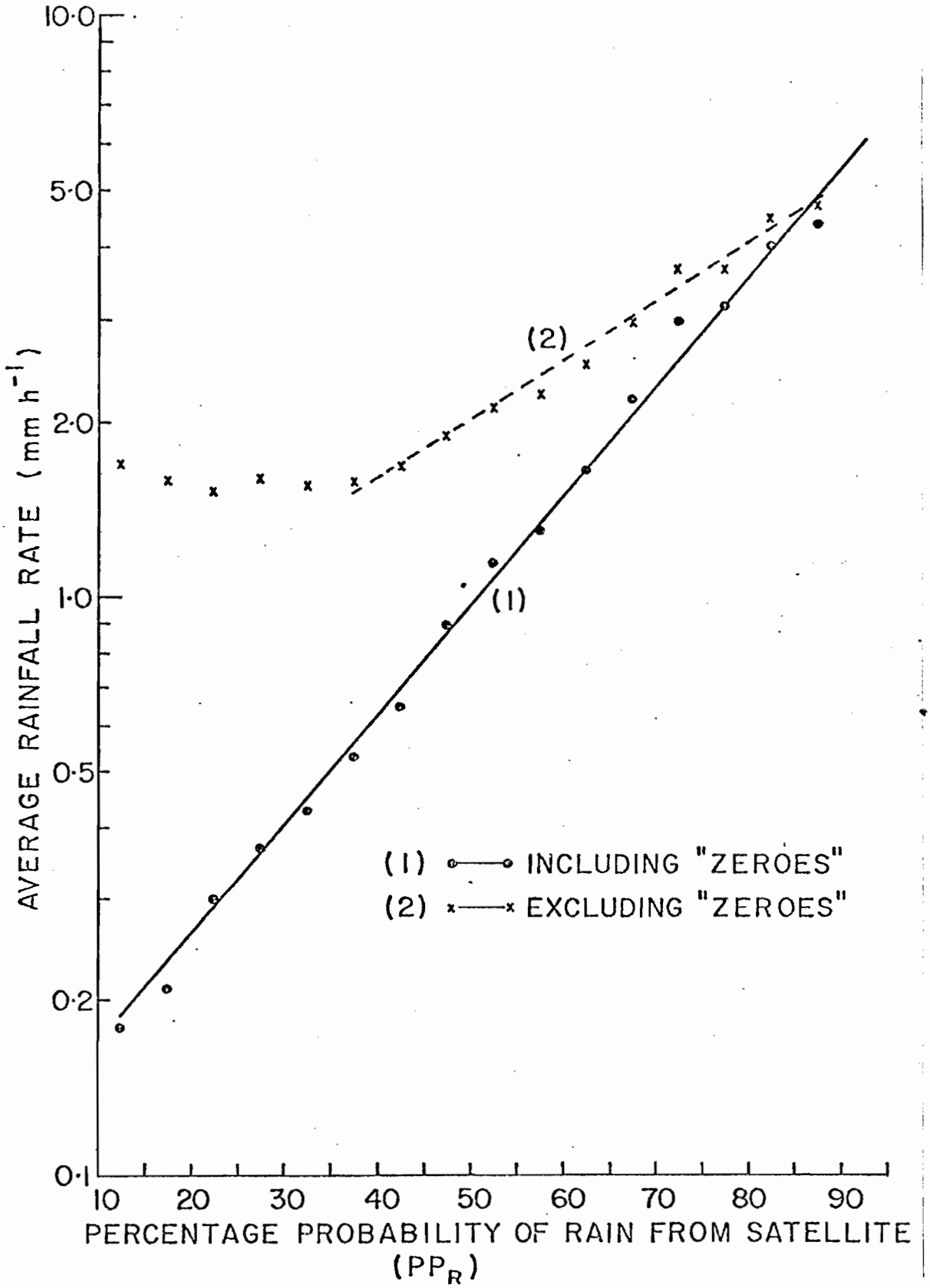

Fig. 7.22. Average rainfall rate corresponding to each PP_R interval, including and excluding the radar echo free grid areas.

points, thus artificially lowering the RF. Hence a $RF_{sat} = f(PP_R)$ relationship was computed by neglecting the non-raining points, curve (2). It is seen that a functional relationship exists only in the $35 \leq PP_R \leq 90$ interval. The slope is also significantly reduced, limiting the dynamic range in rainfall rate to a factor of $5/1.5 \simeq 3$. However, the RMS magnitudes, see Table 7.7, though necessarily reduced, are still large, of the order of 100%.

7.3.3 Hydrological Verification

The skill, if any, of $RF_{sat} = f(PP_R)$ as depicted in Fig. 7.22 can be evaluated only after comparison with other techniques. The relative merit of each is best assessed by computing the volume of water over a certain area. This volumetric rain is then compared with an acceptable ground truth standard, in our case, the radar data.

The total flux of water FØ summed over all the reliable A(I,J) grid areas of a matrix constituting a digital radar map can be formulated as

$$F\emptyset = \sum_{I=1}^{IDIM} \sum_{J=1}^{JDIM} AR(I,J) * RF_{rad}(I,J) \text{ where}$$

$RF_{rad}(I,J)$ is the radar rainfall rate corresponding to each elemental area (I,J) and

$$\sum_{I=1}^{IDIM} \sum_{J=1}^{JDIM} = \sum_{I,J} = N \text{ is the reliable area over an array of}$$

(IDIM x JDIM) ≡ (100 x 100)

For each of the available maps, FØ was compared with that derived from five other methods of flux determination. These are

1) $F1 = AR * \overline{RF}_{rad}$ where

$AR = \sum_{I,J} A(I,J)$ if $RF_{rad}(I,J) \geq$ lowest threshold on digital maps of $0.5\ mmh^{-1}$

$\overline{RF}_{rad}$ is a "climatological" rainfall rate. This average rainfall has been computed from the 3 available sequences of radar data as

$$\overline{RF}_{rad} = \frac{\sum_{i=1}^{20} F\emptyset_i}{\sum_{i=1}^{20} AR} = 2.31 \text{ mmh}^{-1}$$

This method estimates the flux from the measurement of echo coverage AR as provided by the radar.

2) $F2 = AS * \overline{RF}_{rad}$ where AS is the "satellite" rain area contained inside the $PP_R = 45$ contour as determined from Fig. 7.19. This method corresponds to the one adopted by Lovejoy and Austin. Other PP_R thresholds have also been tested to corroborate that $PP_R = 45$ does indeed constitute the best "general" delineation of raining and non-raining areas

3) $F3 = \sum_{I,J} AS(I,J) * (0.01 * PP_R(I,J)) * \overline{RF}_{rad}$

Here it is assumed that the "climatological" rainfall rate $\overline{RF}_{rad}$ applies to only a fraction, as implied by PP_R, of the elemental grid (I,J).

4) $F4 = \sum_{I,J} AS(I,J) * RF_1(I,J)_{sat}$ where

$RF_1(I,J)_{sat}$ is the rainfall rate obtained from curve (1) of Fig. 7.22 applied to the whole AS(I,J) element of the P_{RS} map which contains PP_R

5) $F5 = \sum_{I,J} AS(I,J) * (0.01 * PP_R(I,J)) * RF_2(I,J)_{sat}$ where

$RF_2(I,J)_{sat}$ is the rainfall rate obtained from curve (2) of Fig. 7.22. This rate is applied to a fraction of the AS(I,J) elemental area on a P_{RS} map as given by PP_R in it.

From the 20 maps, the average differences, absolute difference and RMS error of each method "X" has been computed as follows

	METHOD								
	1	2: PP_R value as indicated					3	4	5
		35	40	45	50	55			
DIF	-0.1	45.9	22.8	-0.4	-22.5	-37.7	-5.8	-4.9 (0.8)	-6.9 (-1.3)
|DIF|	18.9	50.9	33.4	20.2	28.3	37.8	19.3	16.8 (18.0)	16.5 (17.1)
RMS	23.5	56.8	37.4	26.5	34.3	45.8	24.5	22.2 (22.5)	22.1 (21.3)

Table 7.8a. Hydrological comparison of the various methods described in the text applied to an area within a 180 km radius from the radar.

	METHOD				
	1	2	3	4	5
No. of Cases	345	365	408	408	408
DIF	-0.1	-3.6	-7.5	-8.4 (-1.1)	-10.2 (-3.1)
|DIF|	40.6	61.3	63.3	54.6 (54.8)	56.0 (55.7)
RMS	79.5	105.4	117.5	100.5 (98.9)	103.2 (100.8)

Table 7.8b. Same as above but applied over the indicated number of subareas, each being (60 x 60) km^2.

$$DIF_X = 100 \sum_{i=1}^{20} \frac{(FX_i - F\emptyset_i)}{\sum_{i=1}^{20} F\emptyset_i} \qquad |DIF_X| = 100 \frac{\sum_{i=1}^{20} |FX_i - F\emptyset_i|}{\sum_{i=1}^{20} F\emptyset_i}$$

$$RMS = 100 \frac{\left\{ \sum_{i=1}^{20} \frac{(FX_i - F\emptyset_i)^2}{20} \right\}^{1/2}}{\overline{F\emptyset}} \qquad \text{were } \overline{F\emptyset} = \frac{\sum_{i=1}^{20} F\emptyset_i}{20}$$

A similar analysis has been carried out over smaller areas. Thus, each of the 20 maps has been divided into 25 sub-areas of (60 x 60) km^2. A comparison has not been performed for sub-areas for which $FX_i = F\emptyset_i = 0$. The results are summarized on Tables 7.8a and 7.8b.

Since by definition all methods are normalized with respect to echo coverage, the magnitude of DIF in Table 7.8a should be zero for all techniques. The various choices in method 2 establish once more $PP_R = 45$ as the optimum value. The negative differences for methods 3, 4 and 5 are not negligible because values of $PP_R < 10$ have been omitted in P_{RS} maps in accordance with the arbitrary rules of section 7.1. The results obtained by multiplying the rainfall rates of methods 4 and 5 by a factor, chosen as 1.06, are shown in brackets. The magnitudes of |DIF| and RMS are generally only marginally altered in both tables. Considering the |DIF| and RMS parameters of Table 7.8a, it is seen that both methods 4 and 5 achieve better estimates of rainfall than either method 1 or 2 with $PP_R = 45$. Thus, the introduction of "satellite" rainfall rates of curves (1) and (2) in Fig. 7.22 yields improved results of the order of 15% in relation to method 2 of rain and no-rain. Perhaps, it is more surprising to realize that significant ($\sim$ 5%) improvements are also observed with method 1. Over the smaller sub-areas, Table 7.8b, the advantage of 4 and 5 over method 2 is reduced, $\sim$ 5% in RMS and

$\sim$ 10% in $|DIF|$. Note the increase in the magnitudes of these parameters as the area is reduced by a factor of $\frac{\pi(180^2)}{60^2} = 28$. Observe that assumption 3 is not as adequate as 4 and 5 and, in fact, is inferior to method 2 over the smaller areas. As expected, the knowledge of the exact echo coverage over a smaller domain from radar, (method 1) yields superior results.

CHAPTER VIII

CONCLUSIONS

8.1 Current SHARP and RAINSAT Status

In our view, an appropriate measure of the degree of success of the work reported here is the extent to which this initial research has been implemented and accepted by the meteorological community. A quick review of the current status of the two main projects, SHARP and RAINSAT, will attest to their usefulness in assisting the forecasters and in the latter's eagerness to obtain more diversified products. In this respect, the outcome is surpassing even the most optimistic expectations at the beginning of this research.

a) SHARP

The SHARP project is in continued operation. The 1978 version was conducted in the same fashion as that described for 1977. However, since during the summer of 1979 the regular analogue output which provided CAPPI's as often as every 5 minutes to the Quebec Forecast Office was discontinued, the SHARP program was updated to supply a greater variety of products more often than once an hour. Hence, archiving of the 3-D raw data was assigned to a smaller PDP11/10 computer, enabling the PDP11/40 to be totally dedicated to SHARP. After consultations with the Quebec Forecast Office personnel, the following hourly schedule was adopted as shown on the table below.

HOURLY SEGMENT	TIME	FUNCTION OR MAP COMPUTED
1	00:00	archive
2	00:05	3 km CAPPI
3	00:10	archive
4	00:15	CAPPHI (at 3 km)
5	00:20	archive
6	00:25	ETPPI
7	00:30	archive
8	00:35	3 km CAPPI as a 2-hour forecast based on 30 minute of history, plus station forecasts

9	00:40	archive
10	00:45	CAPPHI (at 3 km)
11	00:50	archive
12	00:55	hydrology map
1	01:00	archive
2	01:05	3 km CAPPI as a 2-hour forecast based on 30 minute of history, plus station forecasts
3	01:10	archive
4	01:15	CAPPHI (at 3 km)

etc.

Table 8.1 Hourly schedule of radar products sent to the Quebec Forecast Office during summer operation since 1979.

It is seen that two forecasts per hour are issued, each being based on 30 minutes of history. This increased frequency is greatly appreciated by the forecasters in updating the past velocity and the station forecasts. It has been observed that the pattern recognition technique applied to the shorter time interval yielded a more accurate velocity determination, as evidenced by the nearly constant velocities obtained for successive forecasts. This was achieved in spite of the low spatial resolution by improving the method of estimating displacements in fractions of a grid length.

The hydrological output consists of a rainfall accumulation initialized at four specific times (000Z, 0600Z, 1200Z, 1800Z), with a final 24-hour accumulation at 1200Z. An example of the latter is given in Fig. 2.11. It is computed from 10 minute CAPPI's stored during the hourly cycle. The known velocity is used to counteract quantization effects arising when the 10 minute displacement exceeds a grid length.

One important feature which is currently under implementation is the interactive communication through modem between forecasters and the computer. This in fact becomes essential when a cross-section or magnification of a specific echo is desired. The usefulness of these products is evident when scrutiny of high intensity scores is imperative in denoting areas of severe weather or in locating the presence of a bright band as illustrated in Chapter V.

b) RAINSAT

As a consequence of work on this topic, an operational scheme has been devised and is expected to be in real-time operation in Toronto for the summer of 1981. It is realized that the results reported here constitute only a partial step towards the improvement of short range forecasting using satellite data; however, the immediate implementation of a prototype procedure into real-time continuous operation will speed up the evolution of a complete system based on experience and results from a large number of cases. As in SHARP, we hope that it will expand and lead to as many useful products.

8.2 Summary of Thesis

The most salient results and contribution arising from this research are summarized below.

a) In the first two summers of operation, SHARP performed successfully in real-time for nearly 2000 hours at a reliability of about 90%. Dependable forecasts in the form of 3 km CAPPI maps followed by specific station forecasts were automatically issued to a remote weather office. The capability to monitor the approach of high rainfall rates toward particular stations by means of "sector" and "line" forecasts as shown in Fig. 3.3b was considered highly practical. Potentially erroneous forecasts due to anomalous propagation and gross matching errors were correctly rejected by the computer

according to predetermined criteria. The assignment of a computer totally dedicated to SHARP has permitted a rapid expansion of the system in terms of a variety of radar maps since the 1979 summer season.

b) The analysis of results in terms of Critical Success Index indicated that the forecast technique adopted represents nearly the best accuracy that can be attained under the "status quo" assumption. The major portion of forecastibility loss is attributed to the development and dissipation of weather patterns rather than to errors in their forecast motion. This realization precludes the need of more sophisticated models for determining radar echo displacement in the Montreal area. Inclusion of a statistical technique which modifies radar echoes according to their evolution has resulted in minimal improvement. Curves showing the decay with time of the forecast skill of various techniques revealed that the "nowcasting" technique displays skill up to a maximum of three hours.

c) The large amount of data collected during the test permitted the determination of preferred regions of storm development and decay, a significant step into radar climatology. The two-year comparison revealed that some regions associated with growth or decay are related to terrain effects while others vary from year to year.

d) The examination of the vertical structure of precipitation patterns has demonstrated the usefulness of 2 km CAPPI maps for certain weather situations, as well as the necessity of having vertical cross-sections for the localization of a possible bright band. Analysis of trajectories derived from 30- and 60-minute displacements showed that a shorter time interval yields a better motion estimate for a wider variety of weather situations, but in particular for extensive systems associated with snowstorms.

e) The need to extend forecast lead times resulted in a short range precipitation forecast procedure using combined radar and satellite data.

The latter set has been mapped by means of a conic projection on a Cartesian grid with constant resolution in order to reduce distortion and to facilitate overlay with synoptic charts.

f) The "rain, no-rain" scheme originally developed by Lovejoy and Austin (1979a) has been improved by introducing the concept of a probability of rain map which bears a greater resemblance to patterns of radar echoes.

g) A pattern recognition algorithm applied to sub-areas of the entire satellite map has proved successful in tracking the displacement of the probability of rain contours. Good accord was observed between the trajectories of these rain areas and the 700 mb wind.

h) A general relationship between satellite visible-infrared imagery and probability of rain has been compiled to permit functioning of the procedure when radar data are unavailable.

i) An empirical relationship has been formulated between probability of rain from satellite and radar rainfall rate. Its comparison with the "climatological" approach resulted in a reduction of 15% in the RMS error in the computation of rainfall flux over an area comprised within a radar range of 180 km.

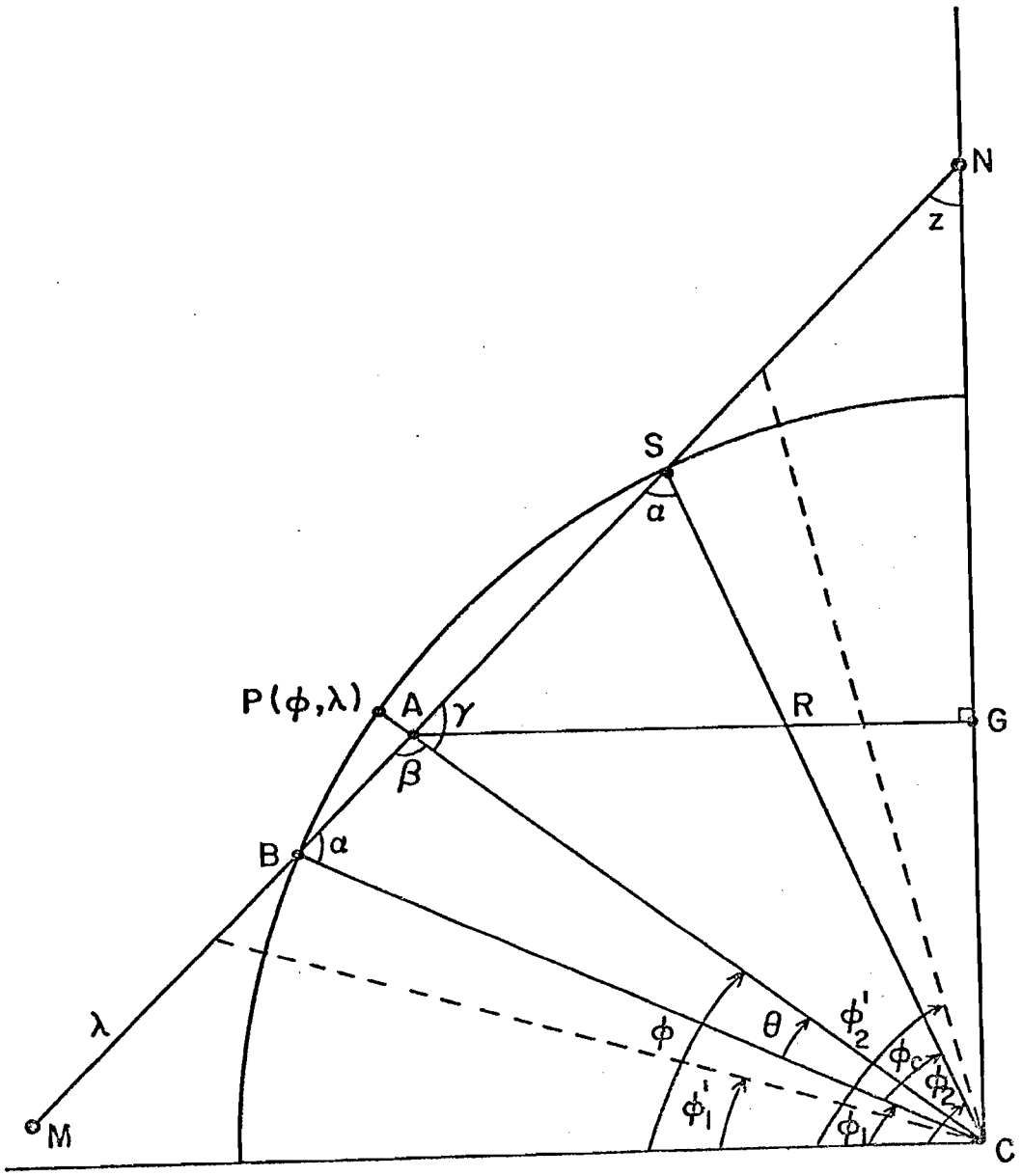

Fig. A.1 Cross-sectional view at any longitude λ of a cone cutting through the earth's surface at latitudes ϕ_1 and ϕ_2 unto which a point $P(\phi,\lambda)$ on the earth's surface is to be projected.

APPENDIX A

Conic Projection of the Earth True at Two Standard Parallels

In Fig. A.1, let R = radius of the earth = 6371.1 km

(ϕ_1, ϕ_2) = the two standard parallels and

(ϕ_1', ϕ_2') = latitudes limiting the size of the projection.

Since 2/3 of the area must be between the two standard parallels in order to keep distortion to a minimum (Maling 1973)

$$\phi_c = \phi_2 - \phi_1 \doteq 2/3\ (\phi_2' - \phi_1')$$

Let NM be a line along any longitude λ on the surface of a cone which cuts the earth's surface at latitudes ϕ_1 and ϕ_2 at points B and S respectively. Let $P(\phi,\lambda)$ be a point on the earth's surface of latitude ϕ and longitude λ to be projected along the earth radius vector R at point A on the cone. Our goal is to derive the equations for x and y measured on a two-dimensional plane, Fig. A.2.

Since BSC is an isosceles triangle,

$$2\alpha + \phi_c = 180^\circ \qquad \alpha = 90 - \frac{\phi_c}{2}$$

In triangle BAC,

$$\beta + \alpha + \theta = 180^\circ \quad \text{where } \theta = \phi - \phi_1$$

$$\beta = \chi + 1/2\ (\phi_2 + \phi_1) \text{ where } \chi = \text{colatitude} = 90 - \phi$$

From the solution of the oblique triangle BAC,

$$CA = R \sin \alpha / \sin\beta \quad \text{eq. (1)}$$

In triangle CSN, $z = \alpha + \phi_2 - 90 = \frac{1}{2}(\phi_1 + \phi_2)$

From the solution of the oblique triangle NAC,

$$NA = CA \cos \phi / \sin z$$

Substituting for CA from eq. (1),

$$NA = R \frac{\sin \alpha \cos \phi}{\sin \beta \sin z} \quad \text{eq. (2)}$$

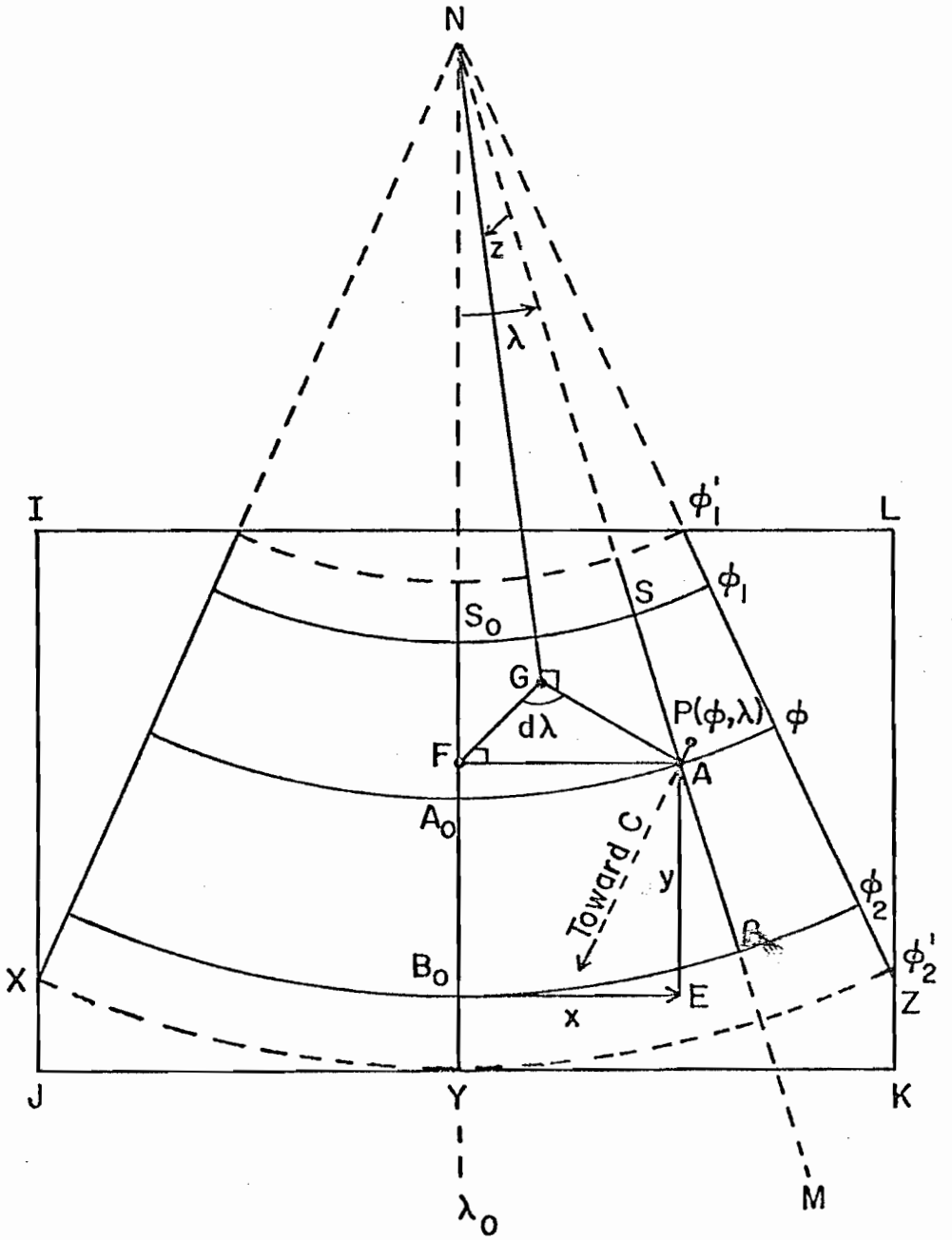

Fig. A.2 Same as Fig. A.1 viewed in its longitudinal extend. Earth's coordinates (ϕ,λ) as transformed into Cartesian components (x,y).

and $NB = R \cos \phi_1 / \sin z$ eq. (3)

Let Fig. A.2 represent the projection of the cone NXYZ into a two-dimensional plane inside rectangle IJKL. Note that Fig. A.1 is a cross-section of Fig. A.2 along line NSABM and the axis through the North Pole.

Let B_o be the origin of the Cartesian axes at the intersection of ϕ_2 and the middle latitude λ_o. In all maps, $\lambda_o = 75°W$.

Visualize G in Fig. A.2 as being into the paper, on the axis through the North pole - see also Fig. A.1 - such that $\angle FGA = d\lambda$ where

$d\lambda = \lambda - \lambda_o$, F is on line NB_o and $\angle GFA = 90$

Then,

$x = GA \sin d\lambda$.

From Fig. A.1, $GA = NA \sin z$ and using eq. (2),

$x = R' \dfrac{\cos\phi \sin d\lambda}{\sin\beta}$ eq. (4) where $R' = R \sin \alpha$

$y = NB_o - NF$

$= NB - NA \cos \gamma$ where $\gamma = \angle FNA$ on the plane of IJKL

Since $x = NA \sin z \sin d\lambda$,

then $\sin z \sin d\lambda = x/NA = \sin \gamma$

From the trigonometric relation $\cos \gamma = \pm \sqrt{1 - \sin^2 \gamma}$ and substituting eqs. (2) and (3),

$$y = \frac{R \cos \phi_1}{\sin z} - R \frac{\sin\alpha \cos\phi}{\sin\beta \sin z} \sqrt{1 - \sin^2 z \sin^2 d\lambda}$$

$$y = R'' \left[K - \frac{\cos \phi}{\sin\beta} \sqrt{1 - \sin^2 z \sin^2 d\lambda}\right] \text{ eq. (5)}$$

where $R'' = \dfrac{R \sin\alpha}{\sin z}$ and $K = \dfrac{\cos \phi_1}{\sin\alpha}$

The pair (x,y) are then translated to a new origin on the NW corner of the map and reduced to a pair of subscripts (I,J) of a two-dimensional matrix by an appropriate scale factor which is a function of the grid length used.

It will be explained that the inverse relationships are more useful to achieve fast computational speeds. They are derived by algebraic manipulations of eq. (4) and (5). They are

$$d\lambda = \sin^{-1} \left(\frac{1}{\sin z \left[1 + \frac{1}{x^2} (R''K - y)^2\right]^{1/2}} \right) \qquad \text{eq. (6)}$$

where $\lambda = \lambda_o + d\lambda$ and

$$\phi = \tan^{-1} \left(\frac{R'' \sin d\lambda}{x} - \cot z \right) \quad \text{eq. (7).}$$

REFERENCES

1. Austin, G.L., and A. Bellon, 1974: The use of digital weather records for short-term precipitation forecasting. Quart. J. Roy. Meteor. Soc., 100, 658-664.

2. Bellon, A. and G.L. Austin, 1977: Short-term automated radar prediction. Final report for AES (DSS) Contract 01SU.KM 601-4-758. [Available from the Stormy Weather Group, McGill University, Montreal, Quebec, Canada]

3. Bellon, A. and G.L. Austin, 1978: The evaluation of two years of real-time operation of a short-term precipitation forecasting procedure (SHARP), J. Appl. Meteor., 17, 1778-1787.

4. Blackmer, R.H., Jr., R.O. Duda and E. Reboh, 1973: Application of pattern recognition techniques to digitized weather radar data. Final Report, covering period 31 March 1972 to April 1973, Contract 1-36072, Stanford Research Institute.

5. Boucher, R.J., 1963: Radar precipitation echo motion and suggested prediction techniques. Proc. 10th Weath. Radar Conf., pp 1-7, Am. Meteorol. Soc., Boston.

6. Browning, K.A., F.F. Hill and C.W. Pardoe, 1974: Structure and mechanism of precipitation and the effect of orography in a wintertime warm sector, Quart. J. Roy. Meteor. Soc., 100, 309-330.

7. Browning, K.A., C.W. Purdoe and F.F. Hill, 1975: The nature of orographic rain at wintertime cold fronts. Quart. J. Roy. Meteor. Soc., 101, 333-352.

8. Browning, K.A., 1979: The FRONTIERS plan; a strategy for using radar and satellite imagery for very short-range precipitation forecasting. Meteorol. Mag. 108, 161-184.

9. Carlson, P.E. and J.S. Marshall, 1972: Measurement of snowfall by radar, J. Appl. Meteor. 11, 494-500.

10. Collier, C.G., S. Lovejoy and G.L. Austin, 1980: Analysis of bright bands from 3-D radar data. Proc. 19th Weather Radar Conf., pp. 44-47 Amer. Meteorol. Soc., Boston.

11. Donaldson, R.J., R.M. Dyer and M.J. Kraus, 1965: An objective evaluation of techniques for predicting severe weather events. Preprints 9th Conf. Severe Local Storms, Norman, Amer. Meteor. Soc., 321-326.

12. Drufuca, G. and I.I. Zawadzki, 1975: Statistics of raingage data. J. Appl. Meteor., 14, 1419-1429.

13. Drufuca, G., 1977: Radar-derived statistics on the structure of precipitation patterns, J. Appl. Meteor., 16, 1029-1035.

14. Duda, R.O. and R.H. Blackmer, Jr., 1972: Application of pattern recognition techniques to digitized radar data. Proc. 15th Weath. Radar Conf., pp 138-143, Am. Meteorol. Soc., Boston.

15. Elvander, R.C., 1976: An evaluation of the relative performance of three weather radar echo forecasting techniques, Proc. 17th Weath. Radar Conf., pp 526-532, Am. Meteorol. Soc., Boston.

16. Endlich, R.M., D.E. Wolf, D.J. Hall and A.E. Brain, 1971: Use of a pattern recognition technique for determining cloud motions from sequences of satellite photographs, J. Appl. Meteorol., 10, 105-117.

17. Follansbee, W., 1973: Estimation of average daily rainfall from satellite cloud photographs. NOAA Tech. Memo. NESS44.

18. Follansbee, W., and V.J. Oliver, 1975: A comparison of infrared imagery and video pictures in the estimation of daily rainfall from satellite data. NOAA Tech. Memo. NESS 62.

19. Greene, D.R., 1972: A comparison of echo predictability: constant elevation vs VIL radar-data patterns., Proc. 15th Weath. Radar Conf., 111-116, Am. Meteorol. Soc., Boston.

20. Griffith, C., and W.L. Woodley, 1973: On the variation with height of the top brightness of precipitating convective clouds, J. Appl. Meteor. 12, 1086-1089.

21. Griffith, C., W.L. Woodley, G. Gruber, D.W. Martin, J. Stout and D.N. Sikdar, 1978: Rain estimation from geosynchronous satellite imagery - visible and infrared studies. Mon. Wea. Rev., 106, 1153-1171.

22. Gruber, A., 1973: Estimating rainfall in regions of active convection. J. Appl. Meteor. 12, 110-118.

23. Harper, W.C., and J.G.D. Beimers, 1958: The Movement of precipitation belts as observed by radar. Quart. J. Roy. Meteor. Soc., 84, 242-249.

24. Hilst, G.R. and J.A. Russo, Jr., 1960: An objective extrapolation technique for semi-conservative fields with an application to radar patterns, Tech. Memo. No. 3, Contract AF30-635-14459, The Travelers Weather Research Center, Inc.

25. Johnson, G.N., P.L. Smith, F.E. Nathanson and L.W. Brooks, 1975: An analysis of techniques for dealing with anomalous propagation. Proc. 16th Weather Radar Conf., 374-377, Am. Meteorol. Soc., Boston.

26. Kessler, E., III, 1961: Appraisal of the use of radar in observation and forecasting. Proc. 9th Weath. Radar Conf., 13-36, Am. Meteorol. Soc. Boston.

27. Kessler, E., III, and J.A. Russo, Jr., 1963: A program for the assembly and display of radar-echo distributions. J. Appl. Meteorol. 12, 582-593.

28. Kessler, E., III, 1966: Computer program for calculating average length of weather radar echoes and pattern bandedness. J. Atmospheric Sciences, 23, No. 5, 569-574.

29. Kilonsky, B.J. and C.S. Ramage 1976: A technique for estimating tropical open-ocean rainfall from satellite observations. J. Appl. Meteor. 15, 972-975.

30. Klein, W.H. and H.R. Glahn, 1974: Forecasting local weather by means of model output statistics, Bull. Amer. Meteor. Soc. 55, 1217-1227.

31. Klein, W.H., 1976: The AFOS program and future forecast applications., Mon. Wea. Rev. 14, 1494-1504.

32. Konrad, T.G., 1978: Statistical models of summer rainshowers derived from fine-scale radar observations. J. Appl. Meteor. 17, 171-188.

33. Leese, J.A., C.S. Novak and B.B. Clark, 1971: An automated technique for obtaining cloud motion from geosynchronous satellite data using cross-correlation. J. Appl. Meteorol. 10, 118-132.

34. Lovejoy, S. and G.L. Austin, 1979a: The delineation of rain areas from visible and IR satellite data for GATE and mid-latitudes. Atmos-Ocean 17, 77-92.

35. Lovejoy, S. and G.L. Austin, 1979b: The sources of error in rain amount estimating schemes from GOES visible and IR satellite data. Mon. Wea. Rev. 107, 1048-1054.

36. Maling, D.H., 1973: Coordinate systems and map projections, George Philip and Sons Ltd., London.

37. Marois, B., 1977: Evaluation du programme SHARP dans l'exploitation d'un bureau de prevision meteorologique. Final report prepared for the Quebec Forecast Office, 44 pages.

38. Marshall, J.S. and C.D. Holtz, 1970: Pattern analysis of one summer's multi-level maps of Montreal rain. Mon. Wea. Rev. 98, 335-345.

39. Marshall, J.S. and E.H. Ballantyne, 1970: McGill Weather Radar: New research and remote displays. Proc. 14th Weather Radar Conf., 407-410, Am. Meteor. Soc., Boston.

40. Marshall, J.S. and E.H. Ballantyne, 1975: Weather surveillance radar, J. App. Meteor., 14, 1317-1338.

41. Martin, D.W., and W.E. Suomi, 1972: A satellite study of cloud clusters over the tropical North Atlantic Ocean. Bull. Amer. Meteor. Soc. 53, 135-156.

42. Martin, D.W., and W.D. Scherer, 1973: Review of satellite rainfall estimation methods. Bull. Amer. Meteor. Soc. 54, 661-674.

43. Mosher, F., 1975, Appendix to: D.W. Martin, J. Stout, and D.N. Sikdar, GATE area rain estimation from satellite images, Report on NOAA grant 04-5-158-47, Space Sci. and Eng. Center, University of Wisconsin, Madison.

44. Mohr, C.G. and R.L. Vaughan, 1979: An economical procedure for cartesian interpolation and display of reflectivity factor data in three-dimensional space, J. Appl. Meteor. 18, 661-670.

45. Muench, H.S., 1976: Use of digital radar data in severe weather forecasting. Bull. Amer. Meteor. Soc. 57, 298-303.

46. Newton, C.W., and S. Katz, 1958: Movement of large convective rainstorms in relation to winds aloft. Bull. Amer. Meteor. Soc. 39, 129-136.

47. Pytlowany, P.J., and W.D. Scherer, 1975: Numerical interpolation techniques of digital radar data from Gate, Proc. 16th Weather Radar Conf., 194-199, Am. Meteorol. Soc., Boston.

48. Reynolds, D., and T.H. Vonder Haar, 1973: A comparison of radar-determined cloud height and reflected solar radiance measured from the geosynchronous satellite ATS-3. J. Appl. Meteor. 12, 1082-1085.

49. Reynolds, D.W., M.L. Brown, E.A. Smith, and T.H. Vonder Haar, 1978: Cloud type separation by spectral differencing of image pairs. Mon. Wea. Rev. 106, 1214-1218.

50. Reynolds, D.W. and E.A. Smith, 1979: A detailed analysis of composited digital radar and satellite data. Bull. Amer. Met. Soc. 60, 1024-1037.

51. Saffle, R.E., 1976: D/RADEX products and field operation, Proc. 17th Weather Radar Conf., 555-559, Am. Meteorol. Soc., Boston.

52. Scofield, R.A. and V.J. Oliver, 1977: A scheme for estimating convective rainfall from satellite imagery. NOAA Tech. Memo. NESS 86.

53. Sikdar, D.N., 1972: ATS-3 observed cloud brightness field related to a meso-to-synoptic-scale rainfall pattern. Tellus 24, 400-413.

54. Smith, E.A. and D.R. Phillips, 1972: Automated cloud tracking using precisely aligned digital ATS pictures. IEEE Trans. Comput. C-21, 715-729.

55. Stout, E.J., D.W. Martin and D.N. Sikdar, 1979: Estimating GATE rainfall with Geosynchronous Satellite Images. Mon. Wea. Rev. 107, 585-598.

56. Thomas, R.D. and D.D. Houghton, 1979: The relationship between cold-frontal radar echoes and selected surface kinematic parameters. Mon. Wea. Rev. 107, 1589-1599.

57. Wilk, K.E. and K.C. Gray, 1970: Processing and analysis techniques used with the NSSL weather radar system, Proc. 14th Weather Radar Conf., 369-374, Am. Meteorol. Soc., Boston.

58. Wilson, J.W., 1966: Movement and predictability of radar echoes. U.S. Weather Bureau, Contract Cwb-11093, The Travelers Weather Research Center, Inc.

59. Wilson, J.W. and E.A. Brandes, 1979: Radar measurement of rainfall - a summary. Bull. Amer. Meteorol.. Soc. 60, 1048-1058.

60. Wolf, D.E., D.J. Hall and R.M. Endlich, 1977: Experiments in automatic cloud tracking using SMS-GOES data. J. Appl. Meteor. 16, 1219-1230.

61. Woodley, W.L. and B. Sancho, 1971: A first step toward rainfall estimation from satellite cloud photographs. Weather 26, 279-289.

62. Wylie, D.P. 1979: An application of a geostationary satellite rain estimation technique to an extra-tropical area. J. Appl. Meteor. 18, 1640-1648.

63. Zawadzki, I.I. and E. Ballantyne, 1968: HARPI, 1967 - The development and use of a height-azimuth-range position indicator. [Available from Stormy Weather Group, McGill University, Montreal, Quebec, Canada].

64. Zawadzki, I.I., 1973: Statistical properties of precipitation patterns. J. Appl. Meteorol. 12, 459-472.

65. Zawadzki, I.I., 1975: On radar-raingage comparison. J. Appl. Meteor. 14, 1430-1436.

66. Zawadzki, I.I. and C.V. Ro, 1978: Correlations between maximum rate of precipitation and mesoscale parameters. J. Appl. Meteor. 107, 1327-1334.

67. Zawadzki, I.I. 1980: On the boundary conditions for convection. Proc. 8th International Cloud Physics Conf., 577-580, Am. Meteorol. Soc., Boston.

68. Zittel, W.D., 1976: Computer applications and techniques for storm tracking and warning. Proc. 17th Weath. Radar Conf. 514-521. Am. Meteorol. Soc., Boston.